An Extended Biphasic Description of the Inhomogeneous and Anisotropic Intervertebral Disc

Von der Fakultät Bau- und Umweltingenieurwissenschaften
der Universität Stuttgart zur Erlangung der Würde
eines Doktor-Ingenieurs (Dr.-Ing.)
genehmigte Abhandlung

Vorgelegt von

Dipl.-Ing. Nils Karajan

aus
Waiblingen

Hauptberichter:	Prof. Dr.-Ing. Wolfgang Ehlers
Mitberichter:	Prof. Dr.-Ing. Jörg Schröder

Tag der mündlichen Prüfung: 31. März 2009

Institut für Mechanik (Bauwesen) der Universität Stuttgart
Lehrstuhl für Kontinuumsmechanik, Prof. Dr.-Ing. W. Ehlers

2009

Report No. II-19
Institut für Mechanik (Bauwesen)
Lehrstuhl für Kontinuumsmechanik
Universität Stuttgart, Germany, 2009

Editor:
Prof. Dr.-Ing. W. Ehlers

© Nils Karajan
Institut für Mechanik (Bauwesen)
Lehrstuhl für Kontinuumsmechanik
Universität Stuttgart
Pfaffenwaldring 7
70569 Stuttgart, Germany

Printed by DIP – Digital Print, Witten, Germany, 2009

ISBN 978 – 3 – 937399 – 19 – 4
(D 93 – Dissertation, Universität Stuttgart)

Acknowledgements

The work presented in this thesis was carried out between 2003 and 2009, while I was an assistant lecturer at the Institute of Applied Mechanics (Civil Engineering) Chair II (Continuum Mechanics), at the Universität Stuttgart. Over this period of time, numerous people at the institute contributed in many ways to the realisation of this work - all their support is most gratefully acknowledged.

First of all I want to thank my supervisor and teacher Professor Wolfgang Ehlers for giving me the opportunity to prepare my thesis at his institute as well as for his scientific support. His door was always open for questions, which often led to very interesting and fruitful discussions. Without any doubt, it is his broad knowledge in the field of continuum mechanics that built the important foundation for this work.

I am also much obliged to Professor Jörg Schröder for taking the first co-chair in my promotion procedure and for preparing the required documents in such an incredibly short amount of time. I always enjoyed meeting him at conferences, where we had the chance to discuss topics in the broad field of mechanics at almost any time of the day.

Next, I want to thank Professor Christian Wieners for our great collaboration regarding the realisation of the parallel computations presented in this work. Without his knowledge and the previous work of my former colleague Dr.-Ing. Martin Ammann concerning the interface of M++/PANDAS, the simulations of such large problems would have caused many more difficulties. In this regard, I owe special thanks to Martin, who introduced me very carefully into the particulars of programming in PANDAS.

Keeping in mind that biomechanics was a rather new experience for me as a civil engineer, I also want to thank Professor Gerhard Holzapfel for his inspiration and for providing access to valuable experimental data. Professor Hans-Joachim Wilke is also acknowledged for giving me the opportunity to actually put me in contact with experiments that used human intervertebral discs.

Moreover, I want to thank all of my colleagues at the institute for creating such a friendly working atmosphere. It was always a pleasure to come to work every morning. I also want to thank Dr.-Ing. Bernd Markert as a partner for prolific discussions. The work of my friends Uwe Rempler and Dr.-Ing. Ayhan Acartürk as system administrators is also highly appreciated regarding their assistance in solving software issues. Finally, I would like to thank Oliver Klar for the great times we had. You are always in my heart.

Last but not least, I want to thank my family and especially my parents, who always believed in my ideas and supported my enthusiasm, no matter what it was. It is through their lovingly and open-minded support that I successfully accomplished all the steps necessary to reach this point in life. Thank you.

Stuttgart, March 2009 Nils Karajan

So einfach wie möglich. Aber nicht einfacher.
Albert Einstein (1879 – 1955)

Contents

List of Figures

Deutsche Zusammenfassung

Motivation

Klinische Gesichtspunkte: In industrialisierten westlichen Ländern hat eigentlich so gut wie jeder schon mindestens einmal in seinem Leben Bekanntschaft mit Rückenschmerzen in der Lendengegend gemacht. Zwei repräsentative Studien von Raspe *et al.* [166] und Schmidt *et al.* [174], die Anfang der Neunziger und zehn Jahre später erneut durchgeführt wurden, bestätigen diesen Sachverhalt für die deutsche Bevölkerung. In Bezug auf die genannten Studien sowie einer weiteren von Latza *et al.* [117] wurden von ca. 40 % der Befragten akute Rückenschmerzen angegeben, wobei 21 % sogar unter heftigen Schmerzen litten. Des Weiteren sind in vielen europäischen Ländern Rückenschmerzen die Nummer eins der arbeitsbedingten Gesundheitsprobleme. Dies bestätigt auch die zweite „European survey on working conditions“ von Paoli [159], die von durchschnittlich 30 % der arbeitenden Bevölkerung mit Rückenschmerzen berichtet. Die vierte Umfrage in 2007 von Parent-Thirion *et al.* [161] hingegen verzeichnet einen leichten Rückgang auf 25 %. Nach dem Bericht der „European Foundation for the Improvement of Living and Working Conditions“ [72] sind die arbeitsbedingten Rückenschmerzen von der Berufsgruppe abhängig und es ergeben sich Extremwerte von 16 % der Betroffenen mit Bürotätigkeit bis zu 58 % der Betroffenen im (maschinisierten) landwirtschaftlichen Bereich. Da beide Berufsgruppen meistens sitzend arbeiten kann der prozentuale Unterschied nur durch die enormen Vibrationen der Ackerbaumaschinen erklärt werden, siehe Lis *et al.* [124].

Diese signifikante Anzahl an Betroffenen hat nicht nur einen bemerkenswerten Einfluss auf die direkten medizinischen Versorgungskosten sondern darüber hinaus auch einen sozioökonomischen Einfluss. In Deutschland fallen zum Beispiel Jahr für Jahr ca. 4 % des gesamten Arbeitskräftepotentials aufgrund von Rückenschmerzen aus. Natürlich spielen neben den monetären Faktoren auch noch die Schmerzen eine große Rolle, die die betroffenen Patienten aushalten müssen. Während die Ursache für Rückenschmerzen bei vielen Patienten immer noch unklar ist, werden geschädigte Bandscheiben als Schmerzquelle weitläufig akzeptiert, siehe Vanharanta *et al.* [215]. Mehr Detailinformationen im Bezug auf die traumatische und degenerierte Bandscheibe sowie deren medizinische Behandlung können in Wilke & Claes [232] nachgelesen werden. In diesem Zusammenhang sind viele Behandlungswege möglich, wobei in schwerwiegenden Fällen am besten die betroffenen Wirbelkörper fusioniert werden bzw. die zerstörte Bandscheibe durch ein geeignetes Implantat ersetzt wird, das im Idealfall auf mechanische Belastung wie die natürliche Bandscheibe reagiert.

Die oben geschilderte Gesundheitsstatistik über Rückenschmerzen in der Bevölkerung war Motivation genug um in den letzten drei Jahrzehnten ein bemerkenswertes wissenschaftliches Interesse an der Problematik der Bandscheiben-Mechanik zu generieren. Gestützt durch das ständig wachsende Potential an Rechenleistung sind sich immer mehr Forscher darüber einig, dass numerische Simulationen weitere Möglichkeiten zur Erklärung und Lösung von Rückenschmerzen bieten.

Biomechanische Gesichtspunkte: Die biomechanische Herausforderung liegt in der strukturellen Komplexität der Wirbelsäule, die sich in stark individuellen Patientendaten sowie unregelmäßigen und schwer bestimmbaren dreidimensionalen anatomischen Geometrien widerspiegelt. Die Bandscheibe, auch Zwischenwirbelscheibe genannt, befindet sich zwischen jeweils zwei benachbarten Wirbelkörpern und bildet mit ihnen ein Bewegungssegment der Wirbelsäule. Wird die Bandscheibe herauspräpariert können in einem axialen Schnitt zwei Bereiche unterschieden werden. Diese sind der gelatineartige Kern als sogenannter *nucleus pulposus* (NP) und ein fasriger lamellenartiger Ring, der *anulus fibrosus* (AF), welcher ausgerichtete Kollagenfasern als dominantes Strukturelement enthält. Beide Regionen weisen jedoch eine poröse Mikrostruktur mit mehreren Komponenten auf, die zum einen aus einer hydratisierten extrazellulären Matrix (ECM) mit anhaftenden Ladungsträgern besteht und zum anderen aus einer ionisierten interstitiellen Porenflüssigkeit. Mit dieser Charakteristik ist das Bandscheibengewebe den quellaktiven Materialien zuzuordnen. Des Weiteren ist die innere Struktur und deshalb die damit verbundenen mechanischen Eigenschaften inhomogen über die dreidimensionale Geometrie verteilt. Mehr Informationen über die inhomogene Struktur finden sich unter anderem in Kapitel 2 sowie in Ayad & Weiss [10], Ehlers *et al.* [66], Marchand & Ahmed [130], Mow & Hayes [145], Urban & Roberts [214] und darin enthaltenen Referenzen. Zusammenfassend kann gesagt werden, dass sich alle Charaktereigenschaften von weichen biologischen (avaskulären) Geweben in der Bandscheibe wiederfinden und diese deshalb als Herausforderung bei der Modellierung angesehen werden kann. Darüber hinaus spielt die Bandscheibe im Bezug auf die Mechanik der Wirbelsäule eine Schlüsselrolle.

Im Hinblick auf numerische Simulationen der Wirbelsäule oder weicher biologischer Gewebe im Allgemeinen hat sich die Finite-Elemente-Methode (FEM) als eine hervorragend geeignete numerische Approximationsmethode der resultierenden Differentialgleichungen des Gesamtproblems bewährt. So ist es nicht verwunderlich, dass in der Vergangenheit bereits etliche FE-Modelle im breiten Feld der Biomechanik zur Anwendung kamen. Jedoch haben die verwendeten Modelle oftmals Defizite in der korrekten Wiedergabe der auftretenden (relevanten) Materialeigenschaften von hydratisierten biologischen Geweben. So ist es zum Beispiel unumstritten, dass einphasige Modelle nicht in der Lage sind die Bewegung des Porenfluids abzubilden bzw. daran gekoppelte Effekte, wie sie bei der Osmose auftreten. Auf der anderen Seite sind die reduzierten Modelle einfacher in ein Programmpaket zu implementieren und kommen während der numerischen Simulation mit weniger Rechenzeit aus als die komplexeren Mehrphasenmodelle. Es gibt aber auch Abstufungen bei den Modellen mit mehr als einer Phase. So sind viele bereits vorhandenen Modelle auf den Bereich der kleinen Verzerrungen beschränkt oder sind nicht in der Lage, die intrinsische Viskoelastizität, die in manchen Anwendungen eine Rolle spielt, darzustellen. Des Weiteren sind die Faserverstärkungen durch Kollagenfasern oft nur mit eindimensionalen Zugelementen abgebildet, die an den Eckknoten des übergeordneten dreidimensionalen Finite-Element-Netzes angreifen. Diese Art der Approximation führt am Ende jedoch zu netzabhängigen Lösungen, da ein vorhandenes Gitter nicht einfach verfeinert werden kann ohne dabei die dominanten Vorzugsrichtungen der Zugelemente zu ändern.

Da es immer noch nicht vollkommen erforscht ist, welche Gewebeeigenschaft sich wie stark auf das Gesamtverhalten eines Bewegungssegmentes auswirkt, ist die computerorientierte

Biomechanik der Bandscheibe immer noch eine wissenschaftliche Herausforderung. Insbesondere im Hinblick auf numerische Simulationen der Wirbelsäule kommen etliche komplexe und gekoppelte Phänomene ins Spiel, die gleichzeitig gelöst werden müssen. Wenn man die Schwierigkeiten resultierend aus dem Kontaktproblem der Wirbelfortsätze einmal außer acht lässt, so ergeben sich im Hinblick auf die Bandscheibe mehrere andere gekoppelte Probleme. Genauer gesagt resultiert das dissipative Verhalten der Bandscheibe zum einen aus der Durchströmung des viskosen Porenfluids, das entweder durch mechanische oder elektro-chemische Einflüsse hervorgerufen wird, und zum anderen aus dem strömungsunabhängigen Teil des intrinsisch viskoelastischen Festkörperskeletts der extrazellulären Matrix. Darüber hinaus ist das Gewebe oft finiten Deformationen ausgesetzt und verhält sich wegen der häufig auftretenden Faserverstärkungen Anisotrop.

Eine weitere Schwierigkeit steckt in der Anwendung des komplexen Mehrphasenmodells. Hierbei ist vor allem die Durchführung und Auswertung geeigneter Experimente zur Identifikation der theoretisch eingeführten Materialparameter zu erwähnen. In diesem Zusammenhang ist es ebenfalls schwierig die korrekten Randbedingungen für die Berechnung realistischer Anfangs-Randwertprobleme mit der FEM zu definieren.

Werden die gewonnen Erkenntnisse auf generelle dreidimensionale Diskretisierungen der Wirbelsäule angewandt, so kommt es bei komplexen Modellen im Rahmen der FEM schnell zu einer großen Anzahl an Freiheitsgraden. Dies rührt nicht nur von den numerisch aufwendigeren gemischten finiten Elementen sondern vor allem auch von der komplexen und unregelmäßigen Geometrie der Wirbelsäule, die bei der örtlichen Diskretisierung eine gewisse Mindestanzahl an finiten Elementen verlangt. Dies führt schlussendlich auf schnell anwachsende Gleichungssysteme mit vielen Unbekannten, die im Laufe einer numerischen Simulation gelöst werden müssen. Beachtet man, dass eine zuverlässige numerische Lösung von der Feinheit der zugrunde liegenden Diskretisierung abhängt so wird schnell klar, dass die Grenzen eines herkömmlichen Personal-Computers (PC) schnell erreicht sind. Deshalb müssen auch parallele Lösungsstrategien mit einbezogen werden, die die Leistung mehrerer PCs simultan nutzbar machen.

Zielsetzung und Vorgehensweise

Ziel dieser Arbeit ist es ein FE-Modell zu entwickeln, das auf der einen Seite so einfach wie möglich gehalten ist aber auf der anderen Seite komplex genug ist, um die relevanten Gewebeeigenschaften der Bandscheibe abzubilden. Der Fokus liegt hierbei auf dem kompletten Spektrum der kontinuumsmechanischen Modellbildung sowie der numerischen Realisation der resultierenden partiellen Differentialgleichungen. Da der benötigte Komplexitätsgrad sowie die relevanten Eigenschaften nicht *a priori* bekannt sind, enthält das Modell sowohl einfachere als auch komplexere Modellierungsansätze, zwischen denen einfach hin und her geschaltet werden kann. Die benötigten Materialparameter werden mit den in der Literatur verfügbaren Versuchsergebnissen bestimmt. Des Weiteren wird eine Sensitivitätsanalyse der involvierten Parameter durchgeführt um den Einfluss einzelner Parameter auf das gesamte Deformationsverhalten eines Bewegungssegments während kurzzeitiger Flexion und langzeitiger Kompression zu bestimmen. Die Effizienz des aufgestellten Modells wird

dann anhand der Ergebnisse zweier Simulationen der Lendenwirbelsäule präsentiert, die mit parallelen Algorithmen auf einem Beowulf-Cluster berechnet wurden.

Konkret wird dabei von einer detaillierten und thermodynamisch konsistenten kontinuumsmechanischen Modellbildung ausgegangen, die in einem ersten Schritt so allgemein wie möglich gehalten wird, um das Verhalten jeglicher geladener hydratisierter Gewebe zu beschreiben. Dabei wird vor allem auf die Theorie Poröser Medien (TPM) zurückgegriffen, die eine modulare Behandlung der benötigten Konstitutivannahmen erlaubt, siehe de Boer [24], Bowen [27], Ehlers [47, 51, 52] oder Mow *et al.* [144]. Des Weiteren werden polyconvexe Materialgesetze zur Beschreibung des partiell viskoelastischen und anisotropen Festkörpers herangezogen, deren Formen polynomiale Charaktere aufweisen, um mit ein und der selben Implementierung mehrere Komplexitätsstufen zu erreichen, siehe Markert *et al.* [134] und Ogden [156]. In diesem Zusammenhang ist es nicht vollständig klar ob der isotrope Anteil der extrazellulären Matrix verantwortlich für die dissipativen Eigenschaften des Gewebes ist oder die Kollagenfasern. In dieser Arbeit wird davon ausgegangen, das sich nur der isotrope Anteil intrinsisch viskoelastisch verhält, während die Kollagenfasern hyperelastisch bleiben. Der Grund hierfür wird durch die Ergebnisse von Holzapfel *et al.* [96] unterstrichen, die wenig bis keine Ratenabhängigkeit bei den durchgeführten Faserzugversuchen der Lamellen des AF aufweisen. Konsequenterweise wird die viskoelastische Formulierung der extrazellulären Matrix rein auf den isotropen Anteil beschränkt und mit einem generalisierten *Maxwell* Modell wie in Ehlers & Markert [61, 63] oder Markert [131] beschrieben. Die Kollagenfasern werden als rein elastisch angesehen und in kontinuumsmechanischer Art und Weise mit Hilfe von Struktur-Tensoren einbezogen, siehe Boehler [22] oder Spencer [192, 193, 194]. Neben anderen Besonderheiten wie der deformationsabhängigen Permeabilität (Eipper [67], Markert [132]) und der Möglichkeit generelle Inhomogenitäten wie zum Beispiel variable Faseranordnungen oder ortsabhängiges mechanisches und chemisches Verhalten zu beschreiben (Ehlers *et al.* [58, 66]), werden osmotische Effekte ebenfalls berücksichtigt. Dabei wird vor allem von der vereinfachenden Annahme von Lanir [116] Gebrauch gemacht. Diese besagt, dass die gelösten Ionen im Porenfluid nicht separat beschrieben werden müssen, wenn schnelle Konzentrationsänderungen des Umgebungsfluids ausgeschlossen werden können. Genau dies ist der Fall bei lebenden biologischen Geweben. Im Detail erlaubt diese Annahme die Berücksichtigung eines osmotischen Druckanteils, der alleinig von der Deformation des Festkörperskeletts und damit von der Deformation der anhaftenden Ladungen abhängt.

Unter Berücksichtigung der oben genannten Punkte wird in der vorliegenden Arbeit die theoretische und numerische Modellierung der intakten Bandscheibe im nicht degenerierten Zustand erarbeitet. Danach ist es dann möglich den strukturellen, den mechanischen sowie den elektro-chemischen Einfluss der einzelnen Komponenten auf das Deformationsverhalten der gesamten Wirbelsäule zu bestimmen. Das entwickelte Modell kann also als numerisches Labor eingesetzt werden, indem man die Bandscheibe in verschiedenen Szenarien virtuell hinsichtlich ihrer Zusammensetzung auf ihr makroskopisches Gesamtverhalten hin untersuchen kann, siehe Ehlers *et al.* [60, 66] oder Karajan & Ehlers [107]. Dieses Wissen ist höchst wertvoll im Hinblick auf die Planung von künstlichen Bandscheibenimplantaten, die ihren natürlichen Vorbildern in Puncto Deformationsverhalten möglichst ähnlich sein müssen. Schließlich könnten nach einer Bestimmung der involvier-

ten Materialparameter derlei Rechnungen als Referenzlösung für die Implantatkonstruktion herangezogen werden.

Um diese Rechnungen durchführen zu können wird das entwickelte Modell mit Hilfe der FEM numerisch diskretisiert. Dabei werden die regierenden Differentialgleichungen in das FE-Tool PANDAS implementiert, das auf die Arbeiten von Ehlers & Ellsiepen [55] und Ellsiepen [70] zurückgeht. Des Weiteren wird ein Interface entwickelt, das das sequentielle Programm PANDAS an den parallelen Löser M++ von Wieners [228] koppelt. Das Interface zwischen diesen beiden Softwarepaketen basiert auf einem bereits existierenden Interface, das von Ammann [4] und Wieners *et al.* [229, 230] entwickelt und erfolgreich angewendet wurde. Damit sind dann numerische Lösungen für Anfangs-Randwerte mit über eine Million Unbekannten möglich, siehe Ehlers *et al.* [60] oder Wieners *et al.* [231].

Zur Zeit sind die unterschiedlichsten Modelle und Module zur Beschreibung von generellen biologischen Weichgeweben verfügbar. Davon erfüllen jedoch nur wenige alle Voraussetzungen zur kontinuumsmechanischen Beschreibung der Bandscheibe. Zum Beispiel enthalten aktuelle Modelle zur Simulation der Wirbelsäule lediglich einphasige Physikroutinen, was somit *a priori* zum Ausschluss von Bewegungen des Porenfluids führt und somit zur Vernachlässigung von osmotischen Effekten. Die ersten ausgeklügelten Berechnungen an der Wirbelsäule wurden mit deformationsabhängigen Materialmodellen auf Basis der *Hooke*schen Theorie und nichtlinearen eindimensionalen Federelementen für die Kollagenfasern von Shirazi-Adl [182, 183] oder Shirazi-Adl *et al.* [184, 185] durchgeführt. Ein ähnliches Modell mit hochwertigeren Materialgesetzen und einer detaillierten Geometrie kann in Schmidt *et al.* [175, 176] gefunden werden. Um die Netzabhängigkeit der eindimensionalen Federelemente bei der Modellierung der Kollagenfasern zu umgehen wurden diese Modelle um kontinuumsmechanische Ansätze zur Beschreibung von Anisotropien nach Boehler [22] und Spencer [192, 193, 194] erweitert. Im Sinne der Kollagenfaser-Modellierung findet man biomechanische Anwendungen in den Arbeiten von Elliott & Setton [69], Holzapfel & Gasser [95] oder Klisch & Lotz [111], während die Arbeiten von Balzani [14], Balzani *et al.* [15], Markert *et al.* [134] oder Schröder & Neff [179] die Gesetze der klassischen Ansätze hinsichtlich polykonvexer Ansätze erweiterten. Dieses Wissen wurde dann in die Simulationen der Lendenwirbelsäule von Eberlein *et al.* [44, 45] mit eingearbeitet.

Da all diese Modelle aber nur einphasig sind können in der Bandscheibe keine Fluidbewegungen beschrieben werden, die zum Beispiel bei der Nährstoffversorgung eine große Rolle spielen, siehe Holm & Nachemson [93] oder Urban & Holm [211]. Um diese Schwachstelle zu beheben muss deshalb mindestens eine zweite Phase, die interstitielle Flüssigkeit, eingeführt werden. In diesem Kontext gibt es etliche zweiphasige Modelle basierend auf den Arbeiten von Biot [18], Bowen [26] sowie Mow *et al.* [146], die sowohl auf allgemeine biologische Weichgewebe angewendet werden als auch speziell auf die Bandscheibe, wie zum Beispiel in den Arbeiten von Argoubi & Shirazi-Adl [7], Ayotte *et al.* [11], Iatridis *et al.* [102], Klisch & Lotz [112], Li *et al.* [120, 121] oder Riches *et al.* [168]. Da jedoch die elektro-chemischen Effekte mittels Osmose sowohl Quell- als auch Schrumpfprozesse hervorrufen können und damit ebenfalls die Fluidbewegung im Gewebe beeinflussen, sollten die mehrphasigen Modelle auch diesbezüglich erweitert werden. Hierbei gibt es zwei Möglichkeiten. Zum einen ist die unabhängige Beschreibung der gelösten Ionen im

Porenfluid zu nennen, die auf ein stark gekoppeltes System von partiellen Differentialgleichungen führt, das numerisch oftmals schwierig zu lösen ist, siehe zum Beispiel Chen *et al.* [33], Ehlers & Acartürk [53], Ehlers *et al.* [64], Frijns *et al.* [76, 77], Huyghe *et al.* [99], Iatridis *et al.* [100], Kaasschieter *et al.* [106], van Loon *et al.* [127] oder Mow *et al.* [143]. Auf der anderen Seite gibt es eine vereinfachende Annahme von Lanir [116], die anstatt des generellen Modells mit etlichen Freiheitsgraden auf ein erweitertes Zweiphasenmodell mit zwei Freiheitsgraden führt. Hierbei wird davon ausgegangen, dass sich die freien Ionen im Porenfluid sehr schnell bewegen und das Gewebe damit immer unmittelbar in chemischem Gleichgewicht ist. Der osmotische Druckanteil kann dann über eine Konstitutivgleichung einfach berechnet werden. Diese vereinfachende Annahme wurde in die zweiphasigen Modelle von Ehlers *et al.* [58, 59, 66], Hsieh *et al.* [97] oder Laible *et al.* [114] eingebaut und angewendet. Ein Vergleich dieser beiden Ansätze zeigt eine sehr gute Übereinstimmung für langsame Konzentrationsänderungen der umgebenden Lösung und eine akzeptable Übereinstimmung bei sehr schnellen Konzentrationsänderungen, siehe Wilson *et al.* [234]. Da aber innerhalb des lebenden Organismus keinerlei rapide Konzentrationsänderungen zu erwarten sind, ist der Ansatz nach Lanir [116] bestens geeignet für die Modellierung der Bandscheibe in der vorliegenden Arbeit.

Gliederung der Arbeit

Kapitel 1 leitet die Arbeit ein und enthält die in dieser deutschen Zusammenfassung aufgeführten Bemerkungen über das Auftreten von Schmerzen im Bereich der Lendenwirbelsäule sowie über die Ziele der vorliegenden Arbeit und die zur Zeit am Markt verfügbaren theoretischen Berechnungsmodelle.

Auf die anatomischen Grundkenntnisse sowie die zu modellierenden Materialeigenschaften der Bandscheiben wird in **Kapitel 2** eingegangen. Da die Bandscheiben in der Wirbelsäule zwischen den Wirbelkörpern eingebettet sind, müssen auch die benachbarten Bauteile wie die knorpelige Endplatte sowie die Wirbelkörper selbst erläutert werden, um später realitätsnahe Beispiele präsentieren zu können. Diskutiert wird insbesondere die Zusammensetzung der Bandscheiben auf der Mikroskale, die ein elektro-chemisch aktives, anisotropes, inhomogenes und stark dissipatives Material darstellt. Auf Wirbel, Wirbelfortsätze, Endplatten und Bänder wird zwar eingegangen, doch werden diese im späteren Simulationsprozess vereinfacht wiedergegeben bzw. weggelassen, da sie nicht Thema dieser Arbeit sind. Des Weiteren werden die Grundbegriffe aus der Chemie erläutert, um ein besseres Verständnis für die benutzten Konzentrationsmaße und den osmotischen Druck zu erhalten.

Kapitel 3 beschreibt die notwendigen kontinuumsmechanischen Grundlagen, die zur Modellierung der porösen Bandscheiben benötigt werden. Im Einzelnen handelt es sich um einen knappen Abriss der Theorie Poröser Medien mit direkter Anwendung auf das elektro-chemisch aktive Gewebe. In einem ersten Schritt werden fünf Komponenten eingeführt, das heisst ein Festkörper (Solid) mit anhaftenden gebundenen Ladungen und ein Porenfluid bestehend aus einem Lösungsmittel (Liquid) und darin gelösten Kationen und Anionen. Darüber hinaus wird auf die finite Kinematik eines inelastischen Festkörperske-

letts eingegangen und diese im Rahmen einer multiplikativen Zerlegung des zugehörigen Deformationsgradienten dargestellt. Die zur Modellierung benötigten fünf Bilanzgleichungen werden anhand einer Masterbilanz hergeleitet und auf das zu beschreibende Material angewendet. Diese stellen ein allgemeingültiges Konzept an beschreibenden Gleichungen dar, die jedoch noch nicht das gewünschte Materialverhalten widerspiegeln.

Kapitel 4 beschäftigt sich mit der sogenannten Konstitutivtheorie, die die allgemeingültigen Gleichungen aus Kapitel 3 mit Leben füllt um das einzigartige Materialverhalten der Bandscheibe widerzuspiegeln. In einem ersten Schritt werden die auftretenden Bilanzen durch geeignete Annahmen vereinfacht, damit das Endergebnis relativ simpel bleibt, jedoch gerade noch osmotische Effekte abbilden kann. Hierbei ist vor allem die *Lanir*'sche Annahme zu nennen, die es erlaubt, ein elektro-chemisch aktives Material mit nur zwei Komponenten zu beschreiben. Nach der Reduktion auf zwei Komponenten werden diese ebenfalls vereinfacht dargestellt, indem man von quasi-statischen Verhältnissen, materieller Inkompressibilität, keinem Massenaustausch zwischen den Komponenten sowie von isothermen Verhältnissen ausgeht. Damit im weiteren das viskose Porenfluid sowie das inhomogene, anisotrope und viskoelastische Festkörperskelett beschrieben werden kann, bedarf es einer konstitutiven Grundauswahl an sogenannten Antwortfunktionen, die von thermodynamisch zulässigen Prozessvariablen abhängen müssen. Um bei der Konkretisierung dieser Antwortfunktionen keine falschen Annahmen zu treffen, werden die maßgeblichen Restriktionen aus der Entropieungleichung herausgearbeitet, die den dissipativen Prozess des viskosen Porenfluids sowie des viskoelastischen Festkörpers steuert.

In diesem Zusammenhang wird auf die Grundlagen der Materialtheorie eingegangen, um grundlegende Begriffe der materiellen Symmetrie und den damit eng verknüpften Symmetriegruppen zu erläutern. Diese werden aber nicht im allgemeinen Sinne aufgegriffen, sondern direkt mit Fokus auf die zu beschreibenden Kollagenfaserverstärkungen sowie die den damit verknüpften Konsequenzen für Strukturtensoren wiedergegeben. Das Prinzip der Bezugs- oder Beobachterinvarianz ist in diesem Kontext eng mit der materiellen Symmetrie verknüpft, bis auf den wesentlichen Unterschied, dass die auferlegten Starrkörperrotationen auf der aktuellen Konfiguration wirken. Die Konsequenzen der Resultate aus materieller Symmetrie und Bezugsinvarianz führen dann auf das Konzept der isotropen Tensorfunktionen, die bei der Konstitutivtheorie Anwendung finden.

In einem weiteren Schritt wird das viskose Porenfluid behandelt sowie eine Spannung-Dehnungs-Beziehung für das anisotrope und viskoelastische Festkörperskelett entwickelt. Mit diesem Wissen können die maßgebenden Gleichungen aufgestellt und das Modell fixiert werden.

Kapitel 5 beschäftigt sich mit der numerischen Umsetzung der in Kapitel 3 und 4 beschriebenen Hauptgleichungen des Modells im Rahmen der gemischten FEM. Hierbei wird auf die Orts- und Zeitdiskretisierung eingegangen, die sowohl eine schwache Formulierung als auch eine konsistente Linearisierung der Hauptgleichungen mit sich bringt. Darüber hinaus bedarf es spezieller gemischter finiter Elemente (*Taylor-Hood* Elemente), damit eine stabile numerische Umsetzung überhaupt möglich ist. Auch in Puncto Speicherkapazität muss die numerische Umsetzung etliches aufweisen, damit die auftretenden Anisotropien und Inhomogenitäten korrekt abgebildet werden können.

Damit jedoch realitätsnahe Probleme der Lendenwirbelsäule auf heute verfügbaren PCs in akzeptabler Rechenzeit simulieren werden können, müssen die Berechnungs-Algorithmen parallelisiert werden. In diesem Zusammenhang wird kurz auf das Interface zwischen den Forschungs-Softwarepaketen PANDAS und M++ eingegangen, wobei Ersteres für die physikalische Beschreibung der einzelnen Elemente benutzt wird und Letzteres den globalen Rahmen (Netzhaushaltung, Zeitintegration, paralleler Löser) darstellt.

Kapitel 6: Um überhaupt reale biomechanische Probleme rechnen zu können bedarf es einer digitalen Geometrieabbildung, die in etwa die Lendenwirbelsäule widerspiegelt. Diese kann mit einer Datenerfassung mittels CT oder Kern-Spin-Tomograph digital erzeugt werden, indem ein dreidimensionales CAD-Tool zu Hilfe genommen wird. Damit diese Geometrie aber mit der FEM berechnet werden kann muss diese noch in endlich kleine finite Elemente unterteilt werden. Des Weiteren müssen dann der diskretisierten Wirbelsäule die notwendigen Parameter über die Faserorientierung sowie der etlichen Inhomogenitäten übergeben werden. Damit dies netzunabhängig geschehen kann wird ein Algorithmus hergeleitet, der anhand der Geometrie die benötigten Daten automatisiert ermittelt. Dies ist auch im Hinblick auf die parallelen Rechnungen notwendig, da ansonsten keine Konvergenzstudien mit hierarchisch verfeinerten Netzen möglich wären.

In einem nächsten Schritt werden die involvierten Materialparameter bestimmt. Dies geschieht soweit dies möglich ist, mit realen Versuchen als auch über eine Abschätzung mit Werten aus der Literatur. Um die Wichtigkeit der jeweiligen Parameter besser einschätzen zu können wird eine Parameterstudie durchgeführt und numerisch Sensitivitäten der Parameter auf ein repräsentatives Druck- und Biegeproblem eines Bewegungssegments bestimmt.

Die ermittelten Parameter werden schließlich benutzt um einen Abschnitt der Lendenwirbelsäule zu simulieren. Da diese Simulationen parallel auf verschiedenen Prozessoren gleichzeitig berechnet wird, dienen diese auch als Anwendungsbeispiel des eingeführten Interface zwischen M++ und PANDAS. Im Einzelnen werden zwei Probleme behandelt; eine Rechnung mit gesunden Bandscheiben und eine, bei der das unterste Bewegungssegment versteift wurde.

Auf abschließende Bemerkungen, eine kurze Diskussion der erlangten Ergebnisse sowie auf mögliche Forschungen im Anschluss wird in **Kapitel 7** eingegangen.

Um aus der Schreibweise resultierenden Missverständnissen vorzubeugen findet der interessierte Leser in **Appendix A** eine kurze Zusammenfassung der in dieser Arbeit benutzten Tensornotation.

Nomenclature

The notation in this monograph follows the conventions that are commonly used in modern tensor calculus, such as in the text books of de Boer [23], Ehlers [50], or Papastavridis [160]. A collection of selected rules thereof may be reviewed in Appendix A if any questions arise while studying this monograph. The symbols used in the context of porous-media theories adhere to the established nomenclature given by de Boer [24] and Ehlers [47, 52].

Conventions

Kernel conventions

$(\bullet)$			place holder for arbitrary quantities
$s, t, \dots$	or	$\sigma, \tau, \dots$	scalars (0^{th}-order tensors)
$\mathbf{s}, \mathbf{t}, \dots$	or	$\boldsymbol{\sigma}, \boldsymbol{\tau}, \dots$	vectors (1^{st}-order tensors)
$\mathbf{S}, \mathbf{T}, \dots$	or	$\boldsymbol{\sigma}, \boldsymbol{\tau}, \dots$	2^{nd}-order tensors
$\overset{n}{\mathbf{S}}, \overset{n}{\mathbf{T}}, \dots$	or	$\overset{n}{\boldsymbol{\sigma}}, \overset{n}{\boldsymbol{\tau}}, \dots$	n^{th}- or higher-order tensors
$\mathbf{s}, \mathbf{t}, \dots$	or	$\boldsymbol{\sigma}, \boldsymbol{\tau}, \dots$	vectors (1st-order tensors)

Index and suffix conventions

$i, j, k, l, \dots$	indices as super- or subscripts range from 1 to N, where $N = 3$ in the usual 3-d space of our physical experience
$(\bullet)_k (\bullet)^k = \sum_k (\bullet)_k (\bullet)^k$	*Einstein*'s summation convention yields a summation over indices that appear twice unless stated otherwise
$(\bullet)_S$, $(\bullet)_F$	capital subscripts indicate kinematical quantities of a constituent within porous-media or mixture theories
$(\bullet)^S$, $(\bullet)^F$	capital superscripts indicate the belonging of non-kinematical quantities to a constituent within mixture theories
$(\bullet)_{0S}^{(\cdot)}$	initial value of a non-kinematical quantity with respect to the referential configuration of the solid
$(\bullet)_{Se}$, $(\bullet)_{Si}$	subscripts "Se" and "Si" indicate elastic and inelastic parts associated with inelastic solid kinematics
$(\bullet)'_\alpha$	material time derivative following the motion of a constituent α with the solid and fluid constituents $\alpha = \{S, F\}$
$(\bullet)_\alpha^\triangle$, $(\bullet)_\alpha^\triangledown$	upper (contravariant) and lower (covariant) *Oldroyd* derivative as a relative time derivative of a spatial quantity

Symbols

Symbol	Unit	Description
α		constituent identifier in super- and subscript, i. e., $\alpha = \{S, F\}$
$\alpha^*_{0(m)},\ \alpha^*_{n(m)}$	[-]	dimensionless *Ogden* parameters (exponents)
β		component identifier (here: $\beta = \{L, +, -\}$)
γ		solute identifier (here: $\gamma = \{+, -\}$)
$\widetilde{\gamma}$		charge identifier (here: $\widetilde{\gamma} = \{+, -, fc\}$)
$\Gamma_{(\cdot)}$		*Dirichlet* and *Neumann* boundaries
γ^{FR}	[N/m^3]	effective fluid weight
$\gamma^S_0,\ \gamma^S_n$	[-]	parameters governing the volumetric response of φ^S
$\tilde{\gamma}^S_m$	[-]	parameters of the anisotropic strain energy (exponents)
$\Delta\pi$	[N/m^2]	osmotic pressure difference
δ^k_l, δ_{kl}	[-]	*Kronecker* deltas
ε, ε^α	[J/kg]	mass specific internal energy of φ and φ^α
$\hat{\varepsilon}^\alpha$	[J/m^3 s]	volume specific direct energy production of φ^α
ζ^S_n	[N s/m^2]	2$^{\text{nd}}$ solid viscosity constant
$\hat{\zeta}^\alpha$	[J/K m^3 s]	volume specific direct entropy production of φ^α
η, η^α	[J/K kg]	mass specific entropy of φ and φ^α
$\hat{\eta}$, $\hat{\eta}^\alpha$	[J/K m^3 s]	volume specific total entropy production of φ and φ^α
η^S_n	[N s/m^2]	solid shear viscosity constant
θ^k_S	[-]	general contravariant curvilinear solid coordinate lines
Θ, Θ^α	[K]	absolute *Kelvin*'s temperature of φ and φ^α
κ	[-]	exponent governing the deformation dependency of K^S
$\lambda_{S1},\ \lambda_{S2},\ \lambda_{S3}$	[-]	eigenvalues of $\mathbf{C}_S$ or $\mathbf{B}_S$ (squared principal stretches)
$\Lambda^S_0,\ \Lambda^S_n$	[N/m^2]	2$^{\text{nd}}$ *Lame* constants of φ^S
$\mu^F,\ \mu^{FR}$	[N s/m^2]	partial and effective dynamic fluid viscosity
$\mu^S_0,\ \mu^S_n$	[N/m^2]	1$^{\text{st}}$ *Lame* constants of φ^S
$\tilde{\mu}^S_m$	[N/m^2]	parameters of the anisotropic part of the strain energy
$\mu^*_{0(m)},\ \mu^*_{n(m)}$	[-]	dimensionless *Ogden* parameters (polynomial coefficients)
ρ	[kg/m^3]	density of the overall aggregate φ
ρ^α, $\rho^{\alpha R}$	[kg/m^3]	partial and effective (realistic) density of φ^α
$\hat{\rho}^\alpha$	[kg/m^3 s]	volume-specific mass production of φ^α
σ, σ^α		scalar-valued supply terms of mechanical quantities
σ_η, σ^α_η		volume specific external entropy supply of φ and φ^α
φ, φ^α		entire aggregate model and constituent α
ϕ^S_0	[-]	half of the fibre angle between two fibres

$\phi^j_{\mathcal{P}}$, $\boldsymbol{\phi}^j_{\mathbf{u}_s}$	[-]	shape functions in a finite element
ψ, ψ^α	[J/kg]	mass-specific *Helmholtz* free energy of φ^α
Ψ, Ψ^α	[$\cdot$/m^3]	volume-specific densities of scalar mechanical quantities
$\hat{\Psi}$, $\hat{\Psi}^\alpha$	[$\cdot$/m^3]	volume-specific productions of scalar mechanical quantities
Ω, $\partial\Omega$		spatial domain and boundary of the aggregate body $\mathcal{B}$
Ω_e, Ω^h		one finite element and the discretised finite element mesh
$\mathcal{B}$, $\mathcal{B}^\alpha$		aggregate body and partial constituent body
c^γ_m	[mol/m^3]	molar concentration of ions or fixed charges
d		differential operator
ds	[m]	length of a line element d$\mathbf{x}$ in the actual config.
d$\widehat{s}_{Si}$	[m]	length of a solid line element d$\widehat{\mathbf{x}}_{Si}$ in the intermediate config.
dS_S	[m]	length of a solid line element d$\mathbf{X}_S$ in the reference config.
dt	[s]	time increment
dm^α	[kg]	local mass element of φ^α
dv^α	[m^3]	local volume element of φ^α
dv	[m^3]	actual volume element of φ
dV_α	[m^3]	reference volume element of φ^α
D	[-]	dimension in space
$\hat{e}^\alpha$	[J/m^3 s]	volume specific total energy production of φ^α
$\mathcal{H}^1(\Omega)$		*Sobolev* function space
$\mathcal{I}_S$	[-]	integrity base containing eigenvalues and mixed invariants
I_{S1}, I_{S2}, I_{S3}	[-]	principal invariants of $\mathbf{C}_S$ or $\mathbf{B}_S$
J_{S1}, J_{S2}, J_{S3}	[-]	basic invariants of $\mathbf{C}_S$ or $\mathbf{B}_S$
J_{S4}, J_{S5}, ...	[-]	mixed invariants of $\mathbf{C}_S$ and $\boldsymbol{\mathcal{M}}^S$
J_α	[-]	*Jacobi*an determinant of φ^α
k^F	[m/s]	*Darcy* flow coefficient (hydraulic conductivity)
K^F	[m^4/N s]	specific permeability
K^S	[m^2]	intrinsic (deformation-dependent) permeability
M^{fc}_m	[kg/mol]	molar mass of an electron
$\mathcal{MG}_3$		group of all symmetry transformations (symmetry group)
n^α	[-]	volume fraction of φ^α
N	[-]	number of *Maxwell* elements
N_A	[mol^{-1}]	*Avogadro*'s number
$N^{\widetilde{\gamma}}$	[mol]	discrete number charges
$\mathcal{O}_3$		group of all orthogonal transformations
$\mathcal{P}$	[N/m^2]	*Lagrange*an multiplier representing the hydraulic pressure
p	[N/m^2]	overall pore pressure including hydraulic and osmotic parts

P^α		material points of φ^α
$\bar{q}$	$[\,\mathrm{m/s}\,]$	volume efflux of φ^F over the boundary Γ_q
r, r^α	$[\,\mathrm{J/kg\,s}\,]$	mass-specific external heat supply of φ and φ^α
R	$[\,\mathrm{J/mol\,K}\,]$	universal gas constant
$\mathcal{S}$, $\mathcal{S}^\alpha$		surface of the aggregate and constituent body
$\mathcal{S}_{\mathbf{u}_s}$, $\mathcal{S}_{\mathcal{P}}$		trial spaces of the primary variables
$\mathcal{SO}_3$		group of all proper orthogonal transformations
$\mathcal{T}_{\mathbf{u}_s}$, $\mathcal{T}_{\mathcal{P}}$		test spaces of the primary variables
t	$[\,\mathrm{s}\,]$	time
X_k	$[\,\text{-}\,]$	coordinate lines defining the position of the human body
$\overline{U}^S_{\mathrm{ISO}}$	$[\,\mathrm{J/m^3}\,]$	volumetric part of the solid strain energy W^S
$\mathcal{U}_3$		group of all unimodular transformations
V, V^α	$[\,\mathrm{m^3}\,]$	overall volume of $\mathcal{B}$ and partial volume of $\mathcal{B}^\alpha$
W^S	$[\,\mathrm{J/m^3}\,]$	volume specific solid strain energy function
$z^{\tilde{\gamma}}$	$[\,+,-\,]$	valences of respective ions or fixed charges
$\boldsymbol{\xi}_1$, $\boldsymbol{\xi}_2$, $\boldsymbol{\xi}_3$		positive oriented orthonormal triad of vectors
$\boldsymbol{\sigma}$, $\boldsymbol{\sigma}^\alpha$		vector-valued supply terms of mechanical quantities
$\boldsymbol{\phi}$, $\boldsymbol{\phi}^\alpha$		general vector-valued mechanical quantities
$\boldsymbol{\phi}_\eta$, $\boldsymbol{\phi}^\alpha_\eta$	$[\,\mathrm{J/K\,m^2\,s}\,]$	entropy efflux vector of φ and φ^α
$\boldsymbol{\Psi}$,$\boldsymbol{\Psi}^\alpha$	$[\,\cdot/\mathrm{m^3}\,]$	volume-specific densities of vectorial mechanical quantities
$\hat{\boldsymbol{\Psi}}$, $\hat{\boldsymbol{\Psi}}^\alpha$	$[\,\cdot/\mathrm{m^3}\,]$	volume-specific productions of vectorial mechanical quantities
$\boldsymbol{\chi}_\alpha$, $\boldsymbol{\chi}_\alpha^{-1}$		motion and inverse motion function of the constituents φ^α
$\mathbf{a}_0^S$, $\mathbf{b}_0^S$	$[\,\text{-}\,]$	unit vectors pointing in the corresponding fibre direction
$\mathbf{a}_{Sk}$, $\mathbf{a}_S^k$	$[\,\text{-}\,]$	co- and contravariant solid actual basis vector
$\mathbf{b}$, $\mathbf{b}^\alpha$	$[\,\mathrm{m/s^2}\,]$	mass specific body force vector
$\mathbf{d}_\alpha$	$[\,\mathrm{m/s}\,]$	diffusion velocity vector of φ^α
$\mathrm{d}\mathbf{a}$	$[\,\mathrm{m^2}\,]$	oriented actual area element
$\mathrm{d}\mathbf{A}_S$	$[\,\mathrm{m^2}\,]$	oriented reference area element of φ^S
$\mathrm{d}\mathbf{f}_c^\alpha$	$[\,\mathrm{N}\,]$	contact force element of φ^α
$\mathrm{d}\mathbf{x}$	$[\,\mathrm{m}\,]$	actual line element
$\mathrm{d}\widehat{\mathbf{x}}_{Si}$	$[\,\mathrm{m}\,]$	intermediate line element of the solid
$\mathrm{d}\mathbf{X}_S$	$[\,\mathrm{m}\,]$	reference line element of the solid
$\mathbf{g}$	$[\,\mathrm{m/s^2}\,]$	constant gravitation vector with $\lvert\,\mathbf{g}\,\rvert = 9.81\,\mathrm{m/s^2}$
$\boldsymbol{\mathcal{F}}$		vector containing the global and local system of equations
$\boldsymbol{\mathcal{G}}$, $\boldsymbol{\mathcal{G}}^h_{\mathbf{u}_s}$, $\boldsymbol{\mathcal{G}}^h_{\mathcal{P}}$		abstract function vectors containing the weak forms
$\mathbf{h}_{Sk}$, $\mathbf{h}_S^k$	$[\,\text{-}\,]$	co- and contravariant solid reference basis vector
$\hat{\mathbf{h}}^\alpha$	$[\,\mathrm{N/m^2}\,]$	volume-specific total angular momentum production of φ^α

$\boldsymbol{\mathcal{L}}$		abstract function vector containing the evolution equations
$\hat{\mathbf{m}}^\alpha$	$[\,\mathrm{N/m^2}\,]$	volume-specific direct angular momentum production of φ^α
$\mathbf{m}_{S(k)}$	$[\,\text{-}\,]$	eigenvectors of $\mathbf{C}_S$ related to the reference configuration
$\mathbf{n}$	$[\,\text{-}\,]$	outward-oriented unit surface normal vector
$\mathbf{n}_{S(k)}$	$[\,\text{-}\,]$	eigenvectors of $\mathbf{B}_S$ related to the actual configuration
$\hat{\mathbf{p}}^\alpha$, $\hat{\mathbf{p}}^\alpha_E$	$[\,\mathrm{N/m^3}\,]$	volume-specific direct and extra momentum production of φ^α
$\mathbf{q}$, $\mathbf{q}^\alpha$	$[\,\mathrm{J/m^2\,s}\,]$	heat influx vector of φ^α
$\boldsymbol{q}$		discrete vector containing the history variables
$\hat{\mathbf{s}}^\alpha$	$[\,\mathrm{N/m^3}\,]$	volume-specific total momentum production of φ^α
$\bar{\mathbf{t}}$	$[\,\mathrm{N/m^2}\,]$	external load vector acting on the boundary $\Gamma_{\mathbf{t}}$
$\mathbf{t}^\alpha$	$[\,\mathrm{N/m^2}\,]$	surface traction vector of φ^α
$\mathbf{u}_S$	$[\,\mathrm{m}\,]$	solid displacement vector
$\boldsymbol{u}$		discrete vector containing the nodal degrees of freedom
$\mathbf{w}_F$	$[\,\mathrm{m}\,]$	fluid seepage velocity vector
$\mathbf{x}$	$[\,\mathrm{m}\,]$	actual position vector of φ
$\widehat{\mathbf{x}}_{Si}$	$[\,\mathrm{m}\,]$	intermediate solid position vector (fictitious)
$\mathbf{X}_\alpha = \mathbf{x}_{0\alpha}$	$[\,\mathrm{m}\,]$	reference position vector of P^α
$\dot{\mathbf{x}}$	$[\,\mathrm{m/s}\,]$	aggregate velocity vector of φ
$\overset{\prime}{\mathbf{x}}_\alpha$	$[\,\mathrm{m/s}\,]$	velocity vector of φ^α
$\ddot{\mathbf{x}}$	$[\,\mathrm{m/s^2}\,]$	aggregate acceleration vector of φ
$\overset{\prime\prime}{\mathbf{x}}_\alpha$	$[\,\mathrm{m/s^2}\,]$	acceleration vector of φ^α
$\widehat{\mathbf{z}}_{Sk}$, $\widehat{\mathbf{z}}^k_S$	$[\,\text{-}\,]$	co- and contravariant solid intermediate basis vector
$\widehat{\boldsymbol{\Gamma}}_S$, $\widehat{\boldsymbol{\Gamma}}_{Si}$, $\widehat{\boldsymbol{\Gamma}}_{Se}$	$[\,\text{-}\,]$	contravariant solid strain tensors of the intermediate config.
$\boldsymbol{\tau}$, $\boldsymbol{\tau}^\alpha$, $\boldsymbol{\tau}^\alpha_E$	$[\,\mathrm{N/m^2}\,]$	*Kirchhoff* (extra - $(\,\cdot\,)_E$) stress tensor of φ and φ^α
$\widehat{\boldsymbol{\tau}}^S_n$	$[\,\mathrm{N/m^2}\,]$	intermediate stress tensor of the n$^{\text{th}}$ *Maxwell* element
$\boldsymbol{\Phi}$, $\boldsymbol{\Phi}^\alpha$		general tensor-valued mechanical quantities
$\mathbf{A}_1, \mathbf{A}_2, \mathbf{A}_3$	$[\,\text{-}\,]$	arbitrary symmetric 2$^{\text{nd}}$-order tensors
$\mathbf{A}_S, \mathbf{A}_{Se}, \mathbf{A}_{Si}$	$[\,\text{-}\,]$	contravariant *Almansi*an solid strain tensors
$\mathbf{B}_S, \mathbf{B}_{Se}, \widehat{\mathbf{B}}_{Si}$	$[\,\text{-}\,]$	left *Cauchy-Green* solid deformation tensors
$\overset{4}{\boldsymbol{\mathcal{B}}}{}^{\mathrm{S}}_{(\cdot)}$, $\overset{4}{\mathbf{B}}_{(\cdot)}$	$[\,\mathrm{N/m^2}\,]$	4$^{\text{th}}$-order elasticity tensors of the reference configuration
$\mathbf{C}_S, \widehat{\mathbf{C}}_{Se}, \mathbf{C}_{Si}$	$[\,\text{-}\,]$	right *Cauchy-Green* solid deformation tensors
$\overset{4}{\boldsymbol{\mathcal{C}}}{}^{\mathrm{S}}_{(\cdot)}$, $\overset{4}{\mathbf{C}}_{(\cdot)}$	$[\,\mathrm{N/m^2}\,]$	4$^{\text{th}}$-order elasticity tensors of the actual configuration
$\mathbf{D}_S, \widehat{\mathbf{D}}_{Si}$	$[\,1/\mathrm{s}\,]$	overall and inelastic rate of deformation tensors
$\overset{3}{\mathbf{E}}$	$[\,\text{-}\,]$	*Ricci* permutation tensor (3$^{\text{rd}}$-order fundamental tensor)
$\mathbf{E}_S, \mathbf{E}_{Se}, \mathbf{E}_{Si}$	$[\,\text{-}\,]$	contravariant *Green-Lagrange*an solid strain tensors

$\mathbf{F}_\alpha$	[-]	material deformation gradient of φ^α
$\mathbf{F}_{Se}, \mathbf{F}_{Si}$	[-]	elastic and inelastic parts of the solid deformation gradient
$\mathbf{G}$	[-]	arbitrary 2^{nd}-order tensor
$\mathbf{H}, \widehat{\mathbf{H}}, \mathbf{Q}$	[-]	proper orthogonal rotation tensors
$\boldsymbol{\mathcal{H}}_{\boldsymbol{\xi}}^{(\phi)}$	[-]	*Euler-Rodrigues* form of a rigid-body rotation
$\mathbf{I}$	[-]	identity tensor (2^{nd}-order fundamental tensor)
$\mathbf{L}_S, \widehat{\mathbf{L}}_{Si}$	[1/s]	spatial and intermediate solid velocity gradients
$\mathbf{M}_S$	[-]	eigentensor of $\mathbf{C}_S$ related to the reference configuration
$\boldsymbol{\mathcal{M}}^S$	[-]	general structural tensor on reference configuration
$\mathbf{N}_S$	[-]	eigentensor of $\mathbf{B}_S$ related to the actual configuration
$\mathbf{P}, \mathbf{P}^\alpha, \mathbf{P}_E^\alpha$	[N/m^2]	1^{st} *Piola-Kirchhoff* or nominal (extra - $(\cdot)_E$) stress tensors
$\mathbf{R}_S, \mathbf{R}_{Se}, \mathbf{R}_{Si}$	[-]	proper orthogonal rotation tensors of the polar decomp. of $\mathbf{F}_S$
$\boldsymbol{\mathcal{R}}_{\boldsymbol{\xi}}$	[-]	reflection tensor in a plane normal to the unit vector $\boldsymbol{\xi}$
$\mathbf{S}$, $\mathbf{S}^\alpha$, $\mathbf{S}_E^\alpha$	[N/m^2]	2^{nd} *Piola-Kirchhoff* (extra - $(\cdot)_E$) stress tensors of φ and φ^α
$\mathbf{T}$, $\mathbf{T}^\alpha$, $\mathbf{T}_E^\alpha$	[N/m^2]	*Cauchy* or true (extra - $(\cdot)_E$) stress tensors of φ and φ^α
$\mathbf{U}_S, \widehat{\mathbf{U}}_{Se}, \mathbf{U}_{Si}$	[-]	right solid stretch tensors of the polar decomposition of $\mathbf{F}_S$
$\mathbf{V}_S, \mathbf{V}_{Se}, \widehat{\mathbf{V}}_{Si}$	[-]	left solid stretch tensors of the polar decomposition of $\mathbf{F}_S$
$\mathbf{W}_S$, $\widehat{\mathbf{W}}_{Si}$	[1/s]	overall and inelastic spin tensors

1 Introduction and Overview

1.1 Motivation

Clinical point of view: In industrialised western countries, almost everybody has been suffering from low back pain (LBP) at least once in his lifetime, for example, in a representative survey carried out in the early nineties and another one conducted ten years later, about 85 % of the German population had already experienced this widespread ailment, cf., e. g., Raspe *et al.* [166] or Schmidt *et al.* [174]. Regarding the same surveys as well as another one carried out by Latza *et al.* [117], current LBP was reported from about 40 % of the people asked, while 21 % of the asked probands were having severe pain. Moreover, low back pain is the number one cause of work-related health problems in many European countries. The second European survey on working conditions conducted by Paoli [159] reported an overall average of 30 % of the working people in Europe suffering from LBP, while the fourth survey of 2007 recorded a slight decrease of the average to 25 %, cf. Parent-Thirion *et al.* [161]. According to European Foundation for the Improvement of Living and Working Conditions [72], these work related LBP problems vary by occupation ranging from 16 % for the administrative staff to 58 % for skilled agricultural workers. Since both occupations work in a seated position, this tremendous difference can only be explained by the enormous vibrations an agricultural worker is exposed to while sitting on farming machines (Lis *et al.* [124]).

This significant number causes not only a substantial amount of direct health-care costs, cf. Frymoyer & Cats-Baril [78], but is also responsible for a significant socioeconomic impact. In Germany for instance, 4 % of all work force is lost every year due to LBP. But besides the monetary factors, there is of course the pain so many people are suffering from. Although the cause of low back pain remains unclear in many patients, it is generally accepted that a deterioration of the intervertebral disc (IVD) plays an important part in the cause of the complaints, cf. Vanharanta *et al.* [215]. More detailed information on traumatic and degenerated IVD, as well as on its medical treatment, can be found in Wilke & Claes [232]. In this regard, many different ways of treatment are possible, but in very severe cases it is best to fusion the involved vertebral bodies or replace the deteriorated IVD by an implant, which should similarly respond to mechanical loading like the original.

These issues were motivation enough to initiate a remarkable research interest in intervertebral disc mechanics over the past three decades. Regarding the steady increase of computing power in the same period of time, more and more researchers are confident that a possible explanation and remedy for LBP lies in numerical simulation techniques.

Biomechanical and computational point of view: The biomechanical challenge lies within the structural complexity of the spine itself arising from a great individuality of the patient data with an irregular and hard to determine 3-d anatomical shape. As the name implies, the intervertebral disc is embedded in-between two vertebral bodies,

thereby forming a motion segment of the spine. Two main regions can be distinguished in an axial cut through the IVD, a gelatinous core, the *nucleus pulposus* (NP) enclosed by a fibrous, lamellar structure, the *anulus fibrosus* (AF), having aligned collagen fibres as dominant structural elements. Both regions are composed of a porous multi-component microstructure consisting of a charged hydrated extracellular matrix (ECM) carrying fixed negative charges, as well as an ionised interstitial fluid yielding a swelling-active material. Additionally, the inner structure and thus, the associated physical properties are inhomogeneously distributed over the 3-d anatomic shape of the tissue. For a more detailed description, the reader is referred to Chapter 2 or to Ayad & Weiss [10], Ehlers *et al.* [66], Marchand & Ahmed [130], Mow & Hayes [145], Urban & Roberts [214] and references therein. Thus, all the properties characterising soft biological tissues in general are unified within the IVD. Moreover, in the context of spine mechanics, the IVD plays an important key role on the overall performance of the spine.

Regarding numerical simulations of the spine or soft biological tissues in general, the finite element method (FEM) has been proven to be a well-suited numerical approximation method of the resulting differential equations describing the overall problem. In the past, numerous finite element models have already been applied to the broad field of computational biomechanics, but often exhibit certain essential deficiencies concerning the reproduction of the relevant material properties occurring in a hydrated soft biological tissue. As a matter of fact, singlephasic models can never predict the interstitial fluid flow or related effects like osmosis, but are, on the other hand, simpler to implement and numerically cheaper than biphasic models, when regarded from an computational point of view. However, quite a few models have more than one phase but are often restricted to the small-strain domain or are not capable of capturing the intrinsic viscoelasticity of the solid skeleton, which might be dominant in some applications. Moreover, the reinforcement of collagen fibres is often captured by 1-d elements spanning between the corner nodes of the respective 3-d finite elements used to discretise the biological soft tissue, thereby causing a mesh dependency of the solution.

Keeping this in mind, computational biomechanics applied to the IVD and especially to one or even several motion segments is still a challenging task, because it is still not solved in detail, to what extent the several tissue properties of the IVD influence the overall behaviour of the spine. Moreover, concerning numerical simulations of the spine, several complex and coupled problems have to be solved simultaneously. Neglecting the difficulties resulting from the contact of the spinous processes via the facet joints or the enormous difference in stiffness between the IVD and the adjacent vertebrae, the IVD exhibits several other coupled effects. In particular, there is the dissipative behaviour resulting from the viscous "fluid flow" inside the tissue, which can either be mechanically or electro-chemically driven, as well as flow-independent (intrinsic) viscoelastic properties of the ECM. Moreover, the tissue is partly reinforced by fibres yielding an anisotropic behaviour and is exposed to large deformations, when computing real-life problems.

Another difficulty arises from the application of the developed numerical model. It is often cumbersome to obtain reliable experimental data to identify the theoretically introduced material parameters. In this regard, it is also difficult to define the boundary conditions for realistic boundary-value problems in the framework of the finite element method (FEM).

Moreover, concerning the FEM, such sophisticated and complex models exhibit many degrees of freedom when applied to a general 3-d discretisation of the spine. This effect is not only due to the numerical expensiveness of the mixed finite elements in use, but also due to the complex geometries involved which have to be approximated in a reasonable way. Following this leads to rapidly growing systems of equations which have to be solved during such a numerical approximation, and thus, to an enormous numerical effort. Considering the fact that a reliable solution depends on the accuracy of the numerical approximation, and thus, relies upon a reasonably fine mesh, the computational limits of a single personal computer (PC) available at present are reached very easily. Hence, parallel computation strategies come into play, in order to combine the power of several PCs to solve the problem simultaneously.

1.2 Scope, Aims and State of the Art

Ranging from the continuum-mechanical modelling to its numerical realisation, it is the aim of this contribution to develop a finite element model, which is as simple as possible, but at the same time complex enough, to capture many of the relevant properties of the IVD influencing the overall behaviour of the spine. As the needed level of complexity as well as the relevant properties are not known *a priori*, the presented model includes simple but also more sophisticated approaches, thereby still providing the possibility to easily switch between them. The needed complexity level and the respective material parameters involved will be identified using experimental results taken from the related literature. Moreover, a parameter sensitivity analysis is carried out for compression-bending problems of a non-degenerated motion segment of the lumber spine in order to obtain the influence of certain parameters on the overall deformation behaviour. Finally, two simulations of the lumbar spine will be carried out in parallel using a multi-processor machine, thereby illustrating the efficiency of the proposed finite element model.

To be more precise, a detailed and thermodynamically consistent continuum-mechanical modelling approach is followed and formulated in a very general way in order to reproduce the behaviour of almost any charged hydrated tissue. Herein, the Theory of Porous Media (TPM), cf. de Boer [24], Bowen [27], Ehlers [47, 51, 52] or Mow *et al.* [144] is applied, which allows for a convenient and modular treatment of the necessary constitutive assumptions covering all (at first sight) relevant tissue properties. Moreover, polyconvex material laws describing the partly viscoelastic and anisotropic behaviour of the ECM are included, where the form of the respective constitutive functions is chosen to be of polynomial character, thereby including several complexity levels within the same implementation (Markert *et al.* [134] and Ogden [156]). In this regard, it is still not clear, to what extent the intrinsic viscoelastic effects stem from the isotropic part of the ECM or the structural collagen found in the AF. In this contribution, only the isotropic part of the ECM is modelled to behave viscoelastic, while the structural collagen fibres of type I remain hyper-elastic. The reason for this assumption becomes clear when the findings of Holzapfel *et al.* [96] are observed, stating that there was little to no rate dependency when a lamella of the AF is pulled in fibre direction. Following this, the intrinsic viscoelastic

formulation of the isotropic part of the ECM is based on a generalised *Maxwell*[1] model as it is described in Ehlers & Markert [61, 63] or Markert [131], whereas the collagen fibres are assumed to behave purely elastic and are modelled in a continuum-mechanical way using structural tensors, cf. Boehler [22] or Spencer [192, 193, 194]. Besides other features like the deformation-dependent permeability (Eipper [67], Markert [132]) and the possibility to include inhomogeneities, e. g., varying fibre alignment or location-dependent mechanical and chemical behaviour (Ehlers *et al.* [58, 66]), osmotic effects are also included. Herein, the simplifying assumption of Lanir [116] is applied stating that a consideration of the free movable ions is needless if no sudden concentration changes of the surrounding fluid occur, which is the case for living soft biological tissues. In this regard, an osmotic pressure contribution is formulated solely depending on the fixed negative charges which can be expressed in terms of the movement of the ECM.

Following this, the scope is to model the IVD in a non-degenerated condition, in order to understand its complex behaviour regarding the interplay of its structural, mechanical, and electro-chemical components as well as their influence on the overall response of the spine. Thus, the model can *a priori* serve as a numerical laboratory, where the influence of different scenarios concerning the composition of the disc are easily obtained, cf. Ehlers *et al.* [66] or Karajan & Ehlers [107]. Moreover, the influence of the IVD on the overall performance of the spine is investigated via computations on motion or spine segments, cf. Ehlers *et al.* [60]. Regarding the design of new IVD implants, this knowledge is of great benefit, as the implant must behave like the non-degenerated original in a best possible manner. After the approximate identification of the involved material parameters, the presented model may then be able to compute reference solutions for the overall design as well as the fine tuning of IVD implants.

In order to perform these computations, the developed model is numerically approximated using the FEM. Herein, the respective governing equations are implemented into the FE-tool PANDAS which is going back to Ehlers & Ellsiepen [55] and Ellsiepen [70]. Moreover, an interface is developed to couple the sequential research code PANDAS to the parallel solver M++ of Wieners [228], whereas the coupling is based on an already existing interface developed by Ammann [4] and Wieners *et al.* [229, 230]. Finally, the numerical solution of even large 3-d problems at suitable computational costs is possible, cf. Ehlers *et al.* [60] or Wieners *et al.* [231].

Currently, there are several models and modules available, which are used to describe soft biological tissues in general. However, most of them do not cover all the requirements needed for the continuum-mechanical modelling of the IVD. For example, the models used for state-of-the-art simulations of the spine are often restricted to singlephasic materials, thereby *a priori* excluding effects resulting from interstitial fluid flow and osmosis. The first spine simulations with an advanced IVD model were carried out by Shirazi-Adl [182, 183] or Shirazi-Adl *et al.* [184, 185] using a deformation-dependent *Hooke*[2]-type ma-

[1] *James Clerk Maxwell* (1831–1879): Scottish mathematician and theoretical physicist who is considered by many other physicists to be the scientist of the nineteenth century with the most influence on twentieth century physics. His most significant achievement was aggregating a set of equations in electricity, magnetism, and inductance; the so-called *Maxwell* equations.

[2] *Robert Hooke* (1635–1703): English natural philosopher and polymath who played an important role

terial tangent and nonlinear spring elements to capture the collagen fibres in the AF. A similar model but using more sophisticated (singlephasic) material models and a detailed geometry approximation can be found in Schmidt *et al.* [175, 176]. In order to overcome the resulting grid dependency of the alignment of the spring elements, the anisotropic continuum theory based on Boehler [22] and Spencer [192, 193, 194] was adopted and applied to the unique behaviour of the collagen fibres by, e. g., Elliott & Setton [69], Holzapfel & Gasser [95] or Klisch & Lotz [111], whereas Balzani [14], Balzani *et al.* [15], Markert *et al.* [134] or Schröder & Neff [179] developed the theory further towards a polyconvex framework. This knowledge was then incorporated in the lumbar spine simulations of Eberlein *et al.* [44, 45].

Since these models are singlephasic, they do not account for the fluid flow in the disc which is important for nutritional purposes and maintaining the biological composition, see, e. g., Holm & Nachemson [93] or Urban & Holm [211]. Hence, at least a second phase, the interstitial fluid, has to be introduced to overcome this deficiency. In this context, several biphasic models, based on the works of Biot [18], Bowen [26] and Mow *et al.* [146], are applied to describe soft biological tissues in general or with application to the IVD, see, e. g., Argoubi & Shirazi-Adl [7], Ayotte *et al.* [11], Iatridis *et al.* [102], Klisch & Lotz [112], Li *et al.* [120, 121] or Riches *et al.* [168]. However, as the occurring osmotic effects influence the fluid flow in the tissue, it also has to be considered. In order to include these electro-chemomechanically driven swelling phenomena, the biphasic models need to be extended, thereby emerging two different approaches. On the one hand, there is the independent description of the freely movable ions of the pore fluid yielding a complex and strongly coupled system of partial differential equations (PDE) leading to a sometimes difficult numerical treatment, cf. Chen *et al.* [33], Ehlers & Acartürk [53], Ehlers *et al.* [64], Frijns *et al.* [76, 77], Huyghe *et al.* [99], Iatridis *et al.* [100], Kaasschieter *et al.* [106], van Loon *et al.* [127] or Mow *et al.* [143]. On the other hand, a much simpler algorithm capable of describing osmotic effects is based on the assumption of an instantaneous chemical equilibrium throughout the domain of the IVD, cf. Lanir [116]. Following this, only the solid skeleton is extended by almost volume-free, fixed negative charges and a constitutively computed osmotic pressure is added to the hydraulic pressure. This procedure is adopted in the context of a two-phase model by Ehlers *et al.* [58, 59, 66], Hsieh *et al.* [97] or Laible *et al.* [114]. A comparison of the two approaches yields a good approximation of the exact solution for the simplified model, even when simulating sudden concentration changes in the external solution, cf. Wilson *et al.* [234]. However, as sudden changes in the surrounding concentration are usually not applicable for living organisms, *Lanir*'s assumption is suitable for the numerical simulation of the IVD for instance.

in the scientific revolution through both experimental and theoretical work. Besides his discovery of plant cells, his greatest achievement was the formulation of one of the fundamental laws in solid mechanics in 1678, i. e., *"ut tensio, sic vis"* meaning "as is the extension, so is the force".

1.3 Outline of the Thesis

Starting with **Chapter 2**, the needed basic anatomical knowledge is reviewed and summarised in the context of the intervertebral disc and its material properties. In particular, the microscopic composition of the IVD is extensively discussed, which finally leads to an electro-chemically active material with anisotropic, inhomogeneous and strongly dissipative behaviour. Since the goal of this thesis is to perform realistic computations on a motion segment as well as a section of the spine, the neighbouring components like the cartilaginous endplates as well as the vertebrae are briefly introduced. Moreover, some fundamental terms of basic chemistry are reviewed, in order to get a better understanding of the involved osmotic process.

Chapter 3 is concerned with the continuum-mechanical fundamentals needed to model the porous IVD. After a brief introduction into the Theory of Porous Media with a direct application to electro-chemically active materials, the IVD is, in a first step, decomposed into its five main components, i. e., the solid, the pore liquid, the fixed negative charges and the dissolved cations and anions. Thereafter, the involved kinematical relations are illustrated, where a particular focus is placed on the multiplicative decomposition of the solid deformation gradient, needed to describe finite inelastic kinematics of a viscoelastic solid skeleton. As a next step, the five classical balance equations as well as a balance for the charges are introduced via the universal master balance concept.

The objective of **Chapter 4** is to characterise the universally valid balance equations with characteristic constitutive assumptions and response functions in order to obtain the desired material behaviour of the IVD. Following this, the introduced balance relations are firstly reduced for a simpler treatment, but without cancelling out the primary effects. In this regard, *Lanir*'s assumption is introduced and the resulting description of the swelling-active material using only a binary model with attached fixed negative charges is discussed. Thereafter, attention is drawn to the fundamentals of material theory. In this regard, the general concept of material symmetry is discussed with a particular focus on fibre-reinforced materials as well as the closely related concept of material frame indifference. Following this will then lead to the concept of isotropic tensor functions, which is needed to specify the respective constitutive equations. Herein, thermodynamically admissible response functions are derived to describe the osmotic influence, the viscoelastic and anisotropic solid skeleton as well as the percolation process of an incompressible viscous pore fluid.

In **Chapter 5**, the derived governing equations are numerically approximated using the framework of the mixed finite element method in space and the finite difference method in time. In this regard, the resulting discrete system of coupled nonlinear partial differential equations is presented and a step within the multilevel *Newton*[3] method is described

[3]Sir *Isaac Newton* (1643–1727): English physicist, mathematician, astronomer, natural philosopher, alchemist and theologian who published the *Philosophiae Naturalis Principia Mathematica* in 1687, which is said to be the greatest single work in the history of science. Herein, he described universal gravitation and the three laws of motion, thereby laying the fundamental work for classical mechanics, which dominates scientific engineering down to the present day.

using the simplest possible but stable time integration, i. e., the implicit *Euler*[4] method. The last part of this chapter describes how the resulting discrete problem is prepared for parallel computations using several CPU at the same time. In this regard, the basic idea of the underlying interface between the two programs PANDAS and M++ is illustrated.

The application of the developed model to realistic problems of the IVD is carried out in **Chapter 6**. Herein, a realistic computation of a motion segment is only possible, when the structural properties are taken into account. Hence, the problem of geometry acquisition and finite element mesh generation is presented in combination with the numerical computation of the respective collagen fibre directions as well as the distribution of the location-dependent material parameters needed to capture the inhomogeneous properties. In this context, an algorithm is derived, which is capable of computing these quantities totally independent of the underlying finite element mesh.

Moreover, the biggest problem of identifying the involved material parameters is discussed and solved using, where available, experimental data as well as material parameters obtained from a vast collection of related literature sources. Since the parameters often appear in a coupled manner, their identification is only possible via inverse computations. Following this, a numerical sensitivity analysis is carried out yielding an indication for the relevant parameters in experiments concerning a motion segment in a short-duration compression-flexion experiment as well as in long-term loading situations. Subsequently, two parallel simulations of a lumbar spine segment are presented. Herein, the healthy state is qualitatively compared to the case of a stiffened L4-L5 motion segment.

A final conclusion and discussion is given in **Chapter 7** including an illustration of further possible developments based on the presented work.

For a better understanding of the discussed topics, additional information regarding the needed mathematical fundamentals is embraced in **Appendix A**.

[4] *Leonard Euler* (1707–1783): Pioneering Swiss mathematician and physicist who is considered to be the preeminent mathematician of the 18th century and one of the greatest of all time. Much of the modern mathematical terminology and notation, particularly for mathematical analysis and number theory, was strongly affected by his research. In mechanics, he contributed pioneering work concerning the description of buckling phenomena and general fluid dynamics.

2 Anatomical and Chemical Fundamentals

Before going into details of the continuum-mechanical modelling procedure, some anatomical, biological and chemical fundamentals regarding the human body, its spinal column and particularly the intervertebral disc are presented in this chapter. As many engineers usually have little knowledge in mechanobiology, this addresses especially the basic anatomical terminology as well as the biological composition and the resulting mechanical behaviour of the IVD.

More detailed information on human anatomy can be found in standard texts, like Agur & Dalley [3] or Netter [151] among others. It is even possible to browse through the data collected by the "Visible Human Male" project [198] at one of the many mirrors available online, cf., e. g., the Visible Human Server [217]. Concerning the biomechanics of the human spine, a comprehensive overview is found in, e. g., Ashton-Miller & Schultz [9], Jayson [105], and White & Panjabi [225], whereas for detailed information on the functioning and microscopic composition of the intervertebral disc in particular, the reader is referred to the standard works by Ayad & Weiss [10], Eyre [73], Hukins [98], Marchand & Ahmed [130], Szirmai [201] or Urban & Roberts [214] and references therein.

For a more comprehensive introduction into the peculiarities of the electro-chemical background, the reader is encouraged to refer to the standard texts of Lide [122] or Adam *et al.* [2], among many others. Concerning biological tissues and membranes, a comprehensive overview can be found in, e. g., Sten-Knudsen [199].

2.1 Anatomical Positions in the Human Body

Roughly spoken, everybody knows that the human body represents the entire physical structure of a human organism and usually consists of a head, neck, torso as well as two arms and two legs. However, a specific terminology has to be introduced, in order to refer to certain parts of the body without confusion. In the context of medical or human anatomy it is (in contrast to the situation in zootomy) possible to rigidly define standard anatomical positions and directions in the human body. This is mainly because of its bilateral symmetry as well as a precisely defined anatomical reference position, i. e., standing erect, arms by sides, and palms of the hands facing forward. In this position the superior, inferior, anterior, posterior, sinister and dexter directions are given, which correspond to the top (head), bottom (feet), frontside (belly), backside (buttocks), left and right side (lateral), respectively. However, when not discussing the body as a whole, the terms dorsal and ventral, originally needed in vertebrate zootomy[1], are frequently used in human anatomy, which are the respective synonyms for anterior and posterior. Following this, the corresponding directions can be understood as a coordinate system

[1]This is often a source of confusion to those accustomed to the standard vertebrate directional terminology, e. g., for quadruped vertebrates like horses, the ventral direction is the "belly side", while the anterior refers to the front of the animal, i. e., the head.

which is pinned to the body, and thus, the head is always superior to the rest of the body, even if the patient is lying down or standing on his head. In this regard, the X_1-axis is defined from posterior to anterior, the X_2-axis from dexter to sinister and the X_3-axis from superior to inferior, cf. Figure 2.1 (a).

Naturally, these directions define three planes which also play an important role when referring to the human body, for instance, in medical imaging techniques such as sonography, computer tomography (CT) or magnet resonance imaging (MRI). In particular, the following definitions hold:

- a coronal (also known as frontal) plane is perpendicular to the X_1-axis and separates anterior from posterior,
- a sagittal (also known as median) plane is perpendicular to the X_2-axis and separates sinister from dexter, where in particular, the midsagittal plane is a specific sagittal plane that divides the body in two halves,
- a transverse (also known as axial or horizontal) plane is perpendicular to the X_3-axis, i. e., parallel to the ground and separates superior from inferior.

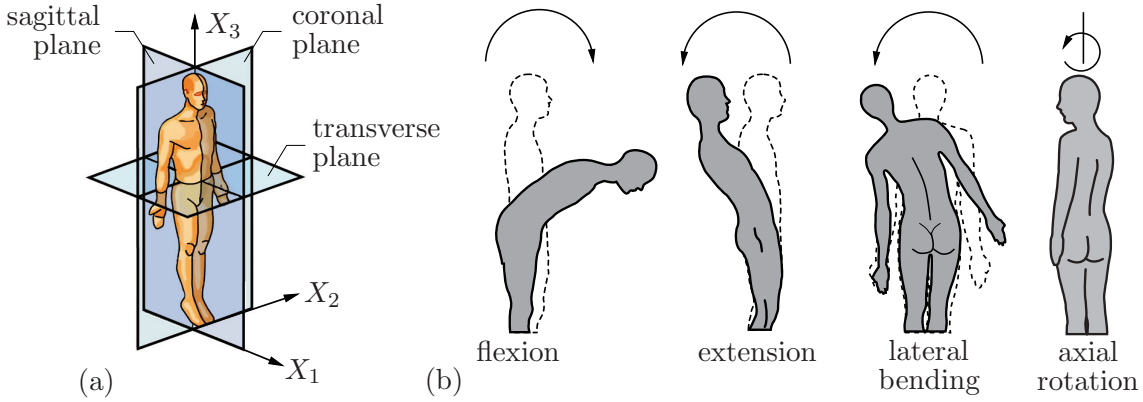

Figure 2.1: *(a) Different planes of the human body and (b) movements in its sagittal, coronal and transverse plane, i. e., flexion/ extension, lateral bending, and axial rotation, respectively.*

It is now possible to define specific movements of the spine as they are shown in Figure 2.1 (b). In particular, simple forward bending of the torso takes place in the sagittal plane and is defined as flexion, whereas leaning backwards is defined as extension. Bending modes in the coronal plane are then simply defined as left and right lateral flexion. Finally, the last possible movement is a rotation of the trunk around the X_3-axis, which is also known as torsion or axial rotation. Naturally, these three basic movements are often superimposed during daily activities, such as lateral bending-torsion for instance.

2.2 Function and Composition of the Human Spine

The spine plays a key role in the human body as it is an important structural element connecting the pelvis with the head. In this regard, it simultaneously has to stabilise the

trunk, transmit loads down to the legs, act as a shock absorber for the brain, and protect the spinal cord[2], while still having to provide a certain flexibility.

To be more precise, without a certain stability of the human spine, it would not be possible to walk in an erect manner. The main structural elements being responsible for this characteristic are the vertebral bodies, which are designed in a very robust and break-proof manner, in order to transmit all possible loads resulting from normal activities such as climbing stairs or carrying loads. As the spinal cord is running down the complete vertebral column, a canal has to be formed in order to securely house the susceptible nervous tissue from external influences, while still allowing for other nerves to enter and exit. In this regard, processes are attached to the posterior side of the vertebral bodies, together constituting the vertebrae. Herein, the spinal canal is totally surrounded by the processes yielding a safe housing for the nervous tissue, cf. Figure 2.2 (c). Following this, the spines flexibility and shock absorbing characteristic must be due to different structural elements, which are called intervertebral discs (IVD), as they are located in-between the respective vertebrae. In particular, the IVD exhibits a much softer behaviour allowing the torso to perform combinations of the three principal motions defined in the preceding section. Since the sole combination of several vertebrae and IVD leads to a highly resistible but flexible structure, it has to be stiffened in order to prevent buckling. This task is accomplished by attached muscles and ligaments running in axial direction of the spine.

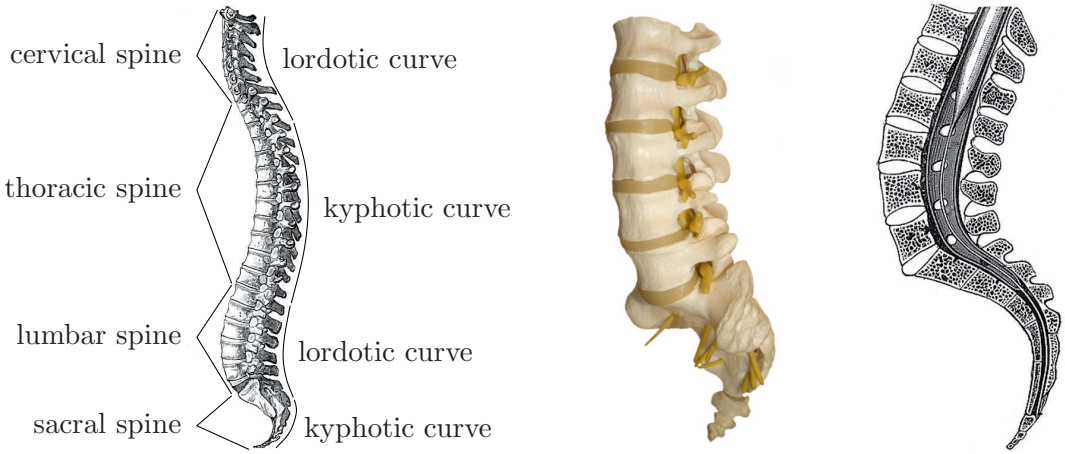

Figure 2.2: *(a) Lateral view on the vertebral column showing the cervical, thoracic, lumbar, and pelvic parts of the spine, (b) latero-frontal view of the lumbar and sacral spine showing how the nerves (yellow) enter and leave the spinal canal, and (c) midsagittal cut through the lower spine region showing the spinal canal. Lithographs are taken from Gray's Anatomy [82].*

The vertebral column is divided into five different sections, namely the cervical, thoracic, lumbar, sacral, and coccygeal spine. The first three correspond to the neck, chest,

[2]The spinal cord (*medulla spinalis*) is a long, thin, tubular bundle of nerves that is an extension of the central nervous system, i. e., the brain. Its main function is the transmission of neural signals between the brain and the rest of the body.

and stomach area of the body, respectively, while the latter two are located at the pelvic area. As it is shown in Figure 2.2 (a), the sections consist of seven cervical vertebrae (C1-C7), twelve thoracic vertebrae (T1-T12), and five lumbar vertebrae (L1-L5), whereas the five sacral vertebrae (S1-S5) and the three to four coccygeal segments (tailbone) are fused together leading to a total of 24 IVD located in-between the respective vertebrae. In this regard, the combined height of all IVD accounts for approximately one-fourth of the total length of the spinal column.

When looking at the spine in a sagittal plane, there are four normal curves to be seen. These are convex anterior (*lordosis*) at the cervical and lumbar levels and convex posterior (*kyphosis*) at the thoracic and pelvic levels. Note that in a newborn infant, the cervical and lumbar levels do not exhibit a lordotic curvature. The cervical *lordosis* will gradually develop when the child starts to hold up its head and sit upright, while the convex anterior curve at the lumbar level is developed when the child begins to walk. Thus, the curvature of the vertebral column can be understood as a structural optimisation and a direct consequence of typical human load cases such as walking erect.

A vertebra is typically composed of a stiff cylindrical block of bone, i. e., the anterior vertebral body, and a bony ring, i. e., the posterior vertebral or neural arch, forming a foramen which is responsible for the housing of the spinal cord. Herein, the vertebral arch is formed by two laminae which are connected to the vertebral body via the two pedicles, cf. Figure 2.3. Moreover, it supports a total of two superior and two inferior articular processes, two transverse processes, and one spinous process. The purpose of the latter three processes is to serve as attachment points for spinal muscles and ligaments, while the former ones articulate with the adjacent vertebrae.

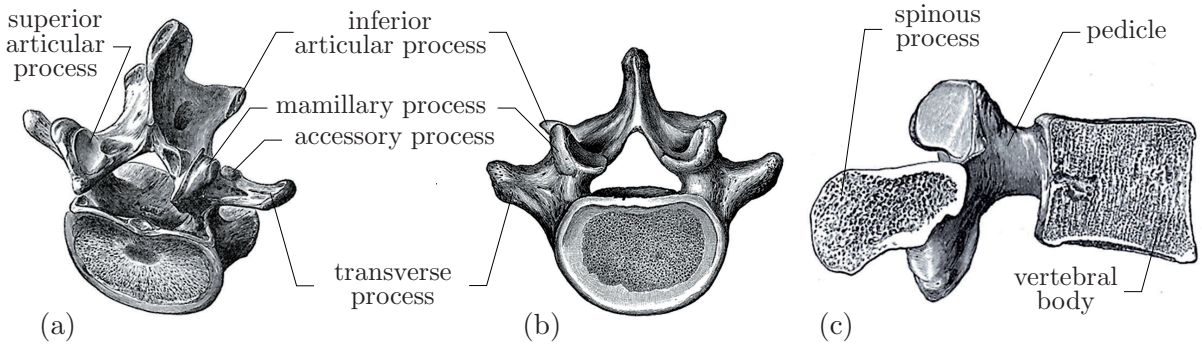

Figure 2.3: *(a) 3-d and (b) axial view of the lumbar vertebrae showing the arrangement of the respective processes. (c) A sagittally cut L5 vertebra enables the view on the typical trabecular structure being surrounded by the dense cortical shell. Lithographs are taken from Gray [82].*

Like in most other bones, the main structural element of a vertebra is the cancellous bone tissue, also known as trabecular or spongy bone, which is saturated by bone marrow and enclosed by a thin coating of compact bone, i. e., the much denser and stiffer cortical shell. Figure 2.3 clearly shows the alignment of the trabecular structure in the vertebral body, which is following the main load direction, i. e., the axial direction. Moreover, one can identify one or two rather large canals in the vertebral body allowing for the reception of veins and arteries, in order to connect the bone marrow with the vascular system. The size of the vertebral bodies is proportional to the magnitude of the axial load, i. e., they

are smallest within the cervical spine and increase in size towards the lumbar spine. Their superior and inferior surfaces as well as the surrounding surface are slightly concave.

Regarding the geometry of the respective spinous processes one will discover that they also vary in shape as well as in position to each other. Thus, they greatly influence the flexibility of the spine. In this context, the greatest movement is possible in the cervical spine, i. e., to allow for a turning movement of the head, and is lowest in the lumbar region, where the articular processes rather contribute to the load carrying characteristic. For more information on the load transmission via contact forces in the facet joints, the reader is referred to, e. g., El-Bohy *et al.* [68], Miller *et al.* [138], and references therein.

The ligaments and muscles contribute a great portion to the overall stability of the spine. When considering a fresh cadaveric spine devoid of muscles and ribs, an axial load of only 20 N applied centrally at T1 already leads to a stability failure and permanent deformations away from its original upright position, cf. White & Panjabi [225]. While the muscles actively provide stability as well as directly control and produce the movements of the vertebral column, the ligaments provide only passive support by carrying large tensile forces when stretched. Thus, the stretched ligaments also allow for a relief of the surrounding muscles and absorb large amounts of energy before failure, if the spine is opposed to traumatic situations, i. e., when nonphysiologically high loads are applied at high speeds, like it is the case during a car accident. In this regard, they also contribute to the protection of the spinal cord, as they prevent excessive elongation of the nervous tissue, in case the spine is exposed to any kind of bending moment or direct tension.

The functionality of the ligaments is mainly due to their uniaxial structure consisting of aligned collagen fibres and their ability to carry high tensile loads. However, as the ligaments buckle when exposed to compression, their geometrical alignment and connection to the spine plays also an important role for their functionality. In this regard, a total of seven ligaments are connected to the spine, thereby allowing for at least one ligament to be stretched, when arbitrary deformation modes are applied. Thus, the ligaments almost totally enclose the spine, cf. Figure 2.4.

In particular, the seven ligaments include an anterior longitudinal ligament (ALL), which is attached to the anterior surface of the vertebral bodies as well as a posterior longitudinal ligament (PLL) attached to all posterior surfaces of the vertebrae and IVD. Both ligaments extend over the whole length of the vertebral column. Moreover, the *ligamenta flava* (LF) are spanning between the antero-inferior border to the postero-superior border of adjacent laminae and the capsular ligaments (CL) connect adjacent articular processes. Similar with the intertransverse ligaments (ITL) and interspinous ligaments (ISL), which connect adjacent transverse processes and spinous processes, respectively, while the supraspinous ligament (SSL) spans only between the tips of adjacent spinous processes and is continuous over the axial elongation of the spine.

The kinematics of the spine is significantly influenced by the behaviour of its motion segments which consist of two adjacent vertebrae and an IVD in-between. In this regard, the response of a motion segment is not only governed by the material behaviour of the respective components, but also by their geometric alignment resulting in a com-

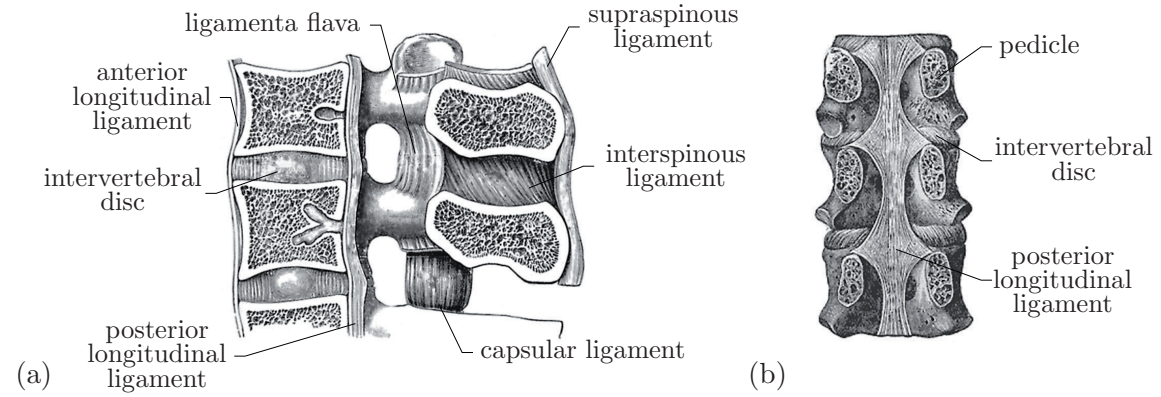

Figure 2.4: *(a) Sagittal cut and (b) dorsal view of a motion segment showing the respective ligaments that are attached to the spine. Lithographs are taken from Gray [82].*

plex interplay between the IVD, the ligaments, the vertebral bodies and their processes. However, it is especially the interaction of the spinous processes and the ligaments which, when under physiological loading conditions, restricts the movement to physiological limits. These limits can be understood as applied motions or loads, which occur during the normal range of physical activities, thereby not damaging any component of the spine. Following this, the greatest possible values for each of the six degrees of freedom in 3-d space leads to the definition of the so-called range of motion (ROM).

As already mentioned above, the geometry of the vertebrae is altered in axial direction, which results in a different ROM for each motion segment. For instance, the L1-L2 motion segment of the lumbar spine reaches its physiological limits in voluntary flexion at an angle of 8° and in left lateral bending at 6°, while the lowest motion segment L4-L5 offers a maximum of 13° in flexion and 2° in left lateral bending, cf., Pearcy *et al.* [162] and Pearcy & Tibrewal [163] among others.

Another important parameter for the characterisation of the movement of a motion segment is the instantaneous axis of rotation (IAR), which is the generalisation of the centre of rotation for the general case of rigid body movements. Although there is a great variation of the IAR from individual to individual, there is one general trend to be observed: In flexion, the IAR is located at the anterior side of the motion segment, while in extension it moves to the posterior side. During lateral bending as well as torsion, the IAR moves to the opposing side of the motion segment, i. e., left lateral bending has the IAR located at the right side.

For the sake of this contribution, this brief excursus to general spine mechanics is ended here, as it should already give a rough idea of this complicated matter. Since the IVD is the key aspect of this monograph, its anatomy as well as its unique tissue properties are excluded and discussed comprehensively in the following section.

2.3 Anatomy and Tissue Properties of the IVD

Like the ligaments and the processes, the intervertebral disc strongly influences the overall behaviour of a motion segment. In particular, the IVD is responsible for the transmission

of the majority of the applied axial loads and is at the same time able to damp non-physiologically high loads or vibrations, such that the brain is protected against excessive shocks. Moreover, when moments are applied to a motion segment, the IVD allows for a certain rotational movement between the adjacent vertebrae, thereby carrying the first part of the applied moment until the ligaments of the processes are stretched far enough to carry the rest of the load. Thus, the IVD also influences the location of the IAR during bending modes.

Compared to the other components of the spine, the IVD has a relatively simple geometry which is more or less adjusted to the adjacent vertebrea. However, from a continuum-mechanical modelling point of view, the IVD is the most challenging material to be described within the spine. This is not only due to its complex and strongly coupled material behaviour, but also due to its inherent inhomogeneous structure leading to an inhomogeneous distribution of the mechanical properties. For the sake of this monograph, only the properties of the lumbar IVD will be illustrated in the following.

2.3.1 Biochemical Composition

Proceeding from a macroscopic examination in the context of a dissection procedure, the geometry of the IVD evolves after its detachment from the rest of the spine. Herein, the overall shape is predetermined by the adjacent vertebrae, i. e., it has a similar axial cross section as well as convex superior and inferior sides. However, while the side surfaces of the vertebrae are concave, the surrounding side surface of the IVD is slightly convex. In general, the size of the discs follows the same tendency as the vertebral bodies, i. e., they are smallest in the cervical and largest in the lumbar region. Regarding the IVD of an adult human between the vertebrae L1 and L5, they exhibit an average height of about $15 - 17\,\mathrm{mm}$ as well as a "diameter" of about $50\,\mathrm{mm}$ [214].

After cutting the IVD through its midaxial plane, it appears as a more or less white material, cf. Figure 2.5 (a), indicating that there is no internal blood supply via blood vessels, i. e., the tissue is avascular. Note in passing that the IVD is the largest avascular structural element to be found in the overall human body [73]. A closer look allows for a rough distinction of two regions, cf. 2.5 (b). Herein, a very soft and gelatinous core can be outlined, i. e., the *nucleus pulposus* (NP), which is surrounded by a slightly firmer lamellar structure, i. e., the *anulus fibrosus* (AF). In this regard, the NP occupies about $50 - 60\,\%$ of the IVD cross section [214]. Moreover, an observation from the side reveals that the lamellae of the AF consist of a fibrous structure, where the fibres run helically around the disc. When the outermost lamella is dissected, the next lamella appears to have an opposite alignment of the fibres. This alternation takes place until the NP is reached yielding a total of 15 to 25 distinct layers [130].

When the IVD is cut through the midsagittal plane, another structural element can be seen which forms the superior and inferior connection to the adjacent vertebrae. These roughly $1\,\mathrm{mm}$ thick layers consist of hyaline cartilage and are known as the cartilaginous endplate (CEP) which completely cover the NP and parts of the inner AF [73].

Following Ayad & Weiss [10], Eyre [73] or Urban & Roberts [214] among others, the IVD

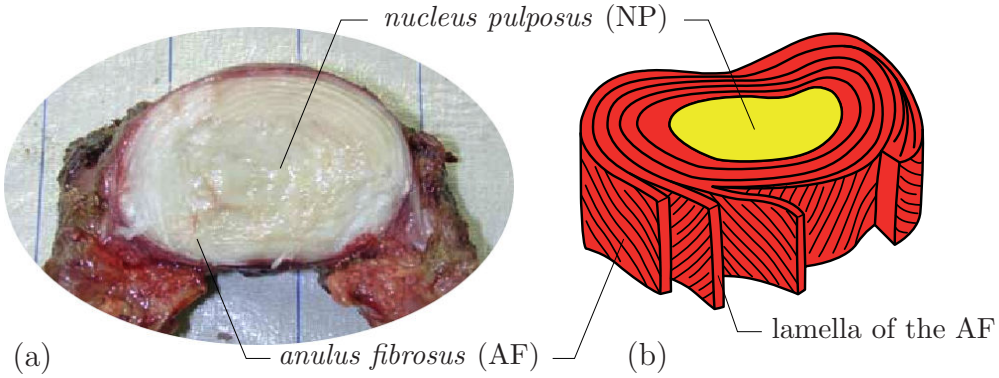

Figure 2.5: *(a) Axial cut through an IVD of an 18-year-old woman (courtesy of H.-J. Wilke) and (b) schematic illustration of the macroscopic composition of the IVD showing the nucleus pulposus (NP) and the lamellar structure of the anulus fibrosus (AF).*

appears as a porous multi-component microstructure composed of a charged hydrated extracellular matrix (ECM). In this regard, 95 % of the tissue's wet weight consists of the ECM, i. e., structural macromolecules like proteoglycans[3] (PG) and collagen, as well as water containing dissolved solutes. To be more precise, PG are large complex biomolecules and are composed of a protein core to which one or more glycosaminoglycan (GAG) chains are covalently attached. Following this, the GAG chains are linear polymers which have a large number of sulphate and carboxylate groups [73], i. e. they are polyanions. Thus, the tissue can be considered to contain a polymer network with fixed negative charges which smaller ions, e. g., the dissolved solutes, can diffuse to. Following this, the fixed charge density (FCD) mainly determines the distribution of the charged solutes.

Out of the at least 18 known different types of collagen [147], there are two main groups to be found within the IVD. Firstly, this is collagen of type I, which is well organised and forms parallel fibre bundles with a diameter ranging from 40 to approximately 330 μm [130]. Thus, these fibre bundles can be seen by the naked eye. In contrast, collagen fibres of type II have a much smaller diameter ranging from 10 to 300 nm [147], and form a loose and randomly oriented network of fibrils. Herein, both types of collagen are found in the AF, while the NP contains only type-II fibrils. However, there is no sharp border in the occurrence of the two types of collagen between the NP and AF, but rather a smooth transition.

In general, the water content of the IVD is highest in the NP reaching about 80 to 90 % of the wet weight and decreases in the AF to an average of 65 % of the wet weight [150, 214]. This water content is by no means stable throughout the life of an individual. For instance, the diurnal loss of water due to a regular loading of the disc is approximately 10 to 20 % of the total water content which is re-imbibed during rest at night due to the water attracting characteristic of the GAG chains in the ECM[4]. Note in passing that the

[3] Proteoglycans is the prevalent term which replaces the old nomenclature of protein polysaccharides. In this context, PG are polyanionic macromolecules consisting of several acidic polysaccharides, mostly referred to as glycosaminoglycan chains in association with a small quantity of protein [10].

[4] *Nuclei pulposi* from young subjects absorb fluid equal to 95 % of their original weight when soaked in saline, while those from adult and aged subjects absorbed the equivalent of 55 % and 25 % of their weight, respectively, cf. Naylor [150] and qualitatively in [201].

main supply of nutrients is not due to the fluid exchange resulting from diurnal interplay of loading and unloading, but is mainly due to diffusion in the pore fluid, cf. Urban *et al.* [212]. In contrast, there is a steady decrease of the water content with age which is an irreversible process due to the degeneration of the tissue.

Moreover, not all of the water content of the disc is found in-between the pores of the ECM. The collagen fibres and fibrils also contribute a considerable amount to the overall water content, as they contain trapped intrafibrillar water which is not able to flow freely inside the disc, but is still able to communicate with the surrounding extrafibrillar water via diffusion [214]. Herein, it is possible to verify the existence of the intrafibrillar water *in vivo*[5] via an MRI analysis but it is not possible yet to quantitatively measure the ratio between the two water compartments, cf. Effelsberg [46]. In this regard, the quantitative diurnal loss of extrafibrillar water has also been proved, while the intrafibrillar water content was constant.

Similarly, the CEP is made of hyaline cartilage, where water contributes approximately 72 % of the wet weight, while collagen of type II and PG account for about 66 % and 18 % of the remaining dry weight, respectively. Herein, the collagen fibrils in the central region of the CEP run tangential to the surface of the vertebrae, while the fibrils in the region of the AF emerge perpendicular, thereby directly reaching into the lamellae of the AF. However, in a band of about 1 cm, the coarse fibres of the outermost AF are anchored directly to the vertebral bodies via the so-called *Sharpey*'s fibres[6] [73].

2.3.2 Inhomogeneous Structure

The IVD exhibits several inhomogeneities regarding the distribution and alignment of its components. According to Eyre [73], Urban & Roberts [214], and Ayad & Weiss [10], the PG account for approximately 60 % of the dry weight throughout the NP, while the portion in the AF is linearly decreasing in radial direction reaching a minimal value of about 10 % of the dry weight. Hence, the FCD resulting from the attached GAG chains is also highest in the centre of the IVD and decreases towards the periphery, which corresponds to measurements performed by Urban & Holm [211] or Urban & Maroudas [213]. As water is attracted by the fixed negative charges, the water content follows a similar progression, i. e., it is highest in the NP reaching about 85 % of the wet weight and gradually decreases within the AF to the lowest percentage of approximately 55 % of the wet weight in the outermost layer [150, 214]. Note in passing that the PG content degenerates with age which causes a decrease of the water content. In particular, Ayad & Weiss [10] and Antoniou *et al.* [5] describe the NP of a 60-year-old subject having a water content of 70 % of the wet weight and a PG content of only 30 % of the dry weight.

A reversed distribution is observed regarding the ubiquitous collagen, where its fraction of the dry weight is highest in the outer AF, while it gradually declines towards the NP. Quantitative measurements in [5, 10, 73] reveal a collagen content of 50 to 60 % of the

[5] *In vivo* means "in the living organism" and is contrary to *ex vivo* standing for "out of the body".

[6] *William Sharpey* (1802–1880): Scottish anatomist, who firstly described the fibres that join together the lamellae of bone in 1846. In Britain he is known as the "father of modern physiology".

dry weight in the peripheral lamellae of the AF, while it decreases more or less linearly towards the NP having a collagen content of 15 to 30 % of the dry weight. Moreover, Eyre & Muir [75] measured the division of the two main types of collagen occurring in the IVD. Herein, more than 85 % of the collagen in the NP is of type II, while the remainder is of type-I collagen. Regarding the overall AF, the collagen division is 44 % type I and 56 % type II having a general tendency of a higher type-I content in the outer AF which is decreasing towards the NP in favour of a rising content of type II [5, 74]. Note in passing that after the age of 25, the fraction of collagen remains essentially constant. Nevertheless, the relative rates of deposition of type I and type II collagen may change with time if, for instance, the diffusion of nutrients into the IVD becomes abnormal [75]. The remaining percentage of the overall dry weight is made of minor non-collageneous proteins which will not be discussed in further detail in this monograph.

Moreover, the AF is not only a complex aggregate due to the inhomogeneous arrangement of its components, but also due to its highly irregular structure, i. e., its morphology. In this regard, it was a common belief that the lamellae of the AF become narrower and less distinct as the AF merges into the NP in what is often termed the transition zone [73]. About ten years later, Marchand & Ahmed [130] proved the opposite by a layer-by-layer peeling of several *anuli fibrosi* at different ages resulting in thinner lamellae in the periphery compared with the inner regions. The overall trend, however, was captured in an identical manner, i. e., anterior layers are, in general, thicker than posterior ones. Furthermore, adjacent lamellae are sometimes partly interwoven leading to incomplete fibre bundles which do not run all the way from the superior to the inferior vertebrae. In this regard, incomplete lamellae primarily occur throughout the posterior AF as well as in the inner regions of the lateral and anterior AF. In contrast, most of the lamellae in the peripheral lateral and anterior AF are continuous. For more detailed information on these measurement, the interested reader is referred to Marchand & Ahmed [130] or Tsuji *et al.* [209]. Thus, regarding the collagen content as well as the continuity of the lamellae, there is a general radial variation throughout the AF, while in circumferential direction only the postero-lateral part is exposed to changes in continuity of the adjacent lamellae.

Another morphological inhomogeneity concerns the alignment of the large type-I collagen fibre bundles within the lamellae of the AF. In this regard, Holzapfel *et al.* [96] performed an extensive study on the IVD of the upper lumbar spine being taken from several age groups. Herein, also a layer-by-layer peeling technique was used, where the inclination of the fibres with respect to the transverse plane was measured at seven circumferentially positioned measuring points. Following this, the inclination angle at the midsagittal ventral position is about 20° and 50° at the midsagittal dorsal position having an almost linear development of the angle in the interjacent circumferential direction. However, there is neither an indication for a variation in radial direction nor in age.

2.3.3 Characteristic Mechanical Behaviour

Biological soft tissues like cartilage in general or the IVD in particular can withstand an enormous amount of load. This is mainly due to the highly hydrated properties of the tissue and the fact of a very low permeability of the ECM. In this context, Szirmai [201]

or Urban & Roberts [214] among others suggest that the rather large PG are entangled and trapped by a type-II collagen network and imbibe water, thereby "inflating" the fine network of fibrils. Thus, the fixed negative charges of the attached GAG chains underlie the same movement as the whole ECM. Following this, the resulting microstructure is able to carry loads via hydrostatic pressure in the interstitial fluid and tension in the collagen fibrils, though none of the components could do so alone. In this context, the ECM of the tissue exhibits a very low permeability to water, which maintains the load-carrying mechanism until the water is expressed from the tissue. Note in passing that IVD tissue is approximately three decades less permeable than clayey silt[7], which is frequently used as a seal unit in embankments and is often regarded as almost impermeable in geomechanics.

On the other hand, this characteristic makes it rather difficult to experimentally determine the mechanical behaviour of the ECM alone, as it always needs to be in a hydrated state in order to obtain reliable results. Thus, volumetric deformations of a soft biological tissue are always coupled to the movement of the pore fluid and therefore, are strongly governed by the permeability of the ECM. Different however is the case of moderate shear deformations in the linear strain regime, where no volumetric changes occur. In fact, this is the most convenient possibility to measure the mechanical characteristics of the ECM, as it is decoupled from volumetric deformations and thus, from the permeability.

Moreover, the loose network of type-II collagen fibrils within the NP is distributed statistically equal, thereby leading to an isotropic behaviour of the NP. Regarding the aligned collagen in the AF, it is obvious that the respective lamellae exhibit a transversely isotropic behaviour. Following this, the mechanical behaviour of the structural collagen fibres of type I can be identified relatively straightforward, when a single lamella of the AF is dissected and tested in fibre direction by a tension apparatus. The prominent stress-strain characteristic of the aligned collagen evolves at first sight as it follows an exponential progression in the tension regime. In this regard, the flat toe region of the characteristic curve is due to the straightening of the coiled collagen fibres which quickly exhibit a locking behaviour with a very steep increase of stress when further strain is applied. This behaviour can be experienced very simply by pulling ones earlobes, i. e., for small elongations there is hardly any resistance, but once a certain point is reached, the required force to elongate any further rises quickly. Note in passing that in analogy to the theory of ropes, the collagen fibres alone are not able to withstand any compressive or shear forces.

According to the experiments carried out by Holzapfel *et al.* [96], the mechanical properties of a lamella are location-dependent and seem to exhibit a similar distribution as the morphological changes in the AF. In this regard, there is a radial variation, where the outer regions of the AF are generally "stiffer" than the corresponding inner regions. This is probably due to the less amount of structural collagen of type I in the inner lamellae of the AF. Moreover, the complex interwoven lamellae of the posterior AF might be responsible for a weaker behaviour compared with the continuous fibres of the lamellae in the anterior region. To be more precise, Holzapfel *et al.* [96] measured the mechanical properties of single lamellae of the antero-lateral and posterior AF at inner and peripheral positions, respectively, and came to the quantitative results shown in Figure 2.6 (b). Other studies

[7] Clayey silt has a hydraulic conductivity of about 10^{-8} m/s [57], while IVD tissue reaches only a value of about 10^{-11} m/s [83, 103].

performed by Ebara *et al.* [43] and Skaggs *et al.* [188] confirm the results of Holzapfel *et al.* [96], but are scarcely valuable for a later continuum-mechanical usage. This is mainly because multi-lamellar specimens were used in Ebara *et al.* [43] and the characteristic curves of the nonlinear single-lamellar response was not provided in Skaggs *et al.* [188].

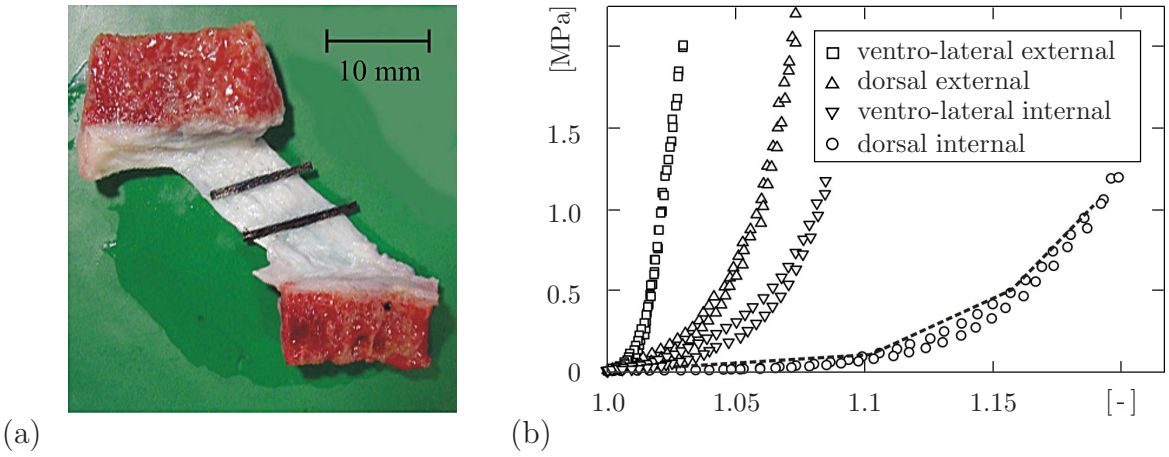

Figure 2.6: *Dissected specimen of a single lamella of the AF, where the load axis is in the direction of the aligned collagen and (b) the resulting characteristic curves measured at outer and inner antero-lateral as well as posterior positions, respectively. Picture and data are taken from Holzapfel et al. [96] with kind permission from G. A. Holzapfel.*

Finally, the IVD tissue is characterised by a strongly coupled dissipative behaviour, which is, to a big extent, due to the interstitial fluid flow. In this regard, fluid flow can be deformation-driven due to applied external mechanical forces or electro-chemically driven, when water is attracted by the fixed negative charges. Thus, fluid flow is coupled to volumetric deformations, which again lead to a electro-chemical imbalance of fixed negative charges and the surrounding dissolved ions.

Another dissipative effect results from the so-called intrinsic viscoelasticity of the ECM, which can only be proved in shear experiments with moderate deformations, in order to decouple the intrinsic effects from the dissipation of the viscous pore fluid. In this regard, it is proven that cartilage and other isotropic tissues exhibit intrinsic viscoelastic behaviour [63, 92]. Torsional shear experiments on cylindrical specimens harvested from the NP show a slight viscoelastic behaviour, which allows for the conclusion of an intrinsically viscoelastic ECM [101]. Herein, most of the stress relaxation occurs rather rapid within approximately three seconds after the shear load is applied. Thus, the time frame of the intrinsic viscoelasticity is much smaller compared to the time needed for fluid flow, which takes place over a period of hours. However, it is still not clear, to which extent the intrinsic viscoelastic effects stem from proteoglycans or collagen. Concerning the AF, the measurements of Holzapfel *et al.* [96] showed only little rate dependency of the type-I collagen fibres in the AF. Following this, it seems that only the loose network of type-II collagen as well as the PG exhibit a viscoelastic behaviour, which contributes to the intrinsic viscoelasticity of the isotropic ECM of cartilage or NP tissue.

2.3.4 Load Transmission Mechanism

The entire IVD has to transmit the majority of loads down the spinal column and due to its inherent flexibility, the load transmission frequently takes place under awkward deformations. Herein, the applied loads do not only result from the body weight and the lifted weights, but also from adjacent muscle activity, which is needed to hold the body in a desired position, cf. Urban & Roberts [214] and references therein. In general, the load can be classified by its duration, i. e., short duration and high-amplitude loads (e. g. jerk lifting) and long duration loads due to normal physiological actions (e. g. standing erect, carrying minor loads). In this regard, Nachemson started to extensively quantify these loads on the IVD in the 1960s and published in his later works [148, 149] that a person having a mass of 70 kg experiences a load of approximately 500 N on the third lumbar IVD, while standing at ease. This magnitude is almost quadrupled, when the same person lifts a weight of only 10 kg, thereby having the knees straight and the back bent over. As a rule of thumb, the least loads are applied when a person is lying supine, i. e., in a horizontal position on its back, the loads increase while standing and sitting, and are highest, when lifting a weight while the upper body is bent and twisted.

Following this, the IVD is often referred to as a hydrodynamic ball bearing [201], where its enormous load-bearing capacity is mainly due to a very ingenious interplay between its highly hydrated NP and its strongly fibre-reinforced AF. In fact, when the disc is mechanically loaded, it deforms and the NP is pressurised because of its considerable resistance against volumetric compression. Thus, the NP bulges into the CEP as well as radially into the AF, thereby setting its fibres into tension. Note in passing that an intradiscal pressure of 0.5 MPa can be measured *in vivo* in the fourth lumbar IVD when a person of 70 kg is standing at ease, while a pressure of 2.3 MPa arises when the same person lifts a weight of 20 kg having the knees straight and the back bent [233]. Because of the unique arrangement of the durable type-I collagen fibres, the AF is able to contain the high bulging-pressure from the NP in analogy to a thick-walled pressure vessel, while still maintaining the ability to be compressed, rotated or bent.

Moreover, due to the water attracting characteristic of the GAG chains, the NP appears to be under constant pressure [201] known as osmotic pressure. Thus, the fixed negative charges additionally carry parts of the applied load [98]. In fact, the more water is driven out of the tissue through a mechanical volumetric compression, the greater the water-attracting capacity of the fixed negative charges inside the tissue gets. For more information on osmotic effects, please refer to Subsection 2.4.2 or to any text on basic biochemistry. Note in passing that this effect can be observed in the diurnal variation of the body height which reaches up to 2 cm, because some of the interstitial fluid is expressed from the tissue during the high loadings of normal daily activities and is re-imbibed at rest during sleep at night [32, 128]. In this regard, the *in vivo* observations of Wilke *et al.* [233] support this statement. In an over-night measurement, the pressure inside the NP increased from about 0.1 MPa in the evening to about 0.24 MPa in the morning yielding a total increase of about 0.14 MPa over the whole night.

2.4 Basic Chemistry

The classical field of continuum mechanics usually includes the description of the response of arbitrary bodies being exposed to mechanical or thermal loading situations. Following this, many engineers working in this field have little knowledge about possible electro-chemical effects which should be included generally in the case of soft biological tissues. In this regard, the following section is by no means complete, rather it should give a brief overview of the necessary relations in order to have them handy when they are needed in the following chapters.

2.4.1 Concentration Measures

Whenever electro-chemically active materials (such as soft biological tissues) are discussed and described, the fixed negative charges mentioned in Section 2.3.1 as well as the ions of at least one dissolved salt in the pore fluid have to be included in the simulation process. Following this, the amount of the chemically active substances needs to quantified. In this regard, a very important quantity is known as *Avogadro*'s number[8] which is frequently used to convert measures from the atomic scale of substances like, for instance, atoms, ions, electrons or molecules to the physical macro scale. To be more precise, in 1971 *Avogadro*'s number entered the *International System of Units* (SI) and its numerical value is formally defined to be the number of carbon-12 atoms in 12 grams of unbound carbon-12 in its rest-energy electronic state. According to the *Committee on Data for Science and Technology* (CODATA), the current best approximated and accepted value for the *Avogadro* constant is $N_A = 6.02214179 \cdot 10^{23}\,\mathrm{mol}^{-1}$ [140]. Thus, one mol of carbon-12 atoms weighs 12 grams and N_A accounts for the number of entities in a mol.

However, regarding classical field theories like, for instance, continuum mechanics, one essential drawback is the fact that the extensive measurement of entities is always leading to an absolute quantity. In this regard, an extensive quantity explicitly depends on the size of the described system, i. e., if a homogeneous system that contains a certain number of entities is divided in two equal parts, the overall number of entities is also divided by two. Thus, it is not possible to assign a unique number of entities to every point of the system. Following this, extensive quantities need to be intensified by relating them to another extensive quantity like mass or volume. One famous representative for intensive quantities is the mass density, where the mass is divided by the volume. Thus, in a homogeneous system, the mass density is constant at every point, no matter how often the overall system is divided into subsystems.

In order to intensively describe fixed charges or dissolved ions in chemistry, a concentration measure can be introduced. Herein, the absolute amount of fixed charges or dissolved ions is related to the fluid volume they are surrounded by or dissolved in, respectively. Thus,

[8] Earl *Amedeo Avogadro* (1776–1856): Italian physicist and chemist who postulated in 1811 that equal volumes of all gases at equal temperature and equal pressure contain the same number of elementary entities. Nowadays this is known as *Avogadro*'s law which is a special case of the ideal gas law.

the so-called molarity can be defined in the context of a molar concentration via

$$c_m^{\widetilde{\gamma}} := \frac{\mathrm{d}N^{\widetilde{\gamma}}}{\mathrm{d}v^F} \quad \left[\frac{\mathrm{mol}}{\mathrm{m}^3}\right], \qquad \text{where} \qquad \widetilde{\gamma} = \{+, -, fc\}\,. \tag{2.1}$$

Herein, $\widetilde{\gamma}$ stands for the dissolved ions as well as for the fixed charges, while the number of moles $N^{\widetilde{\gamma}}$ and v^F are the absolute number of dissolved entities and the fluid volume, respectively. The usage of differential elements on the right hand side of (2.1) implies that arbitrary small quantities are needed to compute the molar concentration. Thus, the molar concentration has the desired field character, as it is possible to define the molar concentration locally at a single point. Following this, the molar concentration of the fixed negative charges c_m^{fc} depends on the number of the fixed charges at the GAG chains (i. e. the fixed charge density) as well as on the surrounding volume of the pore fluid. The pore fluid itself is composed of the solvent, i. e., the liquid L, as well as dissolved solutes like the ions of a electrolyte (salt) or nutrients. However, the most prominent electrolyte in soft biological tissues is the monovalent sodium chloride which dissolves into Na^+ cations and Cl^- anions. Note in passing that a physiological sodium chloride solution has a molar ion concentration of $c_m^+ = c_m^- = 0.15 \cdot 10^{-6}\,\mathrm{mol/m^3} \equiv 0.15\,\mathrm{mol/l}$.

Several other intensive concentration measures can be given like, for instance, the molality, the osmolarity, or the mole and the mass fraction. For example, the molality is computed, when the number of charges is divided by the mass of the solvent, i. e., the liquid L. However, these quantities will not be needed in this monograph and are therefore not discussed any further.

2.4.2 Osmosis

Possibly, the best way to explain the osmotic effect is the example of two partly communicating compartments being separated by a selectively permeable membrane, as is shown in Figure 2.7. In the initial state, both compartments are filled to an equal level, where the left chamber contains a solution of water (solvent) and dissolved ions (solutes), while the right chamber is filled with distilled water. The separating membrane is only permeable for water molecules (H_2O). Thus, the molar concentration of the sum of the solutes in the left compartment can be denoted by $c_m^{\mathrm{left}} \neq 0$, while the concentration of the right compartment is nil, i. e., $c_m^{\mathrm{right}} = 0$, as it does not contain any solutes.

Naturally, the two communicating compartments have the desire to equalise their concentrations of solutes, i. e., if the compartments were infinitely large and no counter pressure was present, an infinite amount of distilled water would move through the semi-permeable membrane in order to dilute the solution in the left chamber. Regarding the situation in Figure 2.7, a mechanical counter pressure in form of a hydrostatic pressure evolves in the left compartment, whenever the solvent is moving in from the right. This mechanical counter pressure forces the solvent to be driven out again, thereby moving back into the right chamber. In this context, a water movement takes place, until the mechanical counter pressure resulting from the higher fluid level in the left compartment equals out the chemically driven desire of the distilled water to enter the left compartment in order to dilute the solution. Following this, osmosis is defined as the net flow of solvent

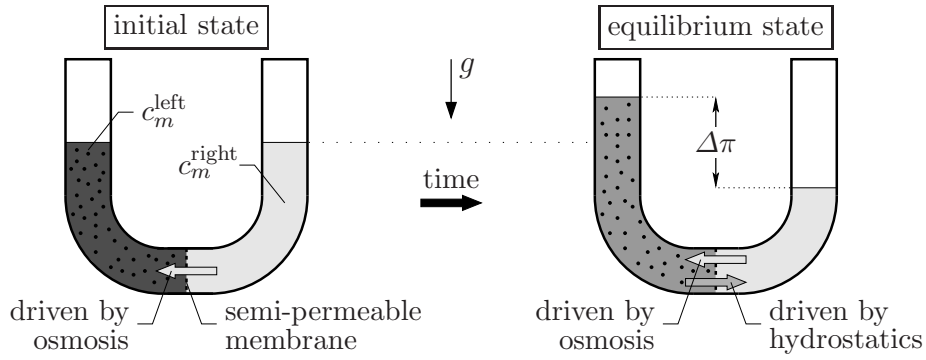

Figure 2.7: *Qualitative osmotic effect between two compartments being separated by a semi-permeable membrane which is only permeable to the solvent. The right side contains the solvent only, while the left side initially contains an ionic solution which is diluted after some time. At equilibrium, the net movement of the solvent at the membrane is zero and the resulting hydrostatic pressure difference is defined as osmotic pressure difference $\Delta\pi$.*

through a semi-permeable membrane that is driven by the difference between the molar solute concentrations of the communicating compartments. Moreover, the osmotic pressure difference is then defined as the measurable hydrostatic pressure difference between the compartments after the net fluid movement comes to a rest at the equilibrium state.

The formula approximating the osmotic pressure difference, is known since the end of the nineteenth century and was firstly described by *van't Hoff*[9]

$$\Delta\pi = R\,\Theta\,(c_m^{\text{left}} - c_m^{\text{right}})\,. \tag{2.2}$$

Herein, $R = 8.314472\,\mathrm{J/(mol\,K)}$ is the molar gas constant [140] and Θ is the absolute *Kelvin*'s temperature[10]. Note the similarity of the above formula to the ideal gas law.

In the case of soft biological tissues, the situation is generally more complicated, as it is also possible that the dissolved ions can pass through the tissue's boundary via diffusion. The reason for this stems from the GAG chains, which are effectively immobilised in the fibrous network of the overall ECM. Following this, every attached fixed negative charge requires a counter-ion, e. g., Na^+ cations, to be nearby maintaining the tissue's electro neutrality. Thus, an excess of cations is attracted to the pore fluid, thereby leading to a greater sum of the molar ion concentrations inside the tissue, compared with the sum of the concentrations of the surrounding physiological solution. This imbalance of ion concentrations leads to the same effect as described above. The solvent of the surrounding fluid (i. e. water), is attracted in order to dilute the ionic solution of the pore fluid, thereby dilating the tissue which in turn leads to tension in the ECM. Thus, the mechanical counter pressure results from the pre-stress in the ECM which tends to drive the excess of fluid back out of the tissue. The resulting pressure in the pore fluid, which

[9] *Jacobus Henricus van't Hoff* (1852–1911): Dutch physical and organic chemist who won the very first Nobel Prize in chemistry in 1901. He helped to define the discipline of physical chemistry as it is known today. His major research was on chemical kinetics, chemical equilibrium, and osmotic pressure.

[10] *William Thomson* (1824–1907): British mathematical physicist and engineer who was knighted Sir *William Thomson* in 1866 and gentled Lord *Kelvin* in 1892. His research in the mathematical analysis of electricity and thermodynamics helped much to emerge the discipline of physics in its modern form.

is measured in the equilibrium state, is then known as *Donnan*[11] osmotic pressure and can be computed in analogy to the above equation via

$$\Delta\pi = R\,\Theta\left[(c_m^+ - c_m^-) - (\bar{c}_m^+ - \bar{c}_m^-)\right]. \tag{2.3}$$

Herein, c_m^γ and $\bar{c}_m^\gamma$ for $\gamma = +, -$ are the molar solute concentrations of the internal and external solutions, respectively. Following this, the concentrations of one solution can be prescribed in the sense of a boundary condition, while the concentrations in the pore fluid may be determined using the Donnan [41] equation,

$$c_m^+\, c_m^- = \bar{c}_m^+\, \bar{c}_m^-\,, \tag{2.4}$$

which provides the chemical equilibrium. Usually, this concept can only be applied to biological membranes and is only valid directly at the boundary surface of a soft tissue like the IVD. However, Lanir [116] states that the diffusion of tiny ions takes place on a much smaller time scale compared to time needed for the percolation process of the pore fluid. Moreover, the natural ion distribution is understood to be ingrown, the chemical equilibrium with the surrounding physiological solution is, therefore, *a priori* fulfilled, and large disturbances on the chemical equilibrium in living tissues do usually not occur. Thus, the applicability of equation (2.4) can be extended from the domain boundary to the whole IVD. Note in passing that if the independent movement of the solutes plays an important role, the diffusion process needs to be included using appropriate flux equations.

Moreover, the concentration of the fixed negative charges needs to be incorporated into (2.3), as they indirectly contribute to the cation concentration of the internal solution. Following this, the electro-neutrality condition is applied, thereby always ensuring enough cations being left to balance out the fixed negative charges. In this context, the below-mentioned relations hold for the external and internal solutions, respectively:

$$\begin{aligned} z^+\bar{c}_m^+ + z^-\bar{c}_m^- = 0 \quad &\longrightarrow \quad \bar{c}_m^- = \bar{c}_m^+ =: \bar{c}_m \qquad \text{(external solution)},\\ z^+c_m^+ + z^-c_m^- + z^{fc}c_m^{fc} = 0 \quad &\longrightarrow \quad c_m^- = c_m^+ - c_m^{fc} \qquad \text{(internal solution)}. \end{aligned} \tag{2.5}$$

Therein, use was made of the corresponding valences for a monovalent salt solution (i. e., Na^+Cl^-) reading $z^+ = 1$ and $z^- = z^{fc} = -1$. Inserting the results of equations (2.5) into the *Donnan* equation (2.4) yields the two relations

$$c_m^+ = \sqrt{\bar{c}_m^2 + \left(\frac{c_m^{fc}}{2}\right)^2} + \frac{c_m^{fc}}{2} \qquad \text{and} \qquad c_m^- = \sqrt{\bar{c}_m^2 + \left(\frac{c_m^{fc}}{2}\right)^2} - \frac{c_m^{fc}}{2} \tag{2.6}$$

also known as the *Donnan* equilibrium. Equations (2.6) and $(2.5)_1$ inserted into (2.3) finally leads to

$$\Delta\pi = R\,\Theta\,[\,\sqrt{4\,\bar{c}_m^2 + (c_m^{fc})^2} - 2\,\bar{c}_m\,]\,, \tag{2.7}$$

where c_m^{fc} is deformation-dependent via volume changes of the pore fluid, cf. (2.1).

[11] *Frederick G. Donnan* (1870–1956): Irish chemist who delivered significant contributions in the field of membrane equilibria, especially the well-known *Donnan* equilibrium from 1911.

Finally, note that the natural state of soft biological tissues is in equilibrium, when the tissue is surrounded by a physiological sodium chloride solution. Whenever the surrounding concentration is changed, the tissue dimensions (volume) change also, but in the opposite direction, i. e., if the external ion concentration is increased, the tissue dimensions decrease. Thus, the natural state is always a swollen state, as the ingrown fixed charges of the GAG chains have already attracted all the counter ions and an excess of solvent, needed to fulfil the electro-neutrality condition and the chemical equilibrium, respectively. Applying this concept to a binary aggregate of materially incompressible solid and fluid constituents means that the ECM is permanently pre-stressed with a hydrostatic stress state resulting from the *Donnan* osmotic pressure.

3 Continuum-Mechanical Fundamentals

The following chapter gives a brief overview of the continuum-mechanical fundamentals needed to understand the modelling process using the framework of the Theory of Porous Media (TPM). In particular, this addresses the concept of volume fractions, the finite kinematical relations, the five balance equations, and the fundamental rules of material theory needed for the constitutive modelling process described in Chapter 4.

3.1 The Theory of Porous Media

Regarding the historical evolution of the TPM, the first continuum-mechanical considerations describing the consolidation problem of biphasic geomaterials trace back to the phenomenological approach by Biot [18]. Shortly after, the Theory of Mixtures (TM) was developed using the framework of general thermodynamical considerations, where the most important works trace back to Truesdell & Toupin [208] and Bowen [26]. The TM was then extended by the concept of volume fractions in the publications of Mills [139] and Bowen [27, 28], which in turn was continuously improved and further developed to the current understanding of the TPM by de Boer & Ehlers [25] and Ehlers [47, 49, 51, 52].

For the purpose of this monograph, the TPM provides an excellent framework to macroscopically describe the complicated microstructure of soft biological tissues without the knowledge of its detailed geometry; which, by the way, is almost impossible to acquire in a quantitative way. In this regard, a representative elementary volume (REV) is locally defined, where its constituents are assumed to be in a state of ideal disarrangement. Following this, the inner structure of the tissue is homogenised (smeared) over the REV by the prescription of a volumetric averaging process leading to a statistical substitution of the original microstructure. Thus, all geometrical and physical quantities are defined as statistical mean values of the occurring actual quantities. Proceeding from the biochemical composition described in Section 2.3.1, a model

$$\varphi = \bigcup_{\alpha} \varphi^{\alpha} = \varphi^{S} \cup \varphi^{F} \tag{3.1}$$

of superimposed and interacting continua can be defined. Herein, the immiscible parts of the model lead to a binary aggregate of solid and fluid constituents φ^{α} denoted by $\alpha = \{S, F\}$, where the solid constituent (i. e., the ECM consisting of PG, GAG chains and collagen) is extended by incorporating the (almost) volume-free fixed negative charges φ^{fc}, cf. Figure 3.1. Furthermore, the interstitial fluid φ^{F} is an ionic solution, which is a miscible mixture of its components φ^{β} denoted by $\beta = \{L, +, -\}$. Herein, water serves as the liquid solvent φ^{L} and the mobile ions Na^{+} and Cl^{-} of the dissolved electrolyte sodium chloride are the solutes φ^{+} and φ^{-}, respectively. Note in passing that the solutes themselves have often their own identifier, i. e., φ^{γ}, where $\gamma = \{+, -\}$.

Following this would lead to a quadriphasic model describing the solid skeleton φ^{S} (including the fixed negative charges φ^{fc}) and each of the components φ^{β} independently, see,

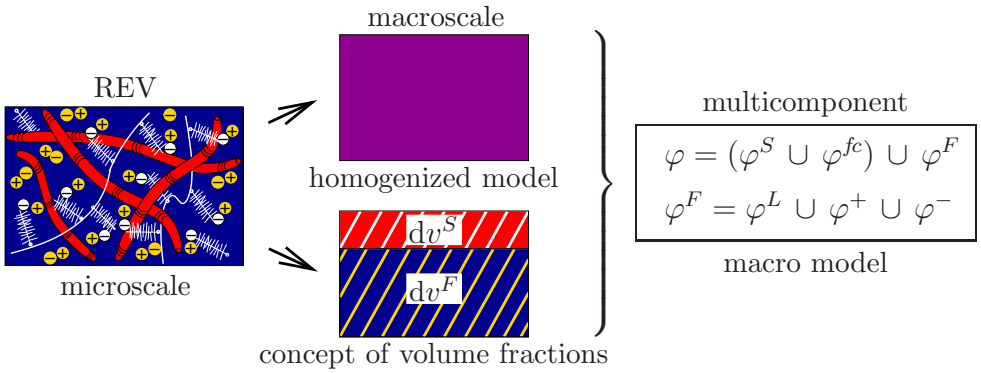

Figure 3.1: *REV of the qualitative microstructure of charged hydrated biological tissues as well as the multicomponent TPM macro model obtained by a volumetric homogenisation process.*

e. g., Frijns *et al.* [76], Lai *et al.* [113] and Acartürk [1]. Exploiting the electro-neutrality condition $(2.5)_2$ allows for a reduction to a triphasic model. This causes the number of independent primary variables, which are needed to describe the remaining constituents in the numerical modelling process, to decrease from four to three, i. e., the solid displacement, the pressure and the cation concentration [64, 65]. As already mentioned in Section 2.4.2, it is possible to further reduce this model by applying the assumption of Lanir [116] stating that the tiny mobile ions are assumed to diffuse rapidly through the liquid and by themselves, do not give rise to concentration gradients. In the context of living soft biological tissues, such as the IVD, this simplification makes sense, because sudden concentration changes of the surrounding fluid yielding large perturbations of the chemical equilibrium do not occur. Hence, the soft biological tissue is always immediately in electro-chemical equilibrium, which allows the application of the Donnan [41] equilibrium not only at the domain boundary, but also in the inside. The arising osmotic properties can therefore be sufficiently described without considering the independent movement of the ions. Following this, the respective ion concentrations may be computed inside the tissue using equations (2.6), and no independent variables need to be introduced for the solutes. Thus, the following chapters will derive an extended biphasic formulation consisting of a solid skeleton carrying volume-free fixed negative charges which interact with a saturating pore fluid. Note in passing that it is common to use the terminology "phase" instead of constituent or component, even though the usual terminology of phase transitions, i. e., solid to liquid to gas, is not meant here.

Remark: First benchmark computations on simple geometries using a triphasic displacement-pressure-concentration formulation were accompanied by oscillations and a general numerical instability, cf. Ehlers & Acartürk [53]. The cause of the oscillations can be traced back to equation $(2.6)_1$, as for this model, it is only valid at the domain boundary. Thus, the concentration boundary condition (BC) implicitly depends on the solution of the solid displacement field inside the domain and a numerical stabilisation is only possible if the BC is weakly fulfilled and included in the iteration process, cf. Ehlers *et al.* [65]. Bearing in mind that future simulations of the intensely inhomogeneous, anisotropic IVD (including the much stiffer, adjacent vertebrae) already evolve several other numerical difficulties, the simpler approach using the extended biphasic formulation is used here.

Note in passing that other theories, which exhibit four primary degrees of freedom [113], i. e., solid displacement and three modified chemical potentials for water, cations and anions, do not suffer from these oscillations, but are from a computational point of view still a lot more 'expensive'. □

In order to account for the inner structure of the model φ, the volume V of the overall aggregate $\mathcal{B}$ is divided into a sum of partial volumes V^α of the constituent bodies $\mathcal{B}^\alpha$

$$V = \int_{\mathcal{B}} \mathrm{d}v = \sum_\alpha V^\alpha \qquad \text{with} \qquad V^\alpha = \int_{\mathcal{B}^\alpha} \mathrm{d}v = \int_{\mathcal{B}} \mathrm{d}v^\alpha =: \int_{\mathcal{B}} n^\alpha \mathrm{d}v \,. \tag{3.2}$$

Herein, the volume fractions n^α of the constituents φ^α are defined as the local ratios of the respective partial volume elements $\mathrm{d}v^\alpha$ with respect to the bulk volume element $\mathrm{d}v$ of the overall aggregate φ yielding

$$n^\alpha := \frac{\mathrm{d}v^\alpha}{\mathrm{d}v} \,, \qquad \text{where} \qquad \begin{cases} n^S : & \text{solidity (including } n^{fc} \approx 0), \\ n^F : & \text{porosity.} \end{cases} \tag{3.3}$$

As a natural consequence of (3.2), the so-called saturation constraint is introduced as

$$\sum_\alpha n^\alpha = n^S + n^F = 1 \,, \tag{3.4}$$

which has to be permanently fulfilled in order to prevent the development of vacant space during possible deformation processes of the overall body $\mathcal{B}$. Moreover, exploiting the concept of volume fractions, a partial density ρ^α can be introduced relating the local constituent mass $\mathrm{d}m^\alpha$ to the bulk volume element $\mathrm{d}v$. If the local constituent mass is related to the partial volume element $\mathrm{d}v^\alpha$ of the constituent φ^α itself, the material or realistic density $\rho^{\alpha R}$ is obtained. Thus, the following relations hold

$$\rho^\alpha = \frac{\mathrm{d}m^\alpha}{\mathrm{d}v} \qquad \text{and} \qquad \rho^{\alpha R} = \frac{\mathrm{d}m^\alpha}{\mathrm{d}v^\alpha} \,, \tag{3.5}$$

which can be related to each other, when equation (3.3) is inserted into (3.5) leading to

$$\rho^\alpha = n^\alpha \rho^{\alpha R}. \tag{3.6}$$

Consequently, the partial density ρ^α of a constituent φ^α may be altered via changes in its volume fraction n^α as well as via changes in its realistic density $\rho^{\alpha R}$. Following this leads to a general bulk compressibility of the overall aggregate, even if its constituents are materially incompressible (i. e. $\rho^{\alpha R} = \text{const.}$), as the partial density may still change due to a deformation-driven change of the corresponding volume fraction n^α.

Finally, the overall density ρ of the aggregate body $\mathcal{B}$ can be obtained by a summation of the partial densities over all constituents yielding

$$\rho = \sum_\alpha \rho^\alpha = \sum_\alpha n^\alpha \, \rho^{\alpha R}. \tag{3.7}$$

3.2 Kinematical Relations

The following sections offer a brief overview of the kinematical relations which are needed to describe the nonlinear deformation process of a porous material. Herein, the overall aggregate body $\mathcal{B}$ is defined as the connected manifold of material points P^α which may follow independent motions that can be described with respect to a fixed origin $\mathcal{O}$. Note that all quantities related to the motion of a constituent are indicated in the subscript $(\bullet)_\alpha$, while all other quantities indicate their affiliation in the superscript $(\bullet)^\alpha$. Moreover, note that due to the reasons given in the preceding section, the introduction of independent motions for the solvents of the pore fluid is omitted here. For a comprehensive introduction of these kinematical quantities, the reader is referred to [1, 53].

3.2.1 Motion of a Porous Material

The idea of superimposed and interacting porous continua $\mathcal{B}$ implies that at any time t each spatial point $\mathbf{x}$ of the current configuration is simultaneously occupied by material points P^α of all constituents φ^α, cf. Figure 3.2. Following this, all particles proceed from different reference positions $\mathbf{X}_\alpha$, which leads to individual vector-valued placement (motion), velocity, and acceleration fields for each constituent reading

$$\mathbf{x} = \boldsymbol{\chi}_\alpha(\mathbf{X}_\alpha, t)\,, \qquad \overset{\prime}{\mathbf{x}}_\alpha = \frac{\mathrm{d}\boldsymbol{\chi}_\alpha(\mathbf{X}_\alpha, t)}{\mathrm{d}t}\,, \qquad \text{and} \qquad \overset{\prime\prime}{\mathbf{x}}_\alpha = \frac{\mathrm{d}^2\boldsymbol{\chi}_\alpha(\mathbf{X}_\alpha, t)}{\mathrm{d}t^2}\,, \tag{3.8}$$

respectively. Note in passing that contrary to the usual convention in this monograph, the referential position vectors are denoted by $\mathbf{X}_\alpha$ instead of $\mathbf{x}_{0\alpha}$ indicating the initial position of the material points P^α at time $t_0 = 0\,\mathrm{s}$. In the following, this is also done for line, area, and volume elements, i. e., $\mathrm{d}\mathbf{X}_\alpha$, $\mathrm{d}\mathbf{A}_\alpha$, and $\mathrm{d}V_\alpha$, respectively.

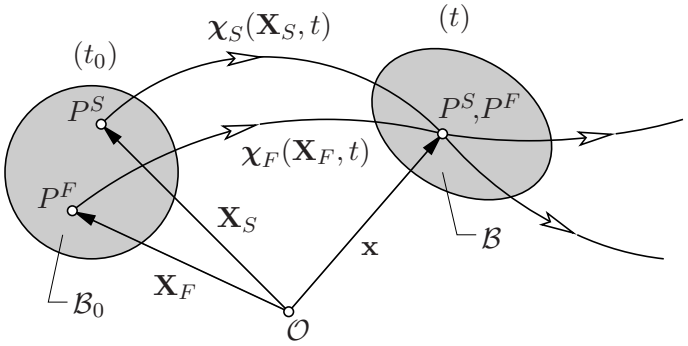

Figure 3.2: *Motion of a binary aggregate.*

Moreover, the requirement of the individual placement functions $\boldsymbol{\chi}_\alpha$ to be unique claims for the existence of unique inverse motion functions $\boldsymbol{\chi}_\alpha^{-1}$ which are only possible to compute, if non-singular functional determinants (*Jacobi*ans[1]) J_α exist, viz.:

$$\mathbf{X}_\alpha = \boldsymbol{\chi}_\alpha^{-1}(\mathbf{x}, t)\,, \qquad \text{if} \qquad J_\alpha := \det \frac{\partial \boldsymbol{\chi}_\alpha}{\partial \mathbf{X}_\alpha} \neq 0\,, \tag{3.9}$$

[1] *Carl Gustav Jacob Jacobi* (1804–1851): German mathematician, who believed that hard problems are best possibly solved when they are addressed backwards, i. e., in an inverted manner.

where $\det(\bullet)$ denotes the determinant operator. Following this, equations (3.8) are expressed in terms of referential coordinates $\mathbf{X}_\alpha$ and represent the *Lagrange*an[2] (material) description of the motion field, while (3.9) is known as its *Euler*ian (spatial) representation as it is expressed with regard to the current configuration. Following this, any physical quantity can either be expressed with regard to material or spatial coordinates. Thus, the spatial representation of the velocity and acceleration fields $(3.8)_{2,3}$ can be obtained by inserting the inverse motion function $(3.9)_1$ yielding

$$\overset{\prime}{\mathbf{x}}_\alpha = \overset{\prime}{\mathbf{x}}_\alpha[\,\boldsymbol{\chi}_\alpha^{-1}(\mathbf{x},t),t\,] = \overset{\prime}{\mathbf{x}}_\alpha(\mathbf{x},t) \qquad \text{and} \qquad \overset{\prime\prime}{\mathbf{x}}_\alpha = \overset{\prime\prime}{\mathbf{x}}_\alpha[\,\boldsymbol{\chi}_\alpha^{-1}(\mathbf{x},t),t\,] = \overset{\prime\prime}{\mathbf{x}}_\alpha(\mathbf{x},t)\,. \tag{3.10}$$

Additionally, the velocity of the overall aggregate can be introduced by the aid of relation (3.7) for the overall density ρ leading to the so-called barycentric velocity

$$\dot{\mathbf{x}} = \frac{1}{\rho}\sum_\alpha \rho^\alpha \overset{\prime}{\mathbf{x}}_\alpha \tag{3.11}$$

of the aggregate φ. Following this, the difference of the velocity of a constituent φ^α to the barycentric velocity $\dot{\mathbf{x}}$ of the aggregate φ is defined as the diffusion velocity

$$\mathbf{d}_\alpha = \overset{\prime}{\mathbf{x}}_\alpha - \dot{\mathbf{x}} \qquad \text{with} \qquad \sum_\alpha \rho^\alpha\,\mathbf{d}_\alpha = 0\,. \tag{3.12}$$

All time derivatives $(\bullet)'_\alpha$ and $(\bullet)^\cdot$ used in the equations above are material time derivatives. In the case of a *Lagrange*an description of the motion $(3.8)_1$, the material (total) time derivative is equivalent to the partial time derivative, as the referential coordinates $\mathbf{X}_\alpha$ are fixed in time by an initial condition at t_0. But care must be taken if the motion is expressed in an *Euler*ian representation, as the spatial variable $\mathbf{x}$ implicitly depends on the time t. Thus, the inner derivative must be included in the material time derivative. For instance, if Ψ and $\boldsymbol{\Psi}$ are arbitrary, steady and sufficiently steady differentiable scalar and vectorial field functions, the respective material time derivatives following the motion of the constituents φ^α and the barycentric motion of the aggregate φ read

$$\begin{aligned}
\overset{\prime}{\Psi}_\alpha(\mathbf{x},t) &= \frac{\mathrm{d}_\alpha\Psi}{\mathrm{d}t} = \frac{\partial\Psi}{\partial t} + \operatorname{grad}\Psi\cdot\overset{\prime}{\mathbf{x}}_\alpha\,, & \dot{\Psi}(\mathbf{x},t) &= \frac{\mathrm{d}\Psi}{\mathrm{d}t} = \frac{\partial\Psi}{\partial t} + \operatorname{grad}\Psi\cdot\dot{\mathbf{x}}\,,\\
\overset{\prime}{\boldsymbol{\Psi}}_\alpha(\mathbf{x},t) &= \frac{\mathrm{d}_\alpha\boldsymbol{\Psi}}{\mathrm{d}t} = \frac{\partial\boldsymbol{\Psi}}{\partial t} + (\operatorname{grad}\boldsymbol{\Psi})\,\overset{\prime}{\mathbf{x}}_\alpha\,, & \dot{\boldsymbol{\Psi}}(\mathbf{x},t) &= \frac{\mathrm{d}\Psi}{\mathrm{d}t} = \frac{\partial\boldsymbol{\Psi}}{\partial t} + (\operatorname{grad}\boldsymbol{\Psi})\,\dot{\mathbf{x}}\,.
\end{aligned} \tag{3.13}$$

Herein, the differential operator $\operatorname{grad}(\bullet)$ is the gradient in the actual configuration, i. e., the partial derivative of $(\bullet)$ with respect to the spatial variable $\mathbf{x}$.

Moreover, comparing equations $(3.8)_1$ and $(3.9)_1$, the material deformation gradients $\mathbf{F}_\alpha$ and their inverses $\mathbf{F}_\alpha^{-1}$ can be formally introduced reading

$$\mathbf{F}_\alpha = \frac{\partial\boldsymbol{\chi}_\alpha(\mathbf{X}_\alpha,t)}{\partial\mathbf{X}_\alpha} =: \operatorname{Grad}_\alpha\mathbf{x} \qquad \text{and} \qquad \mathbf{F}_\alpha^{-1} = \frac{\partial\boldsymbol{\chi}_\alpha^{-1}(\mathbf{x},t)}{\partial\mathbf{x}} = \operatorname{grad}\mathbf{X}_\alpha\,, \tag{3.14}$$

[2] *Joseph Louis Lagrange* (1736–1813): Italian mathematician and astronomer who published the treatise *Mécanique Analytique* which offered the most comprehensive treatment of classical mechanics since *Newton*. Besides many other things, he developed a new approach to interpolation and extended the method to include possible constraints leading to the well-known *Lagrange* multipliers.

respectively. Note that the gradient operator $\mathrm{Grad}_\alpha(\bullet) = \partial\mathbf{x}/\partial\mathbf{X}_\alpha$ denotes the partial derivative with respect to the reference position vector $\mathbf{X}_\alpha$. Proceeding from an undeformed reference configuration at t_0, the associated initial condition $\mathbf{F}_\alpha(t_0) = \mathbf{I}$ holds for the material deformation gradient, where $\mathbf{I}$ denotes the second-order identity tensor. Thus, in combination with the orientation-preserving characteristic of physically sound deformations, equation $(3.9)_2$ is necessarily restricted to

$$J_\alpha = \det\mathbf{F}_\alpha > 0\,, \qquad \text{because} \qquad \det\mathbf{F}_\alpha(t_0) = \det\mathbf{I} = 1\,. \tag{3.15}$$

Furthermore, the description of coupled solid-fluid problems leads to the difficulty of finding a suitable choice for the representation of the independent motions of the constituents. Following this, it is always possible to describe a solid via a *Lagrange*an description, while this is not possible for the fluid, where usually an *Euler*ian approach is chosen. The reason for this is that neighbouring material points on the undeformed solid body are also adjacent to each other in a deformed configuration, while in a fluid this is generally not the case. Following this, it is convenient to express the solid in a *Lagrange*an setting via the displacement vector $\mathbf{u}_S$ and the overall pore fluid in a modified *Euler*ian setting by the seepage velocity $\mathbf{w}_F$ yielding

$$\mathbf{u}_S := \mathbf{x} - \mathbf{X}_S \qquad \text{and} \qquad \mathbf{w}_F := \overset{\prime}{\mathbf{x}}_F - \overset{\prime}{\mathbf{x}}_S\,. \tag{3.16}$$

In this regard, the solid displacement vector $\mathbf{u}_S$ serves as the primary kinematical variable, as the fluid is expressed relative to the deforming solid skeleton. Thus, the material deformation gradient of the fluid $\mathbf{F}_F$ is not needed any more, while the solid material deformation gradient $\mathbf{F}_S$ plays the key role as the basic kinematical quantity in the following sections. Note that the solid deformation gradient and its inverse (3.14) may be computed using the definition of the displacement vector in equation $(3.16)_1$ leading to

$$\mathbf{F}_S = \frac{\partial(\mathbf{X}_S + \mathbf{u}_S)}{\partial\mathbf{X}_S} = \mathbf{I} + \mathrm{Grad}_S\,\mathbf{u}_S \qquad \text{and} \qquad \mathbf{F}_S^{-1} = \frac{\partial(\mathbf{x} - \mathbf{u}_S)}{\partial\mathbf{x}} = \mathbf{I} - \mathrm{grad}\,\mathbf{u}_S\,. \tag{3.17}$$

3.2.2 Inelastic Solid Kinematics

In order to account for the intrinsic viscoelastic behaviour of the ECM, the basic kinematical relations of the underlying rheological model need to be discussed at first. Following this, a fundamental approach is applied utilising the generalised *Maxwell* model given in Figure 3.3 and described in Ehlers & Markert [62], Markert [131] or Reese & Govindjee [167] among many others. Herein, the 1-d rheological model is a parallel assembly of a *Hooke* element which describes the purely elastic response at equilibrium via a single spring, as well as $n = 1, \ldots, N$ *Maxwell* elements accounting for the rate-dependent non-equilibrium response. Following this, the overall deformation is equal in all participating elements, whereas the total deformation is additively decomposed into elastic and inelastic contributions in the *Maxwell* branches. In this context, the dashpots are only sensitive to the deformation velocity at which they are elongated. Hence, whenever the inelastic deformations are constant, the corresponding *Maxwell* elements do not contribute to the overall stress of the model which is computed as the sum over all *Maxwell* branches. In

this regard, the *Maxwell* elements directly reflect the need for independently developing internal inelastic deformation variables which need to be determined using appropriate evolution equations.

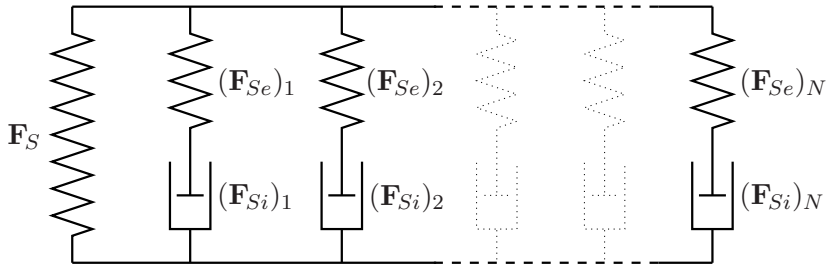

Figure 3.3: *Generalised Maxwell model composed of a Hooke element and N Maxwell elements.*

As usual in finite inelasticity, the solid kinematics is constitutively based on a multiplicative split of the solid deformation gradient

$$\mathbf{F}_S = (\mathbf{F}_{Se})_n \, (\mathbf{F}_{Si})_n \tag{3.18}$$

into elastic and inelastic contributions, respectively. Herein, $\mathbf{F}_S$ and $(\mathbf{F}_{Se})_n$ can be understood as external variables, whereas $(\mathbf{F}_{Si})_n$ has the character of an internal variable, which cannot be determined from the overall process, but has to be determined internally using evolution equations. Following this, an additive decomposition of the resulting finite strain measures into elastic and inelastic parts is achieved, thereby directly reflecting the kinematical structure of the underlying generalised *Maxwell* model, cf. Lee [119], Kleiber [110], or with application to the TPM, the reader is referred Ehlers [47, 48, 49].

Like it is indicated in Figure 3.4, the multiplicative decomposition is connected with locally unloaded intermediate configurations. Herein, the inelastic deformations $(\mathbf{F}_{Si})_n$ operate between the reference and the stress-free intermediate configurations of the n^{th} *Maxwell*

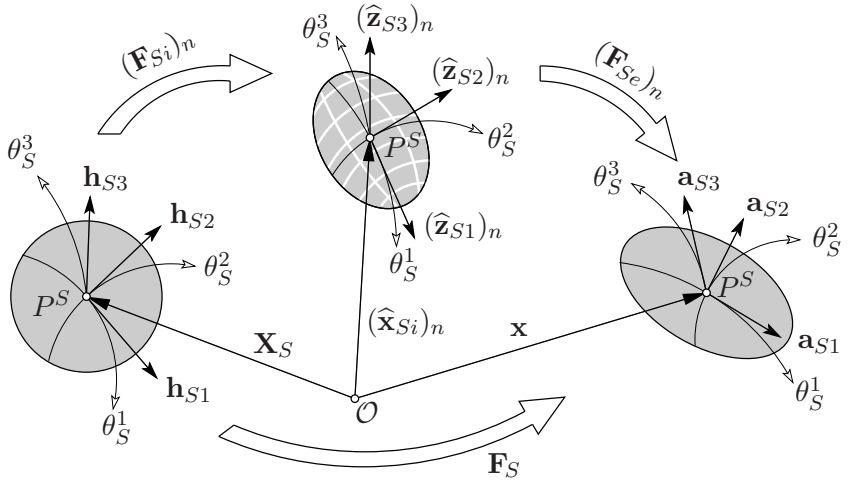

Figure 3.4: *Reference, intermediate and actual configurations with contravariant curvilinear coordinate lines and covariant local basis systems for the solid constituent.*

element, while the elastic deformations $(\mathbf{F}_{Se})_n$ connect the respective n^{th} intermediate configuration with the actual frame. Thus, in contrast to finite plasticity, where the plastic deformation state causes only one intermediate configuration, the rheological model under consideration needs a different multiplicative decomposition for each *Maxwell* branch. It is then possible to generate local deformation states, where the springs in each of the *Maxwell* branches are completely relaxed and stress free.

Remark: The drawback of the multiplicative decomposition is that for the general case of inhomogeneous solid deformations, the local intermediate configuration of a *Maxwell* element is geometrically incompatible. This fact becomes clear with an example from plasticity, where a body is loaded until it locally plastifies, which leads to local residual stresses after unloading. Since the intermediate configuration is defined as stress free, the body has to be cut such that the local plastic deformations do not cause any residual stresses. These cuts are indicated in Figure 3.4 by the white lines on the intermediate configuration. Thus, the multiplicatively decomposed parts $(\mathbf{F}_{Se})_n$ and $(\mathbf{F}_{Si})_n$ loose their gradient field character. Moreover, the (arbitrary) multiplicative decomposition of the solid deformation gradient is not unique. The physical interpretation leads to several intermediate configurations of a single *Maxwell* element, which differ only by rigid-body rotations. This becomes clear, if the rotation tensors $\widehat{\mathbf{H}}_n \in \mathcal{SO}_3$ of the proper orthogonal group $\mathcal{SO}_3$ with the properties $\widehat{\mathbf{H}}_n^T = \widehat{\mathbf{H}}_n^{-1}$ and $\det \widehat{\mathbf{H}}_n = 1$ are inserted into (3.18) yielding

$$\mathbf{F}_S = (\mathbf{F}_{Se})_n \, (\mathbf{F}_{Si})_n = (\mathbf{F}_{Se})_n \, \widehat{\mathbf{H}}_n^T \, \widehat{\mathbf{H}}_n^{-1} (\mathbf{F}_{Si})_n = (\overline{\mathbf{F}}_{Se})_n \, (\overline{\mathbf{F}}_{Si})_n \,, \tag{3.19}$$

where $(\widehat{\cdot})$ denotes a quantity of the intermediate configuration. For more information on the consequences of configurational rotations please refer to Sections 4.2 and 4.3. □

As already indicated in Figure 3.4, the solid deformation gradient as well as its inelastic and elastic parts must have certain linking properties between adjacent configurations. In order to better understand these properties, the respective deformation gradients can be rewritten by means of a natural basis representation. Note that for the sake of clarity only one *Maxwell* element (i. e. $N = 1$) is used in connection with the natural basis representation. Therefore, the identifier $(\,\cdot\,)_n$ is omitted in the rest of this section. Following this, contravariant convective curvilinear coordinate lines θ_S^k are introduced for the solid constituent and are defined to be attached to the solid reference configuration such that they continuously follow the deforming material body. Thus, the deforming coordinate lines θ_S^k can be expressed as functions of the respective position vectors via

$$\theta_S^k = \theta_S^k(\mathbf{X}_S, t_0) \,, \qquad \theta_S^k = \theta_S^k(\widehat{\mathbf{x}}_{Si}, t) \,, \qquad \theta_S^k = \theta_S^k(\mathbf{x}, t) \,. \tag{3.20}$$

Obviously, a unique inversion of (3.20) must exist such that the position vectors of all configurations can be expressed by means of the contravariant coordinate lines θ_S^k yielding

$$\mathbf{X}_S = \mathbf{X}_S(\theta_S^k, t_0) \,, \qquad \widehat{\mathbf{x}}_{Si} = \widehat{\mathbf{x}}_{Si}(\theta_S^k, t) \,, \qquad \mathbf{x} = \mathbf{x}(\theta_S^k, t) \,. \tag{3.21}$$

Taking the derivative of the position vectors (3.21) with respect to the contravariant coordinates θ_S^k leads to covariant tangent vectors at a material point P^S

$$\mathbf{h}_{Sk} = \frac{\partial \mathbf{X}_S}{\partial \theta_S^k} \,, \qquad \widehat{\mathbf{z}}_{Sk} = \frac{\partial \widehat{\mathbf{x}}_{Si}}{\partial \theta_S^k} \,, \qquad \mathbf{a}_{Sk} = \frac{\partial \mathbf{x}}{\partial \theta_S^k} \,, \tag{3.22}$$

which are defined as the local natural basis vectors in the reference, intermediate, and actual configurations, respectively. The corresponding local dual basis vectors can be computed via the respective gradients of (3.20) leading to the contravariant vectors

$$\mathbf{h}_S^k = \frac{\partial \theta_S^k}{\partial \mathbf{X}_S}\,, \qquad \widehat{\mathbf{z}}_S^k = \frac{\partial \theta_S^k}{\partial \widehat{\mathbf{x}}_{Si}}\,, \qquad \mathbf{a}_S^k = \frac{\partial \theta_S^k}{\partial \mathbf{x}}\,. \tag{3.23}$$

It is important to note that the covariant (3.22) and contravariant (3.23) basis vectors, in general, do not span orthonormal basis systems. However, the tangent spaces (3.22) are connected with the respective cotangent spaces (3.23) such that a contravariant basis vector $(\,\cdot\,)^k$ is always orthogonal to two covariant basis vectors $(\,\cdot\,)_l$ for $k \neq l$. Thus the following orthogonality constraints hold

$$\mathbf{h}_S^l \cdot \mathbf{h}_{Sk} = \delta_k^l\,, \qquad \widehat{\mathbf{z}}_S^l \cdot \widehat{\mathbf{z}}_{Sk} = \delta_k^l\,, \qquad \mathbf{a}_S^l \cdot \mathbf{a}_{Sk} = \delta_k^l\,, \tag{3.24}$$

where δ_k^l is the *Kronecker*[3] delta which is equal to unity in the case of $l = k$ and equal to zero in all other cases. Thus, whenever rectangular *Carte*sian[4] coordinate lines are applied, the resulting co- and contravariant basis systems are identical and unified in the standard orthonormal basis of the proper *Euclid*ean[5] 3-d vector space $\mathcal{V}^3$. Note in passing that equations (3.24) represent enough relations to compute the covariant from the contravariant basis vectors and *vice versa*. For a more detailed introduction in the particulars of the natural basis representation, the interested reader is referred to the texts of de Boer [23] or Papastavridis [160].

Applying the chain rule to (3.14), the solid deformation gradients including their elastic and inelastic parts as well as their inverses can be formally introduced in natural basis representation yielding

$$\begin{aligned}
\mathbf{F}_S &= \frac{\partial \mathbf{x}}{\partial \mathbf{X}_S} = \frac{\partial \mathbf{x}}{\partial \theta_S^k} \otimes \frac{\partial \theta_S^k}{\partial \mathbf{X}_S} = \mathbf{a}_{Sk} \otimes \mathbf{h}_S^k\,,\\
\mathbf{F}_S^{-1} &= \frac{\partial \mathbf{X}_S}{\partial \mathbf{x}} = \frac{\partial \mathbf{X}_S}{\partial \theta_S^k} \otimes \frac{\partial \theta_S^k}{\partial \mathbf{x}} = \mathbf{h}_{Sk} \otimes \mathbf{a}_S^k\,,\\
\mathbf{F}_{Se} &= \frac{\partial \mathbf{x}}{\partial \widehat{\mathbf{x}}_{Si}} = \frac{\partial \mathbf{x}}{\partial \theta_S^k} \otimes \frac{\partial \theta_S^k}{\partial \widehat{\mathbf{x}}_{Si}} = \mathbf{a}_{Sk} \otimes \widehat{\mathbf{z}}_S^k\,,\\
\mathbf{F}_{Se}^{-1} &= \frac{\partial \widehat{\mathbf{x}}_{Si}}{\partial \mathbf{x}} = \frac{\partial \widehat{\mathbf{x}}_{Si}}{\partial \theta_S^k} \otimes \frac{\partial \theta_S^k}{\partial \mathbf{x}} = \widehat{\mathbf{z}}_{Sk} \otimes \mathbf{a}_S^k\,,\\
\mathbf{F}_{Si} &= \frac{\partial \widehat{\mathbf{x}}_{Si}}{\partial \mathbf{X}_S} = \frac{\partial \widehat{\mathbf{x}}_{Si}}{\partial \theta_S^k} \otimes \frac{\partial \theta_S^k}{\partial \mathbf{X}_S} = \widehat{\mathbf{z}}_{Sk} \otimes \mathbf{h}_S^k\,,\\
\mathbf{F}_{Si}^{-1} &= \frac{\partial \mathbf{X}_S}{\partial \widehat{\mathbf{x}}_{Si}} = \frac{\partial \mathbf{X}_S}{\partial \theta_S^k} \otimes \frac{\partial \theta_S^k}{\partial \widehat{\mathbf{x}}_{Si}} = \mathbf{h}_{Sk} \otimes \widehat{\mathbf{z}}_S^k\,.
\end{aligned} \tag{3.25}$$

[3] *Leopold Kronecker* (1823–1891): German mathematician who claimed: "God made the integers; all else is the work of man" as an argument that arithmetic and analysis must be found on whole numbers.

[4] *René Descartes* (1596–1650): French philosopher, mathematician, and scientist who was also known as *Renatus Cartesius* in the latinised form. He founded analytic geometry and his most famous statement is: *Cogito ergo sum* meaning "I think, therefore I am".

[5] *Euclid of Alexandria* (about 365–300 BC): Greek mathematician who summarised all the mathematical knowledge of his time. His axiomatic method became exemplary in the following mathematics.

The above equations clearly indicate the special character of the deformation gradients and their inverses. They are mixed-variant with respect to their basis vectors yielding so-called two-field tensors, which operate between two adjacent configurations. In this regard, the deformation gradients $\mathbf{F}_S$ and $\mathbf{F}_S^{-1}$ are exemplary applied to the covariant basis vectors $\mathbf{h}_l$ and $\mathbf{a}_l$ in the context of a linear mapping. Making use of (3.24) leads to the following transport mechanisms

$$\begin{aligned} \mathbf{F}_S\,\mathbf{h}_{Sl} &= (\mathbf{a}_{Sk}\otimes\mathbf{h}_S^k)\,\mathbf{h}_{Sl} = \mathbf{a}_{Sk}\,\delta_l^k = \mathbf{a}_{Sl}\,, \\ \mathbf{F}_S^{-1}\,\mathbf{a}_{Sl} &= (\mathbf{h}_{Sk}\otimes\mathbf{a}_S^k)\,\mathbf{a}_{Sl} = \mathbf{h}_{Sk}\,\delta_l^k = \mathbf{h}_{Sl}\,, \end{aligned} \tag{3.26}$$

which are known as covariant push-forward (reference $\rightarrow$ actual configuration) and pull-back (actual $\rightarrow$ reference configuration) operations, respectively. Obviously, similar transports can be obtained between the intermediate and the actual or the reference configuration, which will not be shown here in detail. Moreover, in order to transport contravariant vectors from one configuration into another, the deformation gradients (3.25) need to be transposed such that the variance of the transported vector stays constant. Thus, the respective contravariant transport mechanisms read

$$\begin{aligned} \mathbf{F}_S^{T-1}\,\mathbf{h}_S^l &= (\mathbf{a}_S^k\otimes\mathbf{h}_{Sk})\,\mathbf{h}_S^l = \mathbf{a}_S^k\,\delta_k^l = \mathbf{a}_S^l\,, \\ \mathbf{F}_S^{T}\,\mathbf{a}_S^l &= (\mathbf{h}_S^k\otimes\mathbf{a}_{Sk})\,\mathbf{a}_S^l = \mathbf{h}_S^k\,\delta_k^l = \mathbf{h}_S^k\,. \end{aligned} \tag{3.27}$$

Proceeding from the definition of covariant differential line elements in the reference configurations, the transport mechanism is naturally given by $\mathbf{F}_S$. The transport theorems for area and volume elements can be deduced from the solid deformation gradient as is described in de Boer [23] yielding

$$\mathrm{d}\mathbf{x} = \mathbf{F}_S\,\mathrm{d}\mathbf{X}_S\,, \qquad \mathrm{d}\mathbf{a} = \operatorname{cof}\mathbf{F}_S\,\mathrm{d}\mathbf{A}_S\,, \qquad \mathrm{d}v = \det\mathbf{F}_S\,\mathrm{d}V_S\,. \tag{3.28}$$

Herein, $\mathrm{d}\mathbf{x}$, $\mathrm{d}\mathbf{a}$, and $\mathrm{d}v$ denote the differential line, (oriented) area, and volume elements of the overall aggregate in the actual configuration, whereas $\mathrm{d}\mathbf{X}_S$, $\mathrm{d}\mathbf{A}_S$, and $\mathrm{d}V_S$ are the respective elements of the solid constituent in the reference configuration. Note in passing that $\operatorname{cof}\mathbf{F}_S = \det\mathbf{F}_S\,\mathbf{F}_S^{T-1}$ represents the cofactor of the solid deformation gradient.

Since the gradient operators include derivatives with respect to the covariant line elements, the gradients of arbitrary scalar- and vector-valued functions Ψ and $\boldsymbol{\Psi}$ lead to contravariant quantities which have to be shifted using a contravariant transport mechanism. Thus, the following relations become apparent:

$$\begin{aligned} \operatorname{Grad}_S\Psi = \frac{\partial\Psi}{\partial\mathbf{X}_S} = \frac{\partial\Psi}{\partial\theta^k}\,\mathbf{h}_S^k \quad \underset{\mathbf{F}_S^T(\,\cdot\,)}{\overset{\mathbf{F}_S^{T-1}(\,\cdot\,)}{\rightleftharpoons}} \quad \frac{\partial\Psi}{\partial\theta^k}\,\mathbf{a}_S^k = \frac{\partial\Psi}{\partial\mathbf{x}} = \operatorname{grad}\Psi\,, \\ \operatorname{Grad}_S\boldsymbol{\Psi} = \frac{\partial\boldsymbol{\Psi}}{\partial\mathbf{X}_S} = \frac{\partial\boldsymbol{\Psi}}{\partial\theta^k}\otimes\mathbf{h}_S^k \quad \underset{(\,\cdot\,)\,\mathbf{F}_S}{\overset{(\,\cdot\,)\,\mathbf{F}_S^{-1}}{\rightleftharpoons}} \quad \frac{\partial\boldsymbol{\Psi}}{\partial\theta^k}\otimes\mathbf{a}_S^k = \frac{\partial\boldsymbol{\Psi}}{\partial\mathbf{x}} = \operatorname{grad}\boldsymbol{\Psi}\,. \end{aligned} \tag{3.29}$$

Therein, the superscript $(\,\cdot\,)^{T}_{23}$ denotes the transposition of the second with the third basis vector of the transporting fourth-order tensor. A complete overview of the transport behaviour of co- and contravariant vectors and tensors of second as well as fourth order between all configurations is given in box (3.30).

Co- and contravariant transports of

vectors (first-order tensors):

$$\mathbf{h}_{Sk} \underset{\mathbf{F}_{Si}^{-1}}{\overset{\mathbf{F}_{Si}}{\rightleftarrows}} \widehat{\mathbf{z}}_{Sk} \underset{\mathbf{F}_{Se}^{-1}}{\overset{\mathbf{F}_{Se}}{\rightleftarrows}} \mathbf{a}_{Sk} \qquad \mathbf{F}_S \text{ over, } \mathbf{F}_S^{-1} \text{ under}$$

$$\mathbf{h}_S^k \underset{\mathbf{F}_{Si}^{T}}{\overset{\mathbf{F}_{Si}^{T-1}}{\rightleftarrows}} \widehat{\mathbf{z}}_S^k \underset{\mathbf{F}_{Se}^{T}}{\overset{\mathbf{F}_{Se}^{T-1}}{\rightleftarrows}} \mathbf{a}_S^k \qquad \mathbf{F}_S^{T-1} \text{ over, } \mathbf{F}_S^{T} \text{ under}$$

second-order tensors:

$$\mathbf{h}_{Sk}\otimes\mathbf{h}_{Sl} \underset{\mathbf{F}_{Si}^{-1}(\widehat{\cdot})\,\mathbf{F}_{Si}^{T-1}}{\overset{\mathbf{F}_{Si}(\cdot)\,\mathbf{F}_{Si}^{T}}{\rightleftarrows}} \widehat{\mathbf{z}}_{Sk}\otimes\widehat{\mathbf{z}}_{Sl} \underset{\mathbf{F}_{Se}^{-1}(\cdot)\,\mathbf{F}_{Se}^{T-1}}{\overset{\mathbf{F}_{Se}(\widehat{\cdot})\,\mathbf{F}_{Se}^{T}}{\rightleftarrows}} \mathbf{a}_{Sk}\otimes\mathbf{a}_{Sl} \qquad \mathbf{F}_S(\cdot)\,\mathbf{F}_S^T \text{ over, } \mathbf{F}_S^{-1}(\cdot)\,\mathbf{F}_S^{T-1} \text{ under}$$

$$\mathbf{h}_S^k\otimes\mathbf{h}_S^l \underset{\mathbf{F}_{Si}^{T}(\widehat{\cdot})\,\mathbf{F}_{Si}}{\overset{\mathbf{F}_{Si}^{T-1}(\cdot)\,\mathbf{F}_{Si}^{-1}}{\rightleftarrows}} \widehat{\mathbf{z}}_S^k\otimes\widehat{\mathbf{z}}_S^l \underset{\mathbf{F}_{Se}^{T}(\cdot)\,\mathbf{F}_{Se}}{\overset{\mathbf{F}_{Se}^{T-1}(\widehat{\cdot})\,\mathbf{F}_{Se}^{-1}}{\rightleftarrows}} \mathbf{a}_S^k\otimes\mathbf{a}_S^l \qquad \mathbf{F}_S^{T-1}(\cdot)\,\mathbf{F}_S^{-1} \text{ over, } \mathbf{F}_S^{T}(\cdot)\,\mathbf{F}_S \text{ under}$$

(3.30)

fourth-order tensors:

$$\overset{4}{\mathbf{H}}{}^{\sharp} \underset{(\mathbf{F}_{Si}^{-1}\otimes\mathbf{F}_{Si}^{-1})^{\overset{23}{T}}(\widehat{\cdot})\,(\mathbf{F}_{Si}^{T-1}\otimes\mathbf{F}_{Si}^{T-1})^{\overset{23}{T}}}{\overset{(\mathbf{F}_{Si}\otimes\mathbf{F}_{Si})^{\overset{23}{T}}(\cdot)\,(\mathbf{F}_{Si}^{T}\otimes\mathbf{F}_{Si}^{T})^{\overset{23}{T}}}{\rightleftarrows}} \overset{4}{\widehat{\mathbf{Z}}}{}^{\sharp} \underset{(\mathbf{F}_{Se}^{-1}\otimes\mathbf{F}_{Se}^{-1})^{\overset{23}{T}}(\cdot)\,(\mathbf{F}_{Se}^{T-1}\otimes\mathbf{F}_{Se}^{T-1})^{\overset{23}{T}}}{\overset{(\mathbf{F}_{Se}\otimes\mathbf{F}_{Se})^{\overset{23}{T}}(\widehat{\cdot})\,(\mathbf{F}_{Se}^{T}\otimes\mathbf{F}_{Se}^{T})^{\overset{23}{T}}}{\rightleftarrows}} \overset{4}{\mathbf{A}}{}^{\sharp}$$

$$(\mathbf{F}_S\otimes\mathbf{F}_S)^{\overset{23}{T}}(\cdot)\,(\mathbf{F}_S^T\otimes\mathbf{F}_S^T)^{\overset{23}{T}} \text{ over, } (\mathbf{F}_S^{-1}\otimes\mathbf{F}_S^{-1})^{\overset{23}{T}}(\cdot)\,(\mathbf{F}_S^{T-1}\otimes\mathbf{F}_S^{T-1})^{\overset{23}{T}} \text{ under}$$

$$\overset{4}{\mathbf{H}}{}^{\flat} \underset{(\mathbf{F}_{Si}^{T}\otimes\mathbf{F}_{Si}^{T})^{\overset{23}{T}}(\widehat{\cdot})\,(\mathbf{F}_{Si}\otimes\mathbf{F}_{Si})^{\overset{23}{T}}}{\overset{(\mathbf{F}_{Si}^{T-1}\otimes\mathbf{F}_{Si}^{T-1})^{\overset{23}{T}}(\cdot)\,(\mathbf{F}_{Si}^{-1}\otimes\mathbf{F}_{Si}^{-1})^{\overset{23}{T}}}{\rightleftarrows}} \overset{4}{\widehat{\mathbf{Z}}}{}^{\flat} \underset{(\mathbf{F}_{Se}^{T}\otimes\mathbf{F}_{Se}^{T})^{\overset{23}{T}}(\cdot)\,(\mathbf{F}_{Se}\otimes\mathbf{F}_{Se})^{\overset{23}{T}}}{\overset{(\mathbf{F}_{Se}^{T-1}\otimes\mathbf{F}_{Se}^{T-1})^{\overset{23}{T}}(\widehat{\cdot})\,(\mathbf{F}_{Se}^{-1}\otimes\mathbf{F}_{Se}^{-1})^{\overset{23}{T}}}{\rightleftarrows}} \overset{4}{\mathbf{A}}{}^{\flat}$$

$$(\mathbf{F}_S^{T-1}\otimes\mathbf{F}_S^{T-1})^{\overset{23}{T}}(\cdot)\,(\mathbf{F}_S^{-1}\otimes\mathbf{F}_S^{-1})^{\overset{23}{T}} \text{ over, } (\mathbf{F}_S^{T}\otimes\mathbf{F}_S^{T})^{\overset{23}{T}}(\cdot)\,(\mathbf{F}_S\otimes\mathbf{F}_S)^{\overset{23}{T}} \text{ under}$$

with the general quantities:

$$\left\{\begin{array}{l} \overset{4}{\mathbf{H}}{}^{\sharp} = (\mathbf{h}_{Sk}\otimes\mathbf{h}_{Sl}\otimes\mathbf{h}_{Sm}\otimes\mathbf{h}_{Sn}) \\ \overset{4}{\widehat{\mathbf{Z}}}{}^{\sharp} = (\widehat{\mathbf{z}}_{Sk}\otimes\widehat{\mathbf{z}}_{Sl}\otimes\widehat{\mathbf{z}}_{Sm}\otimes\widehat{\mathbf{z}}_{Sn}) \\ \overset{4}{\mathbf{A}}{}^{\sharp} = (\mathbf{a}_{Sk}\otimes\mathbf{a}_{Sl}\otimes\mathbf{a}_{Sm}\otimes\mathbf{a}_{Sn}) \end{array}\right\} \quad \text{and} \quad \left\{\begin{array}{l} \overset{4}{\mathbf{H}}{}^{\flat} = (\mathbf{h}_S^k\otimes\mathbf{h}_S^l\otimes\mathbf{h}_S^m\otimes\mathbf{h}_S^n) \\ \overset{4}{\widehat{\mathbf{Z}}}{}^{\flat} = (\widehat{\mathbf{z}}_S^k\otimes\widehat{\mathbf{z}}_S^l\otimes\widehat{\mathbf{z}}_S^m\otimes\widehat{\mathbf{z}}_S^n) \\ \overset{4}{\mathbf{A}}{}^{\flat} = (\mathbf{a}_S^k\otimes\mathbf{a}_S^l\otimes\mathbf{a}_S^m\otimes\mathbf{a}_S^n) \end{array}\right\}$$

3.2.3 Deformation and Strain Measures

The intention of this section is to give a brief introduction into the particulars of finite deformation and strain measures, which result from the consequences of a multiplicative split of the solid deformation gradient. In this regard, the respective quantities will be exemplary derived between the reference and actual configuration and logically extended for the inelastic and elastic parts of one *Maxwell* element, thereafter. For a more comprehensive introduction please consult the works of Lee [119], Ehlers [47, 48, 49] or Markert [131] as well as the respective references therein.

As the name implies, the solid deformation gradients (3.25) contain the information which is needed to quantify the deformation process of the solid constituent. This can be precisely illustrated, when the unique polar decomposition theorem is applied yielding

$$\mathbf{F}_S = \mathbf{R}_S\,\mathbf{U}_S = \mathbf{V}_S\,\mathbf{R}_S\,. \tag{3.31}$$

Herein, $\mathbf{R}_S$ is a proper orthogonal rotation tensor with the properties $\mathbf{R}_S^T = \mathbf{R}_S^{-1}$ and $\det\mathbf{R}_S = 1$, while $\mathbf{U}_S$ and $\mathbf{V}_S$ denote the so-called symmetric positive definite right (material) and left (spatial) stretch tensors, respectively. Inserting the above relation into the covariant transport $(3.28)_1$ leads to

$$\mathrm{d}\mathbf{x} = \mathbf{R}_S\,(\mathbf{U}_S\,\mathrm{d}\mathbf{X}_S) = \mathbf{V}_S\,(\mathbf{R}_S\,\mathrm{d}\mathbf{X}_S)\,, \tag{3.32}$$

which can be interpreted as a concatenation of a stretch and a rotation or a rotation and a stretch, when a referential line element $\mathrm{d}\mathbf{X}_S$ is transported to the actual configuration. Following this, a tensorial deformation measure can be introduced via a linear mapping of the squares of line elements $\mathrm{d}s^2$ of the actual configuration and squares of line elements $\mathrm{d}S_S^2$ of the reference configuration. Herein, the line elements of one configuration are represented by elements of the respective other configuration using

$$\begin{aligned} \mathrm{d}s^2 &= \mathrm{d}\mathbf{x}\cdot\mathrm{d}\mathbf{x} = (\mathbf{F}_S\,\mathrm{d}\mathbf{X}_S)\cdot(\mathbf{F}_S\,\mathrm{d}\mathbf{X}_S) =: \mathrm{d}\mathbf{X}_S\cdot\mathbf{C}_S\,\mathrm{d}\mathbf{X}_S\,,\\ \mathrm{d}S_S^2 &= \mathrm{d}\mathbf{X}_S\cdot\mathrm{d}\mathbf{X}_S = (\mathbf{F}_S^{-1}\,\mathrm{d}\mathbf{x})\cdot(\mathbf{F}_S^{-1}\,\mathrm{d}\mathbf{x}) =: \mathrm{d}\mathbf{x}\cdot\mathbf{B}_S^{-1}\mathrm{d}\mathbf{x}\,. \end{aligned} \tag{3.33}$$

Therein, $\mathbf{C}_S$ and $\mathbf{B}_S$ are known as the right and left *Cauchy*[6]*-Green*[7] deformation tensors

$$\begin{aligned} \mathbf{C}_S &= \mathbf{F}_S^T\,\mathbf{F}_S = \mathbf{U}_S^T\,\mathbf{R}_S^T\,\mathbf{R}_S\,\mathbf{U}_S = \mathbf{U}_S\,\mathbf{U}_S\,,\\ \mathbf{B}_S &= \mathbf{F}_S\,\mathbf{F}_S^T = \mathbf{V}_S\,\mathbf{R}_S\,\mathbf{R}_S^T\,\mathbf{V}_S^T = \mathbf{V}_S\,\mathbf{V}_S\,, \end{aligned} \tag{3.34}$$

which solely depend on the respective stretching parts $\mathbf{U}_S$ and $\mathbf{V}_S$ of $\mathbf{F}_S$. Regarding the multiplicative split of $\mathbf{F}_S$, the corresponding inelastic and elastic stretch and rotation tensors can be introduced by the polar decomposition of $\mathbf{F}_{Si}$ and $\mathbf{F}_{Se}$ yielding

$$\mathbf{F}_{Si} = \mathbf{R}_{Si}\,\mathbf{U}_{Si} = \widehat{\mathbf{V}}_{Si}\,\mathbf{R}_{Si} \qquad \text{and} \qquad \mathbf{F}_{Se} = \mathbf{R}_{Se}\,\widehat{\mathbf{U}}_{Se} = \mathbf{V}_{Se}\,\mathbf{R}_{Se}\,. \tag{3.35}$$

[6] *Augustin Louis Cauchy* (1789–1857): French mathematician and member of the Society of Jesus who published approximately 800 scientific articles in mathematics and physics. He was one of the most important scientists after *Leonard Euler*.

[7] *George Green* (1793-1841): British miller and self-taught mathematician who privately published his major work *An Essay on the Application of Mathematical Analysis to the Theories of Electricity and Magnetism* at his own expense. *Green* received little public recognition in his lifetime and it was *William Thomson* (Lord *Kelvin*) who first recognised the value of his work four years after his death. It turned out that he had already done much of what many other great scientists thought was their original work.

In analogy to the procedure used in equations (3.33), but now involving the squares of line elements $\mathrm{d}\widehat{s}^2_{Si} = \mathrm{d}\widehat{\mathbf{x}}_{Si} \cdot \mathrm{d}\widehat{\mathbf{x}}_{Si}$ of the intermediate configuration, leads to equivalent deformation tensors for the elastic and inelastic parts, viz.:

$$\begin{aligned} \mathbf{C}_{Si} &:= \mathbf{F}_{Si}^T \mathbf{F}_{Si} = \mathbf{U}_{Si} \mathbf{U}_{Si} , \qquad & \widehat{\mathbf{C}}_{Se} &:= \mathbf{F}_{Se}^T \mathbf{F}_{Se} = \widehat{\mathbf{U}}_{Se} \widehat{\mathbf{U}}_{Se} , \\ \widehat{\mathbf{B}}_{Si} &:= \mathbf{F}_{Si} \mathbf{F}_{Si}^T = \widehat{\mathbf{V}}_{Si} \widehat{\mathbf{V}}_{Si} , \qquad & \mathbf{B}_{Se} &:= \mathbf{F}_{Se} \mathbf{F}_{Se}^T = \mathbf{V}_{Se} \mathbf{V}_{Se} . \end{aligned} \tag{3.36}$$

Again, the deformation tensors solely depend on the respective stretch tensors, where quantities of the intermediate configuration are indicated by $(\widehat{\cdot})$. However, care must be taken regarding the resulting transport mechanisms which become apparent in natural basis representation. With the aid of the deformation gradients (3.25), the deformation tensors (3.34) and (3.36) can be given on their respective configurations yielding

$$\begin{aligned} \mathbf{C}_S &= a_{Skl} \; \mathbf{h}_S^k \otimes \mathbf{h}_S^l , \qquad & \widehat{\mathbf{C}}_{Se} &= a_{Skl} \; \widehat{\mathbf{z}}_S^k \otimes \widehat{\mathbf{z}}_S^l , \qquad & \mathbf{B}_{Se} &= \widehat{z}_S^{kl} \; \mathbf{a}_{Sk} \otimes \mathbf{a}_{Sl} , \\ \mathbf{C}_{Si} &= \widehat{z}_{Skl} \; \mathbf{h}_S^k \otimes \mathbf{h}_S^l , \qquad & \widehat{\mathbf{B}}_{Si} &= h_S^{kl} \; \widehat{\mathbf{z}}_{Sk} \otimes \widehat{\mathbf{z}}_{Sl} , \qquad & \mathbf{B}_S &= h_S^{kl} \; \mathbf{a}_{Sk} \otimes \mathbf{a}_{Sl} , \end{aligned} \tag{3.37}$$

with their corresponding inverses

$$\begin{aligned} \mathbf{C}_S^{-1} &= a_S^{kl} \; \mathbf{h}_{Sk} \otimes \mathbf{h}_{Sl} , \qquad & \widehat{\mathbf{C}}_{Se}^{-1} &= a_S^{kl} \; \widehat{\mathbf{z}}_{Sk} \otimes \widehat{\mathbf{z}}_{Sl} , \qquad & \mathbf{B}_{Se}^{-1} &= \widehat{z}_{Skl} \; \mathbf{a}_S^k \otimes \mathbf{a}_S^l , \\ \mathbf{C}_{Si}^{-1} &= \widehat{z}_S^{kl} \; \mathbf{h}_{Sk} \otimes \mathbf{h}_{Sl} , \qquad & \widehat{\mathbf{B}}_{Si}^{-1} &= h_{Skl} \; \widehat{\mathbf{z}}_S^k \otimes \widehat{\mathbf{z}}_S^l , \qquad & \mathbf{B}_S^{-1} &= h_{Skl} \; \mathbf{a}_S^k \otimes \mathbf{a}_S^l . \end{aligned} \tag{3.38}$$

Herein, $(\cdot)_{Skl}$ and $(\cdot)_S^{kl}$ denote the respective co- and contravariant metric coefficients which are matrices containing the nine possible scalar products between two sets of corresponding basis vectors, thereby describing their geometric characteristics. Note in passing how the variance of a deformation tensor changes as it is inverted. Moreover, the deformation tensors (3.37) and (3.38) given in natural basis representation allow for a convenient identification of the configuration they are defined in. Since the deformation tensors are obviously a measure of a single configuration, the two-field character of the solid deformation gradient must be in the rotation tensor $\mathbf{R}_S$. Hence, the stretch and deformation tensors are not transported with $\mathbf{F}_S$ but rotated with $\mathbf{R}_S$. Equations (3.31) and (3.34) allow for the direct conclusion of the following exemplary forward and backward rotations:

$$\left.\begin{aligned} \mathbf{U}_S &= \mathbf{R}_S^T \mathbf{V}_S \mathbf{R}_S , \\ \mathbf{C}_S &= \mathbf{R}_S^T \mathbf{B}_S \mathbf{R}_S , \end{aligned}\right\} \quad \longleftrightarrow \quad \left\{\begin{aligned} \mathbf{V}_S &= \mathbf{R}_S \mathbf{U}_S \mathbf{R}_S^T , \\ \mathbf{B}_S &= \mathbf{R}_S \mathbf{C}_S \mathbf{R}_S^T , \end{aligned}\right. \tag{3.39}$$

where similar rotational transports can also be obtained for the corresponding elastic and inelastic measures. Moreover, the application of the transport mechanisms in box (3.30) on the deformation tensors (3.37) and (3.38) yields a different result. For instance, a contravariant push-forward of $\mathbf{C}_S$ yields the identity $\mathbf{I}$ as the contravariant metric tensor of the actual configuration.

Furthermore, it can be noted that the right *Cauchy-Green* deformation tensors describe the overall as well as the inelastic part of the deformation from the referential frame, while the intermediate configuration functions act as a "reference configuration" for the description of the elastic process. The opposite holds for the left *Cauchy-Green* deformation tensors, which describe the overall and elastic process looking back from the actual configuration and the inelastic part of the deformation from the intermediate frame.

While the deformation tensors characterise the deformation of a configuration itself via the total change in length of a line element, a strain measure does this relative to an initial length. Following this, another dimensionless quantity can be obtained from the idea to compare the lengths of line elements between two configurations. As a first step, the difference of the squared lengths of line elements (3.33) can be computed and expressed with respect to the reference and actual configuration yielding

$$\begin{aligned} \mathrm{d}s^2 - \mathrm{d}S_S^2 &= \mathrm{d}\mathbf{X}_S \cdot \mathbf{C}_S \, \mathrm{d}\mathbf{X}_S - \mathrm{d}\mathbf{X}_S \cdot \mathrm{d}\mathbf{X}_S =: \mathrm{d}\mathbf{X}_S \cdot 2\mathbf{E}_S \, \mathrm{d}\mathbf{X}_S \\ &= \mathrm{d}\mathbf{x} \cdot \mathrm{d}\mathbf{x} - \mathrm{d}\mathbf{x} \cdot \mathbf{B}_S^{-1} \mathrm{d}\mathbf{x} =: \mathrm{d}\mathbf{x} \cdot 2\mathbf{A}_S \, \mathrm{d}\mathbf{x} \,. \end{aligned} \tag{3.40}$$

In this context, $\mathbf{E}_S$ denotes the *Green-Lagrange*an strain tensor and $\mathbf{A}_S$ is known as the *Almansi*an[8] strain tensor with their definitions

$$\mathbf{E}_S = \tfrac{1}{2} \left(\mathbf{C}_S - \mathbf{I} \right) \qquad \text{and} \qquad \mathbf{A}_S = \tfrac{1}{2} \left(\mathbf{I} - \mathbf{B}_S^{-1} \right) . \tag{3.41}$$

Analogously, the elastic and inelastic parts can be obtained with the differences $\mathrm{d}\widehat{s}_{Si}^{\,2} - \mathrm{d}S_S^2$ and $\mathrm{d}s^2 - \mathrm{d}\widehat{s}_{Si}^{\,2}$, which can be expressed on all three configurations leading to

$$\begin{aligned} \mathbf{E}_{Si} &= \tfrac{1}{2} \left(\mathbf{C}_{Si} - \mathbf{I} \right) , & \mathbf{A}_{Si} &= \tfrac{1}{2} \left(\mathbf{B}_{Se}^{-1} - \mathbf{B}_S^{-1} \right) , \\ \mathbf{E}_{Se} &= \tfrac{1}{2} \left(\mathbf{C}_S - \mathbf{C}_{Si} \right) , & \mathbf{A}_{Se} &= \tfrac{1}{2} \left(\mathbf{I} - \mathbf{B}_{Se}^{-1} \right) , \end{aligned} \tag{3.42}$$

for a description on the reference and actual configuration, respectively, and to

$$\widehat{\mathbf{\Gamma}}_S = \tfrac{1}{2} \left(\widehat{\mathbf{C}}_{Se} - \widehat{\mathbf{B}}_{Si}^{-1} \right) , \qquad \widehat{\mathbf{\Gamma}}_{Si} = \tfrac{1}{2} \left(\mathbf{I} - \widehat{\mathbf{B}}_{Si}^{-1} \right) , \qquad \text{and} \qquad \widehat{\mathbf{\Gamma}}_{Se} = \tfrac{1}{2} \left(\widehat{\mathbf{C}}_{Se} - \mathbf{I} \right) , \tag{3.43}$$

for a description on the intermediate configuration. A closer look at the equations above reveals the additive strain concept of the underlying generalised *Maxwell* model and the following relations become apparent:

$$\mathbf{E}_S = \mathbf{E}_{Si} + \mathbf{E}_{Se} \,, \qquad \widehat{\mathbf{\Gamma}}_S = \widehat{\mathbf{\Gamma}}_{Si} + \widehat{\mathbf{\Gamma}}_{Se} \,, \qquad \text{and} \qquad \mathbf{A}_S = \mathbf{A}_{Si} + \mathbf{A}_{Se} \,. \tag{3.44}$$

Comparing the natural basis systems of the involved deformation tensors (3.37) and (3.38) reveals that all presented strain measures are contravariant and thus, the contravariant transports of second-order tensors given in box (3.30) apply. For convenience, a complete overview of the transport properties of the defined contravariant strain tensors can be found in box (B.1) of Appendix B. Moreover, all *Green-Lagrange*an strains are defined on the reference configuration, while the *Almansi*an strains reside on the actual configuration and the remaining strains (3.43) refer to the intermediate frame.

Finally note that there are several other possibilities to define strain measures which are different to the ones mentioned above, but will have no relevance in this monograph. For more information, please refer to Truesdell & Noll [207] or Ogden [157].

[8] *Emilio Almansi* (1869–1948): Italian physicist and mathematician who did significant research in the general theory of elasticity as well as nonlinear problems and defined a strain measure in his treatise *Sulle deformazioni finite dei solidi elastici isotropi*, which appeared in 1911.

3.2.4 Spectral Representation of the Deformation Tensors

For the postulation of finite material laws during the constitutive modelling process, it is often convenient to make use of the spectral representation of the deformation tensors. However, the purpose of the present monograph is to give a brief introduction into the particulars of the spectral representation, whereas more detailed information can be found in Lambrecht [115], Markert [131] and references therein.

Proceeding from (3.39), where the left and right stretch tensors differ only by a proper orthogonal rotation, it is easily concluded that the deformation tensors $\mathbf{C}_S$ and $\mathbf{B}_S$ obey the same eigenvalues, which are the squares of the principal stretches. The principal stretches themselves are the eigenvalues of the stretch tensors. Accordingly, the principal directions of $\mathbf{U}_S$ and $\mathbf{C}_S$ as well as $\mathbf{V}_S$ and $\mathbf{B}_S$ coincide. Following this, the well-known eigenvalue problem can be postulated, i. e., if λ_S is an eigenvalue of $\mathbf{C}_S$ or $\mathbf{B}_S$, then there is an eigenvector $\mathbf{m}_S \neq \mathbf{0}$ or $\mathbf{n}_S \neq \mathbf{0}$ such that

$$\left.\begin{aligned}(\mathbf{C}_S - \lambda_S\,\mathbf{I})\,\mathbf{m}_S &= \mathbf{0}\,,\\ (\mathbf{B}_S - \lambda_S\,\mathbf{I})\,\mathbf{n}_S &= \mathbf{0}\,,\end{aligned}\right\} \quad \longleftrightarrow \quad \left\{\begin{aligned}\mathbf{C}_S\,\mathbf{m}_S &= \lambda_S\,\mathbf{m}_S\,,\\ \mathbf{B}_S\,\mathbf{n}_S &= \lambda_S\,\mathbf{n}_S\,.\end{aligned}\right. \tag{3.45}$$

Moreover, the corresponding eigenvectors are mutually orthogonal satisfying $\mathbf{m}_{S(k)}\cdot\mathbf{m}_{S(l)} = \mathbf{n}_{S(k)}\cdot\mathbf{n}_{S(l)} = \delta_{kl}$. Thus, a distinction in co- and contravariant eigenvectors is not necessary. In order to obtain a non-trivial solution of (3.45), a vanishing characteristic polynomial is needed which can be expressed using the *Cayley*[9]*-Hamilton*[10] theorem, viz.:

$$\det\left(\mathbf{C}_S - \lambda_S\,\mathbf{I}\right) = \det\left(\mathbf{B}_S - \lambda_S\,\mathbf{I}\right) = \lambda_S^3 - I_{S1}\,\lambda_S^2 + I_{S2}\,\lambda_S - I_{S3} = 0\,. \tag{3.46}$$

Due to the symmetry of the deformation tensors, the characteristic polynomial of third order in λ_S delivers three real-valued roots which are the eigenvalues $\lambda_{S(k)}$ with $k = 1, 2, 3$ of $\mathbf{C}_S$ and $\mathbf{B}_S$. Moreover, the principal invariants in (3.46) can be given as

$$\begin{aligned}I_{S1} &= \operatorname{tr}\mathbf{C}_S &&= \operatorname{tr}\mathbf{B}_S &&= \mathbf{F}_S\cdot\mathbf{F}_S\,,\\ I_{S2} &= \operatorname{tr}\left(\operatorname{cof}\mathbf{C}_S\right) &&= \operatorname{tr}\left(\operatorname{cof}\mathbf{B}_S\right) &&= \operatorname{cof}\mathbf{F}_S\cdot\operatorname{cof}\mathbf{F}_S\,,\\ I_{S3} &= \det\mathbf{C}_S &&= \det\mathbf{B}_S &&= (\det\mathbf{F}_S)^2.\end{aligned} \tag{3.47}$$

Note that the eigenvalues are related to the principal invariants via

$$\begin{aligned}&I_{S1} = \lambda_{S1} + \lambda_{S2} + \lambda_{S3}\,, \qquad I_{S2} = \lambda_{S1}\,\lambda_{S2} + \lambda_{S2}\,\lambda_{S3} + \lambda_{S2}\,\lambda_{S3}\,,\\ &I_{S3} = \lambda_{S1}\,\lambda_{S2}\,\lambda_{S3}\,.\end{aligned} \tag{3.48}$$

Following this allows for the spectral representation of the deformation tensors via

$$(\mathbf{C}_S)^m = \sum_{k=1}^{3}(\lambda_{S(k)})^m\,\mathbf{M}_{S(k)} \qquad \text{and} \qquad (\mathbf{B}_S)^m = \sum_{k=1}^{3}(\lambda_{S(k)})^m\,\mathbf{N}_{S(k)}\,, \tag{3.49}$$

[9] *Arthur Cayley* (1821–1895): British mathematician who proved that every square matrix is a root of its own characteristic polynomial. Before his professorship, he worked as a lawyer to finance his research.

[10] *William Rowan Hamilton* (1805–1865): Irish mathematician, physicist, and astronomer who made important contributions to the development of optics, dynamics, and algebra.

where m represents any real-valued power of the deformation tensors. The corresponding eigentensors are then defined with the following dyadic products:

$$\mathbf{M}_{S(k)} = \mathbf{m}_{S(k)} \otimes \mathbf{m}_{S(k)} \qquad \text{and} \qquad \mathbf{N}_{S(k)} = \mathbf{n}_{S(k)} \otimes \mathbf{n}_{S(k)} \,. \tag{3.50}$$

Due to the orthogonality of the eigenvectors, the eigentensors have the properties

$$\begin{aligned} &\sum_{k=1}^{3} \mathbf{M}_{S(k)} = \mathbf{I} \,, \qquad (\mathbf{M}_{S(k)})^m = \mathbf{M}_{S(k)} \,, \qquad \mathbf{M}_{S(k)}\,\mathbf{M}_{S(l)} = \mathbf{0} \quad \forall\, k \neq l \,, \\ &\mathbf{C}_S\,\mathbf{M}_{S(k)} = \mathbf{M}_{S(k)}\,\mathbf{C}_S = \lambda_{S(k)}\,\mathbf{M}_{S(k)} \,, \qquad \mathbf{M}_{S(k)} \cdot \mathbf{M}_{S(l)} = \delta_{kl} \,, \end{aligned} \tag{3.51}$$

where similar relations hold for the eigentensor of $\mathbf{B}_S$. Moreover, exploiting relations (3.34) and (3.49) allows for the direct conclusion that

$$\mathbf{R}_S = \sum_{k=1}^{3} \mathbf{n}_{S(k)} \otimes \mathbf{m}_{S(k)} \qquad \text{and} \qquad \mathbf{F}_S = \sum_{k=1}^{3} \sqrt{\lambda_{S(k)}}\, \mathbf{n}_{S(k)} \otimes \mathbf{m}_{S(k)} \,. \tag{3.52}$$

The rotation behaviour of the referential eigenvectors $\mathbf{m}_{S(k)}$ into the principal directions $\mathbf{n}_{S(k)}$ of the actual configuration can be deduced from (3.39) yielding

$$\mathbf{m}_{S(k)} \underset{\mathbf{R}_S^T\,(\,\cdot\,)}{\overset{\mathbf{R}_S\,(\,\cdot\,)}{\rightleftarrows}} \mathbf{n}_{S(k)} \,, \qquad \mathbf{M}_{S(k)} \underset{\mathbf{R}_S^T\,(\,\cdot\,)\,\mathbf{R}_S}{\overset{\mathbf{R}_S\,(\,\cdot\,)\,\mathbf{R}_S^T}{\rightleftarrows}} \mathbf{N}_{S(k)} \,, \tag{3.53}$$

whereas the transformation behaviour using $\mathbf{F}_S$ can be given by

$$\mathbf{m}_{S(k)} \underset{\mathbf{F}_S^T\,(\,\cdot\,)}{\overset{\mathbf{F}_S\,(\,\cdot\,)}{\rightleftarrows}} \sqrt{\lambda_{S(k)}}\,\mathbf{n}_{S(k)} \,, \quad \mathbf{M}_{S(k)} \underset{\mathbf{F}_S^T\,(\,\cdot\,)\,\mathbf{F}_S}{\overset{\mathbf{F}_S\,(\,\cdot\,)\,\mathbf{F}_S^T}{\rightleftarrows}} \lambda_{S(k)}\,\mathbf{N}_{S(k)} \,. \tag{3.54}$$

Note that the procedure above can be directly applied to the elastic deformation tensors

$$\widehat{\mathbf{C}}_{Se} = \sum_{k=1}^{3} (\lambda_{Se(k)})^m\, \widehat{\mathbf{M}}_{Se(k)} \qquad \text{and} \qquad \mathbf{B}_{Se} = \sum_{k=1}^{3} (\lambda_{Se(k)})^m\, \mathbf{N}_{Se(k)} \,, \tag{3.55}$$

where the respective eigentensors are defined on the intermediate configuration as well as on the actual configuration. The representation of the inelastic quantities will not be needed in this monograph.

Finally, some derivatives need to be provided such that they are handy, when they are needed in the context of isotropic tensor functions in Section 4.4. Herein, the following relations hold for the derivatives of $\lambda_{S(k)}$ with respect to $\mathbf{C}_S$ and $\mathbf{B}_S$

$$\frac{\partial \lambda_{S(k)}}{\partial \mathbf{C}_S} = \mathbf{m}_{S(k)} \otimes \mathbf{m}_{S(k)} = \mathbf{M}_{S(k)} \,, \qquad \frac{\partial \lambda_{S(k)}}{\partial \mathbf{B}_S} = \mathbf{n}_{S(k)} \otimes \mathbf{n}_{S(k)} = \mathbf{N}_{S(k)} \,, \tag{3.56}$$

whereas the derivatives of the respective eigentensors $\mathbf{M}_{S(k)}$ and $\mathbf{N}_{S(k)}$ obtain the form

$$\begin{aligned} \frac{\partial \mathbf{M}_{S(k)}}{\partial \mathbf{C}_S} &= \frac{1}{2} \sum_{\substack{l=1 \\ l \neq k}}^{3} \frac{1}{\lambda_{S(k)} - \lambda_{S(l)}} \left(\overset{4}{\mathbf{M}}_{S[kl]} + \overset{4}{\mathbf{M}}_{S[lk]} \right) =: \overset{4}{\mathbf{M}}_{S[k]} \,, \\ \frac{\partial \mathbf{N}_{S(k)}}{\partial \mathbf{B}_S} &= \frac{1}{2} \sum_{\substack{l=1 \\ l \neq k}}^{3} \frac{1}{\lambda_{S(k)} - \lambda_{S(l)}} \left(\overset{4}{\mathbf{N}}_{S[kl]} + \overset{4}{\mathbf{N}}_{S[lk]} \right) =: \overset{4}{\mathbf{N}}_{S[k]} \end{aligned} \tag{3.57}$$

with the abbreviations $\overset{4}{\mathbf{M}}_{S[kl]} = [\mathbf{M}_{S(k)} \otimes \mathbf{M}_{S(l)}]^{\overset{23}{T}} + [\mathbf{M}_{S(k)} \otimes \mathbf{M}_{S(l)}]^{\overset{24}{T}}$ and a similar abbreviation for $(\mathbf{N}_{S[kl]})\underline{^4}$. In the context of isotropic tensor functions in the form of $\Psi(\lambda_{S1}, \lambda_{S2}, \lambda_{S3})$, the first and second derivative with respect to $\mathbf{C}_S$ can be given by

$$\begin{aligned} \frac{\partial \Psi}{\partial \mathbf{C}_S} &= \sum_{k=1}^{3} \frac{\partial \Psi}{\partial \lambda_{S(k)}} \frac{\partial \lambda_{S(k)}}{\partial \mathbf{C}_S} = \sum_{k=1}^{3} \frac{\partial \Psi}{\partial \lambda_{S(k)}} \mathbf{M}_{S(k)} \,, \\ \frac{\partial^2 \Psi}{\partial \mathbf{C}_S \otimes \partial \mathbf{C}_S} &= \sum_{k,l=1}^{3} \frac{\partial^2 \Psi}{\partial \lambda_{S(k)}\, \partial \lambda_{S(l)}} \mathbf{M}_{S(k)} \otimes \mathbf{M}_{S(l)} + \frac{1}{2} \sum_{\substack{k,l=1 \\ k \neq l}}^{3} \frac{\frac{\partial \Psi}{\partial \lambda_{S(k)}} - \frac{\partial \Psi}{\partial \lambda_{S(l)}}}{\lambda_{S(k)} - \lambda_{S(l)}} \overset{4}{\mathbf{M}}_{S[kl]} \,. \end{aligned} \tag{3.58}$$

The derivatives with respect to $\mathbf{B}_S$ are obtained by a push-forward of (3.58) yielding

$$\begin{aligned} &\mathbf{F}_S \frac{\partial \Psi}{\partial \mathbf{C}_S} \mathbf{F}_S^T = \frac{\partial \Psi}{\partial \mathbf{B}_S} \mathbf{B}_S = \mathbf{B}_S \frac{\partial \Psi}{\partial \mathbf{B}_S} = \sum_{k=1}^{3} \frac{\partial \Psi}{\partial \lambda_{S(k)}} \lambda_{S(k)} \mathbf{N}_{S(k)} \,, \\ &(\mathbf{F}_S \otimes \mathbf{F}_S)^{\overset{23}{T}} \frac{\partial^2 \Psi}{\partial \mathbf{C}_S \otimes \partial \mathbf{C}_S} (\mathbf{F}_S^T \otimes \mathbf{F}_S^T)^{\overset{23}{T}} = \\ &\quad = \sum_{k,l=1}^{3} \frac{\partial^2 \Psi}{\partial \lambda_{S(k)}\, \partial \lambda_{S(l)}} \lambda_{S(k)}\, \lambda_{S(l)}\, \mathbf{N}_{S(k)} \otimes \mathbf{N}_{S(l)} + \frac{1}{2} \sum_{\substack{k,l=1 \\ k \neq l}}^{3} \frac{\frac{\partial \Psi}{\partial \lambda_{S(k)}} - \frac{\partial \Psi}{\partial \lambda_{S(l)}}}{\lambda_{S(k)} - \lambda_{S(l)}} \lambda_{S(k)}\, \lambda_{S(l)}\, \overset{4}{\mathbf{N}}_{S[kl]} \,. \end{aligned} \tag{3.59}$$

Obviously, the rules above are only applicable in the case of distinct eigenvalues. The necessary modifications in cases of equal eigenvalues will be discussed in Section 4.4, where they are applied to the finite material law.

3.2.5 Deformation and Strain Rates

Obviously, when describing rate-dependent material behaviour, deformation and strain rates need to be introduced. According to the preceding section, there are also different possibilities to introduce the corresponding measures. Starting from the material time derivative of the overall and inelastic solid deformation gradients (3.25), the material solid velocity gradients are obtained by

$$\begin{aligned} (\mathbf{F}_S)'_S &= \frac{\mathrm{d}_S}{\mathrm{d}t} \left(\frac{\partial \mathbf{x}}{\partial \mathbf{X}_S} \right) = \frac{\partial \overset{\prime}{\mathbf{x}}_S}{\partial \mathbf{X}_S} = \mathrm{Grad}_S \overset{\prime}{\mathbf{x}}_S = \frac{\partial \overset{\prime}{\mathbf{x}}_S}{\partial \mathbf{x}} \frac{\partial \mathbf{x}}{\partial \mathbf{X}_S} =: \mathbf{L}_S \mathbf{F}_S \,, \\ (\mathbf{F}_{Si})'_S &= \frac{\mathrm{d}_S}{\mathrm{d}t} \left(\frac{\partial \widehat{\mathbf{x}}_{Si}}{\partial \mathbf{X}_S} \right) = \frac{\partial (\widehat{\mathbf{x}}_{Si})'_S}{\partial \mathbf{X}_S} = \mathrm{Grad}_S\, (\widehat{\mathbf{x}}_{Si})'_S = \frac{\partial (\widehat{\mathbf{x}}_{Si})'_S}{\partial \widehat{\mathbf{x}}_{Si}} \frac{\partial \widehat{\mathbf{x}}_{Si}}{\partial \mathbf{X}_S} =: \widehat{\mathbf{L}}_{Si} \mathbf{F}_{Si} \,, \end{aligned} \tag{3.60}$$

thereby defining the respective overall and inelastic spatial solid velocity gradients

$$\mathbf{L}_S = \mathrm{grad}\, \overset{\prime}{\mathbf{x}}_S = (\mathbf{F}_S)'_S \mathbf{F}_S^{-1} \qquad \text{and} \qquad \widehat{\mathbf{L}}_{Si} = \mathrm{grad}_{Si}\, (\widehat{\mathbf{x}}_{Si})'_S = (\mathbf{F}_{Si})'_S \mathbf{F}_{Si}^{-1} \,, \tag{3.61}$$

respectively. Herein, $\mathrm{grad}_{Si}\,(\,\cdot\,)$ denotes the gradient with respect to the spatial variable of the intermediate configuration. Note in passing that the application of the same procedure

to the elastic part $\mathbf{F}_{Se}$ does not yield a physically meaningful definition of an elastic spatial velocity gradient. This is mainly due to the property of $\mathbf{F}_{Se}$, which has both basis systems in time-dependent configurations, cf. Ehlers [47]. Thus, the quotient rule needs to be applied when the material time derivative is taken which leads to a different expression compared to (3.60).

Inserting the definitions of the material velocity gradients (3.60) into the given transport behaviour of covariant line elements $(3.28)_1$, it is easy to conclude that

$$(\mathrm{d}\mathbf{x})'_S = (\mathbf{F}_S)'_S \, \mathrm{d}\mathbf{X}_S = \mathbf{L}_S \, \mathrm{d}\mathbf{x} \qquad \text{and} \qquad (\mathrm{d}\widehat{\mathbf{x}}_{Si})'_S = (\mathbf{F}_{Si})'_S \, \mathrm{d}\mathbf{X}_S = \widehat{\mathbf{L}}_{Si} \, \mathrm{d}\widehat{\mathbf{x}}_{Si} \,, \tag{3.62}$$

thereby keeping in mind that the solid line elements of the reference configuration are independent of the time. For the sake of completeness, the material time derivatives of the remaining (oriented) area and volume elements of (3.28) can be expressed as

$$(\mathrm{d}\mathbf{a})'_S = \left[(\mathbf{L}_S \cdot \mathbf{I}) \, \mathbf{I} - \mathbf{L}_S^T \right] \mathrm{d}\mathbf{a} \qquad \text{and} \qquad (\mathrm{d}v)'_S = (\mathbf{L}_S \cdot \mathbf{I}) \, \mathrm{d}v = \operatorname{div} \overset{\prime}{\mathbf{x}}_S \, \mathrm{d}v \,, \tag{3.63}$$

where $\operatorname{div}(\bullet)$ denotes the divergence operator. Please note that the lengthy derivations of these relations will not be given in this monograph, but can be comprehensively studied in de Boer [23].

Like any other tensor, the spatial solid velocity gradients (3.61) can be decomposed into

$$\mathbf{L}_S = \mathbf{D}_S + \mathbf{W}_S \qquad \text{and} \qquad \widehat{\mathbf{L}}_{Si} = \widehat{\mathbf{D}}_{Si} + \widehat{\mathbf{W}}_{Si} \qquad \text{with} \tag{3.64}$$

$$\begin{aligned} \mathbf{D}_S &= \tfrac{1}{2} (\mathbf{L}_S + \mathbf{L}_S^T) = \quad \mathbf{D}_S^T \,, & \widehat{\mathbf{D}}_{Si} &= \tfrac{1}{2} (\widehat{\mathbf{L}}_{Si} + \widehat{\mathbf{L}}_{Si}^T) = \quad \widehat{\mathbf{D}}_{Si}^T \,, \\ \mathbf{W}_S &= \tfrac{1}{2} (\mathbf{L}_S - \mathbf{L}_S^T) = -\mathbf{W}_S^T \,, & \widehat{\mathbf{W}}_{Si} &= \tfrac{1}{2} (\widehat{\mathbf{L}}_{Si} - \widehat{\mathbf{L}}_{Si}^T) = -\widehat{\mathbf{W}}_{Si}^T \,. \end{aligned} \tag{3.65}$$

Herein, $\mathbf{D}_S$ and $\widehat{\mathbf{D}}_{Si}$ denote the overall and inelastic symmetric rate of deformation tensors, while $\mathbf{W}_S$ and $\widehat{\mathbf{W}}_{Si}$ are the respective skew-symmetric parts known as spin tensors.

Formally applying the material time derivative to the right *Cauchy-Green* deformation tensor $(3.34)_1$ yields the rate of deformation tensor $(\mathbf{C}_S)'_S$ in the referential frame

$$(\mathbf{C}_S)'_S = (\mathbf{F}_S^T \, \mathbf{F}_S)'_S = (\mathbf{F}_S^T)'_S \, \mathbf{F}_S + \mathbf{F}_S^T \, (\mathbf{F}_S)'_S = \mathbf{F}_S^T \, \mathbf{L}_S^T \, \mathbf{F}_S + \mathbf{F}_S^T \, \mathbf{L}_S \, \mathbf{F}_S = 2 \, \mathbf{F}_S^T \, \mathbf{D}_S \, \mathbf{F}_S \,. \tag{3.66}$$

Making use of equations $(3.61)_1$ and $(3.65)_1$ reveals that $(\mathbf{C}_S)'_S$ is simultaneously obtained from a contravariant pull back of the rate of deformation $\mathbf{D}_S$ in the actual frame. Following this, the material time derivative of the inverted left *Cauchy-Green* deformation tensor $\mathbf{B}_S^{-1}$ can be computed according to Ehlers [47] yielding

$$(\mathbf{B}_S^{-1})'_S = -\mathbf{L}_S^T \, \mathbf{B}_S^{-1} - \mathbf{B}_S^{-1} \, \mathbf{L}_S . \tag{3.67}$$

The connection to the related strain rates can be obtained by taking the material time derivative of the squared difference of line elements (3.40) and expressing the result in terms of the reference configuration, viz.:

$$(\mathrm{d}s^2 - \mathrm{d}S_S^2)'_S = (\mathrm{d}\mathbf{X}_S \cdot 2 \, \mathbf{E}_S \, \mathrm{d}\mathbf{X}_S)'_S = \mathrm{d}\mathbf{X}_S \cdot 2 \, (\mathbf{E}_S)'_S \, \mathrm{d}\mathbf{X}_S = \mathrm{d}\mathbf{X}_S \cdot (\mathbf{C}_S)'_S \, \mathrm{d}\mathbf{X}_S \,. \tag{3.68}$$

Utilising the material time derivative of line elements $(3.62)_1$ allows for a representation on the actual configuration yielding

$$\begin{aligned}(\mathrm{d}s^2 - \mathrm{d}S_S^2)'_S &= (\mathrm{d}\mathbf{x}\cdot 2\,\mathbf{A}_S\,\mathrm{d}\mathbf{x})'_S = \mathrm{d}\mathbf{x}\cdot 2\left[\,\mathbf{L}_S^T\,\mathbf{A}_S + (\mathbf{A}_S)'_S + \mathbf{A}_S\,\mathbf{L}_S\,\right]\mathrm{d}\mathbf{x}\\ &=: \mathrm{d}\mathbf{x}\cdot 2\,(\mathbf{A}_S)^{\triangle}_S\,\mathrm{d}\mathbf{x}\,.\end{aligned} \tag{3.69}$$

Herein, $(\,\cdot\,)^{\triangle}_S$ denotes the upper (contravariant) *Oldroyd*[11] derivative which can be interpreted as the relative time derivative of a spatial quantity, where only the time derivative of the coefficient matrix of a tensor is taken, while its (contravariant) spatial basis is held constant:

$$(\,\cdot\,)^{\triangle}_S = (\,\cdot\,)'_S + \mathbf{L}_S^T\,(\,\cdot\,) + (\,\cdot\,)\,\mathbf{L}_S\,. \tag{3.70}$$

Note in passing that (3.70) is also often referred to as a contravariant *Lie*[12] derivative. Moreover, with the definition of the *Green-Almansi*an strain (3.41) inserted into (3.69), a comparison with (3.67) allows for the conclusion

$$(\mathbf{A}_S)^{\triangle}_S = \tfrac{1}{2}\,(\mathbf{L}_S^T + \mathbf{L}_S) = \mathbf{D}_S\,. \tag{3.71}$$

Together with (3.66), this is equivalent to the contravariant transport of the *Green-Lagrange*an strain velocity tensor

$$(\mathbf{A}_S)^{\triangle}_S = \mathbf{F}_S^{T-1}\,(\mathbf{E}_S)'_S\,\mathbf{F}_S^{-1}\,. \tag{3.72}$$

Similarly, the same procedure is applied to the difference of line elements between the intermediate and reference configuration yielding

$$\begin{aligned}(\mathrm{d}\widehat{s}^{\,2}_{Si} - \mathrm{d}S_S^2)'_S &= \mathrm{d}\mathbf{X}_S\cdot 2\,(\mathbf{E}_{Si})'_S\,\mathrm{d}\mathbf{X}_S = \mathrm{d}\widehat{\mathbf{x}}_{Si}\cdot 2\,\mathbf{F}_{Si}^{T-1}\,(\mathbf{E}_{Si})'_S\,\mathbf{F}_{Si}^{-1}\,\mathrm{d}\widehat{\mathbf{x}}_{Si}\\ &=: \mathrm{d}\widehat{\mathbf{x}}_{Si}\cdot 2\,(\widehat{\mathbf{\Gamma}}_{Si})^{\triangle}_{Si}\,\mathrm{d}\widehat{\mathbf{x}}_{Si}\,,\end{aligned} \tag{3.73}$$

where

$$(\,\cdot\,)^{\triangle}_{Si} = (\,\cdot\,)'_S + \widehat{\mathbf{L}}_{Si}^T\,(\,\cdot\,) + (\,\cdot\,)\,\widehat{\mathbf{L}}_{Si}\,. \tag{3.74}$$

denotes the upper inelastic *Oldroyd* derivative. Thus, in analogy to the above,

$$(\widehat{\mathbf{\Gamma}}_{Si})^{\triangle}_{Si} = \tfrac{1}{2}\,(\widehat{\mathbf{L}}_{Si}^T + \widehat{\mathbf{L}}_{Si}) = \widehat{\mathbf{D}}_{Si}\,. \tag{3.75}$$

Following this, the elastic strain rates of the intermediate configuration are obtained via

$$\begin{aligned}(\mathrm{d}s^2 - \mathrm{d}\widehat{s}^{\,2}_{Si})'_S &= \mathrm{d}\mathbf{x}\cdot 2\,(\mathbf{A}_{Se})^{\triangle}_S\,\mathrm{d}\mathbf{x} = \mathrm{d}\widehat{\mathbf{x}}_{Si}\cdot 2\,\mathbf{F}_{Se}^T\,(\mathbf{A}_{Se})^{\triangle}_S\,\mathbf{F}_{Se}\,\mathrm{d}\widehat{\mathbf{x}}_{Si}\\ &=: \mathrm{d}\widehat{\mathbf{x}}_{Si}\cdot 2\,(\widehat{\mathbf{\Gamma}}_{Se})^{\triangle}_{Si}\,\mathrm{d}\widehat{\mathbf{x}}_{Si}\,.\end{aligned} \tag{3.76}$$

[11] *James Gardner Oldroyd* (1921–1982): British Professor of Applied Mathematics and Theoretical Physics who published outstanding articles as a rheologists of the very first generation.

[12] *Marius Sophus Lie* (1842–1899): Norwegian mathematician who largely created the theory of continuous symmetry and applied it to the study of geometry and differential equations. Among all mathematicians he is known as the founder of the theory of transformation groups which then gave rise to the modern theory of the so-called *Lie* groups.

Proceeding from a representation of (3.69) on the intermediate configuration, the additive structure of the strain rates is revealed when comparing to (3.73) and (3.76), viz.:

$$(\mathrm{d}s^2 - \mathrm{d}S_S^2)'_S \;=\; \mathrm{d}\widehat{\mathbf{x}}_{Si} \cdot 2\,(\widehat{\boldsymbol{\Gamma}}_S)^{\triangle}_{Si}\,\mathrm{d}\widehat{\mathbf{x}}_{Si} = \mathrm{d}\widehat{\mathbf{x}}_{Si} \cdot 2\,\big[\,(\widehat{\boldsymbol{\Gamma}}_{Si})^{\triangle}_{Si} + (\widehat{\boldsymbol{\Gamma}}_{Se})^{\triangle}_{Si}\,\big]\,\mathrm{d}\widehat{\mathbf{x}}_{Si}\,. \tag{3.77}$$

All other strain rates may be obtained via contravariant transport mechanisms for second-order tensors which are summarised in box (B.2) of Appendix B.

Please note that these relations can also be obtained for the viscous pore fluid. However, during the constitutive modelling process in Section 4.5, it will turn out that the viscous effects are negligible compared to the fluid-solid momentum exchange resulting from the drag force of the percolating fluid. Thus, they are omitted in this monograph.

3.3 Stress Measures and Dual Variables

In general, the deformation of a body $\mathcal{B}$ is always connected with some kind of resistance. One way of measuring this resistance is achieved by introducing the stress, which has the physical dimension force per unit of area. Thus, this definition directly leads to the introduction of various stress measures, as the area elements may drastically change in the finite deformation range. In this regard, *Cauchy* introduced the stress tensor concept for single-phase materials which can directly be transferred to the framework of the TPM. Following this, the partial *Cauchy* stress tensors $\mathbf{T}^\alpha$ of the constituents can be introduced using *Cauchy*'s theorem, viz.:

$$\mathbf{t}^\alpha(\mathbf{x}, t, \mathbf{n}) = \mathbf{T}^\alpha(\mathbf{x}, t)\,\mathbf{n}\,. \tag{3.78}$$

Herein, all contact forces applied to a constituent φ^α at the boundary surface $\mathcal{S}$ are captured by the surface traction vector $\mathbf{t}^\alpha(\mathbf{x}, t, \mathbf{n})$, which depends on the outward-oriented unit surface normal vector $\mathbf{n}$ of the current configuration. Thus, incremental contact force elements can be introduced via integration of the traction vectors over the surface yielding

$$\mathrm{d}\mathbf{f}_c^\alpha = \mathbf{t}^\alpha\,\mathrm{d}a = \mathbf{T}^\alpha\,\mathbf{n}\,\mathrm{d}a = \mathbf{T}^\alpha\,\mathrm{d}\mathbf{a}\,. \tag{3.79}$$

In this context, the partial *Cauchy* stress $\mathbf{T}^\alpha$ is often referred to as the true stress, as it relates the actual force elements $\mathrm{d}\mathbf{f}_c^\alpha$ to the actual oriented area element $\mathrm{d}\mathbf{a}$. Other stress tensors can be introduced by relating the contact force element $\mathrm{d}\mathbf{f}_c^\alpha$ to the referential area elements $\mathrm{d}\mathbf{A}_\alpha$. Inserting the transport of area elements $(3.28)_2$ into (3.79) leads to

$$\mathrm{d}\mathbf{f}_c^\alpha = \mathbf{T}^\alpha\,\mathrm{d}\mathbf{a} = \mathbf{T}^\alpha\,\det\mathbf{F}_\alpha\,\mathbf{F}_\alpha^{T-1}\,\mathrm{d}\mathbf{A}_\alpha \qquad \text{with} \qquad \begin{cases} \boldsymbol{\tau}^\alpha = \mathbf{T}^\alpha\,\det\mathbf{F}_\alpha\,, \\ \mathbf{P}^\alpha = \mathbf{T}^\alpha\,\det\mathbf{F}_\alpha\,\mathbf{F}_\alpha^{T-1}, \end{cases} \tag{3.80}$$

where, $\boldsymbol{\tau}^\alpha$ is known as the *Kirchhoff*[13] stress or weighted *Cauchy* stress, while $\mathbf{P}^\alpha$ denotes the so-called 1st *Piola*[14]-*Kirchhoff* stress which represents the nominal or engineering

[13] *Gustav Robert Kirchhoff* (1824–1887): German physicist who contributed to the fundamental understanding of electrical circuits, spectroscopy, and the emission of black-body radiation by heated objects. Moreover, he defined the so-called *Kirchhoff* plate in applied mechanics as well as a stress tensor.

[14] *Gabrio Piola* (1794–1850): Italian physicist who had strong abilities as a mechanician and sophisticated skills as a mathematician. Unfortunately, his often uncompleted work can almost certainly be attributed to the lack of confrontation with the international scientific community of these years.

stress, as it relates the actual force element $\mathrm{d}\mathbf{f}_c^\alpha$ to referential (undeformed) area elements $\mathrm{d}\mathbf{A}_\alpha$. Hence, $\mathbf{P}^\alpha$ must have a two-field character which can also be deduced from the incomplete covariant pull-back of the *Kirchhoff* stress yielding an non-symmetric stress

$$\mathbf{P}^\alpha = \boldsymbol{\tau}^\alpha \, \mathbf{F}_\alpha^{T-1}. \tag{3.81}$$

Following this, the introduced stress tensors must be of covariant nature. This fact can also be concluded with the definition of covariant line elements $\mathrm{d}\mathbf{x}$ leading to contravariant oriented area elements $\mathrm{d}\mathbf{a}$ and, thus, to covariant stress measures, as the variance changes when $\mathrm{d}\mathbf{a}$ appears in the denominator. In order to symmetrise $\mathbf{P}^\alpha$, the rest of the pull-back operation in (3.81) has to be applied yielding

$$\mathbf{S}^\alpha = \mathbf{F}_\alpha^{-1} \, \boldsymbol{\tau}^\alpha \, \mathbf{F}_\alpha^{T-1} = \mathbf{F}_\alpha^{-1} \, \mathbf{P}^\alpha, \tag{3.82}$$

known as the 2nd *Piola-Kirchhoff* stress $\mathbf{S}^\alpha$ with its basis system in the reference configuration. Note that $\boldsymbol{\tau}^\alpha$ and $\mathbf{S}^\alpha$ have no direct physical interpretation. Instead, they naturally occur if the invariant stress power is computed on different configurations. In this regard, it is also convenient to define a solid stress measure on the intermediate configuration, which is achieved by an inelastic covariant push-forward of $\mathbf{S}^\alpha$ or an elastic covariant pull-back of $\boldsymbol{\tau}^\alpha$ yielding the solid intermediate stress

$$\widehat{\boldsymbol{\tau}}^S = \mathbf{F}_{Si} \, \mathbf{S}^S \, \mathbf{F}_{Si}^T = \mathbf{F}_{Se}^{-1} \, \boldsymbol{\tau}^S \, \mathbf{F}_{Se}^{T-1}. \tag{3.83}$$

Thus, the following covariant transport relations can be summarised for the solid stresses:

$$\mathbf{S}^S \;\underset{\mathbf{F}_{Si}^{-1}\,(\widehat{\cdot})\,\mathbf{F}_{Si}^{T-1}}{\overset{\mathbf{F}_{Si}\,(\cdot)\,\mathbf{F}_{Si}^{T}}{\rightleftarrows}}\; \widehat{\boldsymbol{\tau}}^S \;\underset{\mathbf{F}_{Se}^{-1}\,(\cdot)\,\mathbf{F}_{Se}^{T-1}}{\overset{\mathbf{F}_{Se}\,(\widehat{\cdot})\,\mathbf{F}_{Se}^{T}}{\rightleftarrows}}\; \boldsymbol{\tau}^S. \qquad \mathbf{F}_S\,(\cdot)\,\mathbf{F}_S^T \;\rightarrow\; \qquad \mathbf{F}_S^{-1}\,(\cdot)\,\mathbf{F}_S^{T-1} \;\leftarrow \tag{3.84}$$

Note that all introduced stresses are usually symmetric quantities, except for the 1st *Piola-Kirchhoff* stress which is non-symmetric due to its incomplete transport (3.81).

Finally, it can be observed that scalar products between stresses and strains of the same configuration are invariant with respect to transports to another configuration. The same holds for scalar products between stresses and strain rates, which can physically be interpreted as the rate of internal mechanical work, often referred to as the stress power. Hence, proceeding from quantities of the reference configuration, the following relations for the solid constituent are easily obtained utilising box (B.1) and equation (3.82), viz.:

$$\mathbf{S}^S \cdot \mathbf{E}_S = (\mathbf{F}_S^{-1} \, \mathbf{F}_S) \, \mathbf{S}^S \cdot \mathbf{E}_S \, (\mathbf{F}_S^{-1} \, \mathbf{F}_S) = (\mathbf{F}_S \, \mathbf{S}^S \, \mathbf{F}_S^T) \cdot (\mathbf{F}_S^{T-1} \mathbf{E}_S \mathbf{F}_S^{-1}) = \boldsymbol{\tau}^S \cdot \mathbf{A}_S \, . \tag{3.85}$$

Applying the same procedure to the other stress and strain measures leads to the conjugate pairs of all configurations:

$$\begin{aligned} \mathbf{S}^S \cdot \mathbf{E}_S \;&=\; \widehat{\boldsymbol{\tau}}^S \cdot \widehat{\boldsymbol{\Gamma}}_S \;=\; \boldsymbol{\tau}^S \cdot \mathbf{A}_S \, , \\ \mathbf{S}_S \cdot (\mathbf{E}_S)'_S \;&=\; \widehat{\boldsymbol{\tau}}^S \cdot (\widehat{\boldsymbol{\Gamma}}_S)^{\triangle}_{Si} \;=\; \boldsymbol{\tau}^S \cdot (\mathbf{A}_S)^{\triangle}_S \, . \end{aligned} \tag{3.86}$$

Moreover, if $\boldsymbol{\tau}^S$ is assumed to be symmetric, the following relation can also be obtained

$$\boldsymbol{\tau}^S \cdot (\mathbf{A}_S)^{\triangle}_S = \boldsymbol{\tau}^S \cdot \mathbf{D}_S = \boldsymbol{\tau}^S \cdot \mathbf{L}_S = (\mathbf{P}^S \, \mathbf{F}_S^T) \cdot [\, (\mathbf{F}_S)'_S \, \mathbf{F}_S^{-1} \,] = \mathbf{P}^S \cdot (\mathbf{F}_S)'_S \, . \tag{3.87}$$

3.4 Balance Relations for Porous Media

The purpose of the next section is to give a brief review of the balance relations used in the TPM. In analogy to the mechanics of single-phase materials, the balances are regarded as materially independent conservation laws which are based on physical observations and, therefore, have an axiomatic character. Following this, the mechanical (mass, momentum, moment of momentum) as well as the thermodynamical quantities (energy and entropy) of the deforming body $\mathcal{B}$ are balanced with external influences resulting from long- and close-range effects (i. e. contact and gravitational forces) and productions inside the body. In particular, the single-phase balances can be interpreted as follows:

Wording of the single-phase balance relations

mass	In a closed system, the mass of a body is constant.
momentum	The temporal change of the body momentum equals the sum of the forces acting on it at the vicinity and from a distance.
moment of momentum	The temporal change of the body moment of momentum equals the sum of moments of all forces acting on the body and taken with respect to the same arbitrary reference point.
energy	The sum of the temporal changes of the internal and kinetic energy of a body equals the sum of the external mechanical and non-mechanical power (1^{st} law of thermodynamics).
entropy	(1) The temporal change of entropy in a body equals the sum of the external change of entropy and the internal entropy production and (2) the entropy production is never negative (2^{nd} law of thermodynamics).

(3.88)

The basis for the formulation of the respective balances within the broad field of multiphase materials is given in *Truesdell*'s[15] metaphysical principles [206] which are given in Box (3.89). Following this, each constituent has to be described by individual motion functions and balance equations, provided that a possible interaction of the constituents is accounted for. However, as these interactions are strongly dependent on the involved (constituents) materials, the quantification of the respective production terms, e. g., for mass, momentum, etc., is part of the constitutive modelling process in Chapter 4. Moreover, the balances for the overall aggregate will then have the same structure as for single-phase

[15] *Clifford Ambrose Truesdell III* (1919–2000): American mathematician, natural philosopher, historian of mathematics, and polemicist, who unified the knowledge on continuum mechanics such that the collected basic principles are still valid at present. Among many fundamental books, there are two milestones: *The Classical Field Theories* [208] and *The Non-linear Field Theories of Mechanics* [207] which represent a basic reference for any specialist in continuum mechanics.

materials and are obtained by a summation of the balances of the involved constituents. Thus, the behaviour of the aggregate is a result of the behaviour of the constituents and the overall aggregate is described like a single-phase material, as the aggregate does not "know" that it may be composed of several constituents.

Truesdell's metaphysical principles

1. *All properties of the mixture must be mathematical consequences of properties of the constituents.*
2. *So as to describe the motion of a constituent, we may in imagination isolate it from the rest of the mixture, provided we allow properly for the actions of the other constituents upon it.*
3. *The motion of the mixture is governed by the same equations as is a single body.*

(3.89)

In this context, the well-known master balance principle from single-phase materials (see, e. g., Haupt [91]) can be applied for the constituents as well as the aggregate. The following two sections contain a brief representation taken from Ehlers [52], where the balances of the overall aggregate are discussed firstly, followed by the balances of the constituents. A more comprehensive description can be found in de Boer & Ehlers [25] or Diebels [38].

3.4.1 Aggregate Balance Relations

Proceeding from the results of classical continuum mechanics, the general balances for volume-specific scalar- and vector-valued mechanical quantities Ψ and $\mathbf{\Psi}$, respectively, of the overall aggregate body $\mathcal{B}$ can be postulated using the master balance principle, viz.:

$$\begin{aligned} \text{scalar-valued:} \quad & \frac{\mathrm{d}}{\mathrm{d}t}\int_{\mathcal{B}} \Psi \,\mathrm{d}v = \int_{\mathcal{S}} (\boldsymbol{\phi}\cdot\mathbf{n})\,\mathrm{d}a + \int_{\mathcal{B}} \sigma \,\mathrm{d}v + \int_{\mathcal{B}} \hat{\Psi}\,\mathrm{d}v\,, \\ \text{vector-valued:} \quad & \frac{\mathrm{d}}{\mathrm{d}t}\int_{\mathcal{B}} \mathbf{\Psi} \,\mathrm{d}v = \int_{\mathcal{S}} (\mathbf{\Phi}\,\mathbf{n})\,\mathrm{d}a + \int_{\mathcal{B}} \boldsymbol{\sigma} \,\mathrm{d}v + \int_{\mathcal{B}} \hat{\mathbf{\Psi}}\,\mathrm{d}v\,. \end{aligned} \tag{3.90}$$

Herein, the right-hand side includes the external influences on the respective mechanical quantity which has to be balanced in the overall aggregate φ. In particular, these are the effluxes $(\boldsymbol{\phi}\cdot\mathbf{n})$ and $(\mathbf{\Phi}\,\mathbf{n})$ of the respective mechanical quantity which directly enter the aggregate body $\mathcal{B}$ over its surface $\mathcal{S}$. The volume-specific supply terms of the external mechanical quantities σ and $\boldsymbol{\sigma}$ result from a distance, whereas the production terms $\hat{\Psi}$ and $\hat{\mathbf{\Psi}}$ allow for the possible couplings of $\mathcal{B}$ with its surrounding.

The integral form of the master balances (3.90) may be brought into a local representation, provided the integrands are steady and steadily differentiable. Applying a proper material time derivative to the left-hand side (i. e. including the time derivative for the actual volume element $\mathrm{d}v$) and rewriting the surface integral of the right-hand side by applying

the *Gaußian*[16] integral theorem leads to the corresponding local balance relations

$$\begin{aligned} \dot{\Psi} + \Psi \operatorname{div} \dot{\mathbf{x}} &= \operatorname{div} \Phi + \sigma + \hat{\Psi} \,, \\ \dot{\boldsymbol{\Psi}} + \boldsymbol{\Psi} \operatorname{div} \dot{\mathbf{x}} &= \operatorname{div} \boldsymbol{\Phi} + \boldsymbol{\sigma} + \hat{\boldsymbol{\Psi}} \,. \end{aligned} \tag{3.91}$$

The specific balance relations for the mass, the momentum, the moment of momentum (m. o. m.), the energy and the entropy can be taken from box (3.92), which essentially represents the capturing of the wordings in box (3.88) into formulae:

	$\Psi,\ \boldsymbol{\Psi}$	$\phi,\ \boldsymbol{\Phi}$	$\sigma,\ \boldsymbol{\sigma}$	$\hat{\Psi},\ \hat{\boldsymbol{\Psi}}$
mass	ρ	$\mathbf{0}$	0	0
momentum	$\rho\,\dot{\mathbf{x}}$	$\mathbf{T}$	$\rho\,\mathbf{b}$	$\mathbf{0}$
m. o. m.	$\mathbf{x} \times (\rho\,\dot{\mathbf{x}})$	$\mathbf{x} \times \mathbf{T}$	$\mathbf{x} \times (\rho\,\mathbf{b})$	$\mathbf{0}$
energy	$\rho\,\varepsilon + \frac{1}{2}\,\dot{\mathbf{x}} \cdot (\rho\,\dot{\mathbf{x}})$	$\mathbf{T}^T\,\dot{\mathbf{x}} - \mathbf{q}$	$\dot{\mathbf{x}} \cdot (\rho\,\mathbf{b}) + \rho\,r$	0
entropy	$\rho\,\eta$	$\boldsymbol{\phi}_\eta$	σ_η	$\hat{\eta} \geq 0$

(3.92)

Herein, $\rho\,\dot{\mathbf{x}}$ denotes the momentum of the entire aggregate, $\mathbf{T}$ is the overall *Cauchy* stress, and $\mathbf{b}$ represents the external mass-specific volume force, usually represented by the scalar gravitational constant g and an additional unit direction vector. The moment of momentum is computed using a lever arm, i. e., $\mathbf{x} \times \rho\,\dot{\mathbf{x}}$. Moreover, ε is the internal energy of the aggregate, while $\mathbf{q}$ denotes the heat influx vector and r the external heat supply. The entropy of the aggregate is denoted by η, while $\boldsymbol{\phi}_\eta$ and σ_η represent the efflux of entropy and the external entropy supply, respectively. It is important to know that the entropy production $\hat{\eta} \geq 0$ can never be negative in order to fulfil the second law of thermodynamics. Inserting the specific balance relations (3.92) into the local master balances (3.91) yields the well-known local forms of the balance equations for single-phase materials and entire aggregates φ in the sense of *Truesdell*'s third metaphysical principle $(3.89)_3$.

Mixture balance equations

$$\begin{aligned} \text{mass:} \quad & \dot{\rho} + \rho \operatorname{div} \dot{\mathbf{x}} = 0 \\ \text{momentum:} \quad & \rho\,\ddot{\mathbf{x}} = \operatorname{div} \mathbf{T} + \rho\,\mathbf{b} \\ \text{m. o. m.:} \quad & \mathbf{0} = \mathbf{I} \times \mathbf{T} \quad \longrightarrow \quad \mathbf{T} = \mathbf{T}^T \\ \text{energy:} \quad & \rho\,\dot{\varepsilon} = \mathbf{T} \cdot \mathbf{L} - \operatorname{div} \mathbf{q} + \rho\,r \\ \text{entropy:} \quad & \rho\,\dot{\eta} \geq \operatorname{div} \boldsymbol{\phi}_\eta + \sigma_\eta \end{aligned} \tag{3.93}$$

In order to obtain equations (3.93), one starts with the mass balance, as the "lowest" balance, before evaluating the "higher" balances like m. o. m., energy, etc., as it is possible to simplify the higher balances by inserting the respective lower balances. Note that due to the definition of the axial vector in Appendix A.1, the balance of moment of momentum directly yields the symmetry of the overall *Cauchy* stress $\mathbf{T}$.

[16] *Johann Carl Friedrich Gauss* (1777–1855): German mathematician and scientist who contributed significantly to many fields, including number theory, statistics, analysis, differential geometry, geodesy, electrostatics, astronomy, and optics. He had a remarkable influence in many fields of mathematics and science and is ranked as one of history's most influential mathematicians, even in today's practise.

3.4.2 Component Balance Relations

Following *Truesdell*'s second metaphysical principle, the general balance relations for the constituents φ^α can be postulated in accordance to (3.90) yielding

$$\begin{aligned} &\text{scalar-valued:} && \frac{\mathrm{d}_\alpha}{\mathrm{d}t}\int_{\mathcal{B}} \Psi^\alpha \,\mathrm{d}v \;=\; \int_{\mathcal{S}} (\boldsymbol{\phi}^\alpha \cdot \mathbf{n})\,\mathrm{d}a \;+\; \int_{\mathcal{B}} \sigma^\alpha \,\mathrm{d}v \;+\; \int_{\mathcal{B}} \hat{\Psi}^\alpha \,\mathrm{d}v\,, \\ &\text{vector-valued:} && \frac{\mathrm{d}_\alpha}{\mathrm{d}t}\int_{\mathcal{B}} \boldsymbol{\Psi}^\alpha \,\mathrm{d}v \;=\; \int_{\mathcal{S}} (\boldsymbol{\Phi}^\alpha\, \mathbf{n})\,\mathrm{d}a \;+\; \int_{\mathcal{B}} \boldsymbol{\sigma}^\alpha \,\mathrm{d}v \;+\; \int_{\mathcal{B}} \hat{\boldsymbol{\Psi}}^\alpha \,\mathrm{d}v\,. \end{aligned} \tag{3.94}$$

Herein, the partial quantities $(\,\cdot\,)^\alpha$ have the same physical meaning as the overall quantities $(\,\cdot\,)$ in (3.90). However, the production terms $(\,\hat{\cdot}\,)^\alpha$ now characterise the interaction of one constituent with another constituent instead of the possible couplings of $\mathcal{B}$ with its surrounding. Following this, the local balance relations for the constituents φ^α are achieved in an analogous manner yielding

$$\begin{aligned} (\Psi^\alpha)'_\alpha \,+\, \Psi^\alpha \operatorname{div} \overset{\prime}{\mathbf{x}}_\alpha &= \operatorname{div} \Phi^\alpha \,+\, \sigma^\alpha \,+\, \hat{\Psi}^\alpha, \\ (\boldsymbol{\Psi}^\alpha)'_\alpha \,+\, \boldsymbol{\Psi}^\alpha \operatorname{div} \overset{\prime}{\mathbf{x}}_\alpha &= \operatorname{div} \boldsymbol{\Phi}^\alpha \,+\, \boldsymbol{\sigma}^\alpha \,+\, \hat{\boldsymbol{\Psi}}^\alpha. \end{aligned} \tag{3.95}$$

Due to *Truesdell*'s first principle, the balances (3.95) must yield the balances (3.91) of the overall aggregate, when summarised over all participating constituents. In this context, summation constraints may be achieved with the aid of equations (3.11) to (3.13) yielding

$$\begin{aligned} \Psi &= \sum_\alpha \Psi^\alpha\,, \quad & \boldsymbol{\phi}\cdot\mathbf{n} &= \sum_\alpha (\,\boldsymbol{\phi}^\alpha - \Psi^\alpha\,\mathbf{d}_\alpha\,)\cdot\mathbf{n}\,, \quad & \sigma &= \sum_\alpha \sigma^\alpha\,, \quad & \hat{\Psi} &= \sum_\alpha \hat{\Psi}^\alpha, \\ \boldsymbol{\Psi} &= \sum_\alpha \boldsymbol{\Psi}^\alpha\,, \quad & \boldsymbol{\Phi}\,\mathbf{n} &= \sum_\alpha (\,\boldsymbol{\Phi}^\alpha - \boldsymbol{\Psi}^\alpha \otimes \mathbf{d}_\alpha\,)\,\mathbf{n}\,, \quad & \boldsymbol{\sigma} &= \sum_\alpha \boldsymbol{\sigma}^\alpha\,, \quad & \hat{\boldsymbol{\Psi}} &= \sum_\alpha \hat{\boldsymbol{\Psi}}^\alpha. \end{aligned} \tag{3.96}$$

The specific balance relations of the constituents φ^α can be derived in analogy to those of single-phase materials (3.92), provided one allows for proper interaction possibilities between the constituents by introducing additional interaction terms, viz.:

	$\Psi^\alpha,\ \boldsymbol{\Psi}^\alpha$	$\boldsymbol{\phi}^\alpha,\ \boldsymbol{\Phi}^\alpha$	$\sigma^\alpha,\ \boldsymbol{\sigma}^\alpha$	$\hat{\Psi}^\alpha,\ \hat{\boldsymbol{\Psi}}^\alpha$
mass	ρ^α	$\mathbf{0}$	0	$\hat{\rho}^\alpha$
momentum	$\rho^\alpha\, \overset{\prime}{\mathbf{x}}_\alpha$	$\mathbf{T}^\alpha$	$\rho^\alpha\, \mathbf{b}^\alpha$	$\hat{\mathbf{s}}^\alpha$
m. o. m.	$\mathbf{x}\times(\rho^\alpha\, \overset{\prime}{\mathbf{x}}_\alpha)$	$\mathbf{x}\times\mathbf{T}^\alpha$	$\mathbf{x}\times(\rho^\alpha\, \mathbf{b}^\alpha)$	$\hat{\mathbf{h}}^\alpha$
energy	$\rho^\alpha\,\varepsilon^\alpha + \frac{1}{2}\,\overset{\prime}{\mathbf{x}}_\alpha\cdot(\rho^\alpha\, \overset{\prime}{\mathbf{x}}_\alpha)$	$(\mathbf{T}^\alpha)^T\, \overset{\prime}{\mathbf{x}}_\alpha - \mathbf{q}^\alpha$	$\overset{\prime}{\mathbf{x}}_\alpha\cdot(\rho^\alpha\, \mathbf{b}^\alpha) + \rho^\alpha\, r^\alpha$	$\hat{e}^\alpha$
entropy	$\rho^\alpha\,\eta^\alpha$	$\boldsymbol{\phi}^\alpha_\eta$	σ^α_η	$\hat{\eta}^\alpha$

(3.97)

Following this, the quantities $(\,\hat{\cdot}\,)^\alpha$ listed in the right column of box (3.97) denote the respective total production terms. In particular, these include the total mass production $\hat{\rho}^\alpha$ accounting for possible mass exchanges or phase transitions between the constituents φ^α. The remaining terms describe the total momentum production $\hat{\mathbf{s}}^\alpha$, the total production of angular momentum $\hat{\mathbf{h}}^\alpha$, the total energy production $\hat{e}^\alpha$, and the total entropy production $\hat{\eta}^\alpha$ of the constituents φ^α. Comparing the specific balance relations of the aggregate

(3.92) with (3.97) as well as considering equations (3.96) allows for the identification of the following specific summation constraints for the total production terms:

$$\sum_\alpha \hat{\rho}^\alpha = 0\,, \qquad \sum_\alpha \hat{\mathbf{s}}^\alpha = \mathbf{0}\,, \qquad \sum_\alpha \hat{\mathbf{h}}^\alpha = \mathbf{0}\,, \qquad \sum_\alpha \hat{e}^\alpha = 0\,, \qquad \sum_\alpha \hat{\eta}^\alpha \geq 0\,. \tag{3.98}$$

Note that the second law of thermodynamics is included in $(3.98)_5$ which led to controversial discussions among researchers, when applied to multiphase materials. The question was, whether the second law should hold for the overall aggregate or for each constituent separately, which turned out to be too restrictive, cf. Ehlers [47] for a historical overview.

Inserting the specific balance relations (3.97) into the local master balances (3.95) and exploiting the respective lower balances when deriving the higher balances finally yields the local balance equations of the constituents φ^α, viz.:

Constituent balance equations

$$\begin{aligned}
&\text{mass:} && (\rho^\alpha)'_\alpha + \rho^\alpha \operatorname{div} \overset{\prime}{\mathbf{x}}_\alpha &&= \hat{\rho}^\alpha \\
&\text{momentum:} && \rho^\alpha \overset{\prime\prime}{\mathbf{x}}_\alpha &&= \operatorname{div} \mathbf{T}^\alpha + \rho^\alpha \mathbf{b}^\alpha + \hat{\mathbf{p}}^\alpha \\
&\text{m. o. m.:} && \mathbf{0} &&= \mathbf{I} \times \mathbf{T}^\alpha + \hat{\mathbf{m}}^\alpha \\
&\text{energy:} && \rho^\alpha (\varepsilon^\alpha)'_\alpha &&= \mathbf{T}^\alpha \cdot \mathbf{L}_\alpha - \operatorname{div} \mathbf{q}^\alpha + \rho^\alpha r^\alpha + \hat{\varepsilon}^\alpha \\
&\text{entropy:} && \rho^\alpha (\eta^\alpha)'_\alpha &&= \operatorname{div} \left(-\frac{1}{\Theta^\alpha}\, \mathbf{q}^\alpha\right) + \frac{1}{\Theta^\alpha}\, \rho^\alpha r^\alpha + \hat{\zeta}^\alpha
\end{aligned} \tag{3.99}$$

Herein, the newly introduced direct productions $\hat{\mathbf{p}}^\alpha$, $\hat{\mathbf{m}}^\alpha$, $\hat{\varepsilon}^\alpha$, and $\hat{\zeta}^\alpha$ correspond to the direct production of mass, momentum, moment of momentum, energy, and entropy, respectively, and are in direct relation with the respective total productions via

$$\begin{aligned}
\hat{\mathbf{s}}^\alpha &= \hat{\mathbf{p}}^\alpha + \hat{\rho}^\alpha \overset{\prime}{\mathbf{x}}_\alpha\,, & \hat{\mathbf{h}}^\alpha &= \hat{\mathbf{m}}^\alpha + \mathbf{x} \times \hat{\mathbf{s}}^\alpha\,, \\
\hat{e}^\alpha &= \hat{\varepsilon}^\alpha + \hat{\mathbf{p}}^\alpha \cdot \overset{\prime}{\mathbf{x}}_\alpha + \hat{\rho}^\alpha \left(\varepsilon^\alpha + \tfrac{1}{2}\, \overset{\prime}{\mathbf{x}}_\alpha \cdot \overset{\prime}{\mathbf{x}}_\alpha\right), & \hat{\eta}^\alpha &= \hat{\zeta}^\alpha + \hat{\rho}^\alpha \eta^\alpha.
\end{aligned} \tag{3.100}$$

Following this, the total productions of a higher physical quantity may include the direct productions of the lower physical quantities. In a solid-fluid aggregate for instance, the total momentum production $\hat{\mathbf{s}}^\alpha$ contains the direct momentum exchanges $\hat{\mathbf{p}}^\alpha$ resulting from the interaction force of the percolating fluid with the solid skeleton as well as indirect parts resulting from mass exchanges $\hat{\rho}^\alpha$.

Moreover, the usual *a priori* constitutive assumptions known from the thermodynamics of single-phase continua can be applied yielding

$$\boldsymbol{\phi}_\eta^\alpha = -\frac{1}{\Theta^\alpha}\, \mathbf{q}^\alpha \qquad \text{and} \qquad \sigma_\eta^\alpha = \frac{1}{\Theta^\alpha}\, \rho^\alpha r^\alpha \tag{3.101}$$

for the entropy efflux and the entropy supply of the constituents φ^α, respectively. Herein, $\Theta^\alpha > 0$ are the absolute *Kelvin* temperatures of the constituents φ^α, thereby allowing for an individual temperature field for each constituent.

Finally, summation relations between the specific quantities of the constituents φ^α and the corresponding overall quantities of the aggregate φ can be obtained through a quantification of (3.96). In accordance to de Boer & Ehlers [25] these relations read:

$$\begin{aligned}
\rho\,\mathbf{b} &= \sum_\alpha \rho^\alpha\,\mathbf{b}^\alpha, & \rho\,\ddot{\mathbf{x}} &= \sum_\alpha \left[\,\rho^\alpha\,\overset{\prime\prime}{\mathbf{x}}_\alpha - \operatorname{div}\left(\rho^\alpha\,\mathbf{d}_\alpha\otimes\mathbf{d}_\alpha\right) + \hat{\rho}^\alpha\,\overset{\prime}{\mathbf{x}}_\alpha\,\right],\\
\mathbf{T} &= \sum_\alpha \left(\mathbf{T}^\alpha - \rho^\alpha\,\mathbf{d}_\alpha\otimes\mathbf{d}_\alpha\right), & \mathbf{q} &= \sum_\alpha \left[\,\mathbf{q}^\alpha - (\mathbf{T}^\alpha)^T\mathbf{d}_\alpha + \rho^\alpha\,\varepsilon^\alpha\mathbf{d}_\alpha + \tfrac{1}{2}\left(\mathbf{d}_\alpha{}'\cdot\,\mathbf{d}_\alpha\right)\mathbf{d}_\alpha\,\right],\\
\rho\,r &= \sum_\alpha \rho^\alpha\left(r^\alpha + \mathbf{b}^\alpha\cdot\,\mathbf{d}_\alpha\right), & \rho\,\varepsilon &= \sum_\alpha \rho^\alpha\left(\varepsilon^\alpha + \tfrac{1}{2}\,\mathbf{d}_\alpha{}'\cdot\,\mathbf{d}_\alpha\right),
\end{aligned} \tag{3.102}$$

3.4.3 Entropy Principle

The entropy principle is a direct consequence from the entropy balance together with the restriction of the second law of thermodynamics, which has to be fulfilled in any thermodynamically consistent process. Following this, the entropy balance is used as a restricting equation which aids the formulation of admissible constitutive relations describing the specific material behaviour. Restricting the sum $(3.98)_5$ of the total entropy productions $(3.100)_4$ of the constituents to non-negative values as well as utilising the local form of the constituent entropy balances $(3.99)_5$ yields the entropy principle for the overall aggregate, viz.:

$$\hat{\eta} = \sum_\alpha \hat{\eta}^\alpha = \sum_\alpha \left[\,\rho^\alpha\,(\eta^\alpha)'_\alpha + \hat{\rho}^\alpha\,\eta^\alpha + \operatorname{div}\left(\frac{1}{\Theta^\alpha}\,\mathbf{q}^\alpha\right) - \frac{1}{\Theta^\alpha}\,\rho^\alpha\,r^\alpha\,\right] \geq 0\,. \tag{3.103}$$

Since this form does not directly contain the constitutive quantities used in this monograph, it is not suitable for the postulation of restrictions. Thus, the partial energy balances $(3.99)_4$ as well as the total energy productions $(3.100)_3$ are inserted under utilisation of the formal introduction of the *Helmholtz*[17] free-energy density

$$\psi^\alpha := \varepsilon^\alpha - \Theta^\alpha\,\eta^\alpha \tag{3.104}$$

yielding the so-called *Clausius*[18]*-Duhem*[19] inequality

$$\begin{aligned}
\sum_\alpha \frac{1}{\Theta^\alpha}\Big\{\;&\mathbf{T}^\alpha\cdot\,\mathbf{L}_\alpha - \rho^\alpha\left[\,(\psi^\alpha)'_\alpha + (\Theta^\alpha)'_\alpha\,\eta^\alpha\,\right] - \hat{\mathbf{p}}^\alpha\cdot\,\overset{\prime}{\mathbf{x}}_\alpha -\\
&-\hat{\rho}^\alpha\left(\psi^\alpha + \tfrac{1}{2}\,\overset{\prime}{\mathbf{x}}_\alpha\cdot\,\overset{\prime}{\mathbf{x}}_\alpha\right) - \frac{1}{\Theta^\alpha}\,\mathbf{q}^\alpha\cdot\operatorname{grad}\Theta^\alpha + \hat{e}^\alpha\,\Big\} \geq 0\,.
\end{aligned} \tag{3.105}$$

[17] *Hermann Ludwig Ferdinand von Helmholtz* (1821–1894): German physician and physicist known for his theories on the conservation of energy as well as on general electrodynamics and thermodynamics.

[18] *Rudolf Julius Emanuel Clausius* (1822–1888): German physicist and mathematician who is considered to be one of the central founders of thermodynamics. In 1850 he stated the basic idea of the second law of thermodynamics and introduced the concept of entropy in 1865.

[19] *Pierre Maurice Marie Duhem* (1861–1916): French physicist, mathematician and philosopher of science, best known for his writings on natural science in the Middle Ages.

Note that the *Legendre*[20] transformation (3.104) in the energetically conjugate variables temperature Θ^α and entropy η^α transforms the internal energy ε^α, which depends on the deformation and the unmeasurable entropy, to the *Helmholtz* free energy ψ^α depending on the deformation and the physically measurable temperature.

The *Clausius-Planck*[21] inequality is obtained, when isothermal processes are prescribed (i. e. all constituents have the same constant temperature $\Theta^\alpha = \Theta = \text{const.}$), or when the overall dissipation inequality (3.105) is additively split into an internal and a thermal part. In the latter case, each part is demanded to be greater or equal to zero separately. Following this, the exploitation of the vanishing total energy production $(3.98)_4$ finally yields the internal dissipation inequality in the form of *Clausius-Planck*

$$\sum_\alpha \left[\mathbf{T}^\alpha \cdot \mathbf{L}_\alpha - \rho^\alpha \left(\psi^\alpha\right)'_\alpha - \hat{\mathbf{p}}^\alpha \cdot \overset{'}{\mathbf{x}}_\alpha - \hat{\rho}^\alpha \left(\psi^\alpha + \frac{1}{2}\, \overset{'}{\mathbf{x}}_\alpha \cdot \overset{'}{\mathbf{x}}_\alpha\right) \right] \geq 0 \,, \tag{3.106}$$

which will remarkably influence the constitutive modelling process in Chapter 4. In other words, if all constitutive assumptions fulfil the inequalities (3.105) and (3.106), the model, i. e., the overall set of equations, is said to be thermodynamically consistent.

[20] *Adrien-Marie Legendre* (1752–1833): French mathematician who did impressive work on elliptic functions including the classification of elliptic integrals as well as in number theory and abstract algebra.

[21] *Max Karl Ernst Ludwig Planck* (1858–1947): One of the most important German physicists who won the Nobel Prize in Physics in 1918 and is considered to be the founder of the quantum theory.

4 Constitutive Modelling

Together with the presented continuum-mechanical fundamentals of the preceding Chapter, the development of several distinct sets of governing equations is possible, thereby representing a manifold of multiphasic models. However, for the purpose of this monograph, the focus lies in the description of the charged hydrated anisotropic inhomogeneous IVD tissue as it is described in Section 2.3. In this regard, the materially independent balance equations and the missing constitutive equations for the involved constituents need to be adjusted to describe the physical response of the soft biological tissue.

4.1 Extended Biphasic TPM Model

The purpose of this Section is to derive the set of balance equations for an extended incompressible biphasic model with the aid of simplifying assumptions as well as the general balance relations given in the preceding Section 3.4. Moreover, the entropy principle will be evaluated leading to concrete restrictions for the postulation of constitutive equations discussed in the Sections thereafter.

4.1.1 Preliminary Assumptions and Resulting Balance Relations

As a first step, the general forms of the local constituent balance relations (3.99) are adapted to the special case of soft biological tissues, where an intrinsically anisotropic dissipative charged ECM is coupled with a viscous pore fluid. The involved ions lead to a coupling between the mechanical and the electro-chemical properties, thereby characterising the tissue as a swelling-active material. However, with the focus on the application to the inhomogeneous IVD, the model under consideration needs to be complex enough to represent the relevant material properties, while simultaneously being simple enough, to allow for a computability of real life spine experiments on today's hardware.

The starting point is the *a priori* assumption made in Section 3.1, where the number of unknown motion functions for the involved charged solid as well as the fluid components $(L, +, -)$ has been reduced to a minimum. Herein, use was made of Lanir's assumption [116] stating that without extreme concentration jumps of the surrounding fluid, the tissue is always in electro-chemical equilibrium. Thus, the free movable ions do not have to be considered separately, but are assumed to be always immediately in a position, where they are needed to fulfil the electro-neutrality condition. The remaining kinematical quantities outline the extended binary model having volume-free fixed negative charges attached to the saturated solid skeleton. In this regard, the fixed charges are kinematically bound to the solid movement, but with regard to the surrounding fluid components, they contribute to an internal ion concentration and thus, almost behave like dissolved ions.

Regarding the aggregate of solid and the fluid constituents, further simplifications are possible when the following assumptions are applied:

- materially incompressible constituents (under physiol. pressure [12]) $\rho^{\alpha R} = \text{const.}$,
- no mass exchange between the constituents (i. e. no growth) $\hat{\rho}^{\alpha} \equiv 0$,
- fully saturated conditions for the aggregate $n^S + n^F = 1$,
- quasi-static conditions (slow deformations) $\overset{\prime\prime}{\mathbf{x}}_{\alpha} \equiv \mathbf{0}$, $\ddot{\mathbf{x}} \equiv \mathbf{0}$,
- uniform bodyforce for all constituents (i. e. gravitation $\mathbf{g}$) $\mathbf{b}^{\alpha} = \mathbf{g}$,
- non-polar constituents (i. e. vanishing m. o. m. productions) $\hat{\mathbf{m}}^{\alpha} \equiv \mathbf{0}$,
- uniform temperature for all constituents (isothermal conditions) $\Theta^{\alpha} \equiv \Theta = \text{const.}$.

Following the first two assumptions while exploiting the definition of the partial density (3.6) leads to the degeneration of the local mass balances $(3.99)_1$ to local volume balances. The volume balance for the overall aggregate is then obtained by the usual procedure of a summation over its solid and fluid constituents yielding

$$\left.\begin{aligned} (n^S)'_S \; + \; n^S \operatorname{div} \overset{\prime}{\mathbf{x}}_S \; &= 0\,, \\ (n^F)'_F \; + \; n^F \operatorname{div} \overset{\prime}{\mathbf{x}}_F \; &= 0 \end{aligned}\right\} \quad \longrightarrow \quad \operatorname{div}\left[\,(\mathbf{u}_S)'_S + n^F\,\mathbf{w}_F\,\right] = 0\,. \tag{4.1}$$

In order to obtain this result, use was made of the material time derivative (3.13) of an arbitrary scalar quantity Ψ and the definition of the seepage velocity $\mathbf{w}_F$ $(3.16)_2$ yielding

$$\left.\begin{aligned} \overset{\prime}{\Psi}_F &= \frac{\partial \Psi}{\partial t} + \operatorname{grad}\Psi \cdot \overset{\prime}{\mathbf{x}}_F\,, \\ \overset{\prime}{\Psi}_S &= \frac{\partial \Psi}{\partial t} + \operatorname{grad}\Psi \cdot \overset{\prime}{\mathbf{x}}_S \end{aligned}\right\} \quad \longrightarrow \quad \overset{\prime}{\Psi}_F = \overset{\prime}{\Psi}_S + \operatorname{grad}\Psi \cdot \underbrace{(\overset{\prime}{\mathbf{x}}_F - \overset{\prime}{\mathbf{x}}_S)}_{\mathbf{w}_F}\,, \tag{4.2}$$

as well as the exploitation of the saturation constraint (3.4) leading to

$$n^S + n^F = 1 \quad \longrightarrow \quad (n^S + n^F)'_S = 0\,. \tag{4.3}$$

Note in passing that $(4.1)_3$ denotes the continuity equation for the binary aggregate resulting from the incompressibility constraint of its constituents. Moreover, the solid volume balance can be analytically integrated from an initial solidity n^S_{0S} yielding

$$(n^S)'_S = -n^S \operatorname{div} \overset{\prime}{\mathbf{x}}_S \quad \longrightarrow \quad n^S = n^S_{0S} \det \mathbf{F}_S^{-1}. \tag{4.4}$$

Thus, the saturation constraint reveals that the porosity n^F is also a function of the solid deformation gradient $\mathbf{F}_S$. After combining relation (3.6) with the analytically integrated volume balance $(4.4)_2$, the dependence of the partial solid density on the deformation gradient $\mathbf{F}_S$ can be expressed by

$$\rho^S = n^S \rho^{SR} \quad \longleftrightarrow \quad \rho^S = \rho^S_{0S} \det \mathbf{F}_S^{-1}, \tag{4.5}$$

where $\rho^S_{0S} = n^S_{0S}\,\rho^{SR}$ is the partial solid density in the initial state at $t = 0\,\text{s}$.

Moreover, in order to include the electro-chemical effects while the tissue is deforming, it is necessary to derive an equation describing the extensive change of the number of fixed negative charges via an intensive concentration measure. As the fixed charges almost behave like dissolved ions when they are surrounded by a pore fluid, the molar concentration

c_m^{fc} of the fixed charges is introduced relating the molar number of charges to the surrounding fluid volume, cf. Subsection 2.4.1. In this regard, there is no distinction between the intra- and extrafibrillar fluid compartments as is described in Subsection 2.3.1. Thus, the fixed charges φ^{fc} are related to the total local fluid volume knowing well that this may lead to an overestimate in the AF, where most of the intrafibrillar water is located in the structural collagen, cf., e. g., Schröder *et al.* [180].

Following this, two different densities can be introduced for the fixed charges, i. e., ρ_F^{fc} relating to the fluid volume and ρ^{fc} relating to the overall volume of the aggregate. Making use of the constant molar mass of a single fixed negative charge, i. e., the molar mass of an electron $M_m^{fc} \approx 5.486 \cdot 10^{-7}\,\mathrm{kg/mol}$ [140], yields

$$\rho^{fc} =: n^F \rho_F^{fc} = n^F c_m^{fc} M_m^{fc}\,. \tag{4.6}$$

Bearing in mind that the fixed charges are attached to the solid skeleton and thus, undergo the same movement, the partial mass balance of the fixed charge density ρ^{fc} with a vanishing charge production $\hat{\rho}^{fc}$ is applied with respect to the deforming solid yielding

$$(\rho^{fc})'_S + \rho^{fc} \operatorname{div} \overset{\prime}{\mathbf{x}}_S = 0\,, \tag{4.7}$$

while insertion of (4.6) and division by the constant molar mass M_m^{fc} yields

$$(n^F c_m^{fc})'_S + n^F c_m^{fc} \operatorname{div} \overset{\prime}{\mathbf{x}}_S = 0\,. \tag{4.8}$$

In analogy to the partial solid volume balance (4.4), the concentration balance (4.8) can be analytically integrated from an initial molar concentration c_{0S}^{fc} yielding

$$c_m^{fc} = c_{0S}^{fc}\, n_{0S}^F\, (\det \mathbf{F}_S - n_{0S}^S)^{-1}. \tag{4.9}$$

The obtained relation can be understood as an evolution equation for the concentration of the fixed charges, needed for the computation of the osmotic pressure contribution (2.7).

Following the adaption process, the next higher balance of momentum is regarded. In this context, the assumption of vanishing mass productions leads to a simplification of the overall momentum production constraint $(3.98)_2$, viz.:

$$\sum_\alpha \hat{\mathbf{s}}^\alpha = \hat{\mathbf{p}}^\alpha + \hat{\rho}^\alpha \overset{\prime}{\mathbf{x}}_\alpha = \mathbf{0} \qquad \longrightarrow \qquad \sum_\alpha \hat{\mathbf{p}}^\alpha = \mathbf{0} \qquad \longrightarrow \qquad \hat{\mathbf{p}}^S = -\hat{\mathbf{p}}^F, \tag{4.10}$$

where the direct momentum production $\hat{\mathbf{p}}^S$ of the solid is inversely proportional to the direct production $\hat{\mathbf{p}}^F$ of the fluid. As a next step, the partial momentum balances can be given under the assumptions of quasi-static conditions and uniform body forces $\mathbf{g}$:

$$\operatorname{div} \mathbf{T}^S + \rho^S \mathbf{g} + \hat{\mathbf{p}}^S = \mathbf{0} \qquad \text{and} \qquad \operatorname{div} \mathbf{T}^F + \rho^F \mathbf{g} + \hat{\mathbf{p}}^F = \mathbf{0}\,. \tag{4.11}$$

The momentum balance of the overall aggregate is obtained by the summation over its constituents and exploitation of the partial density (3.6) as well as relation $(4.10)_2$ yielding

$$\operatorname{div} (\mathbf{T}^S + \mathbf{T}^F) + (n^S \rho^{SR} + n^F \rho^{FR})\, \mathbf{g} = \mathbf{0}\,, \qquad \text{where} \qquad \mathbf{T} = \mathbf{T}^S + \mathbf{T}^F \tag{4.12}$$

denotes the overall stress of the model. At first sight, this is in contradiction to equation $(3.102)_3$ stating that the overall *Cauchy* stress $\mathbf{T}$ contains diffusive contributions, i. e.,

$$\mathbf{T} = \sum_{\alpha} \left(\mathbf{T}^{\alpha} - \rho^{\alpha}\, \mathbf{d}_{\alpha} \otimes \mathbf{d}_{\alpha} \right). \tag{4.13}$$

However, recalling equation $(3.102)_2$ and inserting the assumptions of vanishing mass productions as well as quasi-static conditions reveals that the diffusive contributions naturally vanish, when used in the context of the divergence form in $(4.12)_1$, viz.:

$$\rho\, \ddot{\mathbf{x}} = \sum_{\alpha} \left[\rho^{\alpha}\, \overset{\prime\prime}{\mathbf{x}}_{\alpha} - \operatorname{div}\left(\rho^{\alpha}\, \mathbf{d}_{\alpha} \otimes \mathbf{d}_{\alpha}\right) + \hat{\rho}^{\alpha}\, \overset{\prime}{\mathbf{x}}_{\alpha} \right] = \mathbf{0} \quad \longrightarrow \quad \operatorname{div}\Big(\sum_{\alpha} \rho^{\alpha} \mathbf{d}_{\alpha} \otimes \mathbf{d}_{\alpha}\Big) = \mathbf{0}\,. \tag{4.14}$$

Concerning the balance of angular momentum, the assumption of microscopically non-polar constituents directly leads to the conclusion of symmetric partial *Cauchy* stresses on the macroscale, cf. Hassanizadeh & Gray [89] or Ehlers [52]. In order to accomplish this symmetry, the direct angular momentum productions $\hat{\mathbf{m}}^{\alpha}$ in $(3.99)_3$ need to vanish

$$\mathbf{T}^{\alpha} = \left(\mathbf{T}^{\alpha}\right)^{T} \qquad \longrightarrow \qquad \hat{\mathbf{m}}^{\alpha} = \mathbf{0} \tag{4.15}$$

leading to so-called *Boltzmann*[1] continua, with the corresponding kinematics introduced in Section 3.2.1. Note in passing, that the extension to micro-polar materials (*Cosserat*[2] continua) is usually only practical for the class of granular materials, where the microscopic grains actually possess rotational degrees of freedom. For an overview of extended continua in the context of the TPM, the reader is referred to, e. g., Diebels [38], Diebels & Ehlers [39] or Ehlers [52].

Next, the partial energy balances $(3.99)_4$ can be excluded due to the assumption of isothermal conditions. Thus, they are only implicitly used in order to reformulate the entropy inequality (3.103). Together with the symmetric partial stress tensors, the vanishing mass productions, the inversely proportional direct momentum productions $(4.10)_3$, and the definition of the seepage velocity $(3.16)_2$, the *Clausius-Planck* inequality of the overall aggregate takes the form:

$$\mathbf{T}^{S} \cdot \mathbf{D}_{S} - \rho^{S} \left(\psi^{S}\right)'_{S} + \mathbf{T}^{F} \cdot \mathbf{D}_{F} - \rho^{F} \left(\psi^{F}\right)'_{F} - \hat{\mathbf{p}}^{F} \cdot \mathbf{w}_{F} \geq 0\,. \tag{4.16}$$

Finally, in order to guarantee fully saturated conditions in the overall aggregate at any time during arbitrary processes, the saturation constraint (4.3) is added to the entropy inequality. Proceeding from general thermodynamical considerations described in Ehlers [49] or Svendson & Hutter [200], a *Lagrange*an multiplier $\mathcal{P}$ is introduced in the sense of an incompressibility constraint

$$\mathcal{P}\left(n^{S} + n^{F}\right)'_{S} = -\mathcal{P}\left(n^{S} \operatorname{div} \overset{\prime}{\mathbf{x}}_{S} + n^{F} \operatorname{div} \overset{\prime}{\mathbf{x}}_{F} + \operatorname{grad} n^{F} \cdot \mathbf{w}_{F}\right) = 0\,, \tag{4.17}$$

[1] *Ludwig Boltzmann* (1844–1906): Austrian physicist and philosopher who is famous for his founding contributions in the fields of statistical mechanics and statistical thermodynamics. His fundamental logarithmic connection $S = k \log W$ between entropy and probability ornaments his tombstone.

[2] *Eugène Maurice Pierre Cosserat* (1866–1931), *François Cosserat* (1852–1914): French mathematicians who are considered as the founders of what is known today as kinematically extended continuum theory.

where the expression in parenthesis is equivalent to the aggregate volume balance $(4.1)_3$. The addition to the *Clausius-Planck* inequality $(4.16)_3$ yields

$$\overbrace{(\mathbf{T}^S + n^S\,\mathcal{P}\,\mathbf{I})}^{\mathbf{T}_E^S}\cdot\mathbf{D}_S - \rho^S\,(\psi^S)'_S + \overbrace{(\mathbf{T}^F + n^F\,\mathcal{P}\,\mathbf{I})}^{\mathbf{T}_E^F}\cdot\mathbf{D}_F - \rho^F\,(\psi^F)'_F - \\ - \underbrace{(\hat{\mathbf{p}}^F - \mathcal{P}\,\operatorname{grad} n^F)}_{\hat{\mathbf{p}}_E^F}\cdot\mathbf{w}_F \geq 0\,. \tag{4.18}$$

Herein, use was made of the relation $\operatorname{div}\overset{\prime}{\mathbf{x}}_\alpha = \mathbf{L}_\alpha\cdot\mathbf{I} = \mathbf{D}_\alpha\cdot\mathbf{I}$. Following this, the partial quantities $\mathbf{T}^\alpha$ and $\hat{\mathbf{p}}^F$ can be split into an undetermined part resulting from $\mathcal{P}$ and a so-called extra term $(\,\cdot\,)_E$ to be determined via appropriate constitutive equations, viz.:

$$\mathbf{T}^S = -n^S\mathcal{P}\,\mathbf{I} + \mathbf{T}_E^S\,, \qquad \mathbf{T}^F = -n^F\mathcal{P}\,\mathbf{I} + \mathbf{T}_E^F\,, \qquad \text{and} \qquad \hat{\mathbf{p}}^F = \mathcal{P}\operatorname{grad} n^F + \hat{\mathbf{p}}_E^F\,. \tag{4.19}$$

The overall *Cauchy* stress of the model is simply obtained by a summation of the partial stresses $(4.12)_2$ under utilisation of the saturation condition (3.4) such that

$$\mathbf{T} = -\mathcal{P}\,\mathbf{I} + \mathbf{T}_E \qquad \text{with} \qquad \mathbf{T}_E = \mathbf{T}_E^S + \mathbf{T}_E^F\,, \tag{4.20}$$

where according to Bishop [19] or Skempton [189], $\mathbf{T}_E$ is known as the effective or extra stress. Hence, $\mathcal{P}$ is easily identified as the unspecified hydraulic pore pressure, whereas the extra stress is purely governed by an electro-chemical contribution, the deformation state as well as the fluid viscosity and velocity.

4.2 Basic Thermodynamical Principles

Having adapted the materially independent balance equations for the special case of charged hydrated IVD tissue under quasi static conditions, further constitutive assumptions have to be derived; not only to close the resulting set of governing equations but also to further characterise the material behaviour. This is of particular need, as a sample taken from the isotropic NP will react different to mechanical loading compared to a fibre-reinforced sample of the AF. Thus, the constitutive equations to be derived in the proceeding sections must characterise the physical behaviour of the involved constituents as well as their interaction.

In this regard, care must be taken that none of the constitutive relations violates any of the basic thermodynamical principles of constitutive modelling, which basically trace back to the works of Truesdell [205], Noll [152, 153] and Coleman & Noll [35]. In particular, these are the principles of determinism, equipresence, and local action as well as material frame indifference, universal dissipation, and material symmetry. These can be found in a comprehensive summary with application to the constitutive modelling process in the work of Wang & Truesdell [223]. Note in passing that the satisfaction of these principles is an important premise in order to claim for thermodynamical consistency of the proposed model. For the purpose of this monograph, these principles will be briefly revised and applied in the proceeding sections.

4.2.1 Determinism, Equipresence and Local Action

Following the principle of determinism, the set of undetermined response functions

$$\mathcal{R} = \{\psi^S,\ \psi^F,\ \mathbf{T}^S_E,\ \mathbf{T}^F_E,\ \hat{\mathbf{p}}^F_E\} \tag{4.21}$$

must be uniquely defined at any time t. Due to the principle of equipresence, the response functions $\mathcal{R}(\mathcal{V})$ may depend on the whole set of process variables $\mathcal{V}$, which uniquely characterise the current state of the overall aggregate body as well as its history with respect to temperature, chemical charges, deformation and structural composition. Together with the principle of local action, the process variables may consist of local values only.

As isothermal conditions are prescribed and the chemical state is already defined by the molar concentration of the fixed negative charges (4.9) via the solid deformation gradient, the set $\mathcal{V}$ reduces to quantities characterising the aggregate body and its motion. Following the argumentation of Ehlers [47, 52] for an inhomogeneous incompressible binary aggregate with vanishing mass productions, the set of process variables is given by

$$\mathcal{V} = \{\mathbf{F}_S\,,\ \mathrm{Grad}_S\,\mathbf{F}_S\,,\ \boldsymbol{\mathcal{M}}^S\,,\ \mathbf{X}_S\,,\ \mathbf{w}_F\,,\ \mathbf{D}_F\}\,. \tag{4.22}$$

Herein, the set given in Ehlers [47, 52] has been extended by a structural tensor $\boldsymbol{\mathcal{M}}^S$ which is needed to characterise the inherent anisotropic solid skeleton resulting from the collagen fibre reinforcement. In this regard, the concept of structural tensors was first introduced by Boehler [21] and will play a major role in Subsection 4.2.4, where the characterisation of the type of anisotropy is discussed. Note in passing that the constant referential solid coordinates $\mathbf{X}_S$ are included in order to describe the inhomogeneous solid skeleton.

Moreover, Ehlers [47] introduces the principle of phase separation, where the *Helmholtz* energies ψ^α of the constituents φ^α may only depend on the non-dissipative process variables of the respective constituent itself, i. e., variables describing velocities are excluded. Next, a statement of Bowen [27] is included which addresses the *a priori* choice of process variables $\mathcal{V}$ for the energies ψ^α. Herein, the second deformation gradient $\mathrm{Grad}_S\,\mathbf{F}_S$ is ruled out from the set given in (4.22), as the second-grade character applies only to the production terms in (4.21). For more information on the treatment of second-grade materials, the reader is referred to Ehlers [47, 49]. Moreover, as there is no independent deformation variable for an incompressible pore fluid, the respective set of process variables is empty. Thus, the following dependencies for the energy potentials ψ^α can be concluded:

$$\psi^S = \psi^S[\,\mathbf{F}_S,\,(\mathbf{F}_{Se})_n,\,\boldsymbol{\mathcal{M}}^S\,,\mathbf{X}_S] \qquad \text{and} \qquad \psi^F = \psi^F(\,-\,)\,. \tag{4.23}$$

Keeping in mind the underlying rheological *Maxwell* model, the multiplicative split (3.18) of the solid deformation gradient $\mathbf{F}_S$ is additionally included to the set of solid process variables in (4.23). However, in view of the fact that potential energy can only be stored in the *Hooke* elements of the *Maxwell* branches, only the elastic parts $(\mathbf{F}_{Se})_n$ are incorporated in (4.23). Following this reveals the need for evolution equations for the inelastic deformation variables $(\mathbf{F}_{Si})_n$ as they have no external character and thus, have to be determined internally out of the process. The physical interpretation of this result is straightforward. The energy stored in the elastic Maxwell springs can either be changed through a prescribed total deformation, i. e., via $\mathbf{F}_S$, or while the intermediate configuration is moved by $(\mathbf{F}_{Si})_n$ in order to obtain equilibrium in a Maxwell branch.

4.2.2 Material Frame Indifference

The next principle to be obeyed is the principle of material frame indifference, also known as material objectivity. Following this, the physical meaning is simply that the material properties of the aggregate body, i. e., its constitutive equations (4.21), should not depend on the position of the observer, no matter how he moves. Thus, the mathematical interpretation of such an objectivity condition states that constitutive equations have to be invariant under rigid body rotations $\mathbf{Q}$ of the actual configuration, cf. Noll [152, 153]. Following this, the scalar-valued *Helmholtz* energy of the solid skeleton is subjected to

$$\overset{*}{\psi}{}^{S}[\,\mathbf{F}_S\,,\,(\mathbf{F}_{Se})_n\,,\,\boldsymbol{\mathcal{M}}^S,\,\mathbf{X}_S] = \psi^S[\,\overset{*}{\mathbf{F}}_S\,,\,(\overset{*}{\mathbf{F}}_{Se})_n\,,\,\overset{*}{\boldsymbol{\mathcal{M}}}{}^S,\,\overset{*}{\mathbf{X}}_S] \quad \forall \left\{ \begin{array}{l} \mathbf{Q} \in \mathcal{SO}_3\,,\,\mathbf{F}_S\,, \\ (\mathbf{F}_{Se})_n\,,\,\boldsymbol{\mathcal{M}}^S,\,\mathbf{X}_S\,, \end{array} \right. \tag{4.24}$$

where $(\overset{*}{\cdot})$ indicates the quantities of the rotated actual configuration. Proceeding from the idea of rotated line elements $\overset{*}{\mathbf{x}} = \mathbf{Q}\,\mathbf{x}$ of the actual configuration, the following relations hold for the rotated solid deformation gradients:

$$\left.\begin{aligned} \overset{*}{\mathbf{F}}_S &= \frac{\partial \overset{*}{\mathbf{x}}}{\partial \mathbf{X}_S} = \frac{\partial \overset{*}{\mathbf{x}}}{\partial \mathbf{x}}\frac{\partial \mathbf{x}}{\partial \mathbf{X}_S} = \mathbf{Q}\,\mathbf{F}_S\,, \\ (\overset{*}{\mathbf{F}}_{Se})_n &= \frac{\partial \overset{*}{\mathbf{x}}}{\partial (\widehat{\mathbf{x}}_{Si})_n} = \frac{\partial \overset{*}{\mathbf{x}}}{\partial \mathbf{x}}\frac{\partial \mathbf{x}}{\partial (\widehat{\mathbf{x}}_{Si})_n} = \mathbf{Q}\,(\mathbf{F}_{Se})_n \end{aligned}\right\} \quad \text{with} \quad \mathbf{Q} = \frac{\partial \overset{*}{\mathbf{x}}}{\partial \mathbf{x}} \in \mathcal{SO}_3\,, \tag{4.25}$$

where $\mathcal{SO}_3$ is the special (proper) orthogonal group of all arbitrary rigid body rotations $\mathbf{Q}$ with the properties $\mathbf{Q}^T = \mathbf{Q}^{-1}$ and $\det \mathbf{Q} = 1$. In this context, the structural tensor $\boldsymbol{\mathcal{M}}^S$ and the referential solid coordinate $\mathbf{X}_S$ are *a priori* invariant under rotations of the actual configuration, as they are referential measures having their basis system anchored in the reference configuration which does not notice rotations of the actual configuration. Keeping in mind the natural objectivity of scalar-valued quantities $\overset{*}{\Psi}(\,\cdot\,) = \Psi(\,\cdot\,)$, i. e., their invariance under rigid body rotations, it is easily concluded that the solid deformation gradients are not well suited measures in order to satisfy the invariance condition. Inserting (4.25) into (4.24) reveals the problem

$$\psi^S[\,\mathbf{F}_S\,,\,(\mathbf{F}_{Se})_n\,,\,\boldsymbol{\mathcal{M}}^S\,,\mathbf{X}_S\,] \neq \psi^S[\,\mathbf{Q}\,\mathbf{F}_S\,,\,\mathbf{Q}\,(\mathbf{F}_{Se})_n\,,\,\boldsymbol{\mathcal{M}}^S\,,\mathbf{X}_S\,] \quad \forall \left\{ \begin{array}{l} \mathbf{Q} \in \mathcal{SO}_3\,, \\ \mathbf{F}_S\,,(\mathbf{F}_{Se})_n\,. \end{array} \right. \tag{4.26}$$

Then, applying the special choices $\mathbf{Q} = \mathbf{R}_S^T$ and $\mathbf{Q} = (\mathbf{R}_{Se}^T)_n$ as well as inserting the right polar decompositions of $\mathbf{F}_S$ (3.31) and $\mathbf{F}_{Se}$ (3.35), respectively, the solution is obtained in

$$\psi^S[\,\mathbf{R}_S^T\,\mathbf{R}\,\mathbf{U}_S\,,\,(\mathbf{R}_{Se}^T)_n\,(\mathbf{R}_{Se})_n\,(\widehat{\mathbf{U}}_{Se})_n\,,\,\boldsymbol{\mathcal{M}}^S,\,\mathbf{X}_S\,] = \psi^S[\,\mathbf{U}_S\,,\,(\widehat{\mathbf{U}}_{Se})_n\,,\,\boldsymbol{\mathcal{M}}^S,\,\mathbf{X}_S\,]\,. \tag{4.27}$$

Thus, the *Helmholtz* energy may only depend on the referential stretching parts of the respective overall and elastic solid deformation gradients. Recalling the definitions of the corresponding deformation and strain tensors leads to an equivalent set of variables, viz.:

$$\psi^S[\,\mathbf{C}_S\,,\,(\widehat{\mathbf{C}}_{Se})_n\,,\,\boldsymbol{\mathcal{M}}^S,\,\mathbf{X}_S\,] = \psi^S[\,\mathbf{E}_S\,,\,(\widehat{\boldsymbol{\Gamma}}_{Se})_n\,,\,\boldsymbol{\mathcal{M}}^S,\,\mathbf{X}_S\,]\,. \tag{4.28}$$

Following this, the internal variables characterising the inelastic deformation process may be chosen in accordance to the above findings, i. e., one of the quantities $(\widehat{\mathbf{U}}_{Si})_n$, $(\widehat{\mathbf{C}}_{Si})_n$, or $(\widehat{\boldsymbol{\Gamma}}_{Si})_n$ is chosen instead of the inelastic solid deformation gradients $(\mathbf{F}_{Si})_n$.

Finally, it can be shown that the remaining velocity measures $\mathbf{w}_F$ and $\mathbf{D}_F$ of (4.22) satisfy the conditions for material frame indifference

$$\overset{*}{\mathbf{w}}_F = \mathbf{Q}\,\mathbf{w}_F \qquad \text{and} \qquad \overset{*}{\mathbf{D}}_F = \mathbf{Q}\,\mathbf{D}_F\,\mathbf{Q}^T \tag{4.29}$$

for vector- and tensor-valued quantities, respectively. Starting with the seepage velocity, one quickly finds the proof of material frame indifference with the material time derivatives of the rotated line elements, i. e.,

$$\left.\begin{aligned}(\overset{*}{\mathbf{x}})'_S &= (\mathbf{Q}\,\mathbf{x})'_S = \dot{\mathbf{Q}}\,\mathbf{x} + \mathbf{Q}\,\overset{\prime}{\mathbf{x}}_S \\ (\overset{*}{\mathbf{x}})'_F &= (\mathbf{Q}\,\mathbf{x})'_F = \dot{\mathbf{Q}}\,\mathbf{x} + \mathbf{Q}\,\overset{\prime}{\mathbf{x}}_F\end{aligned}\right\} \quad \longrightarrow \quad \overset{*}{\mathbf{w}}_F = (\overset{*}{\mathbf{x}})'_S - (\overset{*}{\mathbf{x}})'_F = \mathbf{Q}\,\underbrace{(\overset{\prime}{\mathbf{x}}_S - \overset{\prime}{\mathbf{x}}_F)}_{\mathbf{w}_F}\,. \tag{4.30}$$

Herein use was made of the equivalent material time derivatives $\overset{\prime}{\mathbf{Q}}_\alpha = \dot{\mathbf{Q}}$, which can be easily obtained by taking the difference of equations $(3.13)_{3,4}$ and exploiting the gradient-free character of rigid body rotations, i. e., $\operatorname{grad}\mathbf{Q} = \mathbf{0}$, as the rotation $\mathbf{Q}$ is independent of the constituent it is applied to. Proceeding from rotated spatial fluid velocity gradients

$$\begin{aligned}\overset{*}{\mathbf{L}}_F &= (\overset{*}{\mathbf{F}}_F)'_F\,\overset{*}{\mathbf{F}}_F^{-1} &&= (\mathbf{Q}\,\mathbf{F}_F)'_F\,(\mathbf{Q}\,\mathbf{F}_F)^{-1} &&= \dot{\mathbf{Q}}\,\mathbf{Q}^T + \mathbf{Q}\,\mathbf{L}_F\,\mathbf{Q}^T, \\ \overset{*}{\mathbf{L}}_F^T &= \overset{*}{\mathbf{F}}_F^{T-1}\,(\overset{*}{\mathbf{F}}_F^T)'_F &&= (\mathbf{Q}^{T-1}\,\mathbf{F}_F^{T-1})\,(\mathbf{F}_F^T\,\mathbf{Q}^T)'_F &&= \mathbf{Q}\,\dot{\mathbf{Q}}^T + \mathbf{Q}\,\mathbf{L}_F^T\,\mathbf{Q}^T\end{aligned} \tag{4.31}$$

with a similar approach for the rotated fluid deformation gradient $\overset{*}{\mathbf{F}}_F$ as is given in (4.25), the rotated rate of deformation tensor of the fluid satisfies the objectivity condition, viz.:

$$\overset{*}{\mathbf{D}}_F = \tfrac{1}{2}\,(\overset{*}{\mathbf{L}}_F + \overset{*}{\mathbf{L}}_F^T) = \tfrac{1}{2}\,(\mathbf{Q}\,\mathbf{L}_F\,\mathbf{Q}^T + \mathbf{Q}\,\mathbf{L}_F^T\,\mathbf{Q}^T + \underbrace{\dot{\mathbf{Q}}\,\mathbf{Q}^T + \mathbf{Q}\,\dot{\mathbf{Q}}^T}_{(\mathbf{Q}\,\mathbf{Q}^T)^{\cdot} = \mathbf{0}}) = \mathbf{Q}\,\mathbf{D}_F\,\mathbf{Q}^T. \tag{4.32}$$

4.2.3 Universal Dissipation

Following the constitutive modelling process, the principle of dissipation has to be satisfied stating that every admissible thermodynamical process has to fulfil the entropy inequality of the overall aggregate. In this regard, the *Clausius-Planck* inequality in the form of (4.18) is evaluated following the approved procedure of Coleman & Noll [35]. Herein, convenient *a priori* constitutive assumptions, which led to a reduction of the set of process variables, allow for a quick evaluation, where each part of the inequality has to be greater or equal to zero separately. Note in passing that the more general, but also lengthy evaluation procedure by Liu [125] and Liu & Müller [126] involves a *Lagrange* multiplier for each balance relation. However, the final result for the simple case of the present incompressible binary aggregate is identical.

As a first step, the material time derivatives of the constituent *Helmholtz* energies (4.23), where the solid part depends on the set of process variables given in $(4.28)_1$, result in

$$(\psi^S)'_S = \frac{\partial \psi^S}{\partial \mathbf{C}_S} \cdot (\mathbf{C}_S)'_S + \sum_{n=1}^{N} \frac{\partial \psi^S}{\partial (\widehat{\mathbf{C}}_{Se})_n} \cdot [(\widehat{\mathbf{C}}_{Se})_n]'_S \qquad \text{and} \qquad (\psi^F)'_F = 0\,. \tag{4.33}$$

Herein, the material time derivative of ψ^F vanishes due to the empty set of process variables for the incompressible pore fluid. Moreover, use was made of the time independency of the structural tensor $\boldsymbol{\mathcal{M}}^S$ and the referential position vector $\mathbf{X}_S$. After applying the transport behaviour of the strain rate tensors given in box (B.2) of Appendix B, i. e.,

$$(\mathbf{C}_S)'_S = 2\,\mathbf{F}_S^T\,\mathbf{D}_S\,\mathbf{F}_S\,, \tag{4.34}$$

the time derivative $(4.33)_1$ is inserted in the *Clausius-Planck* inequality (4.18) yielding

$$\underbrace{\Big(\mathbf{T}_E^S - 2\rho^S\,\mathbf{F}_S\frac{\partial\psi^S}{\partial\mathbf{C}_S}\mathbf{F}_S^T\Big)\cdot\mathbf{D}_S}_{\text{equilibrium part } = 0}\underbrace{-\,2\rho^S\sum_{n=1}^{N}\frac{\partial\psi^S}{\partial(\widehat{\mathbf{C}}_{Se})_n}\cdot[(\widehat{\mathbf{C}}_{Se})_n]'_S + \mathbf{T}_E^F\cdot\mathbf{D}_F - \hat{\mathbf{p}}_E^F\cdot\mathbf{w}_F}_{\text{dissipation or non-equilibrium part } \geq 0}\geq 0\,, \tag{4.35}$$

which has to be satisfied for arbitrary process variables $\mathcal{V}$. Following the evaluation procedure of Coleman & Noll [35], all resulting parts have to satisfy the inequality separately. Herein, the first part of (4.35) can be fulfilled in an equilibrium (EQ) state by the vanishing expression in parenthesis, while the remaining parts have to be greater than zero, thereby characterising the dissipation or non-equilibrium (NEQ) process.

As a consequence, the EQ part must depend on the process variable $\mathbf{C}_S$ and the NEQ part on $(\widehat{\mathbf{C}}_{Se})_n$. Note that no statement can be made regarding the structural tensor $\boldsymbol{\mathcal{M}}^S$ and the referential position vector $\mathbf{X}_S$, as they do not violate (4.35) at any time. As inhomogeneous material behaviour is usually captured by an implicit dependence of ψ^S on $\mathbf{X}_S$ via material parameters, the referential position vector $\mathbf{X}_S$ is omitted from the list of arguments. Keeping in mind the characteristic mechanical tissue properties of the IVD described in Subsection 2.3.3, only the isotropic part of the ECM behaves viscoelastic and thus, the following constitutive split for the process variables of the solid *Helmholtz* energy becomes apparent:

$$\psi^S[\,\mathbf{C}_S\,,\,(\widehat{\mathbf{C}}_{Se})_n\,,\,\boldsymbol{\mathcal{M}}^S\,] = \psi^S_{\text{EQ}}[\,\mathbf{C}_S\,,\,\boldsymbol{\mathcal{M}}^S\,] + \psi^S_{\text{NEQ}}[\,(\widehat{\mathbf{C}}_{Se})_n\,]\,. \tag{4.36}$$

However, the form of the inequality (4.35) is still not optimal for the determination of the solid extra stress and needs to be rearranged. In this regard, the upper inelastic *Oldroyd* derivative (3.74) as well as box (B.2) allow for a reformulation of the elastic strain rate

$$\begin{aligned}(\widehat{\mathbf{C}}_{Se})'_S &= (\widehat{\mathbf{C}}_{Se})^{\triangle}_{Si} - \widehat{\mathbf{L}}_{Si}^T\,\widehat{\mathbf{C}}_{Se} - \widehat{\mathbf{C}}_{Se}\,\widehat{\mathbf{L}}_{Si}\\ &= 2\,\mathbf{F}_{Se}^T\,\mathbf{D}_S\,\mathbf{F}_{Se} - \widehat{\mathbf{L}}_{Si}^T\,\widehat{\mathbf{C}}_{Se} - \widehat{\mathbf{C}}_{Se}\,\widehat{\mathbf{L}}_{Si}\,,\end{aligned} \tag{4.37}$$

which is given in an exemplary manner for $N = 1$. Moreover, exploiting the symmetric character of $\widehat{\mathbf{C}}_{Se}$ and thus, of the symmetric derivative $\partial\psi^S_{\text{NEQ}}/\partial\widehat{\mathbf{C}}_{Se}$, leads to the identity

$$\frac{\partial\psi^S_{\text{NEQ}}}{\partial\widehat{\mathbf{C}}_{Se}}\cdot\widehat{\mathbf{L}}_{Si}^T\,\widehat{\mathbf{C}}_{Se} = \frac{\partial\psi^S_{\text{NEQ}}}{\partial\widehat{\mathbf{C}}_{Se}}\cdot\widehat{\mathbf{C}}_{Se}\,\widehat{\mathbf{L}}_{Si}\,. \tag{4.38}$$

Together with the definition of a solid strain energy defined per unit reference volume

$$W^S := \rho^S_{0S}\,\psi^S \qquad\longrightarrow\qquad (W^S)'_S = \rho^S_{0S}\,(\psi^S)'_S\,, \tag{4.39}$$

which describes the elastic potential or stored elastic energy in the *Hooke* elements of the generalised *Maxwell* model, the inequality (4.35) can be rearranged for evaluation. Herein, the equilibrium part yields an expression for the solid *Kirchhoff* extra stress $\boldsymbol{\tau}_E^S$

$$\Big[\boldsymbol{\tau}_E^S - \underbrace{2\,\mathbf{F}_S\,\frac{\partial W_{\mathrm{EQ}}^S}{\partial \mathbf{C}_S}\,\mathbf{F}_S^T}_{\boldsymbol{\tau}_{\mathrm{EQ}}^S} - \underbrace{\sum_{n=1}^{N} \overbrace{2\,(\mathbf{F}_{Se})_n\,\frac{\partial W_{\mathrm{NEQ}}^S}{\partial(\widehat{\mathbf{C}}_{Se})_n}\,(\mathbf{F}_{Se}^T)_n}^{\boldsymbol{\tau}_n^S}}_{\boldsymbol{\tau}_{\mathrm{NEQ}}^S}\Big] \cdot \mathbf{D}_S = 0 \quad \forall \begin{cases} \mathbf{D}_S\,,\ \mathbf{F}_S, \\ (\mathbf{F}_{Se})_n\,, \end{cases} \tag{4.40}$$

and a remaining part characterises the dissipative nature of the aggregate, viz.:

$$2\,\frac{\rho^S}{\rho_{0S}^S}\sum_{n=1}^{N}\frac{\partial W_{\mathrm{NEQ}}^S}{\partial(\widehat{\mathbf{C}}_{Se})_n}\cdot[(\widehat{\mathbf{C}}_{Se})_n\,(\widehat{\mathbf{L}}_{Si})_n] + \mathbf{T}_E^F\cdot\mathbf{D}_F - \hat{\mathbf{p}}_E^F\cdot\mathbf{w}_F \geq 0 \quad \forall \begin{cases} (\widehat{\mathbf{C}}_{Se})_n\,,\ \mathbf{D}_F, \\ (\widehat{\mathbf{L}}_{Si})_n\,,\ \mathbf{w}_F\,. \end{cases} \tag{4.41}$$

In order to obtain this result, use was made of the partial solid density $(4.5)_2$ and the definition of the *Kirchoff* stress $(3.80)_2$. Moreover, equation (4.40) reveals the additive character of the stresses in the underlying generalised *Maxwell* model.

The *Kirchhoff* stress in (4.40) of the actual configuration can be shifted to the reference configuration by a covariant transport (3.82) yielding the 2nd *Piola-Kirchhoff* stress

$$\mathbf{S}_E^S = \underbrace{2\,\frac{\partial W_{\mathrm{EQ}}^S}{\partial \mathbf{C}_S}}_{\mathbf{S}_{\mathrm{EQ}}^S} + \underbrace{\sum_{n=1}^{N} \overbrace{2\,(\mathbf{F}_{Si}^{-1})_n\frac{\partial W_{\mathrm{NEQ}}^S}{\partial(\widehat{\mathbf{C}}_{Se})_n}\,(\mathbf{F}_{Si}^{T-1})_n}^{\mathbf{S}_n^S}}_{\mathbf{S}_{\mathrm{NEQ}}^S}\,. \tag{4.42}$$

Together with the covariant transport (3.83), the non-equilibrium intermediate stress of a single *Maxwell* element n can be obtained via

$$\widehat{\boldsymbol{\tau}}_n^S = (\mathbf{F}_{Si})_n\,\mathbf{S}_n^S\,(\mathbf{F}_{Si}^T)_n = (\mathbf{F}_{Se}^{-1})_n\,\boldsymbol{\tau}_n^S\,(\mathbf{F}_{Se}^{T-1})_n \qquad \longrightarrow \qquad \widehat{\boldsymbol{\tau}}_n^S = 2\,\frac{\partial W_{\mathrm{NEQ}}^S}{\partial(\widehat{\mathbf{C}}_{Se})_n}\,. \tag{4.43}$$

It is important to note that a computation of the entire intermediate-state overstress tensor $\widehat{\boldsymbol{\tau}}_{\mathrm{NEQ}}^S$ is only possible for the case of $N = 1$, as the individual intermediate over stresses of more than one *Maxwell* element may operate on different intermediate configurations. For the case of $N > 1$, the summation has to be carried out on the actual or referential configuration using equations (4.40) or (4.42), respectively.

In particular, the following proportionalities can be deduced from (4.41)

$$\widehat{\boldsymbol{\tau}}_n^S \propto (\widehat{\mathbf{D}}_{Si})_n\,, \qquad \mathbf{T}_E^F \propto \mathbf{D}_F\,, \qquad \hat{\mathbf{p}}_E^F \propto -\mathbf{w}_F\,, \tag{4.44}$$

provided the solid density ρ^S is positive and non-zero. In order to obtain $(4.44)_1$, use was made of the positive definiteness of $(\widehat{\mathbf{C}}_{Se})_n$ as well as the symmetric nature of $\widehat{\boldsymbol{\tau}}_n^S$ yielding the identity $\widehat{\boldsymbol{\tau}}_n^S\cdot(\widehat{\mathbf{L}}_{Si})_n = \widehat{\boldsymbol{\tau}}_n^S\cdot(\widehat{\mathbf{D}}_{Si})_n$.

4.2.4 Material Symmetry

The purpose of this section is to deliver a brief understanding of the vast matter on material symmetries. For more comprehensive information on this topic, the reader is referred to the representative works of Truesdell & Noll [207], Boehler [22], Spencer [194, 195], Zheng & Boehler [238], Schröder [177] or Apel [6] and references therein.

The principle of material symmetry is based on observations in the laboratory and can be illustrated by a simple experiment. Imagine a wooden cube which is compressed in fibre direction. In a second test, the cube is brought into a new reference position before being tested again. In this context, the testing device will always record the same response, as long as the cube is only rotated about its fibre direction. A different response will be recorded if the wooden specimen is rotated about any other axis. Thus, in the case of fibre-reinforced or generally anisotropic materials, the amount of stored elastic energy does not only depend on the applied deformation but also on the orientation of the material.

From a continuum-mechanical point of view, these observations may hold for arbitrary small regions, i. e., infinitesimal material elements $\mathcal{M}$, around every material point P^S with the referential coordinate $\mathbf{X}_S$. Following this, there may be different reference configurations which are indistinguishable by any physical response and thus, by any local experiment of $\mathcal{M}$. Note in passing that in this context, the same microscopic structure may be observed, even when the material element $\mathcal{M}$ is expressed with respect to different referential frames. If this is the case, the found transformations $\mathbf{H}$ between the different reference configurations are symmetry transformations of the referential coordinates, i. e.,

$$\overset{\diamond}{\mathbf{X}}_S = \mathbf{H}\,\mathbf{X}_S \quad \forall\,\mathbf{H} \in \mathcal{MG}_3 \subset \mathcal{O}_3 \subset \mathcal{U}_3\,. \tag{4.45}$$

The set of all possible symmetry transformations $\mathbf{H}$ for a material point P^S is then defined as the material symmetry (isotropy) group $\mathcal{MG}_3$. Moreover, $\mathcal{O}_3$ denotes the set of all orthogonal transformations with $\det\mathbf{H} = \pm 1$ and $\mathbf{H}^T = \mathbf{H}^{-1}$ which is a subset of all volume preserving (unimodular) transformations $\mathcal{U}_3$ exhibiting only the less restricting property of $\det\mathbf{H} = \pm 1$.

However, the allowed symmetry transformations $\mathbf{H}$ between the neighbouring reference configurations are by no means arbitrary, as there is no known physical object, in which the stress remains unaltered, when the body is compressed or expanded. Thus, the transformations of the material symmetry group $\mathcal{MG}_3 \subset \mathcal{U}_3$ must be at least a subset of the unimodular group $\mathcal{U}_3$, cf., Gurtin & Williams [85]. Note in passing that $\mathcal{MG}_3 = \mathcal{U}_3$ is the characteristic of an isotropic fluid, cf., Noll [153]. Here, for the purpose of the underlying solid skeleton, further restrictions must hold. According to Wang & Truesdell [223], a solid is a material, where only rigid-body rotations are indiscernible and thus, the symmetry group $\mathcal{MG}_3 \subset \mathcal{O}_3$ must be a subset of the orthogonal group $\mathcal{O}_3$ containing all shape-preserving rotations. Consequently, if $\mathcal{MG}_3 = \mathcal{O}_3$ the solid material has an isotropic behaviour, while anisotropic effects occur for all other cases. The different possible types of anisotropy are numerous and can be divided into two continuous groups as well as eleven finite sub groups describing a total of thirty-two crystal classes. For more general information on these groups, please refer to Spencer [192], Truesdell & Noll [207] or to any text on crystal physics.

Due to the motivation above, the symmetry groups are defined by an invariance condition for the strain energy functional W^S similar to (4.24) and (4.29), but now with respect to rotated referential quantities $(\overset{\diamond}{\cdot})$ yielding

$$W^S_{\mathrm{EQ}}(\mathbf{C}_S\,,\,\boldsymbol{\mathcal{M}}^S) = W^S_{\mathrm{EQ}}(\overset{\diamond}{\mathbf{C}}_S\,,\,\overset{\diamond}{\boldsymbol{\mathcal{M}}}{}^S)\,. \tag{4.46}$$

Proceeding from equation (4.45), the rotated solid deformation gradient can be given by

$$\overset{\diamond}{\mathbf{F}}_S = \frac{\partial \mathbf{x}}{\partial \overset{\diamond}{\mathbf{X}}_S} = \frac{\partial \mathbf{x}}{\partial \mathbf{X}_S}\left(\frac{\partial \overset{\diamond}{\mathbf{X}}_S}{\partial \mathbf{X}_S}\right)^{-1} = \mathbf{F}_S\,\mathbf{H}^{-1}, \qquad \text{with} \qquad \mathbf{H} = \frac{\partial \overset{\diamond}{\mathbf{X}}_S}{\partial \mathbf{X}_S}\,. \tag{4.47}$$

Note that the assumption of vanishing texture developments is applied such that no anisotropies are induced during the inelastic deformation process. Hence, the elastic part of the deformation gradient is not affected by transformations of the referential coordinates and thus, the non-equilibrium part W^S_{NEQ} of the isotropic strain energy is *a priori* invariant with respect to rotations of the reference configuration. Exploiting the definition of the right *Cauchy-Green* deformation tensor $(3.34)_1$ yields the transport

$$\overset{\diamond}{\mathbf{C}}_S = \overset{\diamond}{\mathbf{F}}{}^T_S\,\overset{\diamond}{\mathbf{F}}_S = (\mathbf{F}_S\,\mathbf{H}^{-1})^T\,\mathbf{F}_S\,\mathbf{H}^{-1} = \mathbf{H}^{T-1}\,\mathbf{F}^T_S\,\mathbf{F}_S\,\mathbf{H}^{-1} = \mathbf{H}\,\mathbf{C}_S\,\mathbf{H}^T. \tag{4.48}$$

As the structural tensor is also anchored in the referential frame, its transport to the rotated reference configuration is quickly concluded to

$$\overset{\diamond}{\boldsymbol{\mathcal{M}}}{}^S = \mathbf{H}\,\boldsymbol{\mathcal{M}}^S\,\mathbf{H}^T\,. \tag{4.49}$$

Thus, the definition of the symmetry group can then be obtained by the following relation

$$\left.\begin{aligned} W^S_{\mathrm{EQ}}(\mathbf{C}_S\,,\,\boldsymbol{\mathcal{M}}^S) \;=\; W^S_{\mathrm{EQ}}(\mathbf{H}\,\mathbf{C}_S\,\mathbf{H}^T,\,\mathbf{H}\,\boldsymbol{\mathcal{M}}^S\,\mathbf{H}^T)\,,\\ \boldsymbol{\mathcal{M}}^S = \mathbf{H}\,\boldsymbol{\mathcal{M}}^S\,\mathbf{H}^T \end{aligned}\right\}\;\forall\,\mathbf{H}\in\mathcal{MG}_3\,,\,\mathbf{C}_S\,,\,\boldsymbol{\mathcal{M}}^S. \tag{4.50}$$

In this regard, the first conditional equation in (4.50) is used for the determination of the symmetry group $\mathcal{MG}_3 \subset \mathcal{O}_3$ via a comparison with experimental observations in the lab, while the second one is needed to define the structural tensor $\boldsymbol{\mathcal{M}}^S$ such that it is invariant with respect to the found transformations in $\mathcal{MG}_3$.

Remark: From a physical point of view, some symmetry transformations $\mathbf{H} \in \mathcal{O}_3$ make not much sense, as they are impossible to physically apply or accomplish. A material body, for instance, may not be compressed to a single point and recovered on the other side, like in the case of the central inversion with $\mathbf{H} = -\mathbf{I}$. Thus, the interpretation of the material symmetry group $\mathcal{MG}_3 \subset \mathcal{SO}_3$ being restricted to a sub-group of the rotational group $\mathcal{SO}_3$ is also possible. However, from a purely geometrical point of view, $\mathcal{MG}_3$ may be a subset of the full orthogonal group $\mathcal{O}_3$. □

4.3 Consequences from the Basic Principles

4.3.1 Selected Symmetry Groups and their Structural Tensors

The following section offers a brief introduction into the symmetry groups of interest concerning the modelling of fibre-reinforced materials. Note that these materials play

a rather small role in the many possible symmetry groups found within the thirty-two crystal classes for instance. For more information on the characterisation of all symmetry groups, please refer to the comprehensive overview in, e. g., Apel [6], while in the case of fibre-reinforced materials please consult Spencer [194, 195] among others. An overview of the corresponding structural tensors can then be taken from Zheng & Spencer [239].

According to Truesdell & Noll [207], every material symmetry group $\mathcal{MG}_3$ can be factorised in the two elements $\{\mathbf{I}, -\mathbf{I}\}$ as well as rotations, reflections or combinations thereof. Considering a right-handed set of mutually orthogonal unit vectors $\boldsymbol{\xi}_1$, $\boldsymbol{\xi}_2$, and $\boldsymbol{\xi}_3$ allows for a quantification of these symmetry transformations. Following this, a sub-group of all orthogonal rotations can be given by

$$\boldsymbol{\mathcal{H}}_{\boldsymbol{\xi}_1}^{(\phi)} = \boldsymbol{\xi}_1 \otimes \boldsymbol{\xi}_1 + \sin\phi\,(\boldsymbol{\xi}_1 \times \mathbf{I}) + \cos\phi\,(\mathbf{I} - \boldsymbol{\xi}_1 \otimes \boldsymbol{\xi}_1)\,, \tag{4.51}$$

which is known as the *Euler-Rodrigues*[3] form of a rigid-body rotation about an axis $\boldsymbol{\xi}_1$ with an arbitrary angle $0 \leq \phi < 2\,\pi$. Moreover, a reflection tensor can be introduced via

$$\boldsymbol{\mathcal{R}}_{\boldsymbol{\xi}_1} = \mathbf{I} - 2\,\boldsymbol{\xi}_1 \otimes \boldsymbol{\xi}_1 \tag{4.52}$$

which describes a reflection of a material body in a plane normal to the axis $\boldsymbol{\xi}_1$. Thus, the identity transformation and the central inversion are given by

$$\mathbf{I} = \boldsymbol{\xi}_1 \otimes \boldsymbol{\xi}_1 + \boldsymbol{\xi}_2 \otimes \boldsymbol{\xi}_2 + \boldsymbol{\xi}_3 \otimes \boldsymbol{\xi}_3\,, \qquad -\mathbf{I} = \boldsymbol{\mathcal{R}}_{\boldsymbol{\xi}_1}\,\boldsymbol{\mathcal{R}}_{\boldsymbol{\xi}_2}\,\boldsymbol{\mathcal{R}}_{\boldsymbol{\xi}_3}\,. \tag{4.53}$$

Isotropy: In this case, the material has no preferred direction and all orthogonal transformations are indiscernible for the solid. From a formal point of view, it is possible to define two types of isotropy. One with a centre of symmetry and one without a centre of symmetry, also known as hemitropy. Thus, the material symmetry group is either the full orthogonal subgroup $\mathcal{MG}_3 = \mathcal{O}_3$ or the proper orthogonal group $\mathcal{MG}_3 = \mathcal{SO}_3 \subset \mathcal{O}_3$, respectively. For the purpose of this monograph, however, this distinction will not make a difference. As a result, the only possible structural tensor $\boldsymbol{\mathcal{M}}^S = \mathbf{I}$ is the identity tensor, which will therefore be omitted in the case of isotropy.

Transverse Isotropy: A material with a single preferred direction is said to be transversely isotropic. If the unit vector $\boldsymbol{\xi}_1$ is chosen to denote the preferred direction, then the material symmetry group can be factorised into

$$\mathcal{MG}_3 := \left\{ \pm\,\mathbf{I}\,,\, \boldsymbol{\mathcal{R}}_{\boldsymbol{\xi}_1}\,,\, \boldsymbol{\mathcal{R}}_{\boldsymbol{\xi}_2}\,,\, \boldsymbol{\mathcal{R}}_{\boldsymbol{\xi}_3}\,,\, \boldsymbol{\mathcal{H}}_{\boldsymbol{\xi}_1}^{(\phi)},\, \boldsymbol{\mathcal{H}}_{\boldsymbol{\xi}_2}^{(\pi)},\, \boldsymbol{\mathcal{H}}_{\boldsymbol{\xi}_3}^{(\pi)} \,|\, 0 \leq \phi < 2\,\pi \right\} \subset \mathcal{O}_3\,. \tag{4.54}$$

A classical example for transverse isotropy is a material having a weaker isotropic matrix material reinforced by a single family of fibres, cf. Figure 4.1.

The corresponding structural tensor fulfilling the invariance condition $(4.50)_2$ is then simply obtained by taking the dyadic product of the unit vector $\mathbf{a}_0^S$ pointing in the preferred

[3] *Benjamin Olinde Rodrigues* (1795–1851): Having Portuguese Jewish relatives, he was born and raised in France and was later working as a banker, mathematician, and social reformer. The famous rotation formula is documented in his dissertation dating back to 1816.

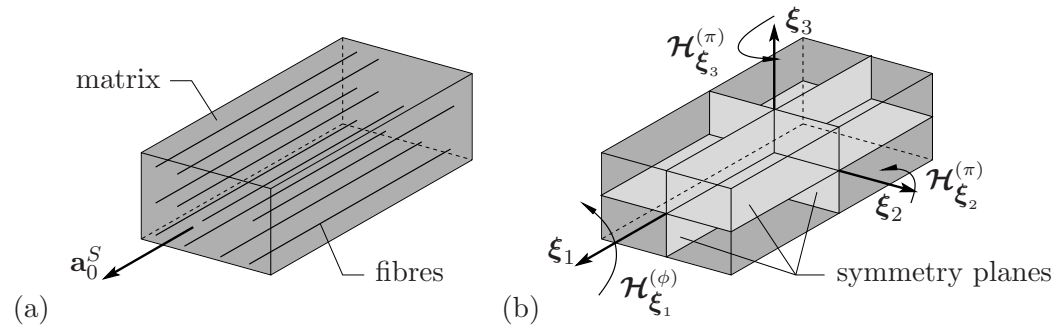

Figure 4.1: *(a) Transversely isotropic material with a preferred direction* $\mathbf{a}_0^S = \boldsymbol{\xi}_1$ *for the reinforcing family of fibres and (b) the corresponding symmetry transformations.*

fibre direction in the undeformed reference configuration. Thus, the structural tensor belongs to the group of simple tensors having the following properties:

$$\boldsymbol{\mathcal{M}}_a^S = \mathbf{a}_0^S \otimes \mathbf{a}_0^S \quad \text{with} \quad \boldsymbol{\mathcal{M}}_a^S = (\boldsymbol{\mathcal{M}}_a^S)^T\,, \quad \boldsymbol{\mathcal{M}}_a^S = \boldsymbol{\mathcal{M}}_a^S\,\boldsymbol{\mathcal{M}}_a^S\,, \quad \operatorname{tr}\boldsymbol{\mathcal{M}}_a^S = 1\,. \tag{4.55}$$

Note that the structural tensor is an even function of the unit fibre vector $\mathbf{a}_0^S$ and thus, the sign (sense) of the fibre vector is eliminated.

Orthogonal (rhombic) symmetry is found in a material which is symmetric under reflections in each of the planes normal to the above defined orthonormal unit vectors $\boldsymbol{\xi}_1$, $\boldsymbol{\xi}_2$ and $\boldsymbol{\xi}_3$. Its material symmetry group can be given by

$$\mathcal{MG}_3 := \{\, \pm\mathbf{I}\,,\, \boldsymbol{\mathcal{R}}_{\boldsymbol{\xi}_1}\,,\, \boldsymbol{\mathcal{R}}_{\boldsymbol{\xi}_2}\,,\, \boldsymbol{\mathcal{R}}_{\boldsymbol{\xi}_3}\,,\, \boldsymbol{\mathcal{H}}^{(\pi)}_{\boldsymbol{\xi}_1},\, \boldsymbol{\mathcal{H}}^{(\pi)}_{\boldsymbol{\xi}_2},\, \boldsymbol{\mathcal{H}}^{(\pi)}_{\boldsymbol{\xi}_3} \,\} \subset \mathcal{O}_3\,. \tag{4.56}$$

Following this, two cases can be distinguished. As depicted in Figure 4.2 (a), the symmetry group includes materials with a reinforcement by two mechanically distinct families of fibres which are embedded in a plane and arranged orthogonally to each other. An example for this kind would be a cross-ply laminate. However, orthogonal symmetry is also implied when two mechanically equivalent families of fibres with arbitrary angle between them are embedded in a plane, cf. Figure 4.2 (b). Herein, orthotropy is observed at the bisectors of the fibres. This material is widely used, e. g., in balanced angle plies. As already mentioned in Subsection 4.2.4, the symmetry group does not necessarily need to be valid for the whole body under consideration. In a helically reinforced water hose, for instance, local orthotropy can be observed by cutting out a representative elementary volume element, where the local unit fibre directions are given by $\mathbf{a}_0^S$ and $\mathbf{b}_0^S$, respectively. The corresponding structural tensors can then be given in accordance to (4.55) yielding

$$\boldsymbol{\mathcal{M}}_a^S = \mathbf{a}_0^S \otimes \mathbf{a}_0^S \quad \text{and} \quad \boldsymbol{\mathcal{M}}_b^S = \mathbf{b}_0^S \otimes \mathbf{b}_0^S \tag{4.57}$$

with the definition of the unit fibre vectors depending on an initial fibre angle ϕ_0^S, viz.:

$$\mathbf{a}_0^S = \sin\phi_0^S\,\boldsymbol{\xi}_1 + \cos\phi_0^S\,\boldsymbol{\xi}_2 \qquad \text{and} \qquad \mathbf{b}_0^S = -\sin\phi_0^S\,\boldsymbol{\xi}_1 + \cos\phi_0^S\,\boldsymbol{\xi}_2\,. \tag{4.58}$$

Prismatic symmetry is strongly related to the orthogonal symmetry group and is found in a material which has two mechanically distinct fibre families with an arrangement depicted in Figure 4.2 (b). The corresponding symmetry group is then reduced to

$$\mathcal{MG}_3 := \{\, \pm\mathbf{I}\,,\, \boldsymbol{\mathcal{R}}_{\boldsymbol{\xi}_3}\,,\, \boldsymbol{\mathcal{H}}^{(\pi)}_{\boldsymbol{\xi}_3} \,\} \subset \mathcal{O}_3\,, \tag{4.59}$$

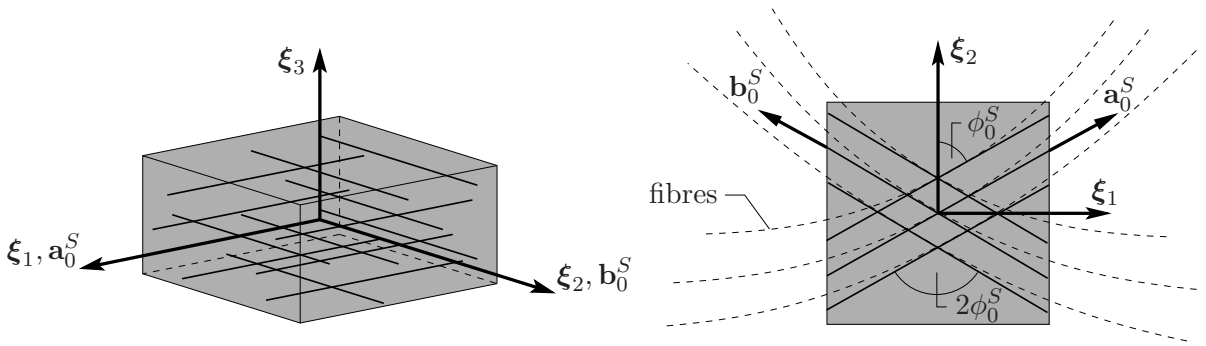

(a) orthogonal fibres (b) non-orthogonal fibres

Figure 4.2: *Orthogonal symmetry with: (a) two distinct, orthogonally arranged families of fibres and (b) two mechanically equivalent families of fibres with arbitrary intersection angle.*

which can be observed in applications using an unbalanced angle ply, for instance. The respective structural tensors are equivalent to the set in (4.57). Note that there are only two structural tensors needed to fully characterise orthotropic or prismatic material behaviour, because the third direction can be expressed by the first two structural tensors.

4.3.2 Representation with Isotropic Tensor Functions

In the context of finite continuum mechanics, representation theorems play a major role in the problem of defining mathematically and physically sound constitutive equations. For instance, the scalar-valued solid strain energy function W_{EQ}^S subjected to condition $(4.50)_1$ is known as an anisotropic tensor function with respect to the argument $\mathbf{C}_S$ under transformations of the symmetry group $\mathcal{MG}_3$. Following this approach leads to dependencies on the basis system in which $\boldsymbol{\mathcal{M}}^S$ is defined. However, in the context of finite continuum mechanics, and especially with respect to the general numerical treatment, such a restriction is undesirable. Therefore, an alternative formulation is sought after, where the representation of anisotropic materials can be accomplished under all orthogonal transformations $\mathcal{O}_3$, thereby automatically including the material symmetry group. In this regard, it is necessary to express the physical properties of an actually anisotropic material element using formally isotropic relations. Exactly this is accomplished by applying the concept of isotropic tensor functions.

In general, two different approaches for the representation with isotropic tensor functions can be distinguished. One is concerned with non-polynomial tensor functions while the other one is restricted to polynomial tensor functions due to mathematical convenience. The former one traces back to the works of Smith [190], Wang [221, 222] and Boehler [20], while important work for the latter case was done by Rivlin & Ericksen [170], Spencer [192, 196], Spencer & Rivlin [197] or Truesdell & Noll [207]. A detailed overview and a slightly different method can be found in Zheng [237]. However, a difference between these approaches is only noticeable for vector- and tensor-valued tensor functions. In this regard, the main problem is to find general, complete and irreducible representations for tensor functions, thereby keeping the resulting parameters at a minimum. Herein, the non-polynomial approach seems to be slightly in favour regarding the involved terms.

For the purpose of this monograph, only scalar-valued tensor functions are needed to formulate the solid strain energy W^S_{EQ}. The resulting tensor-valued stress-strain relation is then obtained from the evaluation of the entropy inequality using relation (4.42). In this regard, the solution to the representation problem of scalar-valued isotropic tensor functions traces back to the classical theory of invariants, which is described in a rather mathematical way in, e. g., Grace & Young [81], Gurevich [84], Weyl [224]. An application to continuum-mechanical problems can be found in Boehler [22] or Spencer [192, 196].

Following this, the requirement for an isotropic tensor function can be obtained from $(4.50)_1$ if the invariance condition is extended to the full group $\mathcal{O}_3$ of orthogonal transformations yielding

$$W^S_{\mathrm{EQ}}(\mathbf{C}_S\,,\,\boldsymbol{\mathcal{M}}^S) = W^S_{\mathrm{EQ}}(\mathbf{H}\,\mathbf{C}_S\,\mathbf{H}^T,\,\mathbf{H}\,\boldsymbol{\mathcal{M}}^S\,\mathbf{H}^T) \quad \forall\,\mathbf{H}\in\mathcal{O}_3\,,\,\mathbf{C}_S\,,\,\boldsymbol{\mathcal{M}}^S. \tag{4.60}$$

In this regard, W^S_{EQ} is called isotropic with respect to its arguments relative to the isotropic symmetry group $\mathcal{MG}_3 = \mathcal{O}_3$. Obviously, this characteristic is not naturally given for symmetry groups other than isotropy, as there is a contradiction when equation $(4.50)_2$ is recalled. The conflict in $(4.50)_2$ is solved using the theory of invariants, where a set of n scalar invariants $\mathcal{I}_S = \{J_{S1}\,,\,J_{S2}\,,\,J_{S3}\,,....\,,\,J_{Sn}\}$ is provided, which have to be used as arguments instead of the tensorial quantities. The problem is now to determine canonical forms for W^S_{EQ} such that the scalar-valued function itself becomes an invariant, thereby *a priori* fulfilling restriction (4.60).

4.3.3 The Idea of the Theory of Invariants

This section offers a brief introduction into the theory of invariants. Herein, the fundamental idea can be postulated with a scalar-valued function $\Psi(\mathbf{u}_i, \mathbf{v}_i, \mathbf{A}_i)$ being exposed to the invariance condition

$$\Psi(\mathbf{u}_i\,,\,\mathbf{v}_i\,,\,\mathbf{A}_i) \;=\; (\det\mathbf{H})^{\rho}\,\Psi(\mathbf{H}\,\mathbf{u}_i\,,\,\mathbf{H}\,\mathbf{v}_i\,,\,\mathbf{H}\,\mathbf{A}_i\,\mathbf{H}^T) \quad \forall\,\mathbf{H}\in\mathcal{O}_3\,, \tag{4.61}$$

where $\mathbf{A}_i$ represent arbitrary symmetric second-order tensors, while $\mathbf{u}_i$ and $\mathbf{v}_i$ denote absolute and axial vectors with $i = 1, 2, ..., m$, respectively. Then, the function Ψ itself is known as an absolute or even invariant if the exponent ρ equals zero. For the other case, where $\rho \neq 0$, Ψ is known to be a relative or odd invariant. For the sake of this monograph, only absolute invariants are relevant and hence, ρ is restricted to zero. This implicates firstly that attention is confined to only proper orthogonal transformations $\mathbf{H}\in\mathcal{SO}_3$ and secondly that a distinction between absolute and axial vectors is not necessary. This is because axial vectors do not change their sign under proper orthogonal transformations. Moreover, the vectors $\mathbf{u}_i$ and $\mathbf{v}_i$ can be associated with their associated skew-symmetric tensors

$$\mathbf{U}_i \;=\; -\overset{3}{\mathbf{E}}\,\mathbf{u}_i \qquad\qquad \text{and} \qquad\qquad \mathbf{V}_i \;=\; -\overset{3}{\mathbf{E}}\,\mathbf{v}_i\,, \tag{4.62}$$

where the third-order tensor $\overset{3}{\mathbf{E}}$ represents the *Ricci*[4] permutation tensor. Note that the skew-symmetric tensors in (4.62) transport just like the symmetric tensors $\mathbf{A}_i$, provided

[4] *Gregorio Ricci-Curbastro* (1853-1925): Italian mathematician whose article *Méthodes de calcul différentiel absolu et leurs applications* is regarded as the foundation of modern tensor algebra. It appeared in *Mathematische Annalen* **54** (1900), 125–201 and was written together with his student *Tullio Levi-Civita*.

that $\mathbf{H} \in \mathcal{SO}_3$. Hence, the task of finding invariants for absolute and axial vectors as well as for second-order tensors under the full orthogonal group $\mathcal{O}_3$ boils down to the problem of considering symmetric and skew-symmetric second-order tensors under the proper orthogonal group $\mathcal{SO}_3$.

The problem is then to find invariants which depend on the argument tensors and form a minimal integrity basis $\mathcal{I}_S$. The existence of such an integrity basis is assured by *Hilbert*'s[5] theorem stating that for any finite set of tensors of any order there exists a finite integrity base. A set $\mathcal{I}_S$ is called minimal, if it contains only irreducible invariants and an invariant is irreducible, if it cannot be expressed as a polynomial of the remaining invariants.

Results for these restrictions can be found in various books on invariant theory like, for instance, in Spencer [192, 196]. For the case of symmetric second-order tensors exposed to the proper orthogonal group $\mathcal{SO}_3$, the corresponding integrity bases for one, two and three argument tensors are listed in Table 4.1.

tensorial arguments	basic and mixed invariants J_{Sn}
$\mathbf{A}_1$	$\operatorname{tr}\mathbf{A}_1\,,\ \operatorname{tr}\mathbf{A}_1^2\,,\ \operatorname{tr}\mathbf{A}_1^3$
$\mathbf{A}_1, \mathbf{A}_2$	$\operatorname{tr}\mathbf{A}_1\,,\ \operatorname{tr}\mathbf{A}_1^2\,,\ \operatorname{tr}\mathbf{A}_1^3\,,\ \operatorname{tr}\mathbf{A}_2\,,\ \operatorname{tr}\mathbf{A}_2^2\,,\ \operatorname{tr}\mathbf{A}_2^3\,,$ $\operatorname{tr}(\mathbf{A}_1\mathbf{A}_2)\,,\ \operatorname{tr}(\mathbf{A}_1\mathbf{A}_2^2)\,,\ \operatorname{tr}(\mathbf{A}_1^2\mathbf{A}_2)\,,\ \operatorname{tr}(\mathbf{A}_1^2\mathbf{A}_2^2)$
$\mathbf{A}_1\,,\ \mathbf{A}_2\,,\ \mathbf{A}_3$	$\operatorname{tr}\mathbf{A}_1\,,\ \operatorname{tr}\mathbf{A}_1^2\,,\ \operatorname{tr}\mathbf{A}_1^3,\ \operatorname{tr}\mathbf{A}_2\,,\ \operatorname{tr}\mathbf{A}_2^2\,,\ \operatorname{tr}\mathbf{A}_2^3,\ \operatorname{tr}\mathbf{A}_3\,,\ \operatorname{tr}\mathbf{A}_3^2\,,\ \operatorname{tr}\mathbf{A}_3^3,$ $\operatorname{tr}(\mathbf{A}_1\mathbf{A}_2)\,,\ \operatorname{tr}(\mathbf{A}_1\mathbf{A}_2^2)\,,\ \operatorname{tr}(\mathbf{A}_1^2\mathbf{A}_2)\,,\ \operatorname{tr}(\mathbf{A}_1^2\mathbf{A}_2^2)\,,$ $\operatorname{tr}(\mathbf{A}_1\mathbf{A}_3)\,,\ \operatorname{tr}(\mathbf{A}_1\mathbf{A}_3^2)\,,\ \operatorname{tr}(\mathbf{A}_1^2\mathbf{A}_3)\,,\ \operatorname{tr}(\mathbf{A}_1^2\mathbf{A}_3^2)\,,$ $\operatorname{tr}(\mathbf{A}_2\mathbf{A}_3)\,,\ \operatorname{tr}(\mathbf{A}_2\mathbf{A}_3^2)\,,\ \operatorname{tr}(\mathbf{A}_2^2\mathbf{A}_3)\,,\ \operatorname{tr}(\mathbf{A}_2^2\mathbf{A}_3^2)\,,$ $\operatorname{tr}(\mathbf{A}_1\mathbf{A}_2\mathbf{A}_3)\,,\ \operatorname{tr}(\mathbf{A}_1^2\mathbf{A}_2\mathbf{A}_3)\,,\ \operatorname{tr}(\mathbf{A}_1\mathbf{A}_2^2\mathbf{A}_3)\,,\ \operatorname{tr}(\mathbf{A}_1\mathbf{A}_2\mathbf{A}_3^2)\,,$ $\operatorname{tr}(\mathbf{A}_1^2\mathbf{A}_2^2\mathbf{A}_3)\,,\ \operatorname{tr}(\mathbf{A}_1^2\mathbf{A}_2\mathbf{A}_3^2)\,,\ \operatorname{tr}(\mathbf{A}_1\mathbf{A}_2^2\mathbf{A}_3^2)$

Table 4.1: *Minimal integrity basis for general tensors exposed to proper orthogonal rotations.*

Note that the expression $\mathbf{A}_i^2$ denotes the tensor product $\mathbf{A}_i\,\mathbf{A}_i$. Moreover, the traces of a single tensor represent basic invariants, while traces of more than one tensor are known as mixed invariants. Another characteristic worth mentioning is that the mixed invariants are also invariant with respect to cyclic permutations of their tensor arguments.

4.3.4 Integrity Bases for Fibre-Reinforced Materials

Whenever fibre-reinforced materials are considered, several of the tensorial arguments of a scalar constitutive function like the equilibrium solid strain energy W^S_{EQ} are not just arbitrary symmetric second-order tensors. Especially, the structural tensors have distinct characteristics which can be reviewed in (4.55). With these properties it is possible to further reduce the integrity bases listed in Table 4.1, thereby eliminating redundant

[5] *David Hilbert* (1862-1943): German mathematician and philosopher. His finiteness theorem for invariant functions was published in *Mathematische Annalen* and is honoured by one of the editors as "without doubt, this is the most important work on general algebra that the *Annalen* has ever published".

invariants. The resulting new set is shown in Table 4.2. Following this, the solid strain energy function may then have the form

$$W^S_{\mathrm{EQ}} \;=\; W^S_{\mathrm{EQ}}(J_{S1}\,,\; J_{S2}\,,\; J_{S3}\,,\ldots,\; J_{Sn}) \tag{4.63}$$

which *a priori* satisfies condition (4.60). The problem is then to find the minimal set of basic and mixed invariants J_{Sn} suitable for the respective symmetry groups. In this monograph, only the results for fibre-reinforced materials are briefly reviewed. For a more comprehensive description, the reader is referred to Spencer [194, 195] or Boehler [22].

tensorial arguments	basic and mixed invariants J_{Sn}	usage
$\mathbf{C}_S$	$\mathrm{tr}\,\mathbf{C}_S\,,\ \mathrm{tr}\,\mathbf{C}_S^2\,,\ \mathrm{tr}\,\mathbf{C}_S^3$	isotropy
$\mathbf{C}_S,\ \boldsymbol{\mathcal{M}}_a^S$	$\mathrm{tr}\,\mathbf{C}_S\,,\ \mathrm{tr}\,\mathbf{C}_S^2\,,\ \mathrm{tr}\,\mathbf{C}_S^3\,,$ $\mathrm{tr}\,(\boldsymbol{\mathcal{M}}_a^S\mathbf{C}_S)\,,\ \mathrm{tr}\,(\boldsymbol{\mathcal{M}}_a^S\mathbf{C}_S^2)\,,$	transverse isotropy
$\mathbf{C}_S,\ \boldsymbol{\mathcal{M}}_a^S,\ \boldsymbol{\mathcal{M}}_b^S$	$\mathrm{tr}\,\mathbf{C}_S\,,\ \mathrm{tr}\,\mathbf{C}_S^2\,,\ \mathrm{tr}\,\mathbf{C}_S^3\,,$ $\mathrm{tr}\,(\boldsymbol{\mathcal{M}}_a^S\mathbf{C}_S)\,,\ \mathrm{tr}\,(\boldsymbol{\mathcal{M}}_a^S\mathbf{C}_S^2)\,,$ $\mathrm{tr}\,(\boldsymbol{\mathcal{M}}_b^S\mathbf{C}_S)\,,\ \mathrm{tr}\,(\boldsymbol{\mathcal{M}}_b^S\mathbf{C}_S^2)\,,$ $\mathrm{tr}\,(\boldsymbol{\mathcal{M}}_a^S\boldsymbol{\mathcal{M}}_b^S\mathbf{C}_S)\,,\ \mathrm{tr}\,(\boldsymbol{\mathcal{M}}_a^S\boldsymbol{\mathcal{M}}_b^S\mathbf{C}_S^2)\,,\ \mathrm{tr}\,(\boldsymbol{\mathcal{M}}_a^S\boldsymbol{\mathcal{M}}_b^S)$	orthotropy/ prismatic symmetry

Table 4.2: *Minimal integrity basis for fibre-reinforced materials.*

Isotropy: The representation for isotropic materials using invariants is widely known and is comprehensively described in Rivlin & Ericksen [170]. Thus, this most general group is only discussed in order to define a consistent notation. The corresponding integrity base can be taken from Table 4.2 yielding $\mathcal{I}_S = \{J_{S1} = \mathrm{tr}\,\mathbf{C}_S\,,\ J_{S2} = \mathrm{tr}\,\mathbf{C}_S^2\,,\ J_{S3} = \mathrm{tr}\,\mathbf{C}_S^3\}$. However, in finite elasticity, a slightly different set is usually applied, which corresponds to the principal invariants I_{Sn} of $\mathbf{B}_S$ and $\mathbf{C}_S$ described in Subsection 3.2.4, yielding

$$\mathcal{I}_S = \{I_{S1}\,,\ I_{S2}\,,\ I_{S3}\} \quad \text{with} \quad I_{S1} = \mathrm{tr}\,\mathbf{C}_S\,, \quad I_{S2} = \mathrm{tr}\,(\mathrm{cof}\,\mathbf{C}_S)\,, \quad I_{S3} = \det\mathbf{C}_S\,. \tag{4.64}$$

This set will be used throughout this work instead of the respective three basic invariants. It can be shown that the basic invariants J_{Sn} are related to the principal invariants via

$$J_{S1} = I_{S1}\,, \qquad J_{S2} = I_{S1}^2 - 2\,I_{S1}\,, \qquad J_{S3} = I_{S1}^3 - 3\,I_{S1}\,I_{S2} + 3\,I_{S3}\,. \tag{4.65}$$

Also note that the principal invariants are related to the eigenvalues $\lambda_{S(k)}$ of $\mathbf{C}_S$ via (3.48). Consequently, the strain energy of an isotropic solid must be a function (polynomial) of either the invariants or eigenvalues (squared principal stretches) $\lambda_{S(k)}$ of $\mathbf{C}_S$ yielding

$$W^S_{\mathrm{EQ}}(\mathbf{C}_S) \quad\longrightarrow\quad W^S_{\mathrm{EQ}}(I_{S1}\,,\ I_{S2}\,,\ I_{S3}) \quad \text{or} \quad W^S_{\mathrm{EQ}}(\lambda_{S1}\,,\ \lambda_{S2}\,,\ \lambda_{S3})\,. \tag{4.66}$$

Transverse isotropy: In the case of transverse isotropy, a unit fibre vector $\mathbf{a}_0^S$ needs to be defined in the reference configuration in order to compute the structural tensor $\boldsymbol{\mathcal{M}}_a^S$. Following this, the mixed invariant J_{S4} can be reformulated yielding

$$J_{S4} = \mathrm{tr}\,(\boldsymbol{\mathcal{M}}_a^S\,\mathbf{C}_S) = (\mathbf{a}_0^S \otimes \mathbf{a}_0^S)^T \cdot \mathbf{C}_S = \mathbf{a}_0^S \cdot \mathbf{C}_S\,\mathbf{a}_0^S = \mathbf{F}_S\,\mathbf{a}_0^S \cdot \mathbf{F}_S\,\mathbf{a}_0^S = \mathbf{a}^S \cdot \mathbf{a}^S. \tag{4.67}$$

Herein, J_{S4} represents the squared fibre stretch (length) in the direction of the mapped fibre orientation $\mathbf{a}^S = \mathbf{F}_S\,\mathbf{a}_0^S$ in the actual configuration. The remaining mixed invariant

$$J_{S5} = \mathrm{tr}\,(\boldsymbol{\mathcal{M}}_a^S\,\mathbf{C}_S^2) = \mathbf{a}_0^S \cdot \mathbf{C}_S^2\,\mathbf{a}_0^S \tag{4.68}$$

has no physical meaning. Hence, the strain energy of a transversely isotropic solid takes the form

$$W_{\mathrm{EQ}}^S(\mathbf{C}_S\,,\,\boldsymbol{\mathcal{M}}_a^S) \quad\longrightarrow\quad W_{\mathrm{EQ}}^S(\lambda_{S1}\,,\,\lambda_{S2}\,,\,\lambda_{S3}\,,\,J_{S4}\,,\,J_{S5})\,. \tag{4.69}$$

Prismatic symmetry is the general case for a reinforcement with two mechanically distinct families of fibres that are arranged in one plane. The special cases for orthogonal symmetries can then be derived from here on. Following this, the respective invariants can be taken from Table 4.2. However, one of the mixed invariants of the list is a constant and yields the cosine of the fibre angle ϕ_0^S in the reference configuration, i. e.,

$$\mathrm{tr}\,(\boldsymbol{\mathcal{M}}_a^S\,\boldsymbol{\mathcal{M}}_b^S) = (\mathbf{a}_0^S \otimes \mathbf{a}_0^S) \cdot (\mathbf{b}_0^S \otimes \mathbf{b}_0^S) = (\mathbf{a}_0^S \cdot \mathbf{b}_0^S)^2 = \cos^2(2\phi_0^S)\,. \tag{4.70}$$

Hence, it will be omitted from the set of invariants to be used as arguments in W_{EQ}^S. The relation above becomes apparent, when Figure 4.2 (b) is recalled, where the fibre vectors $\mathbf{a}_0^S$ and $\mathbf{b}_0^S$ are defined in the local coordinate frame by the fibre angle ϕ_0^S. Using basic geometry, the relation for the fibre angle can be computed from the unit fibre vectors via

$$\cos\,(2\phi_0^S) = \frac{\mathbf{a}_0^S \cdot \mathbf{b}_0^S}{|\mathbf{a}_0^S||\mathbf{b}_0^S|} = \mathbf{a}_0^S \cdot \mathbf{b}_0^S\,. \tag{4.71}$$

Moreover, another invariant can be cancelled out, as the redundant member

$$\mathrm{tr}\,(\boldsymbol{\mathcal{M}}_a^S\,\boldsymbol{\mathcal{M}}_b^S\,\mathbf{C}_S^2) = \cos\,(2\phi_0^S)\,\mathbf{a}_0^S \cdot \mathbf{C}_S^2\,\mathbf{b}_0^S \tag{4.72}$$

can be expressed with the remaining invariants via an identity defined in Spencer [195]. Hence, the minimal set of invariants appropriate to describe prismatic symmetry is given by the sets used for transverse isotropy as well as the three additional members

$$J_{S6} = \mathbf{b}_0^S \cdot \mathbf{C}_S\,\mathbf{b}_0^S\,, \qquad J_{S7} = \mathbf{b}_0^S \cdot \mathbf{C}_S^2\,\mathbf{b}_0^S\,, \qquad J_{S8} = \cos\,(2\Phi)\,\mathbf{a}_0^S \cdot \mathbf{C}_S\,\mathbf{b}_0^S\,. \tag{4.73}$$

Following this, the corresponding strain energy may take the form

$$W_{\mathrm{EQ}}^S(\mathbf{C}_S\,,\,\boldsymbol{\mathcal{M}}_a^S\,,\,\boldsymbol{\mathcal{M}}_b^S) \;\longrightarrow\; W_{\mathrm{EQ}}^S(\lambda_{S1}\,,\,\lambda_{S2}\,,\,\lambda_{S3}\,,\,J_{S4}\,,\,J_{S5}\,,\,J_{S6}\,,\,J_{S7}\,,\,J_{S8})\,. \tag{4.74}$$

Orthogonal symmetry: As already discussed in Subsection 4.3.1, this case includes two sub-cases. Firstly, the case is considered where two mechanically distinct families of fibres are orthogonally arranged within a plane. Following this, the invariant $J_{S8} = \cos\,(2\Phi)\,\mathbf{a}_0^S \cdot \mathbf{C}_S\,\mathbf{b}_0^S = 0$ vanishes from the list of arguments in equation (4.74).

If the two families of fibres are mechanically equivalent, orthogonality is implied by the bisectors of the fibres. Hence, the strain energy function W_{EQ}^S must be symmetric with respect to interchanges of $\mathbf{a}_0$ and $\mathbf{b}_0$. This yields a slightly different integrity basis

$$\mathcal{I}_S = \{\lambda_{S1}\,,\,\lambda_{S2}\,,\,\lambda_{S3}\,,\,J_{S8}\,,\,J_{S9}\,,\,J_{S10}\,,\,J_{S11}\}\,, \tag{4.75}$$

as an appropriate set of arguments for W^S_{EQ}, where the new invariants are computed by

$$\begin{aligned} J_{S9} &= \mathbf{a}^S_0 \cdot \mathbf{C}_S\, \mathbf{a}^S_0 \;+\; \mathbf{b}^S_0 \cdot \mathbf{C}_S\, \mathbf{b}^S_0 \qquad J_{S10} \;=\; (\mathbf{a}^S_0 \cdot \mathbf{C}_S\, \mathbf{a}^S_0)(\mathbf{b}^S_0 \cdot \mathbf{C}_S\, \mathbf{b}^S_0)\,, \\ J_{S11} &= \mathbf{a}^S_0 \cdot \mathbf{C}^2_S\, \mathbf{a}^S_0 \;+\; \mathbf{b}^S_0 \cdot \mathbf{C}^2_S\, \mathbf{b}^S_0\,. \end{aligned} \tag{4.76}$$

However, it can be shown that the logical expansion $J_{S12} = J_{S5}\, J_{S7}$ can be expressed in terms of the other invariants and is hence omitted in this set, cf. Spencer [195]. It can also be proven that the set of invariants (4.76) yields the same integrity basis found in the list of arguments in (4.74).

Remark: Correspondingly, the non-equilibrium part W^S_{NEQ} of the strain energy function has to be represented using also the concept of isotropic tensor functions. Recalling the non-scalar arguments used in equation (4.36) reveals that this requisite is not naturally given. At first sight, the elastic parts of the *Cauchy-Green* deformation tensors are not affected by orthogonal transformation resulting from considerations with respect to the inherent material symmetry, as inelastic texture developments are excluded. Hence, the elastic deformation tensors $(\widehat{\mathbf{C}}_{Se})_n$ do not register rotations of the reference configuration, because their basis systems are defined on the respective n^{th} intermediate configuration. However, recalling that the multiplicative split $\mathbf{F}_S = \mathbf{F}_{Se}\,\mathbf{F}_{Si}$ is not unique reveals the problem. As already mentioned in the remark of Subsection 3.2.2, several intermediate configurations are simultaneously possible, which differ only by proper orthogonal rigid body rotations $\widehat{\mathbf{H}}_n \in \mathcal{SO}_3$. As a result, the non-equilibrium strain energy is automatically subjected to the following invariance condition

$$W^S_{\mathrm{NEQ}}[(\widehat{\mathbf{C}}_{Se})_n] = W^S_{\mathrm{NEQ}}[(\overset{\circ}{\widehat{\mathbf{C}}}_{Se})_n] \quad \forall\, \widehat{\mathbf{H}}_n \in \mathcal{SO}_3\,,\, (\widehat{\mathbf{C}}_{Se})_n\,, \tag{4.77}$$

where $(\overset{\circ}{\widehat{\cdot}})$ indicates the quantities of the rotated intermediate configurations. The idea is now to prove that the non-uniqueness of the multiplicative split of the deformation gradient does not necessarily lead to a weak spot in the underlying finite solid kinematics. In this regard, the procedure of Subsection 4.2.2 is applied yielding the rotated elastic parts of the solid deformation gradients

$$(\overset{\circ}{\mathbf{F}}_{Se})_n = \frac{\partial \mathbf{x}}{\partial(\overset{\circ}{\widehat{\mathbf{x}}}_{Si})_n} = \frac{\partial \mathbf{x}}{\partial(\widehat{\mathbf{x}}_{Si})_n}\,\frac{\partial(\widehat{\mathbf{x}}_{Si})_n}{\partial(\overset{\circ}{\widehat{\mathbf{x}}}_{Si})_n} = (\mathbf{F}_{Se})_n\,\widehat{\mathbf{H}}^{-1}_n \quad \text{with} \quad \widehat{\mathbf{H}}_n = \frac{\partial(\overset{\circ}{\widehat{\mathbf{x}}}_{Si})_n}{\partial(\widehat{\mathbf{x}}_{Si})_n}\,, \tag{4.78}$$

as well as the rotated elastic *Cauchy-Green* deformation tensors

$$(\overset{\circ}{\widehat{\mathbf{C}}}_{Se})_n = \widehat{\mathbf{H}}^{T-1}_n (\mathbf{F}^T_{Se})_n\,(\mathbf{F}_{Se})_n\,\widehat{\mathbf{H}}^{-1}_n = \widehat{\mathbf{H}}_n\,(\widehat{\mathbf{C}}_{Se})_n\,\widehat{\mathbf{H}}^T_n\,. \tag{4.79}$$

Applying the procedure for isotropic tensor functions yields the similar result for

$$W^S_{\mathrm{NEQ}}[(\widehat{\mathbf{C}}_{Se})_n] \qquad \longrightarrow \qquad \begin{cases} W^S_{\mathrm{NEQ}}[(I_{Se1})_n\,,\,(I_{Se2})_n\,,\,(I_{Se3})_n] \quad \text{or} \\ W^S_{\mathrm{NEQ}}[(\lambda_{Se1})_n\,,\,(\lambda_{Se2})_n\,,\,(\lambda_{Se3})_n]\,, \end{cases} \tag{4.80}$$

but now depending of the elastic principal invariants or eigenvalues of $(\widehat{\mathbf{C}}_{Se})_n$ or $(\mathbf{B}_{Se})_n$.

□

4.3.5 Further Requirements for Strain Energy Functions

Having defined a list of suitable scalar arguments for the solid strain energy function W^S, some further restrictions of physical and mathematical nature must be applied, which are briefly discussed in the following.

Physical limitations result firstly from the incompressibility of the solid skeleton and secondly, from the natural observation that infinite elongations require an infinite amount of energy to achieve that deformation state. Having a classical incompressible single-phase solid in mind, the first requirement needs to be adopted regarding the application to porous media. Herein, an aggregate consisting of two incompressible media is still compressible as the respective volume fractions may change. Hence, for materially incompressible constituents, a volumetric deformation is only possible until the fluid has been totally expressed, i. e., until the deformation reaches a state, where the pore space in nil. Hence, volumetric compressions need to be penalised, whenever the solidity n^S comes close to unity. Following this, the resulting restrictions can be formulated yielding

$$W^S_{\mathrm{EQ}} \to +\infty \quad \text{for} \quad \begin{cases} \det \mathbf{F}_S \to n^S_{0S} \\ (\, ||\mathbf{F}_S|| + ||\mathrm{cof}\, \mathbf{F}_S|| + \det \mathbf{F}_S \,) \to +\infty \, , \end{cases} \tag{4.81}$$

where $||(\,\cdot\,)||$ indicates the quadratic norm of a tensor, e. g., $||\mathbf{F}_S|| = \sqrt{\mathbf{F}_S \cdot \mathbf{F}_S}$. Naturally, analogous considerations hold for the non-equilibrium part, viz.:

$$W^S_{\mathrm{NEQ}} \to +\infty \quad \text{for} \quad \begin{cases} \det (\mathbf{F}_{Se})_n \to (n^S_{Si})_n \\ [\, ||(\mathbf{F}_{Se})_n|| + ||\mathrm{cof}\, (\mathbf{F}_{Se})_n|| + \det (\mathbf{F}_{Se})_n \,] \to +\infty \, . \end{cases} \tag{4.82}$$

Herein, the quantities $(n^S_{Si})_n$ denote the limiting inelastic solid volume fractions of a *Maxwell* element which result from inelastic volumetric compressions. Proceeding from the multiplicative decomposition (3.18) of the solid deformation gradient $\mathbf{F}_S$, elastic and inelastic *Jacobian*s can be introduced via

$$J_S = \det \mathbf{F}_S = \det [(\mathbf{F}_{Se})_n \, (\mathbf{F}_{Si})_n] = \det [(\mathbf{F}_{Se})_n] \det [(\mathbf{F}_{Si})_n] =: (J_{Se})_n \, (J_{Si})_n \, . \tag{4.83}$$

Inserting (4.83) into the analytically integrated volume balance $(4.4)_2$ of the solid skeleton and recalling the idea of the inelastic intermediate configurations serving as reference configurations for the respective non-equilibrium strain energies yields similar conditional equations for the inelastic solid volume fractions defined by:

$$n^S = n^S_{0S} \, J_S^{-1} = n^S_{0S} \, [(J^{-1}_{Se})_n \, (J^{-1}_{Si})_n] =: (n^S_{Si})_n \, (J^{-1}_{Se})_n \quad \text{with} \quad (n^S_{Si})_n = n^S_{0S} \, (J^{-1}_{Si})_n \, . \tag{4.84}$$

Mathematical limitations stem from considerations regarding the numerical solution of variational problems, as it will be discussed in Section 5.3. In this regard, the essential requirement is the existence of minimisers in order to obtain solutions for general initial boundary value problems. Following the argumentation of Ball [13] and references therein, the existence of minimisers is guaranteed, if W^S is a convex function in $\mathbf{F}_S$ and $\mathbf{F}_{Se}$, respectively. From a mathematical point of view this requirement comes handy, as the

solutions obtained are also unique. However, from a physical point of view, convexity conflicts with the requirement of material frame indifference. Moreover, the description of material instabilities is *a priori* ruled out, as a strictly convex strain energy is unique, whereas especially its non-uniqueness is essential for the description of buckling.

A suitable condition to overcome this deficiency was introduced by Morrey [142] and is known as quasiconvexity. However, the shortcomings of quasiconvexity are the included growth conditions, which conflict with the requirements $(4.81)_2$ and $(4.82)_2$, as well as its integral character, which is hard to apply on functions. As a consequence, Ball [13] introduced the polyconvexity criterion for strain energy functions which directly implies quasiconvexity without using any growth conditions. Since the proof of polyconvexity is carried out pointwise, it is relatively straightforward to prove. Following this, the strain energies W^S_{EQ} and W^S_{EQ} are polyconvex if and only if there exist functions Ψ_{EQ} and Ψ_{NEQ} (in general non-unique) such that

$$\begin{aligned} W^S_{\mathrm{EQ}}(\mathbf{F}_S) &= \Psi_{\mathrm{EQ}}(\mathbf{F}_S\,,\,\mathrm{cof}\,\mathbf{F}_S\,,\,\det\mathbf{F}_S) \quad \text{and} \\ W^S_{\mathrm{NEQ}}[(\mathbf{F}_{Se})_n] &= \Psi_{\mathrm{NEQ}}[(\mathbf{F}_{Se})_n\,,\,\mathrm{cof}\,(\mathbf{F}_{Se})_n\,,\,\det\,(\mathbf{F}_{Se})_n]\,, \end{aligned} \tag{4.85}$$

where the functions Ψ_{EQ} and Ψ_{NEQ} are convex with respect to each of the principal minors $\mathbf{F}_S$, $\mathrm{cof}\,\mathbf{F}_S$, and $\det\mathbf{F}_S$ as well as $\mathbf{F}_{Se}$, $\mathrm{cof}\,\mathbf{F}_{Se}$, and $\det\mathbf{F}_{Se}$, separately. Exactly this is the case, whenever the second derivatives are positive semidefinite $\forall\,\mathbf{G}\neq\mathbf{0}$, i. e.,

$$\begin{gathered} \frac{\partial^2\Psi_{\mathrm{EQ}}}{\partial\mathbf{F}_S\otimes\partial\mathbf{F}_S}\cdot(\mathbf{G}\otimes\mathbf{G})\geq 0\,, \quad \frac{\partial^2\Psi_{\mathrm{NEQ}}}{\partial(\mathbf{F}_{Se})_n\otimes\partial(\mathbf{F}_{Se})_n}\cdot(\mathbf{G}\otimes\mathbf{G})\geq 0\,, \\ \frac{\partial^2\Psi_{\mathrm{EQ}}}{\partial\,\mathrm{cof}\,\mathbf{F}_S\otimes\partial\,\mathrm{cof}\,\mathbf{F}_S}\cdot(\mathbf{G}\otimes\mathbf{G})\geq 0\,, \quad \frac{\partial^2\Psi_{\mathrm{NEQ}}}{\partial\,\mathrm{cof}\,(\mathbf{F}_{Se})_n\otimes\partial\,\mathrm{cof}\,(\mathbf{F}_{Se})_n}\cdot(\mathbf{G}\otimes\mathbf{G})\geq 0\,, \\ \frac{\partial^2\Psi_{\mathrm{EQ}}}{\partial(\det\mathbf{F}_S)^2}\geq 0\,, \quad \frac{\partial^2\Psi_{\mathrm{NEQ}}}{\partial[\det\,(\mathbf{F}_{Se})_n]^2}\geq 0\,, \end{gathered} \tag{4.86}$$

where $\mathbf{G}$ denotes an arbitrary second-order tensor. Note in passing that the requirements stemming from material frame indifference and material symmetry are not violated, as the respective invariants used in, e. g., equation (4.74), are implicitly depending on the principal minors. Moreover, the physical interpretation of (4.86) is that polyconvexity claims for material stability with respect to perturbations in length, area, and volume, as the principal minors are responsible for the corresponding transports of infinitesimal material elements, cf. equations (3.28).

For a more detailed mathematical description of this issue, please refer to the classical works of Ciarlet [34], Dacorogna [36], Marsden & Hughes [135], Šilhavý [186] as well as to the comprehensive summaries found in Schröder [178] or Balzani [14].

4.4 The Solid Skeleton

The purpose of this Section is to apply all the restrictions of the preceding subsections in order to finally postulate a suitable strain energy function for the solid skeleton of a swelling-active and fibre-reinforced biological soft tissue. In particular, special attention

is drawn on the modular character of W^S, where it is advantageous to *a priori* define a general structure to be used. The actual postulation of the respective strain energies is then carried out thereafter.

4.4.1 Structure of the Strain Energy and its Derivatives

As already discussed in Subsection 4.2.3, the strain energy W^S consists of at least two main parts. An equilibrium part W^S_{EQ}, which is associated with the overall deformation of the underlying rheological model, as well as a non-equilibrium part W^S_{NEQ} characterising the elastic springs in the *Maxwell* elements. Recalling the characteristic properties of the IVD as well as its mechanical behaviour of Section 2.3, the equilibrium part must be capable of capturing the elastic collagen fibres of type I, while the non-equilibrium part is responsible for the viscous over stresses in the isotropic portion of the tissue.

Moreover, osmotic effects must be included regarding the water attracting characteristic of the PG's in the ECM. At first sight, however, it is not comprehensible why the osmotic pressure, which is usually measured in the pore fluid, is computed from the solid strain energy. This fact becomes evident in the context of the underlying extended binary model, where osmosis triggers a diffusion process, thereby causing an influx of the surrounding fluid. In turn, the additional fluid inside the tissue leads to a variation of the volume which is occupied by the incompressible pore fluid, cf. Subsection 2.4.2. Thus, a purely volumetric deformation (dilatation) is initiated in the case of isotropic material behaviour, which may be accompanied by shape changes in cases where type-I collagen fibres are present. Following this, the osmotic pressure is actually a reaction force of hydrostatic character in the solid skeleton which is caused by a permanent "internal displacement boundary condition". As a consequence from the evaluation of the *Clausius-Planck* inequality, the osmotic pressure contribution must be derivable from a solid strain energy function, thereby contributing to a thermodynamically consistent model.

As a next step, the variables of the respective partial strain energies need to be assigned. Proceeding from the idea that two adjacent lamellae of the AF, each exhibiting transverse isotropic behaviour, have equivalent mechanical characteristics of the embedded collagen fibres leads to a locally orthotropic material, as is described in Subsection 4.3.4. Following this, the resulting strain energy is constitutively split into a purely isotropic part (ISO) and an anisotropic contribution (ANISO), which solely depends on the mixed invariants of equation (4.74). Concerning the osmotic contribution (OSM), the most suitable process variable would be $\det \mathbf{F}_S = (\det \mathbf{C}_S)^{\frac{1}{2}}$, which describes the local dilatation of the ECM, while the change in shape is caused by the anisotropic stress response. Thus, the conclusive structure yields

$$W^S = W^S_{\mathrm{EQ}} + W^S_{\mathrm{NEQ}} \quad \left\{ \begin{array}{rcl} W^S_{\mathrm{EQ}} & = & W^S_{\mathrm{OSM}}(\det \mathbf{F}_S) + W^S_{\mathrm{ISO}}(\lambda_{S1}\,,\,\lambda_{S2}\,,\,\lambda_{S3}) + \\ & & + \; W^S_{\mathrm{ANISO}}(J_{S4}\,,\,J_{S5}\,,\,J_{S6}\,,\,J_{S7}\,,\,J_{S8})\,, \\ W^S_{\mathrm{NEQ}} & = & W^S_{\mathrm{NEQ}}[(\lambda_{Se1})_n\,,\,(\lambda_{Se2})_n\,,\,(\lambda_{Se3})_n]\,. \end{array} \right. \tag{4.87}$$

Accordingly, the solid extra stress as well as the material tangent will result in the same split. This is easily verified by inserting the structure of (4.87) into equation (4.42) yielding

the 2nd *Piola-Kirchhoff* stress of the solid skeleton in the reference configuration, viz.:

$$\mathbf{S}_E^S = \overbrace{\underbrace{2\,\frac{\partial W_{\mathrm{OSM}}^S}{\partial \mathbf{C}_S}}_{\mathbf{S}_{\mathrm{OSM}}^S} + \underbrace{2\,\frac{\partial W_{\mathrm{ISO}}^S}{\partial \mathbf{C}_S}}_{\mathbf{S}_{\mathrm{ISO}}^S} + \underbrace{2\,\frac{\partial W_{\mathrm{ANISO}}^S}{\partial \mathbf{C}_S}}_{\mathbf{S}_{\mathrm{ANISO}}^S}}^{\mathbf{S}_{\mathrm{EQ}}^S} + \underbrace{\sum_{n=1}^{N} \overbrace{2\,(\mathbf{F}_{Si}^{-1})_n\,\frac{\partial W_{\mathrm{NEQ}}^S}{\partial (\widehat{\mathbf{C}}_{Se})_n}\,(\mathbf{F}_{Si}^{T-1})_n}^{\mathbf{S}_n^S}}_{\mathbf{S}_{\mathrm{NEQ}}^S} \,. \tag{4.88}$$

All other stresses are obtained by applying the respective covariant transports of Section 3.3, thereby leaving the additive structure of the overall solid extra stress unchanged. Please note that the subscript ISO does not imply an isochoric split of the deformation gradient, like it is used in many other works.

Moreover, regarding the numerical solution of the global system of equations in Section 5.3, the linearisation of the constitutively introduced stresses (4.88) is needed. Herein, the so-called material (continuum) tangent is introduced as a fourth-order tensor, which relates the incremental change of the stress to the incremental change of the conjugated strain tensor. Thus, the following relation holds in the reference configuration:

$$\mathrm{d}\mathbf{S}_E^S = \frac{\partial \mathbf{S}_E^S}{\partial \mathbf{E}_S}\,\mathrm{d}\mathbf{E}_S = \overset{4}{\boldsymbol{\mathcal{B}}}{}^{\mathrm{S}}\,\mathrm{d}\mathbf{E}_S \qquad \text{with} \qquad \overset{4}{\boldsymbol{\mathcal{B}}}{}^{\mathrm{S}} = \frac{\partial \mathbf{S}_{\mathrm{EQ}}^S}{\partial \mathbf{E}_S} + \frac{\partial \mathbf{S}_{\mathrm{NEQ}}^S}{\partial \mathbf{E}_S} = \overset{4}{\boldsymbol{\mathcal{B}}}{}^{\mathrm{S}}_{\mathrm{EQ}} + \overset{4}{\boldsymbol{\mathcal{B}}}{}^{\mathrm{S}}_{\mathrm{NEQ}}\,, \tag{4.89}$$

while the respective quantities of the actual configuration are obtained via a covariant forth-order push-forward operation yielding

$$\overset{4}{\boldsymbol{\mathcal{C}}}{}^{\mathrm{S}} = \overset{4}{\boldsymbol{\mathcal{C}}}{}^{\mathrm{S}}_{\mathrm{EQ}} + \overset{4}{\boldsymbol{\mathcal{C}}}{}^{\mathrm{S}}_{\mathrm{NEQ}} = (\mathbf{F}_S \otimes \mathbf{F}_S)^{\overset{23}{T}} (\overset{4}{\boldsymbol{\mathcal{B}}}{}^{\mathrm{S}}_{\mathrm{EQ}} + \overset{4}{\boldsymbol{\mathcal{B}}}{}^{\mathrm{S}}_{\mathrm{NEQ}})\,(\mathbf{F}_S^T \otimes \mathbf{F}_S^T)^{\overset{23}{T}}. \tag{4.90}$$

In particular, the computation of the equilibrium contribution is straightforward yielding

$$\overset{4}{\boldsymbol{\mathcal{B}}}{}^{\mathrm{S}}_{\mathrm{EQ}} = \underbrace{4\,\frac{\partial^2 W_{\mathrm{OSM}}^S}{\partial \mathbf{C}_S \otimes \partial \mathbf{C}_S}}_{\overset{4}{\boldsymbol{\mathcal{B}}}{}^{\mathrm{S}}_{\mathrm{OSM}}} + \underbrace{4\,\frac{\partial^2 W_{\mathrm{ISO}}^S}{\partial \mathbf{C}_S \otimes \partial \mathbf{C}_S}}_{\overset{4}{\boldsymbol{\mathcal{B}}}{}^{\mathrm{S}}_{\mathrm{ISO}}} + \underbrace{4\,\frac{\partial^2 W_{\mathrm{ANSIO}}^S}{\partial \mathbf{C}_S \otimes \partial \mathbf{C}_S}}_{\overset{4}{\boldsymbol{\mathcal{B}}}{}^{\mathrm{S}}_{\mathrm{ANISO}}} \,. \tag{4.91}$$

However, the non-equilibrium contribution is a bit more challenging as it actually consists of two parts. One resulting from the movement of the actual configuration, thereby keeping the intermediate configurations frozen, and the other one resulting from the movement of the intermediate configurations at a frozen actual configuration, viz.:

$$\overset{4}{\boldsymbol{\mathcal{B}}}{}^{\mathrm{S}}_{\mathrm{NEQ}} = \underbrace{\sum_{n=1}^{N} \overbrace{\frac{\partial \mathbf{S}_n^S}{\partial (\mathbf{E}_{Se})_n}\,\frac{\partial (\mathbf{E}_{Se})_n}{\partial \mathbf{E}_S}}^{\overset{4}{\mathbf{B}}{}_n^S}\Bigg|_{(\mathbf{E}_{Si})_n = \mathrm{const.}}}_{\overset{4}{\mathbf{B}}{}_{\mathrm{NEQ}}^S} + \underbrace{\sum_{n=1}^{N} \frac{\partial \mathbf{S}_n^S}{\partial (\mathbf{E}_{Si})_n}\,\frac{\partial (\mathbf{E}_{Si})_n}{\partial \mathbf{E}_S}\Bigg|_{\mathbf{E}_S = \mathrm{const.}}}_{\overset{4}{\mathbf{B}}{}_{\mathrm{INT}}^S} \,. \tag{4.92}$$

Using the 4th-order identity at constant $(\mathbf{E}_{Si})_n$

$$\frac{\partial(\mathbf{E}_{Se})_n}{\partial\mathbf{E}_S} = \left.\frac{\partial\big[\mathbf{E}_S - (\mathbf{E}_{Si})_n\big]}{\partial\mathbf{E}_S}\right|_{(\mathbf{E}_{Si})_n = \text{const.}} = \frac{\partial\mathbf{E}_S}{\partial\mathbf{E}_S} = (\mathbf{I}\otimes\mathbf{I})^{\frac{23}{T}} = \overset{4}{\mathbf{I}}, \tag{4.93}$$

as well as a rearrangement of relation (4.43) for the over stresses

$$\mathbf{S}_n^S = [(\mathbf{F}_{Si}^{-1})_n \otimes (\mathbf{F}_{Si}^{-1})_n]^{\frac{23}{T}}\, 2\,\frac{\partial W_{\text{NEQ}}^S}{\partial(\widehat{\mathbf{C}}_{Se})_n} = [(\mathbf{F}_{Si}^{-1})_n \otimes (\mathbf{F}_{Si}^{-1})_n]^{\frac{23}{T}}\, \widehat{\boldsymbol{\tau}}_n^S, \tag{4.94}$$

the first part of (4.92) is obtained for constant $(\mathbf{E}_{Si})_n$ and $(\mathbf{F}_{Si})_n$ yielding

$$\begin{aligned}
\overset{4}{\mathbf{B}}{}_n^S &= [(\mathbf{F}_{Si}^{-1})_n \otimes (\mathbf{F}_{Si}^{-1})_n]^{\frac{23}{T}}\, \frac{\partial\widehat{\boldsymbol{\tau}}_n^S}{\partial(\widehat{\boldsymbol{\Gamma}}_{Se})_n}\,\frac{\partial(\widehat{\boldsymbol{\Gamma}}_{Se})_n}{\partial(\mathbf{E}_{Se})_n} \\
&= [(\mathbf{F}_{Si}^{-1})_n \otimes (\mathbf{F}_{Si}^{-1})_n]^{\frac{23}{T}}\, 2\,\frac{\partial\widehat{\boldsymbol{\tau}}_n^S}{\partial(\widehat{\mathbf{C}}_{Se})_n}\,\frac{\partial(\mathbf{F}_{Si}^{T-1})_n\,(\mathbf{E}_{Se})_n\,(\mathbf{F}_{Si}^{-1})_n}{\partial(\mathbf{E}_{Se})_n} \\
&= [(\mathbf{F}_{Si}^{-1})_n \otimes (\mathbf{F}_{Si}^{-1})_n]^{\frac{23}{T}}\, \underbrace{4\,\frac{\partial^2 W_{\text{NEQ}}^S}{\partial(\widehat{\mathbf{C}}_{Se})_n \otimes \partial(\widehat{\mathbf{C}}_{Se})_n}}_{\overset{4}{\widehat{\mathbf{C}}}{}_n^S}\, [(\mathbf{F}_{Si}^{T-1})_n \otimes (\mathbf{F}_{Si}^{T-1})_n]^{\frac{23}{T}},
\end{aligned} \tag{4.95}$$

where $(\widehat{\mathbf{C}}_n^S)^{\underline{4}}$ denotes the partial material tangent of a *Maxwell* element in the intermediate configuration. In order to obtain (4.95), use was made of the derivatives defined in Appendix A.2. The second term $(\mathbf{B}_{\text{INT}}^S)^{\underline{4}}$ in (4.92) denotes the contribution depending on the internal (history) variables, which cannot be computed at this stage, as the derivative $\partial(\mathbf{E}_{Si})_n/\partial\mathbf{E}_S$ depends on the time discretisation method for the solution of the evolution equations of the internal variables. Following this, the computation of the consistent viscoelastic material tangent operator $(\boldsymbol{\mathcal{B}}_{\text{NEQ}}^S)^{\underline{4}}$ will be discussed in Section 5.3.2.

4.4.2 Osmotic Contribution

Starting with the osmotic contribution, the partial strain energy W_{OSM}^S must depend on the volume dilatation of the solid skeleton and is postulated in a straightforward manner using the knowledge of *van't Hoff*'s law described in Subsection 2.4.2. In this regard, it must be shown that a functional W_{OSM}^S exists such that the overall model satisfies the thermodynamical principles of Section 4.2. Thus, a volumetric strain energy is postulated with the aid of equation (4.9) and expressed in terms of the *Jacobi*an $J_S = \det\mathbf{F}_S$.

Osmotic strain energy of the solid skeleton

$$W_{\text{OSM}}^S(c_m^{fc}) = R\,\Theta\,c_{0S}^{fc}\,n_{0S}^F\left[\frac{2\,\bar{c}_m}{c_m^{fc}} - \frac{\sqrt{4\,\bar{c}_m^2 + (c_m^{fc})^2}}{c_m^{fc}} + \operatorname{asinh}\left(\frac{c_m^{fc}}{2\,\bar{c}_m}\right)\right] \quad \text{with} \tag{4.96}$$

$$c_m^{fc}(\det\mathbf{F}_S) = c_{0S}^{fc}\,n_{0S}^F\,(\det\mathbf{F}_S - n_{0S}^S)^{-1}$$

Herein, R denotes the universal gas constant, Θ is the absolute temperature, whereas $\bar{c}_m$ is the molar concentration of the external monovalent salt solution surrounding the tissue and c^{fc}_{0S} is the initial concentration of the fixed charges inside the tissue. Note that in contrast to tri- or quadriphasic swelling models, the external concentration $\bar{c}_m$ is treated as a material parameter and must not be applied via suitable boundary conditions. Next, the 2nd *Piola-Kirchhoff* stress can be computed by inserting (4.96) into (4.88) yielding

$$\begin{aligned}\mathbf{S}^S_{\mathrm{OSM}} &= 2\,\frac{\partial W^S_{\mathrm{OSM}}}{\partial c^{fc}_m}\,\frac{\partial c^{fc}_m}{\partial \det \mathbf{F}_S}\,\frac{\partial \det \mathbf{F}_S}{\partial \det \mathbf{C}_S}\,\frac{\partial \det \mathbf{C}_S}{\partial \mathbf{C}_S} = \det \mathbf{F}_S\,\frac{\partial W^S_{\mathrm{OSM}}}{\partial c^{fc}_m}\,\frac{\partial c^{fc}_m}{\partial \det \mathbf{F}_S}\,\mathbf{C}_S^{-1}\\ &= -\det \mathbf{F}_S\,\underbrace{R\,\Theta\,[\,\sqrt{4\,\bar{c}_m^2 + (c^{fc}_m)^2} - 2\,\bar{c}_m\,]}_{\Delta\pi}\,\mathbf{C}_S^{-1}.\end{aligned} \tag{4.97}$$

Hence, (4.96) yields *van't Hoff*'s osmotic law (2.7) which relates the osmotic pressure difference $\Delta\pi$ to the concentration differences between the pore fluid and the surrounding external solution, cf. Ehlers *et al.* [59]. The hydrostatic nature of (4.97) becomes clear, when the true stress is computed via a covariant push-forward yielding

$$\mathbf{T}^S_{\mathrm{OSM}} = \det \mathbf{F}_S^{-1}\,\boldsymbol{\tau}^S_{\mathrm{OSM}} = \det \mathbf{F}_S^{-1}\,\mathbf{F}_S\,\mathbf{S}^S_{\mathrm{OSM}}\,\mathbf{F}_S^T = -\Delta\pi\,\mathbf{I}\,. \tag{4.98}$$

Following this, an overall pore pressure $p = \mathcal{P} + \Delta\pi$ can be introduced consisting of a hydraulic and an osmotic contribution, respectively, thereby leaving a purely mechanical extra stress $\mathbf{T}^S_{E,mech.}$ for the solid skeleton, viz.:

$$\mathbf{T} = \mathbf{T}^F_E + \mathbf{T}^S_E - \mathcal{P}\,\mathbf{I} = \mathbf{T}^F_E + \mathbf{T}^S_{E,mech.} - (\Delta\pi + \mathcal{P})\,\mathbf{I} \qquad \text{with} \qquad p = \mathcal{P} + \Delta\pi\,. \tag{4.99}$$

Finally, the osmotic contribution for the material tangent (4.91) of the referential frame can be computed yielding

$$\begin{aligned}\overset{4}{\boldsymbol{\mathcal{B}}}{}^{\mathrm{S}}_{\mathrm{OSM}} &= \Big(J_S^2\,\frac{\partial^2 W^S_{\mathrm{OSM}}}{\partial J_S^2} + J_S\,\frac{\partial W^S_{\mathrm{OSM}}}{\partial J_S}\Big)\,\mathbf{C}_S^{-1}\otimes\mathbf{C}_S^{-1} - 2\,J_S\,\frac{\partial W^S_{\mathrm{OSM}}}{\partial J_S}\,(\mathbf{C}_S^{-1}\otimes\mathbf{C}_S^{-1})^{23}_{T}\\ &= \left[\frac{J_S^2\,R\,\Theta\,(c^{fc}_m)^2}{\sqrt{4\,\bar{c}_m^2 + (c^{fc}_m)^2}\,(J_S - n^S_{0S})} - J_S\,\Delta\pi\right]\mathbf{C}_S^{-1}\otimes\mathbf{C}_S^{-1} + 2\,J_S\,\Delta\pi\,(\mathbf{C}_S^{-1}\otimes\mathbf{C}_S^{-1})^{23}_{T}.\end{aligned} \tag{4.100}$$

The respective material tangent of the actual frame is then obtained with the application of a fourth-order covariant push-forward operation described in box (3.30) leading to

$$\overset{4}{\boldsymbol{\mathcal{C}}}{}^{\mathrm{S}}_{\mathrm{OSM}} = \left[\frac{J_S^2\,R\,\Theta\,(c^{fc}_m)^2}{\sqrt{4\,\bar{c}_m^2 + (c^{fc}_m)^2}\,(J_S - n^S_{0S})} - J_S\,\Delta\pi\right]\mathbf{I}\otimes\mathbf{I} + 2\,J_S\,\Delta\pi\,(\mathbf{I}\otimes\mathbf{I})^{23}_{T}. \tag{4.101}$$

Note in passing that the proposed strain energy W^S_{OSM} naturally fulfils the polyconvexity condition of Subsection 4.3.5. This fact is quickly concluded by comparing equation $(4.86)_5$ with (4.100), where the values for R and Θ are restricted to values greater than zero and $J_S \geq n^S_{0S}$ is physically limited by the compaction point.

4.4.3 Isotropic Contribution

In general, soft biological tissues are subjected to large deformations which sometimes cause a complex nonlinear material behaviour. Herein, especially the swelling-active characteristic causes finite volumetric extensions of the ECM. Hence, in order to keep the model as general as possible, an *Ogden*-type formulation [155, 156] is chosen for the isotropic contribution W^S_{ISO} of the purely mechanical part of the equilibrium strain energy W^S_{EQ}. In this regard, only one numerical implementation is needed in order to simulate almost any complexity level, ranging from very simple to highly nonlinear material behaviour. However, the original approach of Ogden [155, 156] is not directly applicable to porous media, as it is not capable to account for the compaction point. Following this, Eipper [67] extended the volumetric extension term of the compressible formulation for a hyperelastic porous solid skeleton, while Markert [131, 133] further improved the volumetric extension towards extremely porous foams, thereby incorporating a viscoelastic material behaviour of the solid skeleton. Herein, both works were only concerned with the resulting stress increase for volumetric deformations close to the compaction point, while a volumetric dilatation was not analysed. Concerning the almost impermeable soft biological tissues, the compaction point is rarely reached, whereas volumetric dilatations frequently occur in cases where the tissue swells.

Isotropic strain energy of the solid skeleton

$$W^S_{\mathrm{ISO}} = \overline{W}^S_{\mathrm{ISO}}\left(\lambda_{S(k)}\right) + \overline{U}^S_{\mathrm{ISO}}(J_S) \qquad \text{with}$$

$$\overline{W}^S_{\mathrm{ISO}} = \mu^S_0 \sum_{m=1}^{M_0} \Big[\sum_{k=1}^{3} \frac{\mu^*_{0(m)}}{\alpha_{0(m)}} \Big(\lambda_{S(k)}^{\alpha_{0(m)}/2} - 1 \Big) - \mu^*_{0(m)} \, \ln\left(J_S\right) \Big]$$

volumetric extension term of Eipper [67]: (4.102)

$$\overline{U}^S_{\mathrm{ISO}} = \frac{\Lambda^S_0}{\gamma^S_0 \big(\gamma^S_0 - 1 + \frac{1}{[1-n^S_{0S}]^2} \big)} \Big(J_S^{\gamma^S_0} - 1 - \gamma^S_0 \, \ln \frac{J_S - n^S_{0S}}{1 - n^S_{0S}} + \gamma^S_0 \, n^S_{0S} \, \frac{J_S - 1}{1 - n^S_{0S}} \Big)$$

volumetric extension term of Markert [133]:

$$\overline{U}^S_{\mathrm{ISO}} = \frac{\Lambda^S_0}{\gamma^S_0 \big(\gamma^S_0 - 1 + \frac{\gamma^S_0 + 1}{[1-n^S_{0S}]^2} \big)} \Big(J_S^{\gamma^S_0} - 2 + \Big[\frac{1 - n^S_{0S}}{J_S - n^S_{0S}} \Big]^{\gamma^S_0} + \gamma^S_0 \, n^S_{0S} \, \frac{J_S - 1}{1 - n^S_{0S}} \Big)$$

However, the purpose of this chapter is only to provide a brief summary of the related equations, while the reader is referred to Eipper [67] or Markert [131, 133] for a comprehensive derivation. Here, two volumetric extension functions $\overline{U}^S_{\mathrm{ISO}}$ are presented in (4.102) which will be compared with respect to their stress development in the volumetric tension regime. Moreover, concerning equations (4.102), the deformation variables are the eigenvalues $\lambda_{S(k)}$ of the right $\mathbf{C}_S$ or the left $\mathbf{B}_S$ solid deformation tensors as well as the *Jacobi*an $J_S = \det \mathbf{F}_S = (\det \mathbf{C}_S)^{\frac{1}{2}} = (\det \mathbf{B}_S)^{\frac{1}{2}}$. All other quantities are material parameters. Herein, M_0 denotes the number of *Ogden* terms to be taken, while $\mu^*_{0(m)}$, $\alpha_{0(m)}$, and γ^S_0 represent dimensionless, real-valued material parameters which determine the nonlinearity of the function. After linearisation around the natural state, the parameters μ^S_0

and Λ_0^S are quickly identified as the first and second *Lamé*[6] constants, respectively, where μ_0^S is also known as the classical ground-state shear modulus. Making specific choices for the following parameters

model	M_0	$\mu^*_{0(m)}$	$\alpha_{0(m)}$
Varga	1	$\mu^*_{0(1)} = 2$	$\alpha_{0(1)} = 1$
neo-*Hooke*	1	$\mu^*_{0(1)} = 1$	$\alpha_{0(1)} = 2$
Mooney-Rivlin	2	$\mu^*_{0(1)} - \mu^*_{0(2)} = 1$	$\alpha_{0(1)} = 2,\ \alpha_{0(2)} = -2$

(4.103)

it turns out that the *Ogden* law $(4.102)_1$ comprises other well-known finite elasticity models, such as the *Varga*, neo-*Hooke*, or *Mooney-Rivlin*[7] model, cf. Mooney [141], Rivlin [169], Varga [216] and Treloar [204].

As a next step, the behaviour of the two volumetric extension terms in (4.102) is observed. Since the first derivative of $\overline{U}^S_{\mathrm{ISO}}$ with respect to the solid *Jacobi*an J_S governs the development of the true stress, the corresponding curves are plotted in Figure 4.3 for different values of the parameter γ_0^S. In this regard, it is apparent that γ_0^S strongly influences the

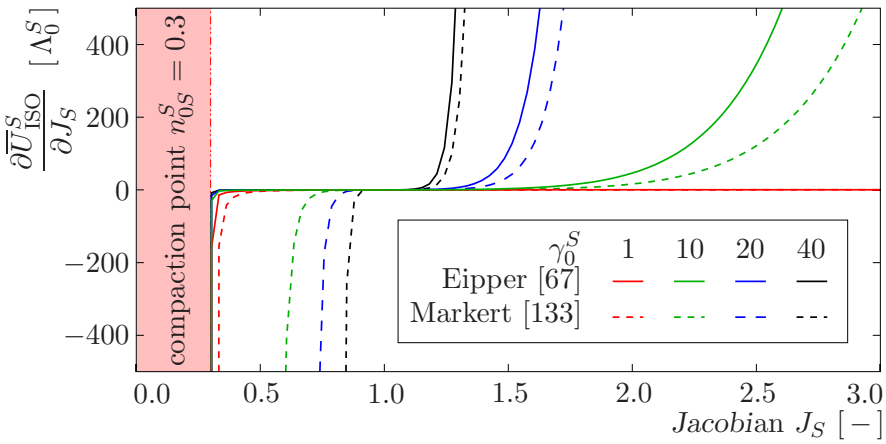

Figure 4.3: *Comparison of the volumetric extension terms of Eipper [67] and Markert [133].*

kind of nonlinearity in the tension and compression zone. Moreover, for large values of γ_0^S, the volumetric extension of Markert [131, 133] yields somewhat unphysical results in the compression zone. Herein, the solid skeleton tends towards an incompressible aggregate which does not allow for much volumetric deformation. However, the very stiff behaviour of soft biological tissues in the volumetric compression regime is rather due to its almost impermeable character and must not be included in the solid extra stress. In contrast, regarding the swelling-active behaviour of the ECM as well as the rapid stiffening effect of the ECM in the volumetric dilatation zone, which is a typical characteristic for soft biological tissues [79], a higher range for γ_0^S between $20 < \gamma_0^S < 40$ seems realistic. Following this, the volumetric extension of Eipper [67] is chosen for further investigation, as it sufficiently embraces the compaction point of the almost impermeable ECM.

[6] *Gabriel Lamé* (1795–1870): French mathematician who became well-known for his general theory of curvilinear coordinates and his notation and study of classes of ellipse-like curves.

[7] *Melvin Mooney* (1893–1968) and *Ronald Samuel Rivlin* (1915–2005): Two American physicists and rheologists who proposed their elasticity model in two independent papers [141, 169]

Next, the corresponding stress and material tangent can be computed by inserting the strain energy (4.102) into (4.88), (4.90) and (4.91) as well as applying the rules of the spectral representation theorem. For more detailed information on the computation process, please consult Markert [131, 133]. Following this, the true stress is given by

$$\begin{aligned}\mathbf{T}^S_{\text{ISO}} \;=\; & \frac{\mu_0^S}{J_S}\sum_{m=1}^{M_0}\sum_{k=1}^{3}\mu^*_{0(m)}\,(\lambda_{S(k)}^{\alpha_{0(m)}/2}-1)\,\mathbf{N}_{S(k)}\;+\\ & +\;\frac{\Lambda_0^S}{\gamma_0^S-1+\frac{1}{[1-n_{0S}^S]^2}}\Big(J_S^{\gamma_0^S-1}-\frac{1}{J_S-n_{0S}^S}+\frac{n_{0S}^S}{1-n_{0S}^S}\Big)\,\mathbf{I}\end{aligned} \tag{4.104}$$

and the material tangent on the actual configuration yields

$$\begin{aligned}\overset{4}{\boldsymbol{\mathcal{C}}}{}^{\text{S}}_{\text{ISO}} \;=\; & 4\sum_{k,l=1}^{3}\frac{\partial^2\overline{W}^S_{\text{ISO}}}{\partial\lambda_{S(k)}\,\partial\lambda_{S(l)}}\,\lambda_{S(k)}\,\lambda_{S(l)}\,\mathbf{N}_{S(k)}\otimes\mathbf{N}_{S(l)}\;+\\ & +\;2\sum_{\substack{k,l=1\\k\neq l}}^{3}\frac{\frac{\partial\overline{W}^S_{\text{ISO}}}{\partial\lambda_{S(k)}}-\frac{\partial\overline{W}^S_{\text{ISO}}}{\partial\lambda_{S(l)}}}{\lambda_{S(k)}-\lambda_{S(l)}}\,\lambda_{S(k)}\,\lambda_{S(l)}\big[(\mathbf{N}_{S(k)}\otimes\mathbf{N}_{S(l)})^{23}_{T}+(\mathbf{N}_{S(k)}\otimes\mathbf{N}_{S(l)})^{24}_{T}\big]\;+\\ & +\;\Big(J_S^2\frac{\partial^2\overline{U}^S_{\text{ISO}}}{\partial J_S^2}+J_S\frac{\partial\overline{U}^S_{\text{ISO}}}{\partial J_S}\Big)\,\mathbf{I}\otimes\mathbf{I}-2\,J_S\,\frac{\partial\overline{U}^S_{\text{ISO}}}{\partial J_S}\,(\mathbf{I}\otimes\mathbf{I})^{23}_{T}\end{aligned} \tag{4.105}$$

with the partial derivatives

$$\begin{aligned}\frac{\partial\overline{W}^S_{\text{ISO}}}{\partial\lambda_{S(k)}} \;=\;& \mu_0^S\sum_{m=1}^{M_0}\frac{1}{2}\,\mu^*_{0(m)}\,\lambda_{S(k)}^{-1}\,(\lambda_{S(k)}^{\alpha_{0(m)}/2}-1)\,,\\ \frac{\partial^2\overline{W}^S_{\text{ISO}}}{\partial\lambda_{S(k)}\,\partial\lambda_{S(l)}} \;=\;& \begin{cases}\mu_0^S\sum_{m=1}^{M_0}\frac{1}{4}\,\mu^*_{0(m)}\,\lambda_{S(k)}^{-2}\,[(\alpha_{0(m)}-2)\,\lambda_{S(k)}^{\alpha_{0(m)}/2}+2] & \text{if}\quad k=l\,,\\ 0 & \text{if}\quad k\neq l\,,\end{cases}\\ \frac{\partial\overline{U}^S_{\text{ISO}}}{\partial J_S} \;=\;& \frac{\Lambda_0^S}{\gamma_0^S-1+\frac{1}{[1-n_{0S}^S]^2}}\Big(J_S^{\gamma_0^S-1}-\frac{1}{J_S-n_{0S}^S}+\frac{n_{0S}^S}{1-n_{0S}^S}\Big)\,,\\ \frac{\partial^2\overline{U}^S_{\text{ISO}}}{\partial J_S^2} \;=\;& \frac{\Lambda_0^S}{\gamma_0^S-1+\frac{1}{[1-n_{0S}^S]^2}}\Big((\gamma_0^S-1)\,J_S^{\gamma_0^S-2}+\frac{1}{(J_S-n_{0S}^S)^2}\Big)\,.\end{aligned} \tag{4.106}$$

Note that around the undeformed reference configuration, the corresponding eigenvalues of $\mathbf{C}_S$ are frequently identical. For these cases, the material tangent (4.105) contains an undetermined expression which has to be solved using *l'Hôpital*'s[8] rule yielding

$$\begin{aligned}\lim_{\lambda_{S(k)}\to\lambda_{S(l)}}\;& \frac{\Big(\frac{\partial\overline{W}^S_{\text{ISO}}}{\partial\lambda_{S(k)}}-\frac{\partial\overline{W}^S_{\text{ISO}}}{\partial\lambda_{S(l)}}\Big)\,\lambda_{S(k)}\,\lambda_{S(l)}}{\lambda_{S(k)}-\lambda_{S(l)}}=\\ &=\;\Big(\frac{\partial\overline{W}^S_{\text{ISO}}}{\partial\lambda_{S(k)}}-\frac{\partial\overline{W}^S_{\text{ISO}}}{\partial\lambda_{S(l)}}\Big)\,\lambda_{S(l)}\;+\;\Big(\frac{\partial^2\overline{W}^S_{\text{ISO}}}{\partial\lambda^2_{S(k)}}-\frac{\partial^2\overline{W}^S_{\text{ISO}}}{\partial\lambda_{S(l)}\partial\lambda_{S(k)}}\Big)\,\lambda_{S(k)}\,\lambda_{S(l)}\,.\end{aligned} \tag{4.107}$$

[8] *Guillaume Franois Antoine, Marquis de l'Hôpital* (1661–1704): French mathematician who is best known for his rule for calculating the limiting value of an undetermined fraction.

Moreover, the strain energy (4.102) is polyconvex if the involved material parameters meet the following requirements:

$$\mu_0^S > 0\,, \qquad \Lambda_0^S > 0\,, \qquad \sum_{m=1}^{M_0} \mu_{0(m)}^* \geq 0\,, \qquad \mu_{0(m)}^*\,\alpha_{0(m)} > 0\,, \qquad \gamma_0^S \geq 1\,. \tag{4.108}$$

Note in passing that a downward compatibility to the *Hooke*an law of linear elasticity is guaranteed if the parameters additionally satisfy the relation

$$\sum_{m=1}^{M_0} \mu_{0(m)}^*\,\alpha_{0(m)} = 2\,. \tag{4.109}$$

4.4.4 Anisotropic Contribution

According to the argumentation of Subsection 4.4.1, the anisotropic part of the equilibrium strain energy may depend on the mixed invariants J_{S4} to J_{S8} of the corresponding integrity base used in (4.74), which is used for prismatic symmetry or local orthotropy. However, the choice of how many mixed invariants are incorporated is of constitutive nature and thus, W^S_{ANISO} may only depend on a subset of selected mixed invariants.

Proceeding from the theory of ropes, collagen fibres are neither capable of carrying any compressive nor shear loads. Thus, the corresponding strain energy is constitutively assumed to depend only on variables describing the fibre stretch, thereby neglecting effects resulting from fibre-matrix or fibre-fibre interaction. Moreover, following the idea of a rather general strain energy function in order to represent several complexity levels in one formulation, an *Ogden*-type formulation is developed for the anisotropic part, cf. Markert *et al.* [134]. Herein, W^S_{ANISO} is also based on a general polynomial formulated in the squared stretches in the respective fibre directions, i. e., in the variables J_{S4} and J_{S6}.

Anisotropic strain energy of the solid skeleton

$$\begin{aligned} W^S_{\text{ANISO}} = &\sum_{m=1}^{M_{f1}} \Big[\frac{\tilde{\mu}^S_{1(m)}}{\tilde{\gamma}^S_{1(m)}} \Big(J_{S4}^{\tilde{\gamma}^S_{1(m)}/2} - 1 \Big) - \tilde{\mu}^S_{1(m)}\, \ln J_{S4}^{1/2} \Big] + \\ &+ \sum_{m=1}^{M_{f2}} \Big[\frac{\tilde{\mu}^S_{2(m)}}{\tilde{\gamma}^S_{2(m)}} \Big(J_{S6}^{\tilde{\gamma}^S_{2(m)}/2} - 1 \Big) - \tilde{\mu}^S_{2(m)}\, \ln J_{S6}^{1/2} \Big] \end{aligned} \tag{4.110}$$

In particular, (4.110) is additively decomposed yielding two transversely isotropic parts, one for each fibre direction. Following this, it is possible to represent two mechanically distinct and orthotropically arranged families of fibres. For local orthotropy with mechanically equivalent fibres, like it is the case in the AF, the material parameters $M_{f1} = M_{f2}$, $\tilde{\mu}^S_{1(m)} = \tilde{\mu}^S_{2(m)}$ and $\tilde{\gamma}^S_{1(m)} = \tilde{\gamma}^S_{2(m)}$ coincide, thereby yielding a simpler form of (4.110), viz.:

$$W^S_{\text{ANISO}} = \sum_{m=1}^{M_f} \Big[\frac{\tilde{\mu}^S_m}{\tilde{\gamma}^S_m} \Big(J_{S4}^{\tilde{\gamma}^S_m/2} + J_{S6}^{\tilde{\gamma}^S_m/2} - 2 \Big) - \tilde{\mu}^S_m\, \ln (J_{S4}\, J_{S6})^{1/2} \Big]\,. \tag{4.111}$$

For the purpose of this monograph, it is sufficient to consider the case of mechanically equivalent fibres. Following this, the stress can be easily computed when (4.111) is inserted into (4.88). Applying the derivatives given in Appendix A.2, it is easy to prove that the 2nd *Piola-Kirchhoff* stress takes the form:

$$\mathbf{S}^S_{\text{ANISO}} = \sum_{m=1}^{M_f} \tilde{\mu}^S_m \left[J_{S4}^{-1} \left(J_{S4}^{\tilde{\gamma}^S_m/2} - 1 \right) \boldsymbol{\mathcal{M}}^S_a + J_{S6}^{-1} \left(J_{S6}^{\tilde{\gamma}^S_m/2} - 1 \right) \boldsymbol{\mathcal{M}}^S_b \right]. \tag{4.112}$$

The true stress is then obtained by applying a covariant push-forward operation yielding

$$\mathbf{T}^S_{\text{ANISO}} = \sum_{m=1}^{M_f} \frac{\tilde{\mu}^S_m}{J_S} \left[J_{S4}^{-1} \left(J_{S4}^{\tilde{\gamma}^S_m/2} - 1 \right) \mathbf{a}^S \otimes \mathbf{a}^S + J_{S6}^{-1} \left(J_{S6}^{\tilde{\gamma}^S_m/2} - 1 \right) \mathbf{b}^S \otimes \mathbf{b}^S \right], \tag{4.113}$$

where $\mathbf{a}^S$ and $\mathbf{b}^S$ denote the rotated and stretched fibre vectors in the actual configuration which are not of length unity anymore. The material tangent on the reference configuration can be computed with the aid of (4.91) yielding

$$\begin{aligned} \overset{4}{\boldsymbol{\mathcal{B}}}{}^{\text{S}}_{\text{ANISO}} = \sum_{m=1}^{M_f} \tilde{\mu}^S_m \Big\{ & J_{S4}^{-2} \left[\left(\tilde{\gamma}^S_m - 2 \right) J_{S4}^{\tilde{\gamma}^S_m/2} - 2 \right] \boldsymbol{\mathcal{M}}^S_a \otimes \boldsymbol{\mathcal{M}}^S_a + \\ & + J_{S6}^{-2} \left[\left(\tilde{\gamma}^S_m - 2 \right) J_{S6}^{\tilde{\gamma}^S_m/2} - 2 \right] \boldsymbol{\mathcal{M}}^S_b \otimes \boldsymbol{\mathcal{M}}^S_b \Big\}, \end{aligned} \tag{4.114}$$

while a covariant push-forward yields the material tangent of the actual configuration

$$\begin{aligned} \overset{4}{\boldsymbol{\mathcal{C}}}{}^{\text{S}}_{\text{ANISO}} = \sum_{m=1}^{M_f} \tilde{\mu}^S_m \Big\{ & J_{S4}^{-2} \left[\left(\tilde{\gamma}^S_m - 2 \right) J_{S4}^{\tilde{\gamma}^S_m/2} - 2 \right] \mathbf{a}^S \otimes \mathbf{a}^S \otimes \mathbf{a}^S \otimes \mathbf{a}^S + \\ & + J_{S6}^{-2} \left[\left(\tilde{\gamma}^S_m - 2 \right) J_{S6}^{\tilde{\gamma}^S_m/2} - 2 \right] \mathbf{b}^S \otimes \mathbf{b}^S \otimes \mathbf{b}^S \otimes \mathbf{b}^S \Big\}. \end{aligned} \tag{4.115}$$

Finally, the corresponding restrictions on the involved material parameters have to be determined, such that the anisotropic strain energy is polyconvex. Inserting (4.111) into $(4.86)_1$, thereby neglecting the derivatives with respect to J_{S6} for brevity, as they yield exactly the same result, the following relation is obtained:

$$\begin{aligned} \frac{\partial^2 W^S_{\text{ANISO}}}{\partial \mathbf{F}_S \otimes \partial \mathbf{F}_S} \cdot (\mathbf{G} \otimes \mathbf{G}) = & \sum_{m=1}^{M_f} 2\, \tilde{\mu}^S_m\, J_{S4}^{-2} \left[J_{S4}^{\tilde{\gamma}^S_m/2} (\tilde{\gamma}^S_m - 2) + 2 \right] (\mathbf{F}_S \boldsymbol{\mathcal{M}}^S_a \cdot \mathbf{G})^2 + \\ & + \sum_{m=1}^{M_f} 2\, \tilde{\mu}^S_m\, J_{S4}^{-1} \left(J_{S4}^{\tilde{\gamma}^S_m/2} - 1 \right) (\mathbf{G} \boldsymbol{\mathcal{M}}^S_a \cdot \mathbf{G}) \overset{!}{>} 0\,. \end{aligned} \tag{4.116}$$

Proceeding from general positive values for $(\mathbf{F}_S \boldsymbol{\mathcal{M}}^S_a \cdot \mathbf{G})^2 > 0$ and $(\mathbf{G} \boldsymbol{\mathcal{M}}^S_a \cdot \mathbf{G}) > 0$, the resulting polyconvexity conditions can be determined by exploiting (4.116) leading to:

$$\begin{aligned} & \sum_{m=1}^{M_f} \tilde{\mu}^S_m \geq 0\,, \qquad \tilde{\mu}^S_m \left(\tilde{\gamma}^S_m - 2 \right) \geq 0 \quad \longrightarrow \quad \left\{ \begin{array}{l} \tilde{\mu}^S_m > 0 \;\rightarrow\; \tilde{\gamma}^S_m \geq 2 \\ \tilde{\mu}^S_m < 0 \;\rightarrow\; \tilde{\gamma}^S_m \leq 2 \end{array} \right\}, \\ & J_{S4} \geq 1\,, \qquad J_{S6} \geq 1\,. \end{aligned} \tag{4.117}$$

Note that the restriction $\{J_{S4}\,,\,J_{S6}\} \geq 1$ underlines the idea that the collagen fibre-reinforcement in the AF can only withstand tensile forces, while compressive forces are not supported, like it is the case in the rope theory.

Finally note that there are numerous other possibilities to model the mechanical behaviour of collagen fibres using polyconvex strain energy functions. For more detailed information on this topic, the reader is referred to Balzani [14], Balzani *et al.* [15], Holzapfel *et al.* [94], Itskov & Aksel [104] or Schröder & Neff [179].

4.4.5 Non-Equilibrium Contribution

The last part of the strain energy to be defined is associated with the springs in the $n = 1, ..., N$ *Maxwell* elements. As Holzapfel *et al.* [96] did not measure any dissipative effects of the oriented collagen, it is assumed that the intrinsic viscoelasticity is stemming solely from the isotropic party of the ECM, i. e., from the randomly distributed type-II collagen. Hence, the NEQ part of the strain energy can be extended straightforward from the isotropic part, but now depending the principle elastic stretches of the intermediate configuration. Again, for the purpose of this monograph, the following results are taken from Markert [131, 133] and are only reviewed briefly in box (4.118). Herein, the inelastic solid volume fractions $(n^S_{Si})_n$ are given by (4.84) and the deformation variables are the eigenvalues $\lambda_{Se(k)}$ of the right $\mathbf{C}_{Se}$ or left $\mathbf{B}_{Se}$ elastic solid deformation tensors as well as their determinants yielding the elastic *Jacobi*an J_{Se}. Moreover, note that the restrictions (4.103), (4.108) and (4.109) for the involved material parameters can be applied correspondingly.

Non-equilibrium strain energy of the solid skeleton

$$
\begin{aligned}
W^S_{\mathrm{NEQ}} &= \overline{W}^S_{\mathrm{NEQ}}\left[(\lambda_{Se(k)})_n\right] + \overline{U}^S_{\mathrm{NEQ}}[(J_{Se})_n] \qquad \text{with} \\
\overline{W}^S_{\mathrm{NEQ}} &= \sum_{n=1}^{N} \mu^S_n \sum_{m=1}^{M_n} \Big\{ \sum_{k=1}^{3} \frac{\mu^*_{n(m)}}{\alpha_{n(m)}} \Big[(\lambda^{\alpha_{n(m)}/2}_{Se(k)})_n - 1 \Big] - \mu^*_{n(m)}\, \ln\left(J_{Se}\right)_n \Big\} \\
\overline{U}^S_{\mathrm{NEQ}} &= \sum_{n=1}^{N} \frac{\Lambda^S_n}{\gamma^S_n\big(\gamma^S_n - 1 + \frac{1}{[1-(n^S_{Si})_n]^2}\big)} \\
&\qquad \Big[(J^{\gamma^S_n}_{Se})_n - 1 - \gamma^S_n\, \ln \frac{(J_{Se})_n - (n^S_{Si})_n}{1-(n^S_{Si})_n} + \gamma^S_n\, (n^S_{Si})_n\, \frac{(J_{Se})_n - 1}{1-(n^S_{Si})_n} \Big]
\end{aligned}
\tag{4.118}
$$

Keeping in mind the similar structure of (4.102) and (4.118), the non-equilibrium part of the true stress is consequently given in accordance to (4.104) yielding

$$
\begin{aligned}
\mathbf{T}^S_{\mathrm{NEQ}} \;=\; & \sum_{n=1}^{N} \Big\{ \frac{\mu^S_n}{J_S} \sum_{m=1}^{M_n} \sum_{k=1}^{3} \mu^*_{n(m)} \Big[(\lambda^{\alpha_{n(m)}/2}_{Se(k)})_n - 1 \Big] (\mathbf{N}_{Se(k)})_n \; + \\
& + \; \frac{\Lambda^S_n\, J_S^{-1}}{\gamma^S_n - 1 + \frac{1}{[1-(n^S_{Si})_n]^2}} \Big[(J^{\gamma^S_n}_{Se})_n - \frac{(J_{Se})_n}{(J_{Se})_n - (n^S_{Si})_n} + \frac{(J_{Se})_n\, (n^S_{Si})_n}{1-(n^S_{Si})_n} \Big] \mathbf{I} \Big\} \,.
\end{aligned}
\tag{4.119}
$$

The partial non-equilibrium material tangent of a single *Maxwell* element on the actual configuration is obtained from (4.105) leading to:

$$\begin{aligned}
\overset{4}{\mathbf{C}}{}^{S}_{n} \;=\; & 4\sum_{k,l=1}^{3} \frac{\partial^2 \overline{W}^{S}_{\mathrm{NEQ}}}{\partial(\lambda_{Se(k)})_n \partial(\lambda_{Se(l)})_n} \,(\lambda_{Se(k)})_n \,(\lambda_{Se(l)})_n \,(\mathbf{N}_{Se(k)})_n \otimes (\mathbf{N}_{Se(l)})_n \;+ \\
& +\; 2\sum_{\substack{k,l=1 \\ k\neq l}}^{3} \frac{\frac{\partial \overline{W}^{S}_{\mathrm{NEQ}}}{\partial(\lambda_{Se(k)})_n} - \frac{\partial \overline{W}^{S}_{\mathrm{NEQ}}}{\partial(\lambda_{Se(l)})_n}}{(\lambda_{Se(k)})_n - (\lambda_{Se(l)})_n} \,(\lambda_{Se(k)})_n \,(\lambda_{Se(l)})_n \,(\overset{4}{\mathbf{N}}_{Se[kl]})_n \;+ \\
& +\; \Big[(J^2_{Se})_n \frac{\partial^2 \overline{U}^{S}_{\mathrm{NEQ}}}{\partial (J^2_{Se})_n} + (J_{Se})_n \frac{\partial \overline{U}^{S}_{\mathrm{NEQ}}}{\partial (J_{Se})_n}\Big] \,(\mathbf{I}\otimes\mathbf{I}) \;-\; 2\,(J_{Se})_n \,\frac{\partial \overline{U}^{S}_{\mathrm{NEQ}}}{\partial (J_{Se})_n} \,(\mathbf{I}\otimes\mathbf{I})^{\overset{23}{T}}
\end{aligned} \tag{4.120}$$

with the abbreviation $(\overset{4}{\mathbf{N}}_{Se[kl]})_n = [(\mathbf{N}_{Se(k)})_n \otimes (\mathbf{N}_{Se(l)})_n]^{\overset{23}{T}} + [(\mathbf{N}_{Se(k)})_n \otimes (\mathbf{N}_{Se(l)})_n]^{\overset{24}{T}}$. In this regard, $(\mathbf{N}_{Se(k)})_n$ denotes the eigentensor of the left elastic deformation tensor $(\mathbf{B}_{Se})_n$ of the respective n^{th} *Maxwell* element. Note that the corresponding derivatives in (4.120) can be computed with reference to the derivatives given by (4.106).

Finally, the inelastic evolution equations resulting from the dashpots in the *Maxwell* elements have to be defined, which are needed to determine the position of the inelastic intermediate configuration and thus, the internal variables $(\mathbf{C}_{Si})_n$. Proceeding from the considerations given in Subsection 4.2.3, the proportionality $(4.44)_1$ is sufficiently satisfied with the simple ansatz

$$\widehat{\boldsymbol{\tau}}^{S}_{n} \propto (\widehat{\mathbf{D}}_{Si})_n \qquad \longrightarrow \qquad (\widehat{\mathbf{D}}_{Si})_n = \frac{1}{2\,\eta^S_n}\,\widehat{\boldsymbol{\tau}}^{S}_{n} - \frac{\zeta^S_n}{2\,\eta^S_n\,(2\,\eta^S_n + 3\,\zeta^S_n)}\,(\widehat{\boldsymbol{\tau}}^{S}_{n}\cdot\mathbf{I})\,\mathbf{I}\,, \tag{4.121}$$

where η^S_n and ζ^S_n are the respective macroscopic shear and bulk viscosities of the dashpot in a *Maxwell* element. In this context, relation $(4.121)_2$ is the inverse from the well-known stress-strain rate relation for a dashpot yielding a linear relation between $\widehat{\boldsymbol{\tau}}^{S}_{n}$ and $(\widehat{\mathbf{D}}_{Si})_n$, see, e. g., Markert [131, 133]. Since inequality (4.41) has to be satisfied, it is easily concluded that the restrictions $\eta^S_n > 0$ and $2\,\eta^S_n + 3\,\zeta^S_n > 0$ must hold for the viscosities. However, regarding the numerical evaluation of the evolution equation, it is most convenient, when the spatio-temporal discretisation of $(4.121)_2$ is carried out on the reference configuration. Applying the transport mechanism of box (B.2) for $\widehat{\mathbf{D}}_{Si}$ as well as a covariant pull-back operation on $\widehat{\boldsymbol{\tau}}^{S}_{n}$ yields the final form of the evolution equation

$$[(\mathbf{C}_{Si})_n]'_S \;-\; \frac{1}{\eta^S_n}\,(\mathbf{C}_{Si})_n\,\mathbf{S}^S_n\,(\mathbf{C}_{Si})_n + \frac{\zeta^S_n}{\eta^S_n\,(2\,\eta^S_n + 3\,\zeta^S_n)}\,[\mathbf{S}^S_n\cdot(\mathbf{C}_{Si})_n]\,(\mathbf{C}_{Si})_n = \mathbf{0}\,, \tag{4.122}$$

where the chosen internal variables $(\mathbf{C}_{Si})_n$ appear in an explicit manner.

4.5 The Viscous Interstitial Fluid

Since the set of process variables is empty for the incompressible fluid, there is no energy to be determined. However, regarding the dissipation inequality (4.41), there are still two proportionalities to be evaluated, i. e., $\mathbf{T}^F_E \propto \mathbf{D}_F$ and $\hat{\mathbf{p}}^F_E \propto -\mathbf{w}_F$, respectively.

However, due to the lingering flow conditions resulting from the almost impermeable ECM, the frictional fluid extra stress is neglected, i. e., $\mathbf{T}_E^F \approx \mathbf{0}$, which is the usual assumption in hydraulics. Herein, the fluid extra stress $\mathbf{T}_E^F$ is much smaller in comparison with the extra momentum production term $\hat{\mathbf{p}}_E^F$, which is responsible for the drag force resulting from the percolating fluid. This fact can be deduced from an order-of-magnitude analysis, see, e. g., Hassanizadeh & Gray [90], Ehlers *et al.* [56] or Markert [132] and quotations therein. Hence, only an admissible ansatz for $\hat{\mathbf{p}}_E^F$ needs to be defined, while the overall *Cauchy* stress of the model is reduces to:

$$\mathbf{T} = \mathbf{T}_E^S - \mathcal{P}\,\mathbf{I} = \mathbf{T}_{E,\,mech.}^S - (\Delta\pi + \mathcal{P})\,\mathbf{I}\,. \tag{4.123}$$

4.5.1 The *Darcy* Filter Law

Following the proportionality between the momentum production $\hat{\mathbf{p}}_E^F$ of the viscous pore fluid and the seepage velocity, the following correlations hold for the averaged aggregate:

- the higher the filter velocity $n^F\mathbf{w}_F$, the greater the absolute momentum exchange,
- the higher the partial viscosity $n^F\mu^{FR}$, the greater the absolute momentum exchange,
- the smaller the permeability (pore size), the greater the absolute momentum exchange.

Thus, the fluid momentum production can be postulated yielding

$$\hat{\mathbf{p}}_E^F \propto -\mathbf{w}_F \qquad \longrightarrow \qquad \hat{\mathbf{p}}_E^F = -\frac{n^F\mu^{FR}}{K^S}\,(n^F\mathbf{w}_F), \tag{4.124}$$

where $\mu^{FR} > 0$ represents the dynamic fluid viscosity and $K^S > 0$ denotes the intrinsic permeability, which is a purely geometric measure expressed in [m^2] relating to the permeable cross sections of the aggregate. Note in passing that this ansatz describes isotropic permeability conditions throughout the computation. Proceeding from the vanishing fluid extra stress, the fluid momentum production (4.124) is inserted in $(4.19)_3$ and then into the fluid momentum balance $(4.11)_2$ yielding the generalised *Darcy*[9] filter law

$$n^F\mathbf{w}_F = -\frac{K^S}{\mu^{FR}}\,(\operatorname{grad}\mathcal{P} - \rho^{FR}\mathbf{g})\,. \tag{4.125}$$

In this regard, the permeability coefficient, which is weighting the hydraulic gradient, can be reformulated and expressed in different units. The three most established forms are the *Darcy* flow coefficient (hydraulic conductivity) k^F, the specific permeability K^F, and the above mentioned intrinsic permeability K^S. They are related to each other via

[9] *Henry Philibert Gaspard Darcy* (1803–1858): French engineer who experimentally found a relation to describe the flow of water through sand while designing the city fountains of Dijon in 1856 [37].

permeability type					unit
Darcy	k^F	$:= \gamma^{FR} K^F$	$= \dfrac{\gamma^{FR}}{\mu^{FR}} K^S$		$\left[\dfrac{\mathrm{m}}{\mathrm{s}}\right]$
specific	K^F	$:= \dfrac{k^F}{\gamma^{FR}}$	$= \dfrac{K^S}{\mu^{FR}}$		$\left[\dfrac{\mathrm{m}^4}{\mathrm{Ns}}\right]$
intrinsic	K^S	$= \mu^{FR} K^F$	$= \dfrac{\mu^{FR}}{\gamma^{FR}} k^F$		$[\,\mathrm{m}^2\,]$

(4.126)

Herein, $\gamma^{FR} = \rho^{FR} g$ is the effective fluid weight with the gravitation constant $g = |\mathbf{g}|$. Keeping in mind that the tissue may be exposed to volumetric deformations and thus, to a reduction or an increase of the pore space, the permeability parameters may vary accordingly. Following Markert [131, 133], the deformation-dependent intrinsic permeability yields

$$K^S(J_S) = K^S_{0S} \left(\frac{J_S - n^S_{0S}}{1 - n^S_{0S}} \right)^{\kappa} \tag{4.127}$$

which tends towards zero if the compaction point is reached and towards infinity whenever infinite volumetric dilatations occur. Following this, K^S_{0S} denotes the initial permeability of the undeformed reference configuration and κ governs the nonlinearity of the deformation dependence. Obviously, if $\kappa = 0$, the deformation dependency is switched off. However, note that the influence of a deformation-dependent permeability should be negligible regarding the almost impermeable character of the ECM. Hence, a more detailed evaluation of this topic involving anisotropic permeabilities is neglected.

5 Numerical Treatment

The purpose of this chapter is to briefly review the numerical tools which are necessary to perform realistic computations of the lumbar spine in Chapter 6. Herein, the first objective is to rearrange the presented set of governing equations such that they are approachable with a suitable numerical solution scheme. In particular, the presented model consists of a set of coupled partial differential equations (PDE) of first order in time and second order in space, respectively. Thus, a suitable temporal and spatial discretisation is needed. For the purpose of this monograph, the spatial discretisation will be carried out using finite elements, while the discretisation in time is accomplished with the finite difference method. Thereafter, a reliable solution scheme is needed to solve for the unknown quantities of the discretised system of equations. However, as the overall complexity of the problem quickly reaches the capacity of a single central processing unit (CPU), a parallelisation technique is additionally discussed in a brief review.

5.1 Finite Element Method in Space

Concerning the numerical treatment of continuum-mechanical problems involving solids as well as porous media, the variational approach offered by the Finite Element Method (FEM) has been proven to provide a suitable framework. In this regard, a vast selection of references on the FEM can be given, i. e., Bathe [16], Braess [29], Schwarz [181] or Zienkiewicz & Taylor [240, 241] among others, whereas Ellsiepen [70], Ehlers & Ellsiepen [55] or Ammann [4] particularly consider the coupled numerical approximation of porous media models using mixed finite elements.

5.1.1 Weak Formulation

As the Finite Element Method (FEM) is a numerical approximation method, the governing equations need to be brought into a form, which is suitable for a numerical treatment. In this regard, the local balances of the overall aggregate need to be converted from a local (strong) form to an integral (weak) form. This crucial step is important, as it is often impossible to determine a closed form solution of the unknown field quantities at every point $\mathbf{x}$ of the underlying spatial domain Ω of the aggregate body $\mathcal{B}$, especially in the case of complicated geometries like they often occur in biomechanics.

Following this, the local balances including the constitutive equations of the preceding chapter, are collected in box (5.1). Herein, the kinematical dependencies of the solid extra stress on the overall and elastic parts of the deformations tensors $\mathbf{C}_S$ and $\widehat{\mathbf{C}}_{Se}$, respectively, are resolved with respect to the solid displacement $\mathbf{u}_S$ and a measure $\mathbf{q}$ representing the internal variables $(\mathbf{C}_{Si})_n$. Note in passing that this section is dedicated to the global system of equations which is needed to solve for the external variables. As usual in computational inelasticity, the internal variables are determined locally by solving

the evolution equation (4.122). The interaction of the solution of the local system with the solution of the global system will be discussed in Section 5.3.

Strong formulation of the governing equations

$$
\begin{aligned}
\mathbf{0} &= \operatorname{div}\mathbf{T} + (n^S\rho^{SR} + n^F\rho^{FR})\,\mathbf{g} \\
0 &= \operatorname{div}\left[\,(\mathbf{u}_S)'_S + n^F\,\mathbf{w}_F\,\right] \\
n^F\mathbf{w}_F &= -\frac{K^S}{\mu^{FR}}\,(\operatorname{grad}\mathcal{P} - \rho^{FR}\mathbf{g}) \\
n^S &= n^S_{0S}\,\det\mathbf{F}_S^{-1} = n^S_{0S}\,\det(\mathbf{I} - \operatorname{grad}\mathbf{u}_S) \quad\longrightarrow\quad n^F = 1 - n^S \\
\mathbf{T} &= -\mathcal{P}\,\mathbf{I} + \mathbf{T}^S_E(\mathbf{u}_S,\,\mathbf{q}) \qquad\qquad \text{according to Section 4.4}
\end{aligned}
\tag{5.1}
$$

As a next step, the corresponding primary variables have to be chosen. A rearrangement of the overall *Cauchy* stress

$$
\mathbf{T} = -\mathcal{P}\,\mathbf{I} - \Delta\pi\,\mathbf{I} + \mathbf{T}^S_{E,\,mech.} = -p\,\mathbf{I} + \mathbf{T}^S_{E,\,mech.}(\mathbf{u}_S,\,\mathbf{q}) \tag{5.2}
$$

reveals the two possibilities, i. e., $\{\mathcal{P},\,\mathbf{u}_S\}$ and $\{p,\,\mathbf{u}_S\}$, respectively. At first sight, both possibilities appear equally suited. Thus, both approaches are further investigated at the domain boundary Γ of Ω, where a pressure distribution according to Figure 5.1 holds. Herein, only the hydraulic pressure $\mathcal{P}$ stays constant over the domain boundary Γ, whereas

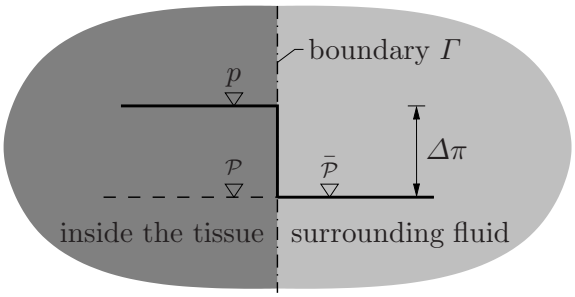

total, hydraulic and osmotic pressure

Figure 5.1: *Pressure situation at the boundary of a charged hydrated porous medium.*

the overall pressure p undergoes a jump of $\Delta\pi$. Hence, the *Dirichlet*[1] (essential) boundary conditions for the overall pressure p implicitly depend on the solution the other primary variable inside the domain, as the osmotic pressure difference $\Delta\pi$ in (4.97) is a function of the solid *Jacobi*an and thus, of the solid displacement vector $\mathbf{u}_S$.

According to Ehlers & Acartürk [53], an approach using p as unknown field quantity would lead to unstable numerical solutions with oscillations in the primary variables $\{p,\,\mathbf{u}_S\}$. Note that these numerical instabilities have also been observed by other authors who use a

[1] *Johann Peter Gustav Lejeune Dirichlet* (1805–1859): German mathematician who worked in the field of partial differential equations and number theory. His name implies his family background which is located in Richelette, Belgium, i. e., *le jeune de Richelette* is French for "the juvenile from Richelette".

triphasic swelling model, cf. Snijders *et al.* [191]. Moreover, such instability problems are also known in other fields addressing fluid-structure interactions, moving boundaries or free surfaces, cf. Dowell & Hall [42], Tezduyar [203] or Wall [220] among others. Following Ehlers & Acartürk [53], the best procedure to overcome these oscillation problems is to weakly impose the corresponding *Dirichlet* boundary conditions in the governing set of equations by a penalty-like method [88, 242]. However, the quickest and simplest way to overcome these problems is to chose the pair $\{\mathcal{P},\, \mathbf{u}_S\}$ as primary variables, which will be the choice for the remaining part of the monograph.

Following the FEM as the chosen variational approach, the corresponding local forms (5.1) of the strong formulation are integrated over the spatial domain Ω which is occupied by the porous aggregate body $\mathcal{B}$ at time t. Subsequently, the variational formulation is obtained, when the respective terms are weighted by independent test functions $\delta\mathbf{u}_S$ and $\delta\mathcal{P}$. In order to allow for the application of *Neumann*[2] boundary conditions, some of the volume integrals have to be transformed into surface integrals. Herein, the overall surface $\Gamma = \partial\Omega$ of the domain Ω is mathematically split for every PDE into

$$\begin{aligned} \Gamma \;&=\; \Gamma_{\mathbf{u}_s} \cup \Gamma_{\mathbf{t}} \qquad \text{with} \qquad \Gamma_{\mathbf{u}_s} \cap \Gamma_{\mathbf{t}} \;=\; \emptyset\,, \quad \text{and} \\ \Gamma \;&=\; \Gamma_{\mathcal{P}} \cup \Gamma_{q} \qquad \text{with} \qquad \Gamma_{\mathcal{P}} \cap \Gamma_{q} \;=\; \emptyset\,, \end{aligned} \tag{5.3}$$

where $\Gamma_{\mathbf{u}_s}$ and $\Gamma_{\mathcal{P}}$ are the *Dirichlet* boundaries for the unknown quantities $\mathbf{u}_S$ and $\mathcal{P}$, while $\Gamma_{\mathbf{t}}$ and Γ_q represent the respective *Neumann* (natural) parts. After applying the product rule and the *Gaußian* integral theorem, the weak formulations for the corresponding balances are obtained, thereby defining the following scalar-valued functionals:

Weak formulation of the governing equations

$$\begin{aligned} \mathcal{G}_{\mathbf{u}_s}(\mathbf{u}_S, \mathcal{P}, \delta\mathbf{u}_S) \;&=\; \int_{\Omega} (\mathbf{T}^S_{E,\,mech.} - p\,\mathbf{I}) \cdot \operatorname{grad} \delta\mathbf{u}_S \,\mathrm{d}v \;- \\ &- \int_{\Omega} (n^S \rho^{SR} + n^F \rho^{FR})\, \mathbf{g} \cdot \delta\mathbf{u}_S \,\mathrm{d}v \;- \int_{\Gamma_{\mathbf{t}}} \bar{\mathbf{t}} \cdot \delta\mathbf{u}_S \,\mathrm{d}a = 0 \\ \mathcal{G}_{\mathcal{P}}(\mathbf{u}_S, \mathcal{P}, \delta\mathcal{P}) \;&=\; \int_{\Omega} \operatorname{div} (\mathbf{u}_S)'_S \,\delta\mathcal{P} \,\mathrm{d}v \;+ \\ &+ \int_{\Omega} \Big[\, \frac{K^S}{\mu^{FR}} (\operatorname{grad} \mathcal{P} - \rho^{FR}\, \mathbf{g}) \,\Big] \cdot \operatorname{grad} \delta\mathcal{P} \,\mathrm{d}v \;+ \int_{\Gamma_q} \bar{q}\, \delta\mathcal{P} \,\mathrm{d}a = 0 \end{aligned} \tag{5.4}$$

Herein, $p = \mathcal{P} + \Delta\pi$ is the overall pressure in the tissue, $\bar{q} = n^F \mathbf{w}_F \cdot \mathbf{n}$ is the volume efflux of φ^F over the boundary Γ_q with the outward-oriented unit surface normal $\mathbf{n}$, while $\bar{\mathbf{t}} = (\mathbf{T}^S_{E,\,mech.} - p\,\mathbf{I})\,\mathbf{n}$ denotes the external load vector acting on the boundary $\Gamma_{\mathbf{t}}$. Since the overall aggregate balances were obtained by addition of the respective

[2] *Carl Gottfried Neumann* (1832–1925): German mathematician who always had a very precise and clear form of expressing himself. Besides his contributions in the field of analytical mechanics and potential theory he worked on the *Dirichlet* principle and a way of applying boundary conditions to PDE.

constituent balances, the corresponding *Neumann* boundaries include the surface fractions of all constituents, i. e., solid and fluid, thereby ensuring physically meaningful boundary conditions. Moreover, while it is possible to set conditions for $\bar{q}$ and $\bar{\mathbf{t}}$ at the same surface, a simultaneous application of a *Dirichlet* and a *Neumann* condition is forbidden according to (5.3). Note in passing how the character of the partial differential equation $(5.1)_1$ is reduced from order two in space to order one in the weak form $(5.4)_1$, as the divergence of overall *Cauchy* stress is not needed anymore.

Finally, an appropriate ansatz for the trial functions of the unknown field quantities $\{\mathbf{u}_S,\, \mathcal{P}\}$ as well as for the corresponding test functions $\{\delta\mathbf{u}_S,\, \delta\mathcal{P}\}$ needs to be formulated. In order to obtain bounded results for (5.4), the first derivatives of the trial and test functions need to be square-integrable on the spatial domain Ω, cf., e. g., Braess [29]. This requirement is *a priori* fulfilled when the respective functions are taken from the *Sobolev*[3] space $\mathcal{H}^1(\Omega)$. Following this, the corresponding trial and test spaces yield

$$\begin{aligned}
\mathcal{S}_{\mathbf{u}_s}(t) &= \{\ \mathbf{u}_S \in \mathcal{H}^1(\Omega)^D\ :\ \mathbf{u}_S(\mathbf{x}) = \bar{\mathbf{u}}_S(\mathbf{x},t) \text{ on } \Gamma_{\mathbf{u}_s}\ \}\,,\\
\mathcal{S}_{\mathcal{P}}(t) &= \{\ \mathcal{P} \in \mathcal{H}^1(\Omega)\ :\ \mathcal{P}(\mathbf{x}) = \bar{\mathcal{P}}(\mathbf{x},t) \text{ on } \Gamma_{\mathcal{P}}\ \}\,,\\
\mathcal{T}_{\mathbf{u}_s} &= \{\,\delta\mathbf{u}_S \in \mathcal{H}^1(\Omega)^D\ :\ \delta\mathbf{u}_S(\mathbf{x}) = \mathbf{0} \text{ on } \Gamma_{\mathbf{u}_s}\,\}\,,\\
\mathcal{T}_{\mathcal{P}} &= \{\ \delta\mathcal{P} \in \mathcal{H}^1(\Omega)\ :\ \delta\mathcal{P}(\mathbf{x}) = 0 \text{ on } \Gamma_{\mathcal{P}}\ \}\,,
\end{aligned} \tag{5.5}$$

where $D \in [1,2,3]$ is an integer denoting the dimension in space. For given *Neumann* boundary conditions $\bar{q}$ and $\bar{\mathbf{t}}$, the trial functions $\mathbf{u}_S(\mathbf{x},t) \in \mathcal{S}_{\mathbf{u}_s}(t)$ and $\mathcal{P}(\mathbf{x},t) \in \mathcal{S}_{\mathcal{P}}(t)$ are then called a weak solution, if they fulfil the governing equations (5.4) at any time $t \in [0,T]$ for arbitrary test functions $\delta\mathbf{u}_S \in \mathcal{T}_{\mathbf{u}_s}$ and $\delta\mathcal{P} \in \mathcal{T}_{\mathcal{P}}$.

5.1.2 Spatial Discretisation Using Mixed Finite Elements

As a next step, the continuous domain Ω needs to be spatially (semi) discretised. Herein, the overall domain is partitioned into several smaller and non-overlapping subdomains Ω_e, which in sum yield the approximated domain Ω^h, viz.:

$$\Omega \approx \Omega^h = \bigcup_{e=1}^{E} \Omega_e\,. \tag{5.6}$$

The subdomains Ω_e are also known as finite elements (FE) and the total number of elements E constitutes the FE mesh Ω^h. The FE themselves are defined by N_e nodal points leading to a total of N_E nodes in the FE mesh. Following this allows for the transformation of the infinite-dimensional trial and test spaces (5.5) into the discrete N_E-dimensional spaces $\mathcal{S}^h_{(\cdot)}$ and $\mathcal{T}^h_{(\cdot)}$, respectively. In particular, this is achieved with the

[3] *Sergei L'vovich Sobolev* (1908–1989): Russian mathematician who introduced the *Sobolev* function spaces in the 1930s which immediately led to a whole area of functional analysis.

definition of discrete trial and test functions in the form of

$$\begin{aligned}
\mathbf{u}_S(\mathbf{x},t) \;\approx\; \mathbf{u}_S^h(\mathbf{x},t) \;=\; \bar{\mathbf{u}}_S^h(\mathbf{x},t) \;+\; \sum_{j=1}^{N_{\mathbf{u}_s}} \boldsymbol{\phi}_{\mathbf{u}_s}^j(\mathbf{x})\, \boldsymbol{u}_S^j(t) \;\in\; \mathcal{S}_{\mathbf{u}_s}^h(t)\,, \\
\mathcal{P}(\mathbf{x},t) \;\approx\; \mathcal{P}^h(\mathbf{x},t) \;=\; \bar{\mathcal{P}}^h(\mathbf{x},t) \;+\; \sum_{j=1}^{N_{\mathcal{P}}} \phi_{\mathcal{P}}^j(\mathbf{x})\, \mathcal{P}^j(t) \;\in\; \mathcal{S}_{\mathcal{P}}^h(t)\,, \\
\delta\mathbf{u}_S(\mathbf{x}) \;\approx\; \delta\mathbf{u}_S^h(\mathbf{x}) \;=\; \sum_{j=1}^{N_{\mathbf{u}_s}} \boldsymbol{\phi}_{\mathbf{u}_s}^j(\mathbf{x})\, \delta\boldsymbol{u}_S^j \;\in\; \mathcal{T}_{\mathbf{u}_s}^h\,, \\
\delta\mathcal{P}(\mathbf{x}) \;\approx\; \delta\mathcal{P}^h(\mathbf{x}) \;=\; \sum_{j=1}^{N_{\mathcal{P}}} \phi_{\mathcal{P}}^j(\mathbf{x})\, \delta\mathcal{P}^j \;\in\; \mathcal{T}_{\mathcal{P}}^h\,.
\end{aligned} \tag{5.7}$$

In this context, $\bar{\mathbf{u}}_S^h(\mathbf{x},t)$ and $\bar{\mathcal{P}}^h(\mathbf{x},t)$ define the *Dirichlet* boundary conditions, while $\boldsymbol{u}_S^j(t) = [u_{S1}^j, \dots, u_{SD}^j]^T$ and $\mathcal{P}^j(t)$ represent the time-dependent nodal degrees of freedom (DOF), respectively. Note that the number of displacement nodes $N_{\mathbf{u}_s} \leq N_E$ (i. e. nodes where displacements are defined) and the number of pressure nodes $N_{\mathcal{P}} \leq N_E$ may differ according to the chosen accuracy of the approximation. Furthermore, $\boldsymbol{\phi}_{\mathbf{u}_s}^j(\mathbf{x}) = \mathrm{diag}\,[\phi_{u1}^j(\mathbf{x}), \dots, \phi_{uD}^j(\mathbf{x})]$ and $\phi_{\mathcal{P}}^j(\mathbf{x})$ represent the global basis functions for the trial and test functions, respectively. Hence, the time-dependency of the primary variables is totally decoupled from the basis functions, as it is solely found in the nodal DOF. For the purpose of this monograph, the standard *Bubnov-Galerkin*[4] method is applied, where the basis functions for the trial and test functions coincide. As a consequence, the trial functions $\delta\mathbf{u}_S$ and $\delta\mathcal{P}$ naturally vanish at *Dirichlet* boundaries $\Gamma_{\mathbf{u}_s}$ and $\Gamma_{\mathcal{P}}$, where discrete values are prescribed. The spatially discretised variational problem can then be summarised to:

$$\text{Find} \quad \left\{ \begin{array}{l} \mathbf{u}_S^h \;\in\; \mathcal{S}_{\mathbf{u}_s}^h \\ \mathcal{P}^h \;\in\; \mathcal{S}_{\mathcal{P}}^h \end{array} \right\} \quad \text{such that} \quad \left\{ \begin{array}{ll} \boldsymbol{\mathcal{G}}_{\mathbf{u}_s}^h(\mathbf{u}_S^h, \mathcal{P}^h, \delta\mathbf{u}_S^h) \;=\; \mathbf{0} & \forall\, \delta\mathbf{u}_S^h \in \mathcal{T}_{\mathbf{u}_s}^h \\ \boldsymbol{\mathcal{G}}_{\mathcal{P}}^h(\mathbf{u}_S^h, \mathcal{P}^h, \delta\mathcal{P}^h) \;=\; \mathbf{0} & \forall\, \delta\mathcal{P}^h \in \mathcal{T}_{\mathcal{P}}^h \end{array} \right\} \tag{5.8}$$

at any time $t \in [0,T]$ for a given set of *Neumann* boundary conditions. Herein, the function vectors $\boldsymbol{\mathcal{G}}_{\mathbf{u}_s}^h$ and $\boldsymbol{\mathcal{G}}_{\mathcal{P}}^h$ in (5.8) represent a system of $D \cdot N_{\mathbf{u}_s} + N_{\mathcal{P}}$ linearly independent equations, which are obtained by setting one discrete test function to unity, while setting the remaining ones to zero, e. g., $\delta\mathcal{P}^1 = 1$, while $\delta\mathcal{P}^j = 0$ for $j = 2, \dots, N_{\mathcal{P}}$ and $\delta u_{S(d)}^j = 0$ for $d = 1, \dots, D$ and $j = 1, \dots, N_{\mathcal{P}}$.

Moreover, for a convenient implementation of the trial and test functions (5.7), the finite elements also serve as discrete local carriers for the respective basis functions. Herein, the basis functions are defined on a single reference element and are often referred to as shape or interpolation functions. This leads to an efficient applicability of numerical integration techniques like the *Gauß* quadrature, for instance, which is important regarding the numerical integration of the weak forms (5.4). Following this, the standard reference

[4] *Ivan Grigorevich Bubnov* (1872–1919): Russian mathematician and ship engineer who worked with *Boris Grigoryevich Galerkin* (1871–1945), also mathematician but civil engineer, at the Saint Petersburg Polytechnical University. *Bubnov* developed and applied this method for a specific problem, while it was *Galerkin* who generalised the technique towards a common procedure for solving general PDE, thereafter.

element is expressed in local coordinates $\boldsymbol{\xi}$, while the global basis functions are obtained from a geometry transformation to the global position $\mathbf{x}$. As is usual in the FEM, the geometry transformation is carried out using an isoparametric concept, where geometry and displacements are expressed by the same set of basis functions.

Concerning the particular choice of shape functions, special care must be taken, as the governing equations represent a strongly coupled solid-fluid model [241], i. e., the unknown field quantities $\mathbf{u}_S$ and $\mathcal{P}$ appear in both equations of (5.4). Hence, the unknowns have to be approximated simultaneously yielding a so-called mixed finite element formulation. Regarding the aggregate volume balance $(5.4)_2$, the gradient of the hydraulic pressure field needs to be computed leading to at least a linear discretisation of $\mathcal{P}^h$. Moreover, as the solid *Cauchy* extra stress tensor $\mathbf{T}^S_{E,mech.}$ implicitly depends on the gradient of the discretised displacement field $\mathbf{u}^h_S$, its approximation needs to be one order higher compared with the approximation used for the hydraulic pressure field $\mathcal{P}^h$. Then, an equal order approximation of the first term in equation $(5.4)_1$ is achieved. Thus, according to Sandhu & Wilson [172], the natural choice yields the usage of an element type, which is suggested by Taylor & Hood [202] having quadratic basis functions for the displacement $\mathbf{u}^h_S$ and linear basis functions for the hydraulic pressure $\mathcal{P}^h$, cf. Figure 5.2.

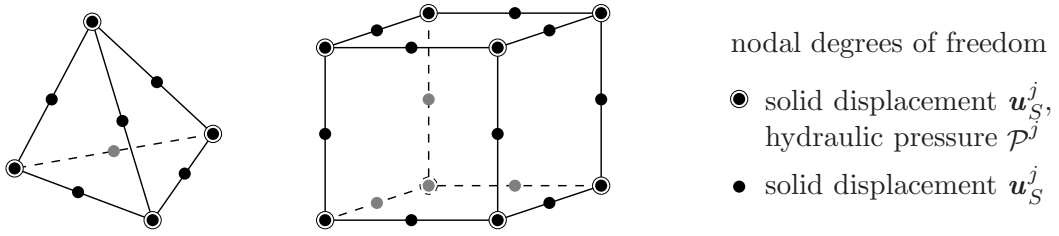

Figure 5.2: *3-d (10-noded) tetrahedral and (20-noded) hexahedral Taylor-Hood elements.*

Regarding numerical accuracy, stability and numerical costs, the suitable choice of mixed finite element formulations is by no means phenomenological, but rather strictly mathematical. In this regard, the inf-sup condition, often referred to as *Ladyzhenskaya*[5]*-Babuška-Brezzi*[6] (LBB) condition, needs to be fulfilled, cf., e. g., Brezzi & Fortin [31], Braess [29] or Wieners [227]. Following this, the *Taylor-Hood* elements fulfil the LBB condition and are the best possible choice from a stability and accuracy point of view. In regard of the complex geometries frequently involved in computational biomechanics, the quadratic discretisation also leads to a good geometry approximation, even with a relatively small number of elements. However, concerning the general 3-d case, the enormous number of mid nodes in finer meshes causes quite large systems of equations, which often have to be solved in parallel, cf. Wieners *et al.* [231] or Ehlers *et al.* [60]. One possibility to overcome this problem is to use the so-called MINI element suggested by Arnold *et al.* [8], which has an enriched linear shape function for $\mathbf{u}^h_S$ using a bubble node. This leads to stable results but the obtained solution is not as accurate anymore, especially concerning the pressure field. Note that a linear-linear approximation of $\mathbf{u}^h_S$ and $\mathcal{P}^h$ leads

[5] *Olga Aleksandrovna Ladyzhenskaya* (1922–2004), Russian mathematician who provided the first rigorous proofs of the convergence of the finite difference method for the *Navier-Stokes* equation.

[6] The mathematicians *Ivo M. Babuška* and *Franco Brezzi* are fortunately still alive.

to strange instabilities causing mesh dependent solutions due to the so-called spurious pressure modes, see, e. g., Braess [29], Brezzi & Fortin [31].

5.1.3 Semi Discrete Initial-Value Problem

As a next step, the spatially discretised but (still) time-continuous governing equations need to be characterised in order to chose a suitable time-discretisation method. In this context, an abstract illustration of all involved quantities is selected for clarity reasons and will be given in accordance to Ellsiepen [70] and Ehlers & Ellsiepen [55]. Following this, the space-discrete variables at the $N_{\mathbf{u}_s}$ displacement nodes and the $N_{\mathcal{P}}$ pressure nodes are unified in the vector $\boldsymbol{u}$, while the internal variables, i. e., the history variables $(\mathbf{C}_{Si})_n$ for the N *Maxwell* elements at the Q quadrature points are combined in the vector $\boldsymbol{q}$ yielding

$$\left.\begin{aligned} \boldsymbol{u} &= \big[\,(\boldsymbol{u}_S^1,\mathcal{P}^1),\dots,(\boldsymbol{u}_S^{N_{\mathcal{P}}},\mathcal{P}^{N_{\mathcal{P}}}),\dots,(\boldsymbol{u}_S^{N_{\mathbf{u}_s}})\,\big]^T,\\ \boldsymbol{q} &= \big[\,(\mathbf{C}_{Si})_1^1,\dots,(\mathbf{C}_{Si})_N^1,\dots,(\mathbf{C}_{Si})_1^Q,\dots,(\mathbf{C}_{Si})_N^Q\,\big]^T \end{aligned}\right\} \quad \boldsymbol{y} = (\boldsymbol{u}^T,\boldsymbol{q}^T)^T. \tag{5.9}$$

Thus, all $D\cdot N_{\mathbf{u}_s}+N_{\mathcal{P}}$ nodal DOF in $\boldsymbol{u}$ and all $N\cdot Q$ tensorial history variables in $\boldsymbol{q}$ are combined in the general vector of unknowns $\boldsymbol{y}$. Herein, $Q=E\cdot Q_e$ denotes the overall number of integration points used for the quadrature rule, while Q_e represents the number of integration points per element.

The space discrete function vectors in (5.8) can also be combined yielding a function vector $\boldsymbol{\mathcal{G}}=[\boldsymbol{\mathcal{G}}^h_{\mathbf{u}_s}\,,\,\boldsymbol{\mathcal{G}}^h_{\mathcal{P}}]^T$ containing the complete global system of equations. Moreover, a local vector $\boldsymbol{\mathcal{L}}$ can be introduced containing the $N\cdot Q$ evolution equations (4.122), which are needed to solve for the internal variables in $\boldsymbol{q}$. Thus, the local evolution equations at an integration point q can be given by the vector

$$\boldsymbol{\mathcal{L}}_q=\begin{bmatrix} [(\mathbf{C}_{Si})_1]'_S \;-\; \frac{1}{\eta_1^S}\,(\mathbf{C}_{Si})_1\,\mathbf{S}_1^S\,(\mathbf{C}_{Si})_1 \;+\; \frac{\zeta_1^S}{\eta_1^S\,(2\,\eta_1^S+3\,\zeta_1^S)}\,[\mathbf{S}_1^S\cdot(\mathbf{C}_{Si})_1]\,(\mathbf{C}_{Si})_1\\ \dots \qquad\qquad \dots \qquad\qquad \dots\\ [(\mathbf{C}_{Si})_N]'_S \;-\; \frac{1}{\eta_N^S}\,(\mathbf{C}_{Si})_N\,\mathbf{S}_N^S\,(\mathbf{C}_{Si})_N \;+\; \frac{\zeta_N^S}{\eta_N^S\,(2\,\eta_N^S+3\,\zeta_N^S)}\,[\mathbf{S}_N^S\cdot(\mathbf{C}_{Si})_N]\,(\mathbf{C}_{Si})_N \end{bmatrix}=\boldsymbol{0}\,. \tag{5.10}$$

Note that the vector above actually contains $\frac{D}{2}\cdot(D+1)\cdot N$ scalar-valued differential equations, i. e., one for each of the linearly independent scalar entries of the coefficient matrix of the symmetric history variables $(\mathbf{C}_{Si})_n$. Keeping in mind that the mechanical solid extra stress $\mathbf{T}^S_{E,\,mech.}$ in (5.4) implicitly depends on the internal variables $\boldsymbol{q}$, the variational problem (5.8) can be condensed using the space-discrete vector $\boldsymbol{\mathcal{F}}$ yielding the implicit initial value problem:

$$\boldsymbol{\mathcal{F}}(t,\boldsymbol{y},\boldsymbol{y}')=\begin{bmatrix}\boldsymbol{\mathcal{G}}(t,\boldsymbol{u},\boldsymbol{u}',\boldsymbol{q})\\ \boldsymbol{\mathcal{L}}(t,\boldsymbol{q},\boldsymbol{q}',\boldsymbol{u})\end{bmatrix}=\begin{bmatrix}\boldsymbol{M}\,\boldsymbol{u}' \;+\; \boldsymbol{k}(\boldsymbol{u},\boldsymbol{q}) \;-\; \boldsymbol{f}\\ \boldsymbol{A}\,\boldsymbol{q}' \;-\; \boldsymbol{r}(\boldsymbol{q},\boldsymbol{u})\end{bmatrix}\overset{!}{=}\boldsymbol{0}\,. \tag{5.11}$$

Herein, the abbreviation $(\,\cdot\,)'=(\,\cdot\,)'_S$ is used for simplicity and initial conditions can be accounted for by applying $\boldsymbol{y}(t_0)=\boldsymbol{y}_0$ at an initial time $t_0<t$. Moreover, $\boldsymbol{M}$ represents the so-called generalised mass matrix, $\boldsymbol{k}$ is the generalised stiffness vector containing the

nonlinear dependencies on $\boldsymbol{u}$ and $\boldsymbol{q}$, while $\boldsymbol{f}$ denotes the generalised force vector of the externally applied *Neumann* load functionals.

Next, the abstract system (5.11) needs to be classified with regard to the type of differential equations it contains. This is accomplished by a formal comparison of (5.11) with the corresponding weak forms and evolution equations, respectively. Following this, the aggregate momentum balance $(5.4)_1$ has no explicit dependence on the temporal change of the primary variables in $\boldsymbol{u}$, while the aggregate volume balance $(5.4)_2$ has only a dependence on the temporal change of the displacements $(\boldsymbol{u}_S^j)'$ but not the temporal change of the hydraulic pressure $(\mathcal{P}^j)'$. This characteristic leads to a singular generalised mass matrix $\boldsymbol{M}$ and thus, the global system $\boldsymbol{\mathcal{G}}$ can be classified as an index-1 system of differential-algebraic equations (DAE) of first order in time, cf. Ellsiepen [70]. A comparison of (5.10) and $(5.11)_2$ quickly reveals that $\boldsymbol{A}$ is a regular identity matrix, which classifies the local system $\boldsymbol{\mathcal{L}}$ to be a system of ordinary differential equations (ODE) of first order in time.

5.2 Finite Difference Method in Time

In order to solve the spatially discretised initial value problem (5.11), the system has to be discretised in time using a suitable numerical time integration method. Herein, the most important class of single step methods for differential equations of first order in time is collected in the so-called *Runge-Kutta*[7] methods, which simultaneously include implicit and explicit integration schemes. A detailed overview of these finite difference schemes can be found in Brenan *et al.* [30], Hairer *et al.* [86] or Hairer & Wanner [87] and references therein. However, the drawback of such a stepwise time integration on a spatially fixed FE discretisation is that the system of DAE turns into a system of stiff differential equations. Thus, an explicit time integration scheme will result in unstable numerical results unless the step size is chosen unreasonably small. Regarding the soft biological tissues under study, the deformation processes of interest are on a much larger time scale and thus, explicit time integration schemes are excluded in favour of the implicit ones. Following this, the so-called stiffly accurate s-stage diagonally implicit *Runge-Kutta* (DIRK) method has been proven to provide a suitable numerical integration scheme for the underlying problem. For more information about the DIRK method with regard to the computability of large DAE systems, the stability of the solution, as well as the possibility for an error controlled time increment control, the reader is referred to the works of Diebels *et al.* [40], Ehlers & Ellsiepen [55] or Ellsiepen [70].

Nevertheless, for the purpose of this monograph, only the implicit (backward) *Euler* scheme, which is naturally included in the DIRK method, will be reviewed briefly in order to gain an insight in the needed solution procedure. Herein, the temporal change $\boldsymbol{y}'_n$ of the primary and history variables in the unknown n^{th} time (*Euler*) step is approximated with a difference quotient by looking back to the previous known time step $n-1$

[7] *Carl David Tolmé Runge* (1856–1927) and *Martin Wilhelm Kutta* (1867–1944), both German mathematicians, developed their method to numerically solve ordinary differential equations in 1901.

yielding

$$\boldsymbol{y}'_n = \boldsymbol{y}'(t_n) = \frac{\boldsymbol{y}_n - \boldsymbol{y}_{n-1}}{\Delta t_n} = \frac{\Delta \boldsymbol{y}_n}{\Delta t_n} \qquad \text{with} \qquad \boldsymbol{y}_n = \boldsymbol{y}_{n-1} + \Delta \boldsymbol{y}_n \,, \tag{5.12}$$

where $\Delta t_n = t_n - t_{n-1}$ denotes the time increment in a time series $0 = t_0 < t_1 < ... < T$. Following this, (5.12) is inserted into (5.11) yielding a system of nonlinear equations, where the unknown increment $\Delta \boldsymbol{y}_n$ appears in an implicit manner, viz.:

$$\boldsymbol{\mathcal{F}}(t, \boldsymbol{y}, \boldsymbol{y}') = \boldsymbol{0} \quad \longrightarrow \quad \boldsymbol{\mathcal{F}}_n(t_n \,,\, \boldsymbol{y}_{n-1} + \Delta \boldsymbol{y}_n \,,\, \frac{1}{\Delta t_n} \Delta \boldsymbol{y}_n) =: \boldsymbol{R}_n(\Delta \boldsymbol{y}_n) = \boldsymbol{0} \,. \tag{5.13}$$

Thus, the vector $\boldsymbol{y}_n$ of the n^{th} time step is computed for given values $\boldsymbol{y}_{n-1}$ of the preceding time step by solving for the unknown increment $\Delta \boldsymbol{y}_n$, such that $(5.13)_2$ is fulfilled. Note that for the s-stage DIRK method, the nonlinear system $(5.13)_2$ is solved s times until the time increment is fully integrated. Recalling the global and local systems in (5.11), the nonlinear system is formulated in terms of the corresponding increments yielding

$$\begin{bmatrix} \boldsymbol{G}_n(\Delta \boldsymbol{u}_n \,,\, \Delta \boldsymbol{q}_n) \\ \boldsymbol{L}_n(\Delta \boldsymbol{u}_n \,,\, \Delta \boldsymbol{q}_n) \end{bmatrix} \equiv \begin{bmatrix} \boldsymbol{\mathcal{G}}_n(t_n \,,\, \boldsymbol{u}_{n-1} + \Delta \boldsymbol{u}_n \,,\, \frac{1}{\Delta t_n} \Delta \boldsymbol{u}_n \,,\, \boldsymbol{q}_{n-1} + \Delta \boldsymbol{q}_n) \\ \boldsymbol{\mathcal{L}}_n(t_n \,,\, \boldsymbol{q}_{n-1} + \Delta \boldsymbol{q}_n \,,\, \frac{1}{\Delta t_n} \Delta \boldsymbol{q}_n \,,\, \boldsymbol{u}_{n-1} + \Delta \boldsymbol{u}_n) \end{bmatrix} = \begin{bmatrix} \boldsymbol{0} \\ \boldsymbol{0} \end{bmatrix} . \tag{5.14}$$

5.3 Solution of the Resulting Nonlinear System

Usually, the nonlinear functional $\boldsymbol{R}_n(\Delta \boldsymbol{y}_n)$ of (5.13) is solved straightforward by applying a *Newton-Raphson*[8] scheme for instance. In order to do so, the *Jacobi*an (tangent) matrix

$$\boldsymbol{J}_n = \frac{\mathrm{d}\boldsymbol{R}_n}{\mathrm{d}\Delta \boldsymbol{y}_n} = \left. \frac{\partial \boldsymbol{\mathcal{F}}}{\partial \boldsymbol{y}} \right|_{\boldsymbol{z}} + \frac{1}{\Delta t_n} \left. \frac{\partial \boldsymbol{\mathcal{F}}}{\partial \boldsymbol{y}'} \right|_{\boldsymbol{z}} \tag{5.15}$$

is needed, where $\boldsymbol{z} = (t_n, \boldsymbol{y}_n, \boldsymbol{y}'_n)$ represents the current set of arguments. Following this, the *Jacobi*an of (5.14) takes the form:

$$\boldsymbol{J}_n = \left[\begin{array}{c:c} \dfrac{\partial \boldsymbol{G}_n}{\partial \Delta \boldsymbol{u}_n} & \dfrac{\partial \boldsymbol{G}_n}{\partial \Delta \boldsymbol{q}_n} \\ \hdashline \dfrac{\partial \boldsymbol{L}_n}{\partial \Delta \boldsymbol{u}_n} & \dfrac{\partial \boldsymbol{L}_n}{\partial \Delta \boldsymbol{q}_n} \end{array}\right] = \left[\begin{array}{c:c} \dfrac{\partial \boldsymbol{\mathcal{G}}}{\partial \boldsymbol{u}} + \dfrac{1}{\Delta t_n} \dfrac{\partial \boldsymbol{\mathcal{G}}}{\partial \boldsymbol{u}'} & \dfrac{\partial \boldsymbol{\mathcal{G}}}{\partial \boldsymbol{q}} \\ \hdashline \dfrac{\partial \boldsymbol{\mathcal{L}}}{\partial \boldsymbol{u}} & \dfrac{\partial \boldsymbol{\mathcal{L}}}{\partial \boldsymbol{q}} + \dfrac{1}{\Delta t_n} \dfrac{\partial \boldsymbol{\mathcal{L}}}{\partial \boldsymbol{q}'} \end{array}\right] \tag{5.16}$$

Herein, the upper left block matrix represents a usual sparse FE matrix consisting of the generalised stiffness matrix $\boldsymbol{K} = \partial \boldsymbol{\mathcal{G}} / \partial \boldsymbol{u}$ and the generalised mass matrix $\boldsymbol{M} = \partial \boldsymbol{\mathcal{G}} / \partial \boldsymbol{u}'$, which are obtained by a consistent linearisation of the space-discrete nodal *Galerkin* equations (5.8). In this regard, the directional *Gâteaux*[9] derivative is needed, which describes

[8] *Joseph Raphson* (1648–1715): British mathematician who published a method for approximating the roots of an equation in *Analysis Aequationum Universalis* in 1690. Almost 20 years earlier, *Newton* developed a very similar but more sophisticated formula, which was not published until 1736.

[9] *René Gâteaux* (1889–1914): French mathematician who was killed in World War I at the age of 25.

the change of the linearised function $\boldsymbol{\mathcal{G}}_n$ at $\boldsymbol{u}_n$ in the direction of $\Delta\boldsymbol{u}_n$, cf. Wriggers [235] and references therein. For an application of this derivative to multi-phasic problems in the finite strain regime, the reader is referred to Eipper [67], Mahnkopf [129], Markert [131], whereas the resulting derivatives are provided in Appendix C. Moreover, the lower right block matrix is sub-structured into Q diagonal blocks representing the linearisation of the space-discrete system of evolution equations (5.10) at the Q integration points.

Following this, it is devastating to solve the nonlinear function vector $\boldsymbol{R}_n(\Delta\boldsymbol{y}_n)$ with the *Jacobi*an (5.16), because the partially sparse structure would be completely destroyed. Hence, a suitable blockwise solution is needed in order to retain the sparse structure of the time- and space-discrete FE system $\boldsymbol{G}_n$ and to solve the equations $\boldsymbol{L}_n$ at the integration points in a decoupled fashion on element level.

5.3.1 Multilevel *Newton* Method

In order to exploit the block-structured nature of (5.16), a generalisation of the Block *Gauß-Seidel*[10]*-Newton* method is applied, which is known as multilevel or two-stage *Newton* procedure. Herein, the implicit dependence of the local $\boldsymbol{L}$-equations on the linearisation of the global $\boldsymbol{G}$-equations is considered. This method is strongly related to the term "algorithmically consistent linearisation", which was established by Simo & Taylor [187] in the context of computational finite elastoplasticity. For a more detailed introduction into the solution procedure, the reader is referred to Diebels *et al.* [40], Ehlers & Ellsiepen [55], Ellsiepen [70] or Ellsiepen & Hartmann [71].

Following this, the local system needs to be solved before the global system. This corresponds to the physical interpretation, where the locations of the intermediate configurations are computed at a frozen actual configuration, while the location of the actual configuration is iteratively determined thereafter using frozen intermediate configurations. Thus, in the first substep of the global *Newton* iteration, the nonlinear evolution equations $\boldsymbol{L}_n$ are solved for the local increments $\Delta\boldsymbol{q}_n$ of the history variables. The local solution is then carried out separately at each integration point Q using a local *Newton-Raphson* scheme with fixed (given) increments of the primary variables $\Delta\boldsymbol{u}_n$. Provided that the local system $\boldsymbol{L}_n$ is solved sufficiently exact, the local increments $\Delta\boldsymbol{q}_n$ can be understood as a function of the global increments $\Delta\boldsymbol{u}_n$, viz.:

$$\boldsymbol{L}_n(\Delta\boldsymbol{u}_n\,,\,\Delta\boldsymbol{q}_n) = \boldsymbol{0} \qquad \longrightarrow \qquad \Delta\boldsymbol{q}_n = \Delta\boldsymbol{q}_n(\Delta\boldsymbol{u}_n)\,. \tag{5.17}$$

Thus, the differential of $\boldsymbol{L}_n[\Delta\boldsymbol{u}_n\,,\,\Delta\boldsymbol{q}_n(\Delta\boldsymbol{u}_n)]$ with respect to $\Delta\boldsymbol{u}_n$ also vanishes yielding

$$\frac{\mathrm{d}\boldsymbol{L}_n}{\mathrm{d}\Delta\boldsymbol{u}_n} = \frac{\partial\boldsymbol{L}_n}{\partial\Delta\boldsymbol{u}_n} + \frac{\partial\boldsymbol{L}_n}{\partial\Delta\boldsymbol{q}_n}\,\frac{\partial\Delta\boldsymbol{q}_n}{\partial\Delta\boldsymbol{u}_n} = \boldsymbol{0} \qquad \longrightarrow \qquad \frac{\partial\Delta\boldsymbol{q}_n}{\partial\Delta\boldsymbol{u}_n} = -\left[\frac{\partial\boldsymbol{L}_n}{\partial\Delta\boldsymbol{q}_n}\right]^{-1}\frac{\partial\boldsymbol{L}_n}{\partial\Delta\boldsymbol{u}_n}\,. \tag{5.18}$$

Accordingly, due to the block-diagonal structure of the matrix $\partial\boldsymbol{L}_n/\partial\Delta\boldsymbol{q}_n$, the small linear system above can be solved in a decoupled fashion on integration point level.

[10] *Philipp Ludwig Ritter von Seidel* (1821–1896): German mathematician, optician and astronomer who is well known for his five *Seidel* aberrations as well as his iterative numerical solution method.

The second step of the global *Newton* iteration is to compute the algorithmically consistent linearisation of $\boldsymbol{G}_n[\Delta\boldsymbol{u}_n, \Delta\boldsymbol{q}_n(\Delta\boldsymbol{u}_n)]$, i. e., the total differential with respect to $\Delta\boldsymbol{u}_n$, yielding the consistent global *Jacobi*an (tangent) matrix

$$\boldsymbol{J}_{\boldsymbol{G}_n} := \frac{\mathrm{d}\boldsymbol{G}_n}{\mathrm{d}\Delta\boldsymbol{u}_n} = \frac{\partial\boldsymbol{G}_n}{\partial\Delta\boldsymbol{u}_n} + \frac{\partial\boldsymbol{G}_n}{\partial\Delta\boldsymbol{q}_n}\frac{\partial\Delta\boldsymbol{q}_n}{\partial\Delta\boldsymbol{u}_n} = \frac{\partial\boldsymbol{G}_n}{\partial\Delta\boldsymbol{u}_n} - \frac{\partial\boldsymbol{G}_n}{\partial\Delta\boldsymbol{q}_n}\left[\frac{\partial\boldsymbol{L}_n}{\partial\Delta\boldsymbol{q}_n}\right]^{-1}\frac{\partial\boldsymbol{L}_n}{\partial\Delta\boldsymbol{u}_n}\,. \tag{5.19}$$

Herein, the first term $\partial\boldsymbol{G}_n/\partial\Delta\boldsymbol{u}_n$ denotes the *Gâteaux* derivatives of the weak forms (5.4) at frozen intermediate configurations, while the remaining term corresponds to the missing term $(\mathbf{B}^S_{\mathrm{INT}})^{\underline{4}}$ of the non-equilibrium material tangent (4.92) resulting from a frozen actual configuration. In this context, the global *Jacobi*an given in Appendix C is consistent, as long as the correct non-equilibrium material tangent $(\boldsymbol{\mathcal{B}}^S_{\mathrm{NEQ}})^{\underline{4}}$ is inserted.

Finally, the sparse linear system can be postulated

$$\boldsymbol{J}_{\boldsymbol{G}_n}\,\Delta\boldsymbol{u}_n = -\boldsymbol{G}_n[\Delta\boldsymbol{u}_n\,,\,\Delta\boldsymbol{q}_n(\Delta\boldsymbol{u}_n)] \tag{5.20}$$

and solved for the global *Newton* increment $\Delta\boldsymbol{u}_n$, which is needed in order to update the old global vector $\boldsymbol{u}_{n-1}$ of the preceding time step. This procedure is repeated until a user-defined criterion, such as the norm of the function vector $||\boldsymbol{G}_n|| < TOL_{\boldsymbol{G}_n}$, is met. Note that the total *Euler* increment $\Delta\boldsymbol{u}_n$ is actually never computed, as it is continuously updated during the iterative *Newton-Raphson* procedure.

Note in passing that the linear system (5.20) belongs to the class of saddle point problems which are characterised by their indefiniteness and frequently occurring poor spectral properties. In this regard, special care must be taken regarding the choice of a suitable solver. A good overview on this topic can be found in Benzi *et al.* [17] and references therein. In general, the so-called *Krylov*[11] subspace methods provide stable solutions. For the purpose of this monograph, the generalised minimal residual method (GMRES) of Saad & Schultz [171] is applied, which is extensively discussed in Wieners *et al.* [230] in the context of an inelastic multi-phasic model.

Moreover, in the context of a numerical implementation, the following substeps have to be carried out for every global *Newton* step k of the current time increment n:

1. Compute the defect $\boldsymbol{G}^k_n(\boldsymbol{u}^k_n, \boldsymbol{q}^k_n)$ of the new time step including the *Neumann* boundary conditions and proceed to the next time step, if the user-defined criterion for $||\boldsymbol{G}^k_n||$ is met. If $||\boldsymbol{G}^k_n|| > TOL_{\boldsymbol{G}_n}$, start the global *Newton* iteration and proceed to step two. Note that the defect is computed element wise via a quadrature rule. In order to do so, the stress needs to be computed at every integration point which requires the solution of the local evolution equations $(5.17)_1$. Thus, the evaluation of the defect $\boldsymbol{G}^k_n(\boldsymbol{u}^k_n, \boldsymbol{q}^k_n)$ automatically leads to the determination of the current vector of the internal variables $\boldsymbol{q}^k_n(\boldsymbol{u}^k_n) := \boldsymbol{q}^{k,m+1}_n = \boldsymbol{q}^{k,m}_n + \Delta\boldsymbol{q}^{k,m}_n(\Delta\boldsymbol{u}^k_n)$ in m local *Newton* iterations, respectively.

2. Compute the consistent *Jacobi*an matrix $\boldsymbol{J}^k_{\boldsymbol{G}_n}$ as is given in (5.19).

[11] *Alexei Nikolaevich Krylov* (1863–1945): Russian ship engineer and applied mathematician who was first to propose gyroscopic damping which is now the most common way of damping the roll of a ship.

3. Solve the sparse linear system (5.20) for $\Delta \boldsymbol{u}_n^k$.
4. Update the global variables $\boldsymbol{u}_n^{k+1} = \boldsymbol{u}_n^k + \Delta \boldsymbol{u}_n^k$.
5. Compute the new defect $\boldsymbol{G}_n^{k+1}(\boldsymbol{u}_n^{k+1}, \boldsymbol{q}_n^{k+1})$ and check for convergence. If $||\boldsymbol{G}_n^{k+1}|| > TOL_{\boldsymbol{G}_n}$, repeat from step two, whereas if $||\boldsymbol{G}_n^{k+1}|| < TOL_{\boldsymbol{G}_n}$, proceed to next time increment and start with step one again.

5.3.2 Solid Stress Computation

During every iteration step of the multilevel *Newton* method, a finite element code requires an algorithm which computes the solid extra stress tensor $\mathbf{T}_{\mathrm{E}}^S$ and the consistent material tangent $(\boldsymbol{\mathcal{C}}^S)^{\underline{4}}$ at every integration point of the numerical quadrature. In particular, the solid stress is needed for the evaluation of the defect, while the computation of the consistent *Jacobi*an matrix (5.19) demands for the stress and the material tangent.

As a first step in the stress computation, the purely elastic *Cauchy* stress $\mathbf{T}_{\mathrm{EQ}}^S$ is computed using the actual deformation gradient $(\mathbf{F}_S)^{\mathrm{act}}$ of the running global iteration step by accumulating the osmotic (4.98), isotropic (4.104) and anisotropic (4.113) contributions, respectively. Herein, the eigenvalues and eigentensors of the actual left solid deformation tensor $(\mathbf{B}_S)^{\mathrm{act}}$ need to be provided, as well as the invariants containing the right solid deformation tensor $(\mathbf{C}_S)^{\mathrm{act}}$. Thereafter, the local *Newton* iteration starts and an independent elastic trial state

$$(\mathbf{B}_{Se})_n^{\mathrm{trial}} = (\mathbf{F}_S)^{\mathrm{act}} \, (\mathbf{C}_{Si}^{-1})_n^{\mathrm{last}} \, (\mathbf{F}_S^T)^{\mathrm{act}} \tag{5.21}$$

is computed via a transport of the last inelastic deformation tensor $(\mathbf{C}_{Si}^{-1})_n^{\mathrm{last}}$ taken from the last time step, but using the actual deformation gradient $(\mathbf{F}_S)^{\mathrm{act}}$ as transporting quantity. Then, the individual trial overstresses $(\mathbf{T}_n^S)^{\mathrm{trial}}$ of the individual *Maxwell* elements are computed in accordance to (4.119) using the elastic eigenvalues and eigentensors of the respective trial deformation tensors $(\mathbf{B}_{Se})_n^{\mathrm{trial}}$. Since the viscoelastic evolution equations (5.10) contain the non-equilibrium trial stresses expressed in the referential frame, the non-equilibrium trial stresses are pulled back using the covariant transport $(\mathbf{S}_n^S)^{\mathrm{trial}} = \det(\mathbf{F}_S)^{\mathrm{act}} \, (\mathbf{F}_S^{-1})^{\mathrm{act}} \, (\mathbf{T}_n^S)^{\mathrm{trial}} \, (\mathbf{F}_S^{T-1})^{\mathrm{act}}$. Thereafter, the local system $\boldsymbol{L}_n$ (5.17) containing the evolution equations $\boldsymbol{\mathcal{L}}_q$ of the corresponding *Maxwell* elements is solved at the respective quadrature point using *Newton*'s method. The iterative procedure is then locally repeated until a user-defined criterion is met, i. e., $||\boldsymbol{L}_n|| < TOL_{\boldsymbol{L}}$. Thereafter, the local iteration is stopped and the non-equilibrium *Cauchy* stress $\mathbf{T}_{\mathrm{NEQ}}^S = \sum_{n=1}^N \mathbf{T}_n^S$ is obtained by accumulating the last trial stresses $\mathbf{T}_n^S$ satisfying (5.10). Finally, the solid *Cauchy* extra stress tensor $\mathbf{T}_{\mathrm{E}}^S = \mathbf{T}_{\mathrm{EQ}}^S + \mathbf{T}_{\mathrm{NEQ}}^S$ is computed and the history variables $(\mathbf{C}_{Si})_n$ are updated for the proceeding time step.

Note that the determination of eigenvalues and eigenvectors for the coefficient matrices of the left deformation tensors $\mathbf{B}_S$ and $\mathbf{B}_{Se}$ is a very sensitive issue in computational mechanics. Following this, a robust algorithm is needed regarding the treatment of identical eigenvalues, like they naturally occur in the undeformed referential frame. According to Markert [131], one of the most efficient techniques for finding eigenvalues and eigenvectors

of real symmetric matrices is the combination of the *Householder*[12] reduction followed by a QL decomposition, cf. Press *et al.* [165].

Moreover, if the global *Jacobi*an matrix (5.19) needs to be computed, the consistent material tangent $(\boldsymbol{\mathcal{C}}^S)\underline{^4}$ is required additionally to the solid extra stress. Following equations (4.90) and (4.92), this is achieved by

$$\overset{4}{\boldsymbol{\mathcal{C}}}{}^{\mathrm{S}} = \overset{4}{\boldsymbol{\mathcal{C}}}{}^{\mathrm{S}}_{\mathrm{EQ}} + \overset{4}{\boldsymbol{\mathcal{C}}}{}^{\mathrm{S}}_{\mathrm{NEQ}} = \overset{4}{\boldsymbol{\mathcal{C}}}{}^{\mathrm{S}}_{\mathrm{OSM}} + \overset{4}{\boldsymbol{\mathcal{C}}}{}^{\mathrm{S}}_{\mathrm{ISO}} + \overset{4}{\boldsymbol{\mathcal{C}}}{}^{\mathrm{S}}_{\mathrm{ANISO}} + \sum_{n=1}^{N} \overset{4}{\mathbf{C}}{}^{S}_{n} + (\mathbf{F}_S \otimes \mathbf{F}_S)^{\overset{23}{T}} \overset{4}{\mathbf{B}}{}^{S}_{\mathrm{INT}} (\mathbf{F}_S^T \otimes \mathbf{F}_S^T)^{\overset{23}{T}}, \quad (5.22)$$

where the osmotic, isotropic, anisotropic, and non-equilibrium contributions are computed in accordance to (4.101), (4.105), (4.115), and (4.120), respectively. The missing part

$$\overset{4}{\mathbf{B}}{}^{S}_{\mathrm{INT}} = \sum_{n=1}^{N} \frac{\partial \mathbf{S}^S_n}{\partial (\mathbf{E}_{Si})_n} \frac{\partial (\mathbf{E}_{Si})_n}{\partial \mathbf{E}_S} \Bigg|_{\mathbf{E}_S = \mathrm{const.}} = \sum_{n=1}^{N} 2 \frac{\partial \mathbf{S}^S_n}{\partial (\mathbf{C}_{Si})_n} \frac{\partial (\mathbf{C}_{Si})_n}{\partial \mathbf{C}_S} \Bigg|_{\mathbf{C}_S = \mathrm{const.}} . \quad (5.23)$$

is computed by exploiting the solution of the local linear system $(5.18)_2$. In this context, the unknown partial derivative $\partial(\mathbf{C}_{Si})_n / \partial \mathbf{C}_S$ of the n^{th} *Maxwell* element is included in the partial derivative $\partial \Delta \boldsymbol{q}_n / \partial \Delta \boldsymbol{u}_n$ of the n^{th} *Euler* step obtained from $(5.18)_2$. Moreover, the derivative of $\mathbf{S}^S_n$ with respect to $(\mathbf{C}_{Si})_n$ can be reformulated with the aid of the corresponding covariant transport mechanism yielding

$$\begin{aligned}
\frac{\partial \mathbf{S}^S_n}{\partial (\mathbf{C}_{Si})_n} &= (\mathbf{F}_S^{-1} \otimes \mathbf{F}_S^{-1})^{\overset{23}{T}} \frac{\partial \boldsymbol{\tau}^S_n}{\partial (\mathbf{B}_{Se})_n} \frac{\partial (\mathbf{B}_{Se})_n}{\partial (\mathbf{C}_{Si})_n} \\
&= (\mathbf{F}_S^{-1} \otimes \mathbf{F}_S^{-1})^{\overset{23}{T}} \frac{\partial \boldsymbol{\tau}^S_n}{\partial (\mathbf{B}_{Se})_n} (\mathbf{F}_S \otimes \mathbf{F}_S)^{\overset{23}{T}} \frac{\partial (\mathbf{C}^{-1}_{Si})_n}{\partial (\mathbf{C}_{Si})_n} \\
&= -(\mathbf{F}_S^{-1} \otimes \mathbf{F}_S^{-1})^{\overset{23}{T}} \frac{\partial \boldsymbol{\tau}^S_n}{\partial (\mathbf{B}_{Se})_n} \left[\mathbf{F}_S (\mathbf{C}^{-1}_{Si})_n \otimes \mathbf{F}_S (\mathbf{C}^{-1}_{Si})_n\right]^{\overset{23}{T}}.
\end{aligned} \quad (5.24)$$

The missing derivative can then be given by

$$\begin{aligned}
\frac{\partial \boldsymbol{\tau}^S_n}{\partial (\mathbf{B}_{Se})_n} &= 2 \sum_{k,l=1}^{3} \frac{\partial^2 \overline{W}^S_{\mathrm{NEQ}}}{\partial (\lambda_{Se(k)})_n \partial (\lambda_{Se(l)})_n} (\lambda_{Se(l)})_n (\mathbf{N}_{Se(l)})_n \otimes (\mathbf{N}_{Se(k)})_n + \\
&+ 2 \sum_{k=1}^{3} \frac{\partial \overline{W}^S_{\mathrm{NEQ}}}{\partial (\lambda_{Se(k)})_n} (\mathbf{N}_{Se(k)})_n \otimes (\mathbf{N}_{Se(k)})_n + \\
&+ \sum_{\substack{k,l=1 \\ k \neq l}}^{3} \frac{\frac{\partial \overline{W}^S_{\mathrm{NEQ}}}{\partial (\lambda_{Se(k)})_n} (\lambda_{Se(k)})_n - \frac{\partial \overline{W}^S_{\mathrm{NEQ}}}{\partial (\lambda_{Se(l)})_n} (\lambda_{Se(l)})_n}{(\lambda_{Se(k)})_n - (\lambda_{Se(l)})_n} \overset{4}{(\mathbf{N}_{Se[kl]})_n} + \\
&+ \frac{1}{2} \left[(J^2_{Se})_n \left(\frac{\partial^2 \overline{U}^S_{\mathrm{NEQ}}}{\partial (J^2_{Se})_n} + n^S \frac{\partial^2 \overline{U}^S_{\mathrm{NEQ}}}{\partial (J_{Se})_n \partial (n^S_{Si})_n} \right) + (J_{Se})_n \frac{\partial \overline{U}^S_{\mathrm{NEQ}}}{\partial (J_{Se})_n} \right] (\mathbf{B}^{-1}_{Se})_n \otimes \mathbf{I}
\end{aligned} \quad (5.25)$$

[12] *Alston Scott Householder* (1904–1993): American mathematician who specialised in mathematical biology and numerical analysis.

with the abbreviation $(\overset{4}{\mathbf{N}}_{Se[kl]})_n = [(\mathbf{N}_{Se(k)})_n \otimes (\mathbf{N}_{Se(l)})_n]^{\overset{23}{T}} + [(\mathbf{N}_{Se(k)})_n \otimes (\mathbf{N}_{S(l)})_n]^{\overset{24}{T}}$. Note that the derivatives in (5.25) have to be taken of the overall non-equilibrium strain energy $W^S_{\mathrm{NEQ}} = \overline{W}^S_{\mathrm{NEQ}} + \overline{U}^S_{\mathrm{NEQ}}$, where the volumetric extension term is a function of the elastic *Jacobi*ans $(J_{Se})_n$ and the inelastic solid volume fractions $(n^S_{Si})_n = n^S\,(J_{Se})_n$.

5.3.3 Admissible Initial Conditions

Due to the choice of $\mathcal{P}$ as primary variable, the presented model does not *a priori* exhibit a stress-free reference configuration. This becomes clear when the overall stress (4.123) of the model is computed, thereby using values of the natural state, i. e., $\mathbf{u}_S = \mathbf{0}$ and $\mathcal{P} = 0$. Following this, equations (4.97) and (4.98) will always develop an initial osmotic pressure

$$\Delta\pi_{0S} := R\Theta\,[\sqrt{4\,\bar{c}_m^2 + (c^{fc}_{0S})^2} - 2\,\bar{c}_m]\,. \tag{5.26}$$

In this context, there are two possibilities to obtain a stress-free reference configuration in the sense of classical continuum mechanics, i. e., $\mathbf{T}_{0S} = \mathbf{0}$. Herein, the first approach leads to an addition of the constant part $\Delta\pi_{0S}\,\mathbf{I}$ onto the mechanical extra stress $\mathbf{T}^S_{E,\,mech.}$ yielding a pre-stressed solid skeleton without any deformation, viz.:

$$\mathbf{T}_{0S} = \mathbf{T}^S_{E0S,\,mech.} - (\mathcal{P} + \Delta\pi_{0S}) \overset{!}{=} \mathbf{0} \qquad \longrightarrow \qquad \mathbf{T}^S_{E0S,\,mech.} = \Delta\pi_{0S}\,\mathbf{I}\,. \tag{5.27}$$

The other possibility leads to an initial swelling process of the tissue until the initial osmotic pressure $\Delta\pi_{0S}\,\mathbf{I}$ is compensated by tension in the mechanical extra stress $\mathbf{T}^S_{E,\,mech.}$. Herein, the initial stress of the overall model

$$\mathbf{T}_{0S} = \mathbf{T}^S_{E0S,\,mech.} - (\mathcal{P} + \Delta\pi_{0S}) \neq \mathbf{0} \tag{5.28}$$

is left unbalanced leading to an iteration process which is completed, when the primary variables $\mathbf{u}_S$ and $\mathcal{P}$ have reached values such that $\mathbf{T}_{0S} = \mathbf{0}$. The physical interpretation of this would be something like an inverse consolidation process yielding a pre-stressed solid skeleton accompanied by a compatible volumetric deformation.

Regarding general nonlinear material laws, it makes a big difference which approach is followed, as the superposition principle of linear elasticity cannot be applied. In this regard, the problem can be visualised by drawing the response of the volumetric mechanical extra stress $T^S_m = \frac{1}{3}\mathbf{T}^S_{E,\,mech.} \cdot \mathbf{I}$ over the volumetric solid deformation J_S for each of the two possibilities. Following this, Figure 5.3 (a) shows the situation for the first method which leads to a shift in the origin, while the second method depicted in Figure 5.3 (b) does not exhibit this shift. Concerning general nonlinear material laws, the method of choice depends on the specimens available for parameter identification. Note that for biomaterials or living tissues it is always impossible to obtain a specimen which has a decoupled pre-stressed solid skeleton, since this is understood as an *a priori* "ingrown" natural stress state. In this regard, the specimens obtained are always in equilibrium, when taken out of the organism and thus, testing occurs always on pre-stressed samples having no initial deformation. Hence, if the parameters obtained from such experiments are used for the second approach, the stress-strain relationship will actually describe a

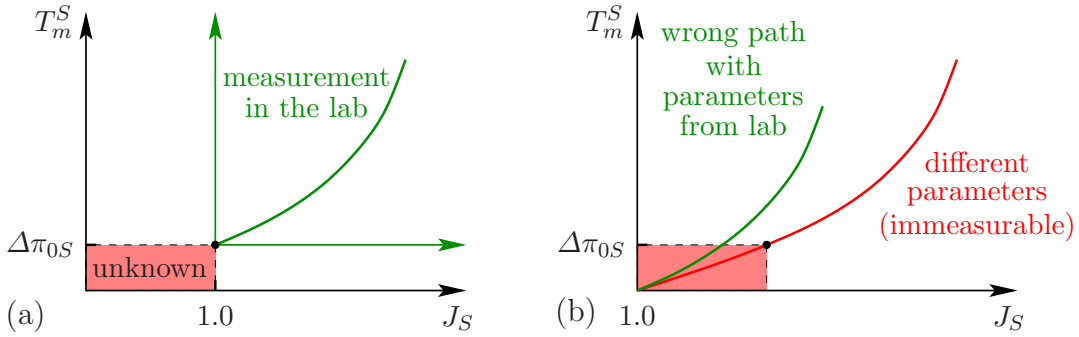

Figure 5.3: *Illustration of two different approaches to treat pre-stressed soft biological tissues. Herein, the solid skeleton can either be pre-stressed by $\Delta\pi_{0S}$ without an initial deformation (a) or with an initial deformation (b).*

different behaviour. Following this, the first approach is chosen for later computations of the IVD, as this is the only approach allowing for a convenient determination of the material parameters.

Moreover, if the initial osmotic pressure is always added onto the mechanical solid extra stress, then the corresponding material tangent $(\boldsymbol{\mathcal{C}}^S_{\mathrm{OSM}})^{\underline{4}}$ needs to be modified as well. This will be discussed in Appendix C, where the consistent linearisation of the governing equations is given.

5.4 Parallelisation of the Finite Element Simulation

The underlying model as well as the numerical solution scheme were implemented into the sequential research code PANDAS[13] which traces back to Ehlers & Ellsiepen [54, 55] and Ellsiepen [70]. However, as already mentioned before, the numerical solvability (computability) of the presented nonlinear coupled differential equations is reached relatively soon on single CPU machines. This is mainly due to the involved complex geometries in computational biomechanics, like in the case of the spine, for instance. Herein, a large number of elements is needed to approximate the geometry, which in turn leads to a large number of unknowns and thus, to large linear systems to be solved in (5.20). Especially the quadratic approximation of the displacements in the *Taylor-Hood* elements leads to a quickly rising number of the DOF in 3D. Moreover, 3-d adaptive strategies with remeshing are rather difficult to achieve due to the irregular geometries and lie beyond the scope of this monograph. Alternatively, the described solution procedure can be carried out in parallel using several PCU simultaneously. Since the development of a new parallel code lies also beyond the focus of this work, the research program PANDAS is coupled with the parallel solver M++[14] by extending an already existing interface. In this regard, the interface was originally designed by Ammann [4] and Wieners *et al.* [229] for the computation

[13] Porous media Adaptive Nonlinear finite element solver based on Differential Algebraic Systems [158].
[14] Mesh, Multigrid and More [226]

of large geotechnical BVP, where it is possible to set up a coarsely discretised BVP in PANDAS and almost directly solve finer discretised grids in parallel using M++.

The purpose of this Section is to provide a brief overview on the capabilities of the two codes as well as to give an introduction to the basic idea of the interface.

5.4.1 Capabilities of PANDAS and M++

PANDAS is a very sophisticated FE code which was originally developed for research purposes and is continuously enhanced at the Institute of Applied Mechanics (Continuum Mechanics) at the Universität Stuttgart. Its structure is designed to allow for a very efficient treatment of mixed finite elements and is held general enough to enable the implementation of almost every possible coupled problem. Even the treatment of general inelastic material behaviour is structured in such a way that it is possible to implement the respective theories without going into the details of the whole FE code. Herein, the user is provided with several interfaces to the PANDAS core, which allow for a convenient handling of the material parameters, the history variables, the element properties, the numerical integration of the governing equations and the consistent linearisation on element level, as well as the solution of the local DAE system among many other features. Especially useful is a library containing all the routines needed for tensor calculus, i. e., it is possible to directly compute the respective tensor products without the need to program them using loops. Moreover, it contains space (only in 2D) and time adaptive strategies as well as a direct and several iterative solvers for linear systems of equations. Another really big benefit is the way the boundary conditions can be incorporated. Herein, one has almost any possibility to set initial conditions as well as *Neumann* and *Dirichlet* conditions on external boundaries or even at distinct nodes in the inside of the discretised domain.

On the other hand, there is the program M++ of Wieners [226] which is designed to pursue a different goal. Following the name Mesh, Multigrid and More (M++), it becomes obvious that the main interest is not on the physical side but on its parallel algorithms for the numerical solution of the arising of strongly coupled problems. In this regard, M++ was built to perform on MIMD (multiple instruction stream, multiple data stream) architectures and is based on the parallel programming model MPI (Message Passing Interface) of Walker & Dongarra [219]. Note that an MIMD architecture is basically a cluster of several individual workstations which are connected by a network. The workstations themselves are mostly classical personal computers (PC) of the *von Neumann*[15] type [80, 218] which have a single instruction and a single data stream (SISD). This requires the need for a parallel data structure which uniquely defines the elements or cells of a finite element mesh on all the computing nodes. In M++ this is realised using the so-called Distributed Point Objects (DPO) as is described in Wieners *et al.* [229]. Regarding the solution of the nonlinear and time-dependent simulation, the most sensible part of the parallelisation is the solution of the linear problems (5.20) within every *Newton* step. Herein, M++ uses a

[15] *John von Neumann* (1903–1957): Hungarian American mathematician who made major contributions to a vast range of fields including theoretical an applied mathematics, quantum mechanics, and computer science. Herein, he was highly involved in the design of nuclear weapons which were dropped on Hiroshima and Nagasaki and developed a computer architecture which *de facto* became today's standard.

parallel GMRES method, as is described in Wieners *et al.* [230], together with a domain decomposition preconditioner.

From numerical experiments it is well-known that overlapping domain decomposition preconditioners with coarse grid correction applied to the *Navier*[16]-*Stokes*[17] system using *Taylor-Hood* elements are very efficient, see Klawonn & Pavarino [108, 109]. Hence, this type of preconditioning is a good choice for the discussed application to complex biomechanical structures which leads to a similar system. Although, two major modifications are required due to the following reasons: Only a moderate number of processors is used so that the subdomain problems are too large for exact solving. Moreover, the underlying geometry is too complex to allow for a small coarse mesh. Thus, an inexact sub-domain solver is used (a multilevel incomplete LU factorisation (ILU) with pivoting and dropping strategy by Mayer [136, 137]) and the coarse problem is constructed on an independent overlay mesh. Last but not least, M++ provides the possibility to uniformly refine a given finite element mesh which allows for convergence studies regarding the mesh size.

Thus, in order to simultaneously use the conveniences of PANDAS during the design of a user element as well as the power of the parallel solver M++, an interface needs to be defined which will be discussed in the following subsection.

5.4.2 Interface M++/PANDAS

Following the idea of keeping PANDAS for the definition of the physics-specific routines as well as for the definition of the BC, the simplest possibility is to incorporate the interface on element level. The benefit is that PANDAS does not need to be modified at all and a BVP set up in PANDAS can be computed directly in parallel using M++ as a black box solver. In this regard, M++ manages only the global FE mesh with its unknowns as well as the corresponding element specific data (history variables, inhomogeneous material parameters). PANDAS is then initiated in the background and called E times during the global assembly of the defect $\boldsymbol{G}_n^k(\boldsymbol{u}_n^k, \boldsymbol{q}_n^k)$ and the *Jacobi*an matrix $\boldsymbol{J}_{\boldsymbol{G}_n}^k$. Thus, these routines have a key function, as they are called fairly often within a *Newton* step. Moreover, due to the parallel data structure of M++, these routines can be executed simultaneously on several processors without any network communication. The difficult task of solving the global system on several processors is then performed by M++ needing network communication.

In particular, PANDAS is initiated with only a single element. The nodal coordinates, the vector of unknowns and the history variables are then changed for each of the E elements, every time an element is passed from M++ to PANDAS. Hence, the interface needs to provide the following routines [4]:

- `Pandas_Init`: Initiates PANDAS with the required types of finite elements. Herein, the PANDAS data structure is constructed and the element is linked with the de-

[16] *Claude Louis Marie Henri Navier* (1785–1836): French engineer and physicist who specialised in mechanics. His major contribution however remains the *Navier-Stokes* equations of 1822.

[17] *Sir George Gabriel Stokes, 1st Baronet* (1819–1903): British mathematician and physicist who made important contributions to fluid dynamics, optics, and mathematical physics.

sired physics routine containing the weak forms of the global system, the evolution equations as well as the corresponding material parameters.

- `InitInhomo`: Initially computes the inhomogeneous distribution of the fibre vectors and the involved material parameters as is described in Subsection 6.1.2. This has to be carried out within the interface, as the respective algorithms for the computation of the inhomogeneous distributions depend on data of the overall mesh, which is never fully available in PANDAS.
- `Pandas_Dirichlet`: Evaluates the *Dirichlet* boundary conditions.
- `Pandas_Defect`: Evaluates the *Neumann* boundary conditions and computes the defect (residual) on element level. Herein, the solution of the local system on quadrature point level is performed by PANDAS. Thus, besides the element residual vector, the newly obtained history variables are also returned to M++ in this routine.
- `Pandas_Tangent`: Computes the algorithmically consistent tangent on element level.
- `Pandas_Update`: Updates the history variables in PANDAS.
- `InitElem`: Converts the data format of M++ into the data structure of PANDAS, every time before one of the four routines above is called.

Note that this idea can also be used as a general structure for user elements in commercial FE codes like ABAQUS, ANSYS, LSDyna, etc. For more detailed information on such an interface between PANDAS and ABAQUS, the reader is referred to Schenke [173].

6 Application to the Intervertebral Disc

Concerning the simulation of soft biological tissues in general and the IVD or spine in particular, the creation of the underlying finite element mesh is not straightforward, as the involved geometries are rather complex. Thus, an extra section about this topic will be presented, wherein the creation of a realistic geometry model as well as the inclusion of inhomogeneously distributed quantities like the fibre vectors is addressed.

In a next step, the theoretically introduced parameters need to be identified. As the author does not have the possibility to perform experiments on living tissues, the identification is carried out with experimental results obtained from literature. Subsequently, a numerical sensitivity analysis is carried out in order to judge the influence of the respective parameters on a compression-bending experiment of a motion segment as a representative deformation mode of the spine. Herein, the model can be understood as a numerical laboratory, where the influence of certain parameters or effects can be obtained nicely.

Finally, the determined parameters will be used for a computation of the lumbar spine consisting of four motion segments. Due to the enormous amount of finite elements needed to resolve the geometry, these computations are carried out in parallel on multiple CPU using the interface M++/PANDAS.

6.1 Modelling the Intervertebral Disc

This section offers a brief introduction into the arising problems, when the previously developed governing equations are applied to numerically simulate the behaviour of the IVD. Herein, the 3-d geometry needs to be acquired and spatially discretised using arbitrary amounts of finite elements. Moreover, as the IVD exhibits a very inhomogeneous material behaviour, the respective theoretical material parameters, which characterise the mechanical behaviour, need to be inhomogeneously distributed in the discretised domain. In particular, this addresses the varying fibre orientations and the material parameters affecting the anisotropic stress response in the AF, as well as the inhomogeneous distribution of the fixed negative charges throughout the IVD.

6.1.1 Geometry Model and Finite Element Mesh

For simple geometrical problems, the finite element mesh may be directly generated by defining the respective basic geometrical objects in a finite element mesher, like it can be achieved, for instance, in the program package CUBIT[1]. However, for complex geometries, such as the spine, a 3-d geometry model needs to be defined firstly which is imported into the finite element mesher for spatial discretisation thereafter.

In the context of computational biomechanics, the geometrical data of internal organs

[1]CUBIT: Geometry and Mesh Generation Toolkit, URL: `http://cubit.sandia.gov`

can usually not be obtained *ex vivo* using 3-d scanners, as a "quick removal" from the organism is (unless post mortem) either impossible or undesired. Instead, the geometric data is acquired using either Computed Tomography (CT scans) or Magnetic Resonance Imaging (MRI). Herein, a CT scan is based on 2-d X-ray images which are continuously taken around a single axis of rotation. Thus, CT scans are most suitable for the examination of hard (calcified) tissues which are composed of elements of a higher atomic number compared to the surrounding tissue, like it is the case for bones being surrounded by muscles for instance. MRI, on the other hand, uses a strong magnetic field in combination with non-ionising radio-frequency signals to acquire its images. In this regard, the magnetic field causes the hydrogen protons of the water molecules in the body to align in field direction. The radio-frequency fields are then used to systematically alter the alignment of this magnetisation, thereby causing the hydrogen protons to produce a rotating magnetic field, which is detectable by the scanner. Thus, MRI is best suited for soft biological (non-calcified) tissues containing large amounts of pore fluid.

However, both non-invasive methods produce sliced images of the body, where the different tissues are indicated by different grey scales. Figure 6.1 shows the author of this monograph in an MRI scanner as well as the typical output of such a scanner, i. e., grey-scaled images of a coronal and a sagittal slice of the lumbar spine region. With a

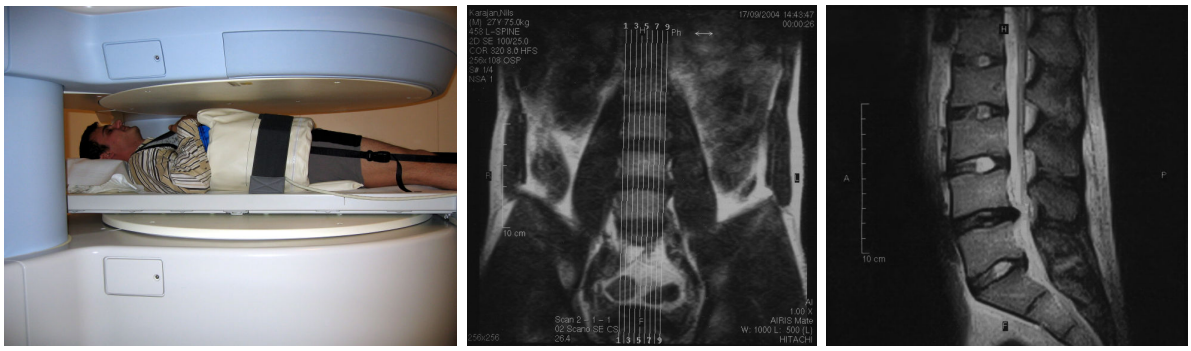

(a) (b) (c)

Figure 6.1: *(a) The author in the MRI scanner "AIRIS mate" of Dr. Ulrich Schott at the Radiology, Herrenberg Hospital, Germany. (b) Coronal and (c) sagittal scans of the lumbar spine. Note that the bright areas indicate a high pore fluid content, e. g., in the NP of an IVD.*

sufficient number of slices it is usually possible to directly render 3-d objects with similar grey values using a software package like Amira[2], for instance, where it is even possible to simultaneously generate a finite element mesh. However, as the available MRI scanner had only a magnetic field strength of 0.2 tesla[3] it was not possible to obtain high resolution scans needed by Amira, and thus, a different approach was chosen. Herein, any 3-d CAD program can be used which supports the established 3-d data formats, whereas the commercial software package Rhinoceros[4] was used in the present monograph. In

[2] Amira: Visualize · Analize · Present, URL: `http://www.amiravis.com`

[3] *Nikola Tesla* (1856–1943): Ethnic Serb of the Austrian Empire who became an American citizen later. His invention of alternating current electric power (AC) systems including the polyphase power distribution systems and the AC motor significantly ushered the second industrial revolution.

[4] Rhinoceros: NURBS Modeling Toolkit, URL: `http://www.rhino3d.com`

this context the lengthy structure of the spine allows to proceed from several axial slices. Herein, splines have to be defined manually within each slice such that they render the geometry of the vertebrae and the IVD with its NP and AF, respectively. Note that the complex spinous processes are neglected here, because the focus of this monograph lies on the description of the IVD. As a next step, the respective splines can be lofted in axial direction yielding the side surfaces of the vertebrae, NP and AF. The creation of the corresponding volumetric entities is then quickly achieved by combining the respective side surfaces with appropriate top and bottom surfaces, cf. Figure 6.2.

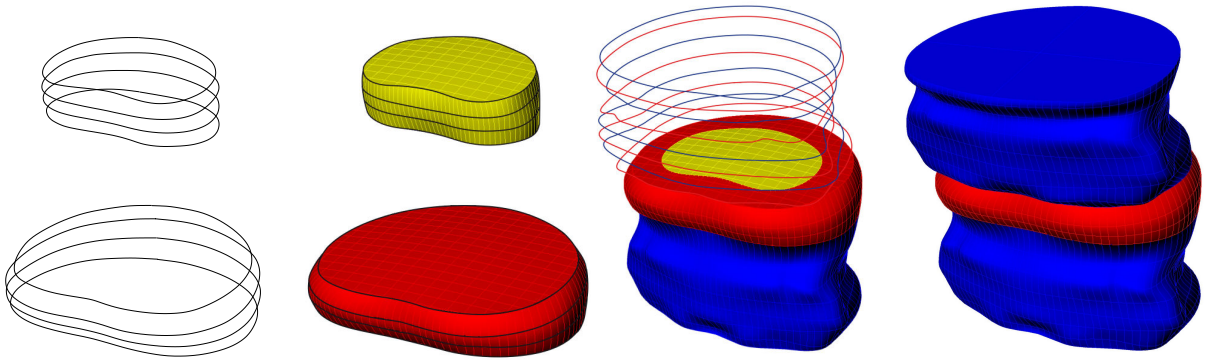

Figure 6.2: *Process of creating the 3-d geometry model of the spine. Firstly, the splines are defined on the axial slices obtained from MRI scans, thereby rendering the components of the spine. Then, the respective side surfaces are created by lofting the splines in axial direction which allows to define the volumetric entities of the vertebrae, NP and AF, thereafter.*

Next, the volumetric entities of the motion segment are exported in the STEP (Standard for the Exchange of Product model data) file format which can be imported in the CUBIT meshing program, where it is ready for spatial discretisation using *Taylor-Hood* elements.

6.1.2 Modelling Inhomogeneities

As is described in Section 2.3, the inhomogeneities of the IVD mainly occur in the AF. Following this, an algorithm needs to be defined which allows for a radial and tangential variation of the mechanical properties. In the context of the FEM, the inhomogeneous material behaviour is captured via location-dependent material parameters inside the IVD and thus, extra storage needs to be provided on quadrature (*Gauß*) point ($\mathcal{GP}$) level, just like it is the case for the internal (history) variables. Hence, additional storage is needed for scalar quantities which, in contrast to the history variables, stay constant over the computation. In particular, these are the initial molar concentration c_{0S}^{fc} of the fixed negative charges, the parameters characterising anisotropic stress response, $\tilde{\mu}_m^S$ and $\tilde{\gamma}_m^S$, as well as the fibre angle ϕ_0^S. Moreover, the varying fibre alignment is captured by the referential fibre vectors $\mathbf{a}_0^S$ and $\mathbf{b}_0^S$, which leads to six additional scalar values to be stored.

Due to the irregular geometries, it is rather difficult to define a closed-form (analytical) function for the initial distribution of the material parameters and fibre vectors. Hence, an algorithm is developed which merely depends on the tangential planes of the given

geometry. This feature allows to distribute the respective quantities in a straightforward manner, even in arbitrary patient-specific situations. Starting with the computation of the fibre vectors, the respective axial symmetry planes of the IVD need to be computed. These are defined by the position vectors $\mathbf{X}_k$ of the centres of gravity (COG) of the corresponding k^{th} IVD as well as the normal vectors $\mathbf{n}_{1(k)}$ of the symmetry planes $E_{1(k)}$, cf. Figure 6.3 (a). Next, every $\mathcal{GP}$ has to be projected onto the surrounding outer side surface, cf. Figure 6.3 (b) and the corresponding surface normal vector $\mathbf{n}_2$ needs to be computed at the projected *Gauß* point $\overline{\mathcal{GP}}_2$, thereby defining the plane E_2. Finally, the

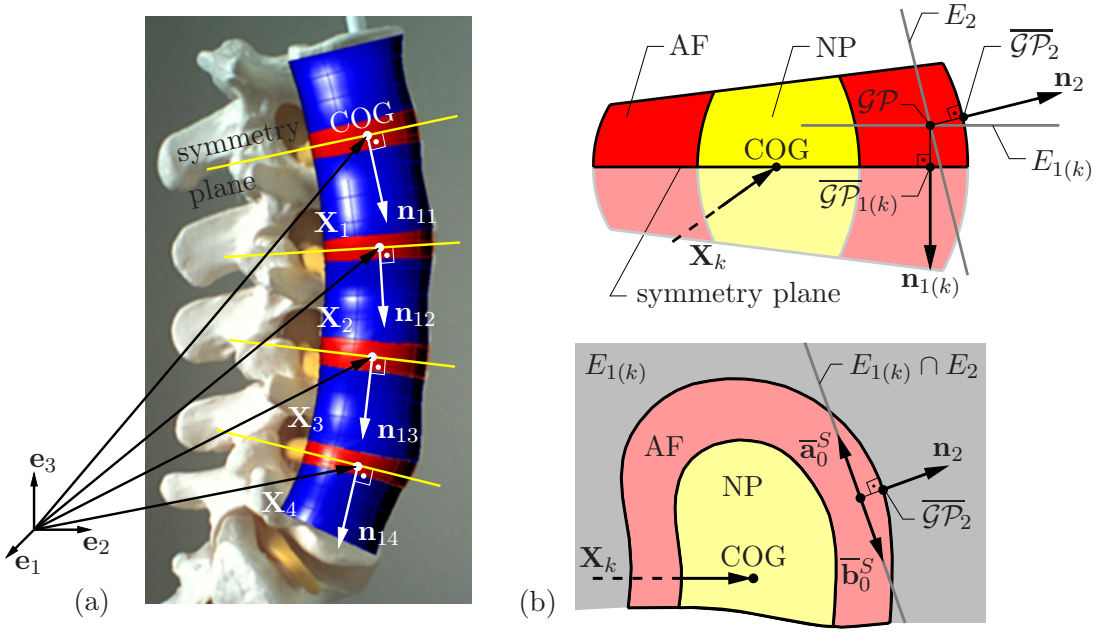

Figure 6.3: *(a) Definition of the symmetry planes in the lumbar spine and (b) illustration of the algorithm for the computation of the fibre vectors using tangential planes.*

projected fibre vectors $\overline{\mathbf{a}}_0^S = \mathbf{n}_2 \times \mathbf{n}_{1(k)} \in E_{1(k)} \cap E_2$ and $\overline{\mathbf{b}}_0^S = -\overline{\mathbf{a}}_0^S$ can be calculated, which yield the desired fibre vectors after a rotation in E_2, i. e.,

$$\mathbf{a}_0^S = \sin\phi_0^S\,\overline{\mathbf{a}}_0^S - \cos\phi_0^S\,\overline{\mathbf{n}}_{1(k)} \qquad \text{and} \qquad \mathbf{b}_0^S = \sin\phi_0^S\,\overline{\mathbf{b}}_0^S - \cos\phi_0^S\,\overline{\mathbf{n}}_{1(k)}\,. \tag{6.1}$$

Herein, $\overline{\mathbf{n}}_{1(k)} \in E_2$ is the projected normal vector $\mathbf{n}_{1(k)}$ as is depicted in Figure 6.4 (a) and ϕ_0^S is the fibre angle, which is defined independently as a material parameter. Note that this algorithm guarantees perfectly aligned fibre vectors [58], whereas the concept can also be adopted for the computation of the fibre directions in arteries.

Moreover, in order to allow for a tangential distribution of the material parameters, the polar angle δ is introduced in the axial symmetry plane in order to define the tangential position of a $\mathcal{GP}$, cf. Figure 6.4 (b). Concerning the radial distribution in the AF, the non-circular cross section of the IVD impedes the usage of the simple distance between the COG and the $\mathcal{GP}$. Hence, the distances d_1 and d_2 are introduced instead, which result from the projection of the $\mathcal{GP}$ onto the surrounding inner and outer side surfaces of the AF, respectively. It is now possible to define interpolating functions in tangential and radial direction of the AF. For the purpose of this monograph, the normalised polar

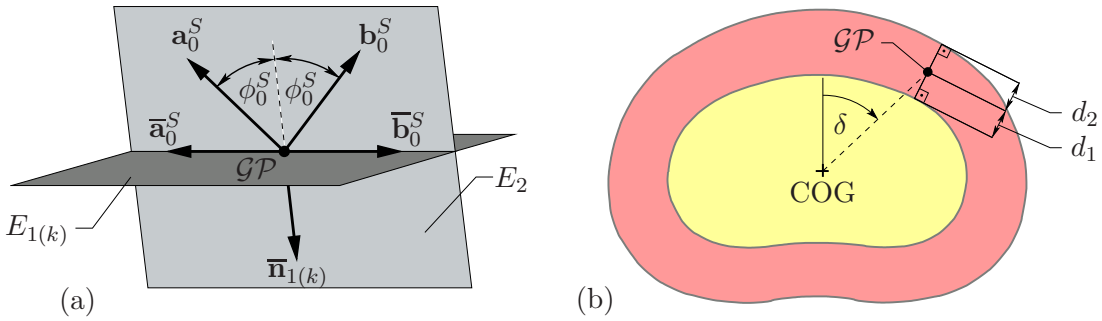

Figure 6.4: *(a) Inhomogeneously distributed fibre angles ϕ_0^S are used to compute the final fibre orientations and (b) interpolation of inhomogeneous quantities on Gauß point level.*

angle $\delta^* = \delta/180°$ as well as the normalised distance $d^* = d_1/(d_1 + d_2)$ are introduced, thereby allowing for a convenient linear interpolation in the tangential and radial direction, respectively, provided that extremal values are given at the respective start and end points.

6.2 Parameter Identification

In general, it is extremely difficult to realise suitable experiments on living soft biological tissues, which is mainly due to the following problems. Because it is virtually impossible to perform *in vivo* experiments, i. e., while still in the living organism, an *ex vivo* testing setup is preferable. In this regard it is extremely difficult to obtain "fresh" specimens within a reasonable time frame, which is usually only 24 hours post decease before degeneration effects start to evolve. Besides the difficulty of obtaining these fresh tissue samples, the experimental testing is also not a trivial task. Firstly, the tissue exhibits a strongly coupled behaviour in time and thus, it is almost impossible to distinguish between dissipative effects resulting from the viscoelastic solid skeleton or the viscous fluid flow. Moreover, concerning the swelling-active material behaviour, the surrounding fluid in the test chamber is also an important issue. In this regard, one can either perform tests using a physiological solution surrounding the tissue (in order to prevent swelling or shrinking processes) or a humidity chamber, which prevents the specimens from drying out. If these difficulties are overcome, one still has the problem that the acquired data is extremely "patient specific" and may vary if a person of different age is considered.

Due to the extreme lack of representative experimental data in this field, the present monograph is making use of real experiments only when they meet the above described restrictions. To the knowledge of the author, there are only two data sources available in literature which are directly suitable for the identification of the involved material parameters in the presented TPM model. These are the very detailed data on the behaviour of the collagen fibres in the AF acquired by Holzapfel *et al.* [96] and the torsional shear experiments on NP specimens performed by Iatridis *et al.* [101]. Moreover, an extensive study of the related literature has been carried out in order to obtain mean values for the remaining parameters.

6.2.1 Structural Collagen in the Anulus Fibrosus

As is already described in Section 2.3, the collagen fibres in the AF exhibit not only structural inhomogeneities but also a location-dependent mechanical behaviour. Both will be addressed in the following.

Structural observations:
According to Eberlein *et al.* [44] and Holzapfel *et al.* [96], the collagen fibre inclination in the AF varies linearly in circumferential direction, whereas it is fairly constant in radial direction. In this regard, the fibre angle ϕ_0^S was measured at six distinct points $(A-F)$ with different polar angles δ as is shown in Figure 6.5.

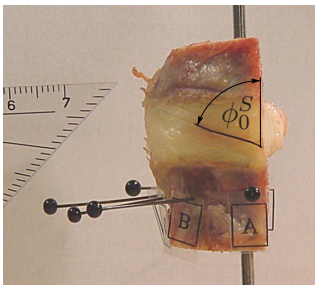

	A	B	C	D	E	F
δ	0.3°	34.0°	69.2°	104.8°	143.7°	179.2°
ϕ_0^S	64.6°	63.0°	59.7°	54.7°	47.6°	42.3°

Figure 6.5: *Measured fibre angles ϕ_0^S in the AF at six positions with different polar angles δ. Image and data address the lumbar spine and are taken from Holzapfel et al. [96].*

Numerically, this variation can be expressed by a linear regression of the fibre angle [44, 96]

$$\phi_0^S(\delta) = 66,8° - 0.13\,\delta\,, \tag{6.2}$$

where δ denotes the polar angle with respect to the COG of the IVD. Herein, $\delta = 0°$ and $\delta = 180°$ indicate the ventral and dorsal positions, respectively. The resulting distribution of the fibre vectors $\mathbf{a}_0^S$ and $\mathbf{b}_0^S$ is obtained, when the linear regression (6.2) is inserted into equations (6.1) yielding an alignment as is shown in Figure 6.6.

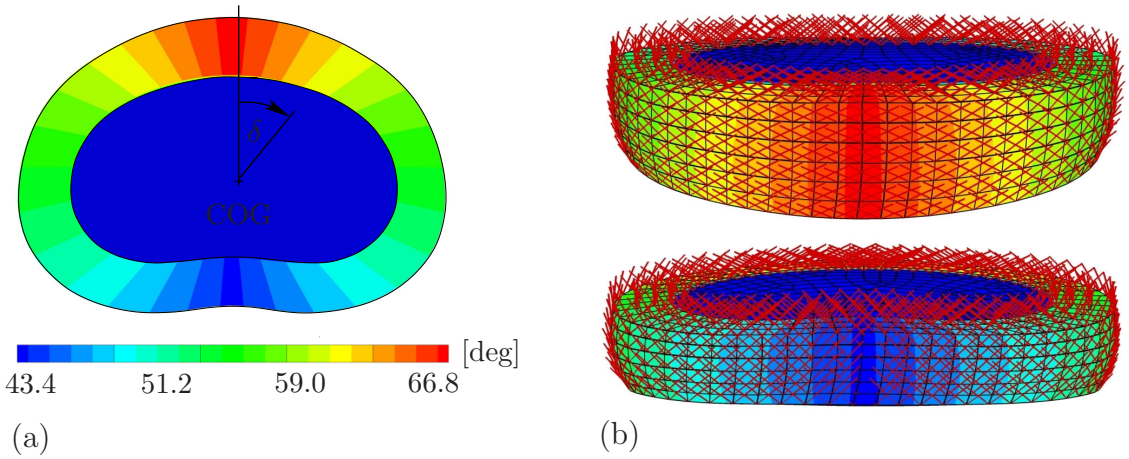

Figure 6.6: *(a) Distribution of the varying fibre angle ϕ_0^S and (b) resulting alignment of the fibre vectors $\mathbf{a}_0^S$ and $\mathbf{b}_0^S$ in the AF, which are displayed as red lines.*

Mechanical behaviour:
Furthermore, the variation of the mechanical behaviour of the type-I collagen fibres has to be considered locally at every $\mathcal{GP}$. Herein, Holzapfel *et al.* [96] measured the characteristic curves of the collagen fibres at four important key positions in the AF by pulling a single lamella in fibre direction. In this regard, the precise mechanical behaviour was recorded at the ventrolateral inner (VLI) and outer (VLO) parts of the AF as well as the dorsal inner (DI) and outer (DO) regions. As a first step, the nonlinear material law for the incorporation of the fibre-reinforcement of Subsection 4.4.4 is fitted to the experimental data of Holzapfel *et al.* [96] using the constraint optimisation by linear approximation (COBYLA) algorithm of Powell [164]. Herein, the material parameters were determined using the 1st *Piola-Kirchhoff* stress, as the nominal stress was recorded during the experiments. The results are displayed in Figure 6.7 showing the accuracy of the fitting process as well as the final material parameters $\tilde{\mu}_1^S$ and $\tilde{\gamma}_1^S$ for the respective regions in the AF.

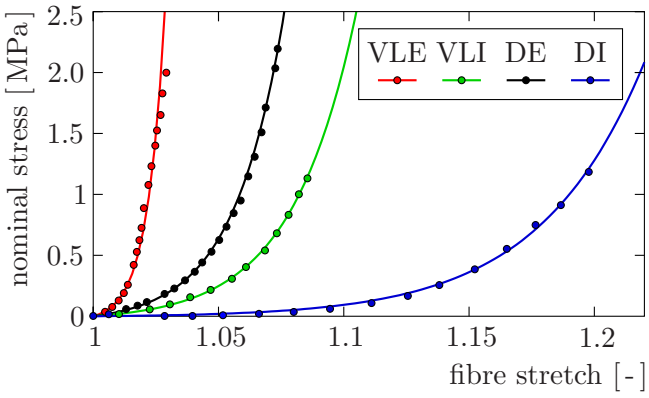

	$\tilde{\mu}_1^S$ [kPa]	$\tilde{\gamma}_1^S$ [-]
VLE	40.20	148.1
VLI	34.33	44.05
DE	50.79	54.24
DI	5.973	30.46

Figure 6.7: *Plot of the resulting 1st Piola-Kirchhoff stress in fibre direction at four distinct positions in the AF and overview of the acquired material parameters for the anisotropic stress computation. Herein, the coloured dots indicate the measured data of Holzapfel et al. [96].*

Proceeding from the parameter fit at these four discrete points, the corresponding spatial distribution of the material parameters $\tilde{\mu}_1^S$ and $\tilde{\gamma}_1^S$ in the AF is assumed according to Figure 6.8. Note that the chosen distribution can be motivated by changes in the morphological microstructure of the lamellae, cf. Tsuji *et al.* [209] and Subsection 2.3.2. In

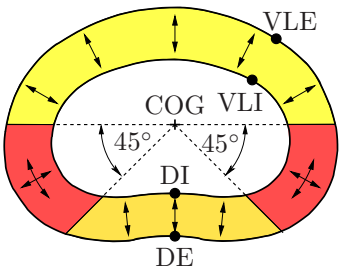

	lamellae	radially	tangentially
	continous	variable	constant
	transient	variable	variable
	discont.	variable	constant

Figure 6.8: *Assumed directions for the distribution of the fibre stiffness.*

particular, this addresses areas highlighted in red, where a change in continuity of the lamellae can be observed in tangential direction. Moreover, due to the varying type-I

collagen content in radial direction, a linear distribution assumed throughout the AF. The result of the distributed material parameters in radial and tangential direction of the AF is displayed in Figure 6.9.

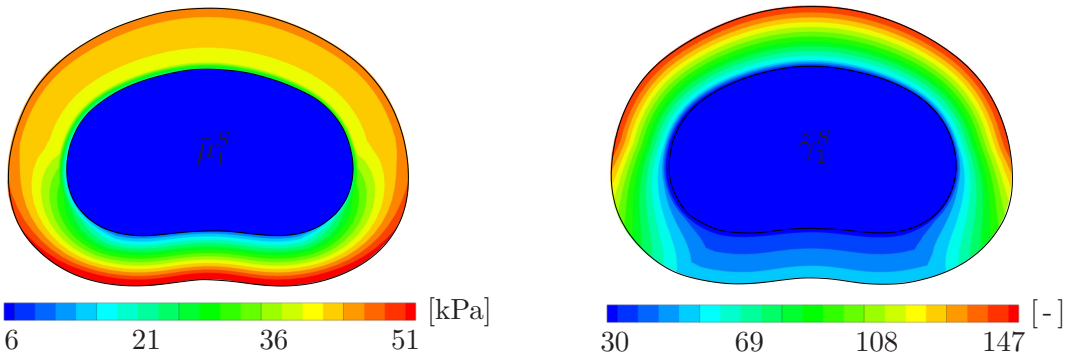

Figure 6.9: *Resulting distribution of the anisotropic material parameters* $\tilde{\mu}_1^S$ *and* $\tilde{\gamma}_1^S$.

6.2.2 Isotropic Viscoelasticity of the Nucleus Pulposus

Next, the parameters related to the intrinsic viscoelastic material behaviour of the solid skeleton in the NP are determined. This is accomplished with the aid of a torsion experiment of a non-degenerated cylindrical NP specimen, which was performed by Iatridis *et al.* [101]. Herein, the specimens were harvested from shock frozen IVD (region L2–L5) and directly placed in a humidity chamber of a testing apparatus. According to preliminary swelling tests performed by Iatridis *et al.* [101], a humidity chamber provided the most stable hydration environment yielding a relatively constant water content of the discs over the three hours of testing time, i. e., no swelling occurred due to the extraction of the specimen from its natural environment. The specimens were then imposed to an axial compression of 10 % of the original height of the disc, before an angular displacement φ was applied thereafter. Note that the axial pre-compression is needed to ensure a sufficient grip between the specimen and the two fully planar and impermeable testing plates. The relaxation of the recorded torque M_T of the top platen was then measured over time, whereas the respective average maximum shear stress τ was computed using *Saint-Venant*'s[5] theory for a circular cross section, i. e.,

$$\tau = \frac{2\,M_T}{\pi\,r^3}\,, \tag{6.3}$$

where r is the radius of the cylinder. For the numerical parameter fit of the presented model to the performed experiments, the disc was discretised using 441 20-noded mixed *Taylor-Hood* elements, as it is seen in Figure 6.10. The boundary conditions where applied such that the lower surface of the disc is totally fixed in space, whereas the upper surface is displacement-driven in axial direction for 2.0 s until a deformation of 0.144 mm

[5] *Adhémar Jean Claude Barré de Saint-Venant* (1797–1886): French mechanician and mathematician who contributed to the fields of stress analysis and hydraulic engineering. In 1843 he published the correct derivation of the *Navier-Stokes* equations for a viscous flow, which is two years before *Stokes* did.

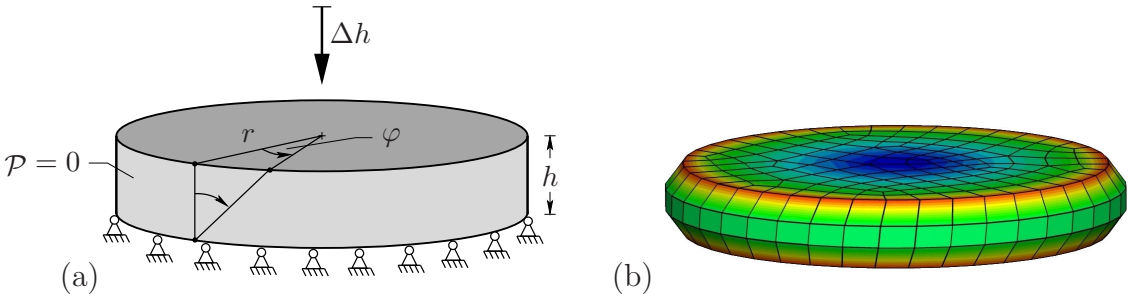

Figure 6.10: *(a) Average dimensions (radius $r = 4\,mm$, height $h = 1.44\,mm$) of the cylindrical NP specimen with boundary conditions (vertical displacement $\Delta h = 0.144\,mm$, rotation angle φ) and (b) spatial discretisation (441 elements) for the torsion experiment. The colouring indicates the qualitative distribution of the shear stress τ directly after the vertical displacement Δh and the rotation angle φ was applied.*

is reached, thereby preventing a horizontal movement. This vertical displacement is then held constant for the rest of the computation as well as the hydrostatic pressure $\mathcal{P} = 0\,\text{MPa}$ at the hoop surface and the concentration $\bar{c}_m = 0\,\text{mol/l}$ of the external solution. Six hundred seconds after the vertical displacement was applied, a rotation angle φ is induced on the top surface within 0.025 s and is again held constant for another 600 s. For a better comparability of the experiments of Iatridis *et al.* [101] and in order to overcome the problem of local solution deficiencies, the torque M_T is computed, i. e., the corresponding shear stresses are integrated over the top surface, and inserted into (6.3) thereafter.

In a first approach, the isotropic NP specimen is modelled using one of the simpler material laws included in (4.102) and (4.118), i. e., the neo-*Hooke*an model with parameters according to (4.103). In contrast, a total number of two *Maxwell* elements is needed, in order to reproduce the rapid relaxation of the shear stress depicted in Figure 6.11. Moreover, all body forces are neglected due to the small dimensions of the specimen.

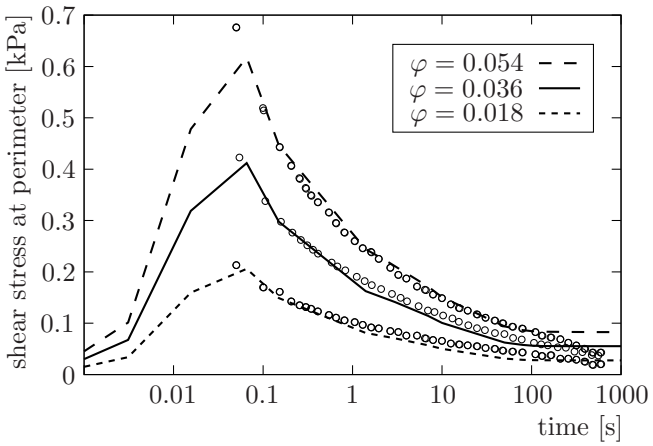

Figure 6.11: *Results of the parameter fit for the torsion experiment of Iatridis et al. [101]. The lines (dashed, solid, dotted) show the shear-stress relaxation of the numerical simulation, while the dots are the measured points at three different rotation angles, respectively.*

Herein, the lines indicate the computed curves using the presented model, whereas the circles display the measured values of Iatridis *et al.* [101]. The material parameters were

fit manually to the curve corresponding to an angular displacement of $\varphi = 0.036$. The other two curves, i. e., for an angular displacement of $\varphi = 0.018$ and $\varphi = 0.054$, were computed thereafter keeping the identified parameters constant.

In particular, the obtained material parameters for the NP, i. e. μ_0^S and Λ_0^S for the equilibrium contribution and μ_n^S, Λ_n^S, η_n^S, and ζ_n^S with $n = 1, 2$ for the non-equilibrium contribution, are listed in Table 6.1. However, as a natural consequence of the torsion experiment, only the shear deformation mode of the NP is addressed. Hence, no information is gathered concerning the (dissipative) volumetric behaviour (i. e. Λ_j^S and ζ_j^S for $j = 0, 1, 2$) of the isotropic solid skeleton. To overcome this problem, the assumption of a constant *Poisson*[6] ratio was made and the relation stemming from the linear theory $\Lambda_j^S = 2\,\mu_j^S\,\nu/(1-2\,\nu)$ with $\nu = 0.2$ [103] for $j = 0, 1, 2$ has been used; even though this is in a strict sense only valid around the natural state. Moreover, it was assumed that the volumetric viscosities have the same values as the solid shear viscosities, i. e., $\zeta_j^S = \eta_j^S$.

Finally note that the main deformation mode of the NP under bending is volumetric compression and thus, the information gathered by Iatridis *et al.* [101] is not sufficient to reliable determine this behaviour. Moreover, a volumetric compression is also coupled to the dissipative effects resulting from the viscous fluid flow inside the NP. Regarding the time scale on which the intrinsic dissipative effects of the solid skeleton occur, one can assume that the intrinsic viscoelasticity plays a negligible role in the context of long term analyses. This is because interstitial fluid flow takes place over a much greater period of time compared to the few seconds of stress-relaxation in the torsion experiment.

6.2.3 Inhomogeneous Distribution of the Fixed Negative Charges

Another inhomogeneity addresses the concentration of the fixed negative charges which was analysed in a detailed study by Urban & Maroudas [213]. For a young and healthy IVD they discovered a constant value inside the NP and a linear radial variation in the AF, which corresponds to the green curve in Figure 6.12 (a). While the tissue is ageing,

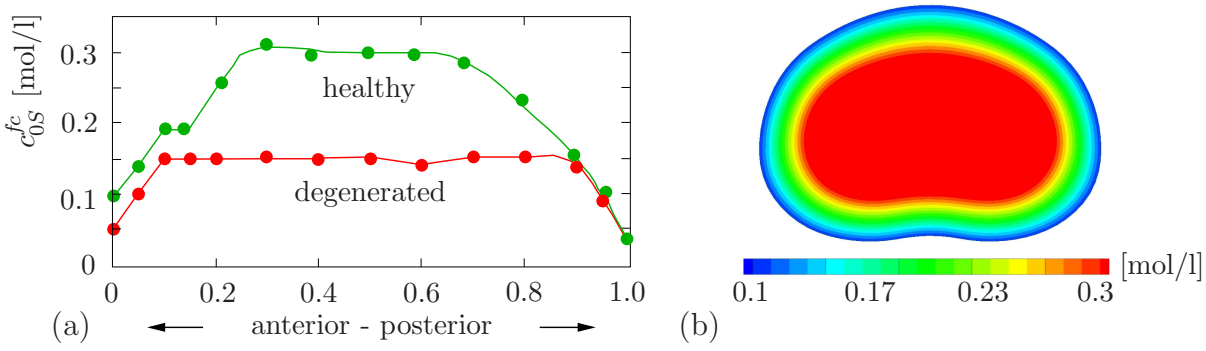

Figure 6.12: *(a) Measured distribution of the concentration of the fixed negative charges by Urban & Maroudas [213] and (b) computed initial distribution of c_{0S}^{fc} in the IVD.*

[6] *Siméon-Denis Poisson* (1781–1840): French physicist and mathematician who published well over three hundred works, whereas his memoirs on the theory of electricity and magnetism were certainly the most original and permanent ones in their influence and created a new branch of mathematical physics.

the IVD gradually looses its fixed negative charges, which leads to the degenerated curve displayed in red. Here, the healthy state is modelled leading to a distribution of the initial concentration c_{0S}^{fc} of the fixed negative charges as is shown in Figure 6.12 (b). In order to obtain this distribution, the algorithm according to Subsection 6.1.2 was applied.

6.2.4 Parameters Obtained from the Literature

The remaining parameters were determined by an extensive study of the related literature. In this context, it was not always possible to directly find exactly the same parameters for the respective nonlinear material laws of this monograph, because most of the times, other authors use linear material models. As a consequence, these parameters are adopted, thereby knowing well that they only apply to the small strain domain. As a consequence of the lack of reliable data, only the neo-*Hooke*an approach is used for the solid skeleton, while the more sophisticated *Mooney-Rivlin* or *Ogden* approaches are left as a possibility for further studies, when more detailed data is available.

Moreover, because this work is concerned with the behaviour of the IVD, the vertebrae are only modelled as a smeared porous continua, thereby neglecting the proper composition of a dense cortical shell and a porous spongy bone. Herein, the respective quantities found in literature were averaged according to the volume fractions of the cortical shell and the spongy bone in the overall vertebra.

The parameters γ_j^S for $j = 0, 1, 2$ were chosen to limit the disc bulge in the swelling experiment of the IVD, as seen in Figure 6.15 (c), whereas the remaining isotropic parameters for the AF as well as for the vertebrae were taken in accordance to averaged values given in Argoubi & Shirazi-Adl [7], Eberlein *et al.* [45], Iatridis *et al.* [101, 103], Lee *et al.* [118], Lim & Hong [123], Ochia & Ching [154], Shirazi-Adl *et al.* [185], Wu & Chen [236] and references therein. Note that according to Gu *et al.* [83], the young AF has an anisotropic permeability which becomes isotropic with age or degeneration. Due to the almost impermeable character of the AF and the fact that the directional variation of the permeability is "only" of factor two, while the values given in the related literature span over decades, the anisotropic permeability of the AF is neglected.

Vertebrae: Treated with no distinction between cortical shell and *spongiosa*.							
$K^S_{0S} = 2.7 \cdot 10^{-5}$	[mm^2]	$n^S_{0S} = 0.2$	[-]	$\mu^S_0 = 96.0$	[MPa]	$\kappa = 0.0$	[-]
$\mu^{FR} = 3.8 \cdot 10^{-8}$	[MPa·s]	$c^{fc}_{0S} = 0.0$	[mol/l]	$\Lambda^S_0 = 112.7$	[MPa]	$\gamma^S_0 = 1.0$	[-]
Nucleus pulposus: Treated as isotropic, viscoelastic and charged material.							
$K^S_{0S} = 3.5 \cdot 10^{-12}$	[mm^2]	$n^S_{0S} = 0.2$	[-]	$\mu^S_0 = 0.5$	[kPa]	$\kappa = 0.0$	[-]
$\mu^{FR} = 6.9 \cdot 10^{-10}$	[MPa·s]	$c^{fc}_{0S} = 0.3$	[mol/l]	$\Lambda^S_0 = 0.3$	[kPa]	$\gamma^S_0 = 50.0$	[-]
1st *Maxwell* element:		$\zeta^S_1 = 0.37$	[kPa·s]	$\mu^S_1 = 2.8$	[kPa]		[-]
		$\eta^S_1 = 0.37$	[kPa·s]	$\Lambda^S_1 = 1.9$	[kPa]	$\gamma^S_1 = 12.0$	[-]
2nd *Maxwell* element:		$\zeta^S_2 = 10.0$	[kPa·s]	$\mu^S_2 = 0.85$	[kPa]		[-]
		$\eta^S_2 = 10.0$	[kPa·s]	$\Lambda^S_2 = 0.57$	[kPa]	$\gamma^S_2 = 12.0$	[-]
Anulus fibrosus: Treated as inhomogeneous anisotropic charged material.							
$K^S_{0S} = 6.2 \cdot 10^{-12}$	[mm^2]	$n^S_{0S} = 0.35$	[-]	$\mu^S_0 = 0.95$	[MPa]	$\kappa = 0.0$	[-]
$\mu^{FR} = 6.9 \cdot 10^{-10}$	[MPa·s]	$c^{fc}_{0S} = 0.1$	[mol/l]	$\Lambda^S_0 = 2.2$	[MPa]	$\gamma^S_0 = 1.0$	[-]

	VLE	VLI	DE	DI
$\tilde{\mu}^S_1$ [kPa]	40.20	34.33	50.79	5.973
$\tilde{\gamma}^S_1$ [-]	148.1	44.05	54.24	30.46

Table 6.1: *Material parameters of the biphasic model for the vertebrae, nucleus pulposus and anulus fibrosus, respectively, whereas the isotropic contributions are always described using the neo-Hookean model.*

6.2.5 Swelling Behaviour of the Nucleus Pulposus

Comparison of the swelling mechanism with more sophisticated models:
In order to generally validate the capabilities of the presented model with respect to the swelling mechanisms in soft biological tissues, a 1-d swelling experiment is carried out, thereby comparing the presented biphasic approach with a triphasic approach of Acartürk [1], Ehlers & Acartürk [53] and Lai *et al.* [113]. Herein, only the results of the respective computations will be presented without going into the details of the more sophisticated triphasic model.

Following this, a porous tissue specimen is modelled with dimensions given in Figure 6.13 (a) using 40 20-noded mixed *Taylor-Hood* elements. In this context, the top surface is drained (i. e. $\mathcal{P} = 0$) and chemically loaded with $\bar{c}_m$, while all other surfaces have only prevented solid displacements normal to the boundaries, cf. Figure 6.13 (b). The chosen material parameters correspond to a tissue sample of the NP and are given in Table 6.1. However, the triphasic model of Acartürk [1] is not capable of representing a viscoelastic solid skeleton. Hence, the NEQ contribution is neglected and relaxed material parameters $\mu^S_0 = 0.5$ MPa, $\Lambda^S_0 = 0.01$ MPa, and $\gamma^S_0 = 1.0$ are chosen for the EQ part. Moreover, the

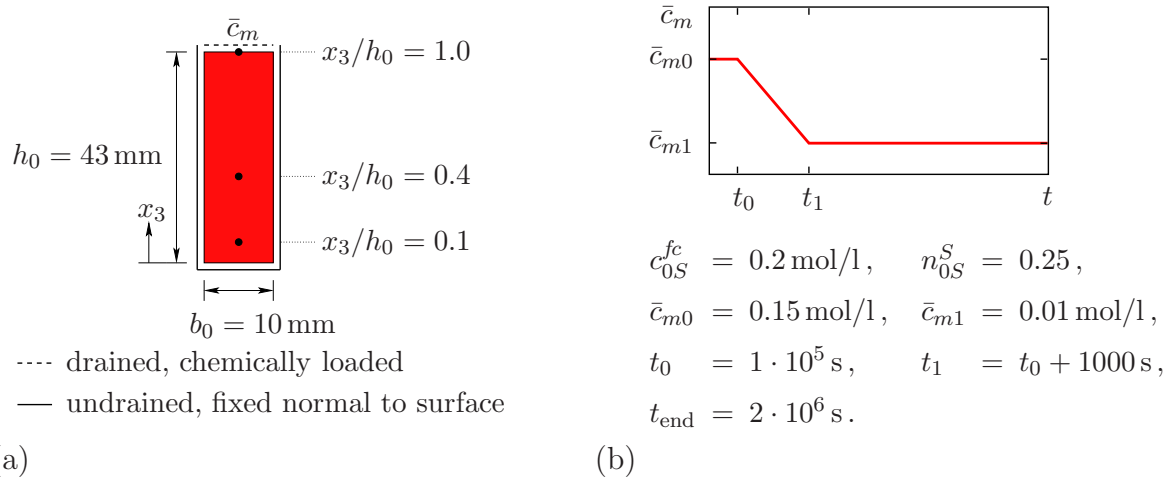

Figure 6.13: *Boundary conditions for the 1-d swelling experiment. (a) Geometry of the tissue sample as well as the positions where displacements and concentrations were recorded and (b) applied chemical loadings of the top surface.*

tissue was assumed to be at a temperature of 25° C yielding $R\Theta = 2477.6\,\mathrm{J/mol}$.

As expected, the initial and final values for the molar cation concentration as well as the vertical solid displacement match perfectly, while there is a discrepancy in between the starting and end points, cf. Figure 6.14. Especially the development of the molar cation concentration is captured rather poor, as it is not a degree of freedom in the extended binary approach. This is mainly due to *Lanir*'s assumption stating that the tissue is always instantaneous in chemical equilibrium and thus, an independent movement of the solutes is prohibited. Interestingly, the progressions of the vertical solid displacements match fairly well. Hence, if the focus lies only in the reproduction of the tissue's deformation behaviour, the extended biphasic approach is sufficient.

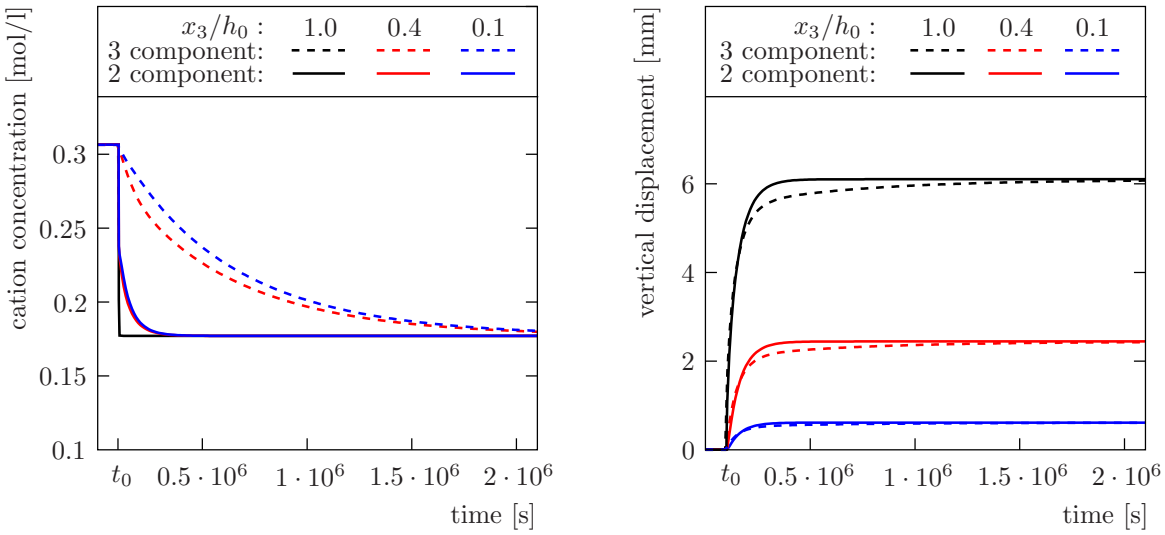

Figure 6.14: *Comparison of the development of the molar cation concentration (a) and the vertical solid displacement (b) at the control points over time. The dashed line corresponds to the triphasic model [53] and the solid line to the presented extended binary model.*

Moreover, another argument why the extended two-field formulation is followed can be motivated with a comparison of the numerical costs. Herein, the presented approach needs less DOF, and it takes less than a third of the computation time. A detailed overview on the numerical costs for the 1-d swelling experiment can be found in Table 6.2. Hence,

	3-field ($\mathbf{u}_S$ - p - c_m^+) formulation	2-field ($\mathbf{u}_S$ - $\mathcal{P}$) formulation
time steps	128	128
elements	40	40
DOF	1161	1062
comp. time	$\approx$ 27 min.	$\approx$ 8 min.

Table 6.2: *Comparison of the numerical costs for the 1-d swelling experiment.*

regarding the other numerical difficulties stemming from the viscoelastic solid skeleton, the occurring inhomogeneities and anisotropies as well as the combination of stiff vertebrae with the weak IVD in between, the simpler approach seems reasonable.

Swelling experiment of a sagittally cut NP:
The second example concerns the swelling capability of the presented model, when it is applied to the IVD. In this context, a swelling phenomenon is computed, which occurred while Holzapfel *et al.* [96] performed an experiment on a sagittally cut motion segment. Right after the specimen was cut in half and placed on the laboratory table, the NP started to swell out of the IVD and reached a maximum bulge of 4.9 mm, cf. Figure 6.5.

This behaviour is clearly a result of the tissue being removed from its physiological setting, i. e., the state where the net movement of fluid over the tissue boundary is balanced out between the osmotically driven influx of fluid and the mechanically driven efflux due to the pre-stressed solid skeleton. Whenever this equilibrium is disturbed, the tissue tends to gain chemical equilibrium again. For example, the excess of ions inside the tissue attracts the surrounding fluid with a lower ion concentration to get sucked inside, until equilibrium is reached with the resulting excess of tension in the solid skeleton. The cylindrical NP specimens could not swell as they were not surrounded by any fluid. Even though the sagittally cut motion segment is also not surrounded by a fluid, the IVD is still connected with the adjacent vertebrae, and hence, to the bone marrow. The results of the computation in Figure 6.15 (b) show clearly that the influx of fluid, which is responsible for the bulge, stems from the vertebrae.

The simulation is carried out on a sagittally cut geometry of an L4-L5 motion segment, which is discretised using 1898 20-noded *Taylor-Hood* elements yielding a total of 28 832 DOF, cf. Figure 6.15 (a), where the vertebrae, the NP, and the AF are highlighted in blue, red and yellow, respectively. The corresponding material parameters are listed in Table 6.1, whereas the inhomogeneities are modelled as is described in the preceding subsections. Following the swelling experiment, only essential boundary conditions are applied, which do not lead to a mechanical loading of the tissue. In this regard, the top and bottom surfaces of the vertebrae are fixed in space and a drainage ($\mathcal{P} = 0\,\mathrm{MPa}$) is ensured on all free surfaces. Furthermore, the concentration of the external solution is lowered from $\bar{c}_m = 0.15$ to $0.0\,\mathrm{mol/l}$ within $50\,\mathrm{s}$ and is then held constant at zero for another $5000\,\mathrm{s}$. Again, a tissue temperature of $25^\circ\,\mathrm{C}$ was assumed yielding $R\,\Theta = 2477.6\,\mathrm{J/mol}$.

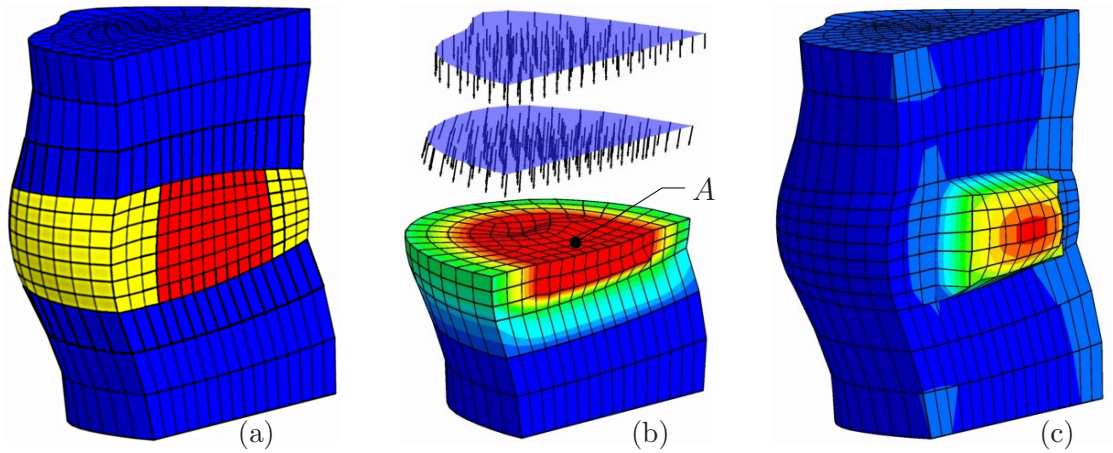

Figure 6.15: *(a) Discretisation of the L4-L5 motion segment using 1898 Taylor-Hood elements (28 832 DOF), where the vertebrae are displayed in blue, the NP in red and the AF in yellow. (b) Visualisation at $t = 50\,s$, where the arrows indicate the seepage velocity of the fluid inside the vertebra and the colours display the osmotic pressure contribution (red $\widehat{=}$ 0.78 MPa and blue $\widehat{=}$ 0.0 MPa). (c) The colouring indicates the bulge of the NP with a peak value of 5.7 mm.*

Figure 6.15 (b) shows the tendency of the fluid movement when $\bar{c}_m$ reaches zero, i. e., at $t = 50\,\mathrm{s}$. The seepage velocity of the bone marrow, which is indicated by the black arrows, is directed towards the IVD with its maximum osmotic pressure difference $\Delta\pi = 0.78\,\mathrm{MPa}$ highlighted in red. The reason for the fluid being attracted by an excess of pressure becomes clear when Figure 6.16 (a) is observed, which shows the evolution of p, $\Delta\pi$, and $\mathcal{P}$ measured at point A depicted in Figure 6.15 (b). In the beginning of the computation, i. e., at $t_0 = 0\,\mathrm{s}$, there is an initial osmotic pressure of $\Delta\pi_0 = 0.31\,\mathrm{MPa}$, which is solely carried via an "ingrown" pre-stress in the solid skeleton. Hence, the hydraulic pressure vanishes at $t_0 = 0\,\mathrm{s}$. As the concentration $\bar{c}_m$ of the surrounding fluid is lowered, the osmotic pressure difference $\Delta\pi$ rises gradually inside the NP and the fluid starts to flow into the IVD to equal out the excess of ions, thereby causing a volume dilatation.

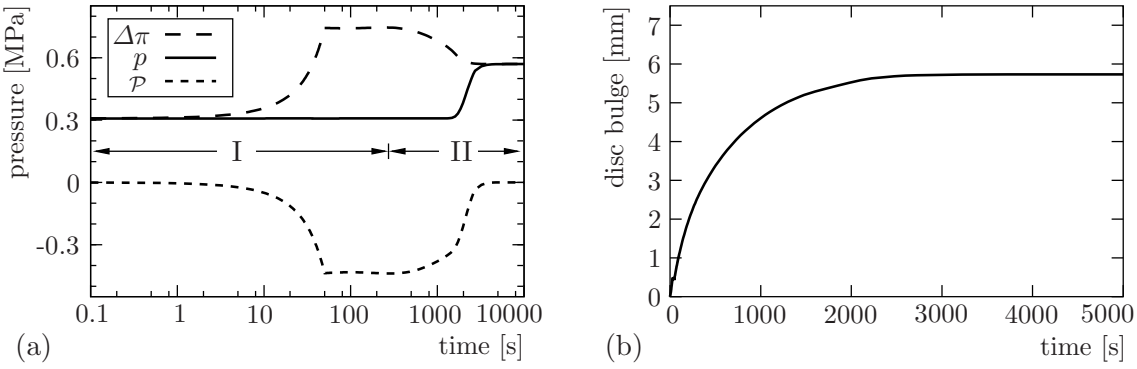

Figure 6.16: *(a) Evolution of the osmotic pressure difference $\Delta\pi$, the hydraulic pressure $\mathcal{P}$ and the overall pressure p measured at point A, cf. Figure 6.15 (b), inside the NP and (b) development of the NP bulge for the viscoelastic computation of the swelling experiment.*

Due to the almost impermeable characteristics of the IVD, the inflow is constrained, and hence, the volume dilatation inside the IVD happens really slow. Thus, the excess osmotic pressure difference is firstly carried via a suction power of the hydraulic pressure

$\mathcal{P}$ (part I in Figure 6.16 (a)) and is then gradually released into tension carried by the dilated solid skeleton (part II). The duration of this process is strongly dependent upon the filter velocity of the fluid that gets sucked inside, which is finally a function of the gradient of the negative hydraulic pressure and the resistance (permeability) of the tissue. In principle, this behaviour is reverse to the consolidation problem from geomechanics, where a load on the top surface is firstly carried by the pore fluid alone. Then, some of the incompressible pore fluid is gradually expelled due to the arising hydraulic pressure gradient, thereby causing a volumetric compression of the aggregate. Finally, when the consolidation process is finished, the load is carried by the volumetric solid extra stress alone. Note that if the medium was permeable without any resistance, the consolidation or the swelling process would be finished just after applying the load or concentration drop. The endpoint of the present swelling process is reached, when the negative hydraulic pressure inside the tissue is discharged. According to Figure 6.16, this is the case at about $t \approx 3000\,\mathrm{s}$. The resulting bulge of the NP can be seen in Figure 6.15 (c) with the maximum bulge of 5.7 mm, whereas the development of the bulge is depicted in Figure 6.16 (b).

6.3 Compression-Bending Experiment of an L4-L5 Motion Segment

As seen in the previous section, the identification of the involved material parameters is not straightforward, because many effects occur in a coupled fashion. As a consequence, these parameters may more conveniently be determined via inverse computations. Following this, the influence (sensitivity) of the involved parameters on dominant deformation modes of the IVD needs to be computed, in order to conclude a statement about their determinability. Here, a compression-bending experiment of an L4-L5 motion segment with dissected processes and ligaments will be used, where the material parameters of Table 6.1 are taken as a reference. Several computations will then be carried out, thereby varying only one parameter at a time.

In this context, the geometry of an L4-L5 motion segment is discretised using 7 504 20-noded *Taylor-Hood* elements yielding a total of 107 034 DOF. The discretised motion segment is then exposed to boundary conditions as is shown in Figure 6.17, i. e., the bottom surface is totally fixed in space, whereas the top surface is mechanically loaded with a linearly increasing load vector $\bar{\mathbf{t}}$ during the period of one second. This leads to a maximum axial load of 400 N (load equivalent to a person standing at ease) and a bending moment (flexion) of 22 Nm. Moreover, all free surfaces are perfectly drained ($\mathcal{P} = 0\,\mathrm{MPa}$) and the concentration $\bar{c}_m$ of the surrounding solution is kept constant at 0.15 mol/l to prevent the IVD from swelling. Here, a tissue temperature of 37° C was assumed yielding $R\Theta = 2577.5\,\mathrm{J/mol}$. Due to the large number of DOF, the simulations were carried out in parallel[7] using the interface M++/PANDAS. Herein, all computations were performed on

[7] Calculations were executed on the Beowulf Linux cluster of the Institute of Applied Mechanics (Chair of Continuum Mechanics) at the Universität Stuttgart. It consists of 98 Opteron CPU (2.2 GHz, 47 dual boards and one quad board), 104 GB RAM (at least 1 GB/CPU) and two Gigabit networks, which share the load stemming from the system administration and the data transfer of the parallel computations.

14 CPU simultaneously, which reduced the average computation time to approximately two hours. However, note that the computation time may vary tremendously, as extreme variations of a parameter sometimes lead to poorly conditioned linear systems of equations. Moreover, a constant time increment $\Delta t_n = 0.01\,\mathrm{s}$ is chosen for all computations yielding a total of 100 time steps for each run.

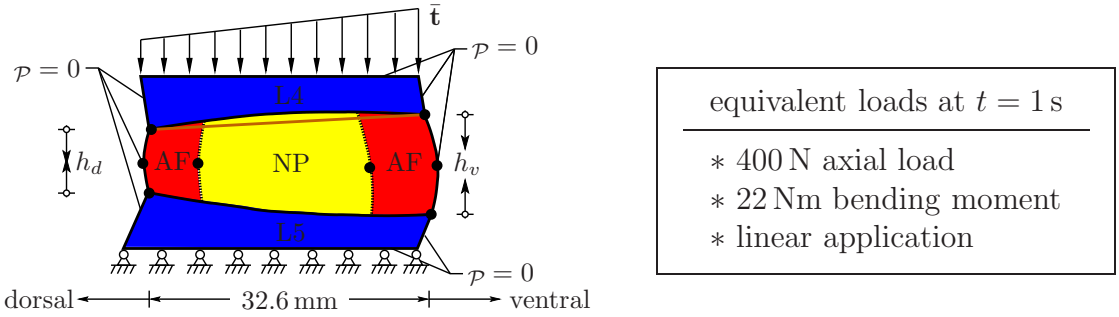

Figure 6.17: *Boundary conditions for the compression-bending experiment of the L4-L5 motion segment, whereas the black dots indicate the measuring points for the sensitivity analysis.*

Figure 6.18 shows the results of a computation at four different points in time (i. e. $t = 0\,\mathrm{s}$, $t = 0.33\,\mathrm{s}$, $t = 0.66\,\mathrm{s}$, and $t = 1.0\,\mathrm{s}$) using the reference set of material parameters given in Table 6.1. For convenience, the intrinsic viscoelasticity of the solid skeleton is neglected in this study. Instead, relaxed material parameters $\mu_0^S = 0.5\,\mathrm{MPa}$ and $\Lambda_0^S = 0.75\,\mathrm{MPa}$ are used as a reference for the EQ part of the solid skeleton of the NP, which lie in the range given in Argoubi & Shirazi-Adl [7] or Iatridis *et al.* [103].

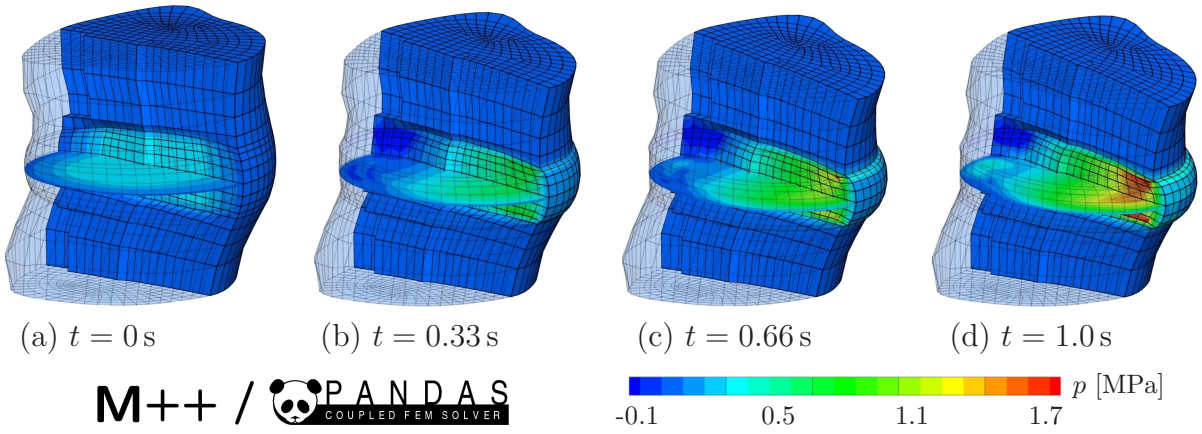

Figure 6.18: *Numerical results of the L4-L5 compression-bending experiments showing the deformation behaviour and total pressure at four points in time.*

Starting with Figure 6.18 (a), an initial osmotic pressure $\Delta\pi_{0S} = 0.3\,\mathrm{MPa}$ is shown in the NP which is fully compensated by the pre-stressed solid skeleton without any initial deformations, cf. Subsection 5.3.3. Subsequently, Figures 6.18 (b)–(d) show the gradually evolving total pore pressure p, which is mainly dominated by the hydraulic pressure contribution $\mathcal{P}$ as a result of the volumetric deformation of the solid skeleton. Since a bending moment is applied, the stiffer vertebrae undergo a tilting movement in the axial

plane, thereby squeezing the IVD in the ventral area, while expanding the AF in the dorsal region. Thus, the pore pressure p is highest, where the stiff vertebrae intrudes the anterior AF, whereas a suction power can be observed at the posterior AF.

6.3.1 Survey on the Influence of the Involved Parameters

As a next step, several numerical analyses are performed in order to obtain the influence of a certain parameter on the response of the IVD during the compression-bending experiment of the preceding subsection. Herein, only one parameter is varied per computation, while keeping the others constant. Subsequently, the response of the IVD is measured at ventral and dorsal positions which are indicated as black dots in Figure 6.17. Following this, three variations are carried out for each parameter in a range of $10-200\,\%$ (except for K_{0S}^{S}, which was varied by decades) with respect to the reference set given in Table 6.1. More precisely, this concerns parameters addressing the type-I collagen fibre stiffnes ($\tilde{\mu}_1^S$, $\tilde{\gamma}_1^S$), the mechanical behaviour of the isotropic solid skeleton (μ_0^S, Λ_0^S, γ_0^S), the initial intrinsic permeability (K_{0S}^S), the initial solidity (n_{0S}^S), and the initial molar concentration of the fixed negative charges (c_{0S}^{fc}). Note that the anisotropic parameters $\tilde{\mu}_1^S$ and $\tilde{\gamma}_1^S$ are varied together as well as the two *Lamé* constants which are altered, thereby enforcing a constant *Poisson* ratio using the well-known relations from linear elasticity

$$\nu_0^S = \frac{\Lambda_0^S}{2\,(\mu_0^S + \Lambda_0^S)} = \text{const.} \quad \longrightarrow \quad \Lambda_0^S = \frac{2\,\mu_0^S\,\nu_0^S}{1-2\,\nu_0^S} \quad \text{with} \quad \begin{cases} \text{NP: } \nu_0^S = 0.30 \\ \text{AF: } \nu_0^S = 0.35 \end{cases} . \tag{6.4}$$

During the simulations, data is recorded concerning the development of the disc height $h_{[d,v]}$ between the two vertebrae, the disc bulge $d_{[d,v]}$ at the perimeter, the total pressure $p_{[d,v]}$ at the NP-AF borderline, and the rotation $\Delta\phi$ about the brown line in Figure 6.17. The indices d and v denote a dorsal or ventral position, respectively.

Starting with the variation of the fibre stiffness in the AF, the resulting continuous curves of the measured responses are shown in Figure 6.19. Herein, the black curves correspond to the reference set of material parameters, whereas the coloured ones indicate higher or lower values for $\tilde{\mu}_1^S$ and $\tilde{\gamma}_1^S$, respectively. Moreover, a solid line represents the results of the dorsal region, while the dashed lines indicate results from ventral positions. Note in passing that a regular mesh refinement (i. e. one 20-noded element is divided into eight new brick elements) led to exactly the same results. Hence, the convergence of the model is proven and the presented coarser grid can be used without any approximation errors.

In view of the results given in Figure 6.19, it can easily be concluded that the type-I collagen fibres of the AF must be a very dominant structural element, as they significantly influence all measured responses. However, in order to quantitatively judge the influence of a parameter on a response, an indicator is introduced in the context of a sensitivity

$$S_{R,P} = \frac{R - R_{\text{REF}}}{R_{\text{REF}}}\,\frac{P_{\text{REF}}}{P - P_{\text{REF}}} = \frac{\text{percentage of the variation of the response}}{\text{percentage of the variation of the parameter}}\,[-]\,. \tag{6.5}$$

Herein, P and P_{REF} denote the values of the modified and reference material parameters, respectively, while R and R_{REF} relate to the corresponding measured results stemming

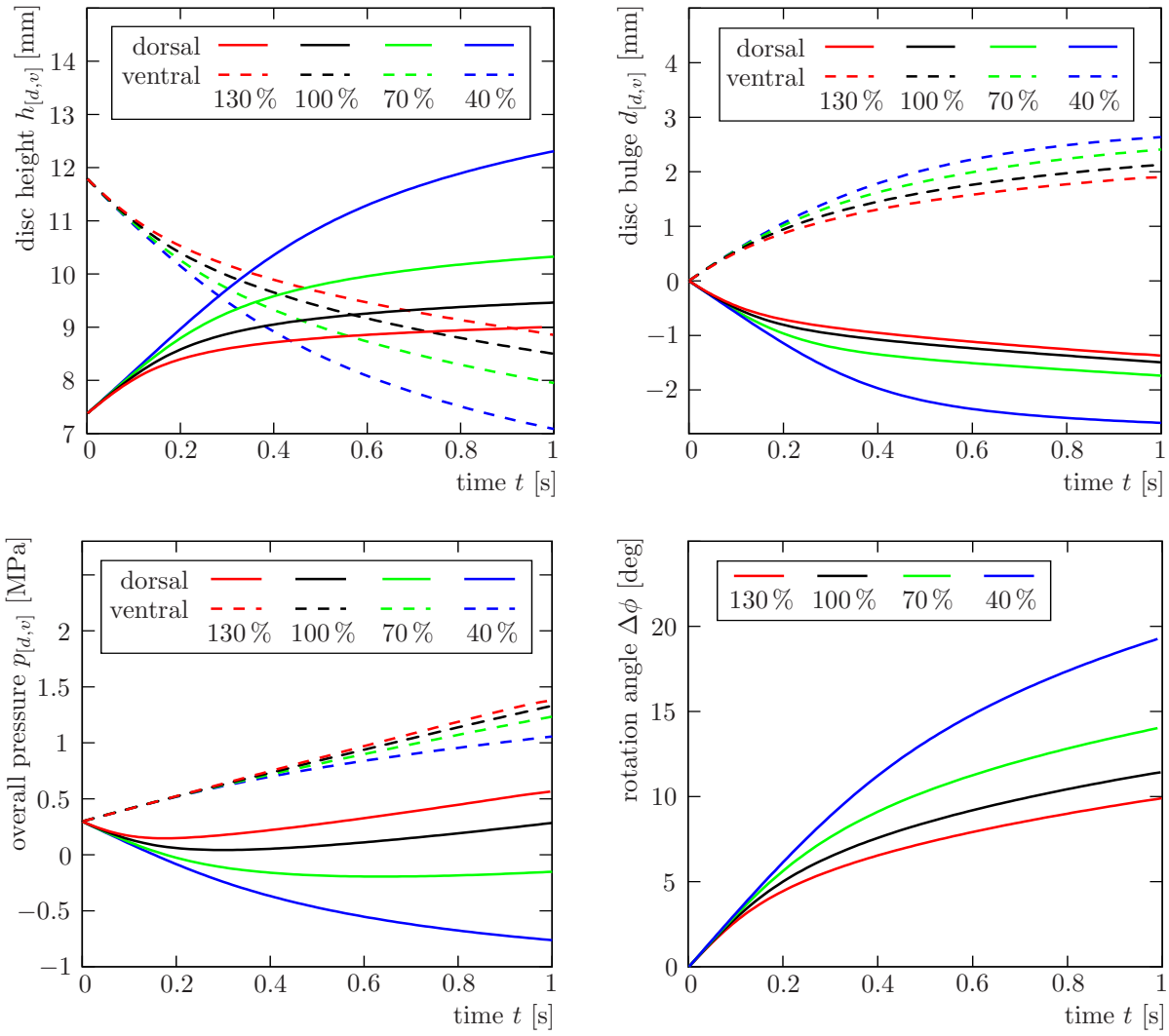

Figure 6.19: *Influences of the fibre stiffness ($\tilde{\mu}_1^S$ and $\tilde{\gamma}_1^S$) on the response of the IVD during the compression-bending experiment. The black curves correspond to the reference set of material parameters of Table 6.1, while the coloured curves indicate higher or lower values. Moreover, solid and dashed lines represent the results of the dorsal and ventral regions, respectively.*

from the respective numerical simulations. For example, a sensitivity of $S_{R,P} = 0.5$ implies that an increase of the material parameter by 1% causes an increase of the response by 0.5%. Here, the constitutively chosen critical value is $S_{R,P} = 0.1$. Note that the computation of sensitivities is usually carried out analytically but regarding the complexity of the model, they are more easily obtained via the presented numerical determination.

In particular, the sensitivity (6.5) is computed at $t = 1\,\mathrm{s}$ and the results for each of the variations of $\tilde{\mu}_1^S$ and $\tilde{\gamma}_1^S$ are presented in Table 6.3. Following this, the greatest influence of the fibres in this particular experiment can be observed in the overall dorsal pore pressure. All other sensitivities lie approximately in the same range. As a next step, the absolute arithmetic average is computed for each of the considered responses. Since a variation of the remaining material parameters does not yield such a dominant result, the respective

variation	h_d	h_v	d_d	d_v	p_d	p_v	$\Delta\phi$
130 %	−0.79	−0.43	−0.20	−0.30	3.69	0.20	−0.47
70 %	−1.38	−0.55	−0.56	−0.44	5.12	0.25	−0.76
40 %	−2.28	−0.72	−1.24	−0.40	6.19	0.34	−1.15
absolute mean	1.48	0.57	0.67	0.38	5.00	0.26	0.79

Table 6.3: *Computed sensitivities (6.5) of the parameter variations for $\tilde{\mu}_1^S$ and $\tilde{\gamma}_1^S$ (fibre stiffness in the AF) on the measured responses during the L4-L5 compression-bending experiment.*

continuous curves will not be presented. Instead the resulting absolute arithmetic means of the corresponding parameter variations are given in Table 6.4, where "sensitive" values are highlighted in red.

variation	location	h_d	h_v	d_d	d_v	p_d	p_v	$\Delta\phi$
$\tilde{\mu}_1^S$, $\tilde{\gamma}_1^S$	AF	1.48	0.57	0.67	0.38	5.00	0.26	0.79
μ_0^S	AF	0.04	0.29	0.05	0.19	1.84	0.21	0.12
μ_0^S	NP	0.01	0.08	0.03	0.02	0.88	0.32	0.04
c_{0S}^{fc}	NP + AF	0.00	0.01	0.00	0.00	1.65	0.36	0.01
K_{0S}^S	NP + AF	0.00	0.01	0.00	0.00	0.01	0.00	0.00
n_{0S}^S	NP + AF	0.00	0.02	0.00	0.00	0.00	0.00	0.01
γ_0^S	NP + AF	0.00	0.01	0.00	0.00	0.00	0.01	0.00

Table 6.4: *Computed absolute arithmetic mean values of the sensitivities (6.5) for all parameters on the measured responses. "Sensitive" values are highlighted in red.*

Proceeding from the results given in Table 6.4, a considerable influence can be noticed for the *Lamé* constants of the AF and a smaller influence for the isotropic stress contribution of the NP. In this context, it would be interesting to know if these sensitivities drastically change, when a more sophisticated material model is used for the corresponding stress computation. Following this, the general *Ogden* model offers too many possibilities concerning a systematic variation of all involved parameters and thus, it is not reasonable for such a rough study. In contrast, the *Mooney-Rivlin* approach requires only two additional parameters ($\mu^*_{0(1)}$ and $\mu^*_{0(2)}$) which are constrained according to (4.103), (4.108) and (4.109). Keeping this in mind, the same experiment is used to identify the influence of the additional parameters on the behaviour of the AF and NP. In particular, five computations are performed for the AF and NP, respectively, thereby using the previous reference set of *Lamé* constants, while varying the constrained parameters such that

$$\begin{aligned}
&\text{(a)}\ \mu^*_{0(1)} = 0.9\,, \quad \mu^*_{0(2)} = -0.1\,, && \text{(b)}\ \mu^*_{0(1)} = 0.8\,, \quad \mu^*_{0(2)} = -0.2\,,\\
&\text{(c)}\ \mu^*_{0(1)} = 0.7\,, \quad \mu^*_{0(2)} = -0.3\,, && \text{(d)}\ \mu^*_{0(1)} = 0.6\,, \quad \mu^*_{0(2)} = -0.4\,,\\
&\text{(e)}\ \mu^*_{0(1)} = 0.5\,, \quad \mu^*_{0(2)} = -0.5\,.
\end{aligned} \tag{6.6}$$

This procedure will give an indication of how the *Mooney-Rivlin* model influences the behaviour of the IVD in a compression-bending mode. The corresponding results are

given in Table 6.5 in the form of absolute percentage deviations of the response at $t = 1\,\mathrm{s}$ with respect to the computations using the neo-*Hooke*an model in combination with the corresponding set of reference parameters. Herein, note how the influence of the

combination	location	h_d	h_v	d_d	d_v	p_d	p_v	$\Delta\phi$
(a)	NP	0.00	0.00	0.00	0.00	−0.04	−0.01	0.00
(a)	AF	0.00	0.00	0.01	0.00	−0.04	−0.01	0.00
(b)	NP	0.00	0.00	0.00	0.00	−0.07	−0.02	0.00
(b)	AF	0.00	0.00	0.01	0.00	−0.07	−0.03	−0.01
(c)	NP	0.00	0.00	0.00	0.00	−0.11	−0.03	0.00
(c)	AF	0.00	0.01	0.00	−0.01	−0.11	−0.04	−0.01
(d)	NP	0.00	0.00	0.00	0.00	−0.14	−0.04	0.00
(d)	AF	0.00	0.01	0.01	−0.01	−0.14	−0.05	−0.01
(e)	NP	0.00	0.00	0.00	0.00	−0.14	−0.04	0.00
(e)	AF	0.00	0.01	0.01	−0.01	−0.18	−0.06	−0.01

Table 6.5: *Influence of the additional Mooney-Rivlin parameters on the L4-L5 compression-bending experiment. The values denote absolute percentage deviations from the reference computation using the neo-Hookean model and the corresponding set of reference parameters.*

Mooney-Rivlin approach only affects the overall dorsal pore pressure, whereas its influence increases from (a) to (e) for the chosen combinations in (6.6). As a next step, the same variations for the *Lamé* constants μ_0^S and Λ_0^S of the AF and NP, respectively, are carried out again for each of the five different combinations (a) through (e) in (6.6). Again, the resulting sensitivities are computed at $t = 1\,\mathrm{s}$ in accordance to (6.5) and are summarised as absolute arithmetic mean values in Table 6.6. As expected, the sensitivities of the *Mooney-Rivlin* part of the isotropic solid extra stress are comparable to the influence using the simpler neo-*Hooke*an approach.

combination	location	h_d	h_v	d_d	d_v	p_d	p_v	$\Delta\phi$
(a)	AF	0.07	0.45	0.09	0.31	3.23	0.24	0.23
(b)	AF	0.07	0.40	0.09	0.32	2.93	0.39	0.27
(c)	AF	0.07	0.48	0.08	0.31	3.31	0.41	0.23
(d)	AF	0.06	0.47	0.09	0.30	3.54	0.36	0.23
(e)	AF	0.06	0.48	0.09	0.33	3.38	0.40	0.23
(a)	NP	0.01	0.07	0.03	0.02	0.92	0.32	0.04
(b)	NP	0.01	0.07	0.03	0.02	0.97	0.32	0.04
(c)	NP	0.01	0.07	0.03	0.02	1.05	0.32	0.05
(d)	NP	0.01	0.07	0.03	0.02	1.11	0.32	0.05
(e)	NP	0.01	0.08	0.03	0.02	1.13	0.32	0.05

Table 6.6: *Influence of the Lamé constants of the NP and AF on the L4-L5 compression-bending experiment using the Mooney-Rivlin model. The values denote the mean average sensitivities according to (6.5) and "sensitive" values are highlighted in red.*

6.3.2 Interpretation of the Results

After having performed several computations with varying material parameters, it is now possible to conclude and interpret the results of the last subsection. Proceeding from the idea of using the L4-L5 compression bending experiment to either determine or validate the involved material parameters, it is obvious that this cannot be achieved for parameters which do not have an influence on the measurable response. Moreover, a strong and coupled influence of all responses is also undesirable for such an approach. In this case, the material parameter plays a major role and many measurements of the response have to be recorded and controlled simultaneously. Hence, these parameters should, if possible, rather be determined directly using independent experiments instead. In contrast, a material parameter with a medium influence can conveniently be determined using inverse computations by measuring the response at the most important points in the IVD.

From Table 6.4, it is straightforward to conclude that a striking dominance can be adjudicated to the AF, where particularly the type-I collagen fibres have by far the greatest influence. In conclusion, it is preferable to determine the corresponding material parameters $\tilde{\mu}_1^S$ and $\tilde{\gamma}_1^S$ via independent fibre elongation tests, as they were performed by Holzapfel *et al.* [96], for instance. Moreover, the dominant behaviour also reveals the need to incorporate the inhomogeneous distribution and alignment of the structural collagen fibres as well as their location-dependent mechanical properties. However, in order to describe the distribution of the involved material parameters more accurately, it would be of great benefit to perform lamellae tension tests at even more distinct points in the AF.

Moreover, also the *Lamé* constants μ_0^S and Λ_0^S of the AF, which characterise the isotropic elasticity, seem to play an important role. However, since they are not as dominant as the collagen fibres, they may be determined via inverse computations using the compression bending experiment. This is actually of great benefit, because it is not possible to obtain an AF specimen that is decoupled from the influence of its type-I collagen fibres. In particular, the difficulty arises from the ingrown (embedded) characteristic of the structural collagen in the PG network. Hence, it is not possible to determine the isotropic characteristic of the AF via an independent experiment. Similar to the *Lamé* constants of the NP which can also be obtained by inverse computations of compression bending experiment, but in contrast to the AF, it is also possible to obtain a NP specimen for separate and independent testing. However, due to the almost impermeable nature of NP tissue, it is rather difficult to measure the influence of the solid skeleton alone, as deformations are coupled to viscous interstitial fluid flow.

A possibility to overcome this problem is to apply the so-called porous indenter test, where the indenter is locally driven into the tissue sample. But again, due to the impermeable characteristic of the NP, such an experiment takes place over hours until the specimen is fully drained and decoupled from fluid flow. Another possibility is the torsional shear test which is free of any volumetric deformations within the small strain domain and thus, in theory independent of interstitial fluid flow. Such an experiment was carried out by Iatridis *et al.* [101] and is used for the identification of the viscous parameters in Subsection 6.2.2. However, the drawback of this experiment is that the NP specimen has to be pre-compressed in order to obtain a sufficient grip between the testing device and

the specimen, which again leads to undesired volumetric deformations. Thus, the method of inverse computations is convenient, even if only used to verify parameters obtained from other experiments.

Regarding the measured response of the IVD, the *Lamé* constants of the NP seem to play a minor role in comparison to the influence of the structural collagen as well as the isotropic part of the solid skeleton in the AF. Moreover, the second study of the effect of the isotropic mechanical behaviour of the NP and AF on the deformation behaviour of the IVD reveals that the influence of the five different possibilities for the *Mooney-Rivlin* approach are not relevant in comparison to the neo-*Hooke*an approach. In particular, there is a slight noticeable increase in the influence of the dorsal pore pressure, as the parameters $\mu^*_{0(1)}$ and $\mu^*_{0(2)}$ are varied from case (a) to (e) in (6.6). However, a variation of the respective *Lamé* constants for the combinations (a) through (e) does not append new sensitive responses to the ones already given in Table 6.4. It is therefore not suggested to model the EQ part of the AF and NP using a more sophisticated approach than the elastic neo-*Hooke*an model. Following this, it is also not recommended to account for the numerically expensive viscoelastic model of the NP during the simulation of the compression-bending experiment, because the gain in information is in no relation to the quickly rising numerical effort. However, the intrinsic viscoelasticity may play a role, when focusing on the damping characteristic of the IVD or other short-term load cases.

Naturally, the initial molar concentration c^{fc}_{0S} of the fixed negative charges has only an influence on the internal pore pressure. This is somewhat obvious, as the initial osmotic pressure $\Delta\pi_{0S}$ is always subtracted from the solid extra stress in order to obtain a stress-free reference configuration without any initial volumetric deformations. Hence, this parameter will only have an influence, if the molar concentration $\bar{c}_m$ of the solutes in the surrounding solution changes. As a consequence, this parameter cannot be determined using the compression-bending experiment but must be identified separately as is done in Urban & Maroudas [213].

For various reasons, the remaining parameters of the study have no influence at all. In particular, the permeability K^S_{0S} of the solid skeleton has no effect on the deformation behaviour of the IVD, because the time frame, during which the compression-bending experiment takes place, is too short to uncover consolidation effects. Hence, as long as the permeability is not greater than a certain upper bound, the loading time of one second is too short for a reduction of the pore pressure inside the IVD. Note that this effect also explains why the isotropic elasticity of the NP is playing a minor role in the deformation behaviour of the short-term compression-bending experiment. Because the tissue has not enough time for consolidation, there is not much volumetric compression noticeable which in turn leads to a negligible contribution of the (compressive) solid extra stress. As a consequence, the solidity n^S_{0S} has also no influence, because the compaction point is rarely reached due to the almost impermeable characteristic of the IVD. Hence, the overall aggregate of the IVD behaves almost incompressible during short term loadings. The same holds for the parameter γ^S_0 which activates the volumetric extension term in (4.102) by governing its non-linearity. Thus, this parameter will only influence great swelling mechanisms which are accompanied by large volumetric dilatations, cf. Figure 4.3, as well as long-term deformations of the IVD, where the compaction point is reached. Following

this, all three parameters need to be determined independently or can be taken from the related literature. However, in the proceeding subsection, long-term loading conditions are observed with respect to the influence of the permeability K_{0S}^{S} of the solid skeleton.

6.4 Long-Term Compression of a Motion Segment

After the performance investigation of the proposed model during short-term loading conditions like the compression-bending experiment, this section addresses the effects resulting from an axial compression of the IVD over a much longer period of time. Following this, the present study is motivated by the diurnal variation of the body height which results from a long loading period during the daytime and an "unloaded" resting period thereafter. In particular, the loads during every day activities cause the pore fluid to be expelled from the IVD which in turn leads to a higher concentration of the fixed negative charges inside the disc as well as an increase of the solid extra stress. As a consequence, the excess of c_m^{fc} triggers the osmotic effect which causes a diffusion process of the surrounding fluid into the IVD. Whenever the disc is unloaded during rest at night, the solid extra stress is released and the original disc height will be obtained in the next morning. In this regard, the development of the disc height over time is strongly influenced by the permeability of the tissue. Hence, this study is concerned with different values for K_{0S}^{S} as well as for κ, which triggers the deformation dependency of the intrinsic permeability.

Proceeding from these rough ideas, the diurnal variation of the body height was numerically approximated by Broberg [32] according to Figure 6.20, whereas the measured points trace back to the work of Tyrrell *et al.* [210]. Herein, the subject stood up at $t = 0\,\mathrm{h}$ which immediately diminished the body height due to a spontaneous elastic compression of the discs. Thereafter, the suspect followed normal day activity for 16.5 h which is directly followed by a sleeping period of 7.5 h. The simulations of Broberg [32] were performed on a single L3-L4 motion segment. In this regard, the concluding result for the height-change of the overall spine was achieved by assuming that the axial deformation of this particular IVD is approximately one-fifteenth of the total variation in body height.

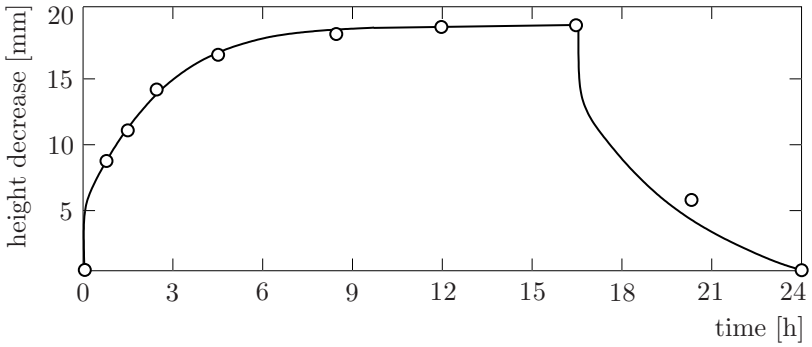

Figure 6.20: *Diurnal variation of the body height during normal day activity* ($t < 16.5\,\mathrm{h}$) *and rest at night* ($t > 16.5\,\mathrm{h}$). *The solid line corresponds to the numerical simulation of Broberg [32], while the points indicate measured data originally acquired by Tyrrell et al. [210].*

For convenience, the discretised geometry of the L4-L5 motion segment of the preceding

section is used again for the numerical simulations in the present long-term compression study. The same holds for the material parameters given in Table 6.1. Moreover, as the influence of the intrinsic viscoelasticity of the NP is only noticeable during short-term loadings, it is neglected and relaxed material parameters ($\mu_0^S = 0.5\,\mathrm{MPa}$ and $\Lambda_0^S = 0.75\,\mathrm{MPa}$) are chosen according to the previous study.

In particular, the normal day activity of the motion segment is simulated by a linear application of an equivalent axial load of 400 N on the top surface within one second, which is held constant for 16.5 h thereafter. The removal of the top load is also carried out in one second, whereas the IVD is left unloaded for the remaining period of 7.5 h. At all times during the computations, the side-surfaces are perfectly drained ($\mathcal{P} = 0\,\mathrm{MPa}$), the molar concentration $\bar{c}_m$ of the surrounding solution is held constant at 0.15 mol/l, and the bottom surface is totally fixed in space. Following this, several computations are carried out, thereby varying the intrinsic permeability as well as the parameter κ for the deformation-dependent permeability in (4.127). In particular, the following permeabilities

	AF	NP
(a)	$K_{0S}^S = 6.2 \cdot 10^{-12}\,\mathrm{mm}^2$	$K_{0S}^S = 3.5 \cdot 10^{-12}\,\mathrm{mm}^2$
(b)	$K_{0S}^S = 6.2 \cdot 10^{-13}\,\mathrm{mm}^2$	$K_{0S}^S = 3.5 \cdot 10^{-13}\,\mathrm{mm}^2$
(c)	$K_{0S}^S = 6.2 \cdot 10^{-14}\,\mathrm{mm}^2$	$K_{0S}^S = 3.5 \cdot 10^{-14}\,\mathrm{mm}^2$

(6.7)

are investigated in combination with different values for the parameter κ (AF & NP)

$$\text{(i)} \quad \kappa = 0.0\,, \qquad \text{(ii)} \quad \kappa = 10.0\,, \qquad \text{(iii)} \quad \kappa = 20.0\,. \tag{6.8}$$

In order to cancel out possible bending effects due to the irregular geometry of the motion segment, the variation of the disc height is always measured at the dorsal and ventral points as indicated in Figure 6.17, whereas the arithmetic mean of the two values is computed thereafter. The recorded development of the (mean) height decrease of the IVD over time is given in Figure 6.21. Even though none of the presented curves match

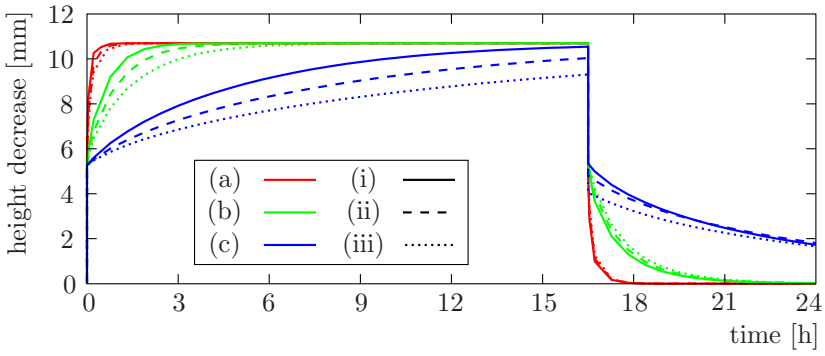

Figure 6.21: *Simulation results of the long-term compression experiment using different parameter combinations as indicated in (6.7) and (6.7). The curves show the height change of the overall spine, i. e., data obtained from the L4-L5 motion segment is multiplied by fifteen.*

perfectly with the measured curve given in Figure 6.20, the qualitative effect is represented fairly well. Herein, a substantial influence of the intrinsic permeability can be observed

with respect to the long-term deformation development of the IVD. Moreover, while the parameter κ does not have much influence in the "permeable" case indicated by the red line, it becomes more dominant in less permeable cases, which are drawn in green and blue, respectively. Note that in contrast to the short-term compression-bending experiment, there is a remarkable influence of the mechanical behaviour of the isotropic solid skeleton on the maximum height change in the present example. This characteristic is easily explained with the fully consolidated deformation state, which is obtained after one hour to 16.5 hours or more depending on the permeability. At this state, enough incompressible pore fluid is expelled such that the applied load is entirely carried by the solid extra stress. Thus, the smaller maximum deformation compared with the computations performed by Broberg [32] is due to the chosen numerical values for the *Lamé* constants of the isotropic part of the tissue, which seem to be too large.

For the intention of this monograph, however, it is sufficiently proved that the presented model is capable of reproducing the effect of the diurnal variation of the body height. Note that a more accurate description using the present approximation with absence of processes as well as ligaments and spine muscles is not possible in the first place, as it is not clear how big the actual loads on the IVD are. Moreover, the applied load of 400 N is probably an underestimation of the actual loads applied during normal day activities, which may also include dynamic load cases. Thus, in order to exploit this kind of experiment for parameter identification, the complete spine should be modelled and representative loads need to be determined.

6.5 Bending of the Lumbar Spine (L1-L5)

Finally, the applicability of the proposed model is demonstrated by numerical simulations of large-scale problems which address the deformation behaviour of the lumbar spine with removed processes. This leads to the challenge that even on up-to-date PC systems, the numerical solution of an initial BVP involving several motion segments cannot be computed efficiently on a single-CPU machine anymore. In this regard, computation time and memory utilisation, needed to solve the resulting large linearised systems of equations, increase quickly to multiple days and several GB of Random Access Memory (RAM), respectively. Hence, a parallel solution strategy will be applied using the interface M++/PANDAS as is described in Section 5.4. Following this, two computations are carried out. One consisting of intact discs throughout the lumbar spine and one having a stiffened L4-L5 motion segment, where the parameters for the lowest IVD are set such that they reproduce the mechanical behaviour of the surrounding stiff vertebrae.

In particular, the simulation of the healthy section of the lumbar spine is presented in the following subsection, thereby investigating the efficiency of the numerical implementation of the parallel solution strategy. Thereafter, the deformation behaviour of the degenerated lumbar spine is computed in order to analyse the influence of a stiffened L4-L5 motion segment in comparison to the results obtained for the healthy state.

6.5.1 Deformation Behaviour of the Healthy State

In the present study, the lumbar spine is modelled without processes and is represented by the geometry shown in Figure 6.3 (a), which was obtained by approximating the dimensions of the illustrative model of the lower spine in Figure 2.2 (b). The 3-d geometry is discretised using 72 320 quadratic 20-noded *Taylor-Hood* elements yielding a total of 982 044 DOF. In order to induce a bending movement on the lumber spine, boundary conditions are set such that the lower surface of the L5 vertebra is totally fixed in space ($\mathbf{u}_S = \mathbf{0}$), while the top surface of the L1 vertebra is loaded with the traction vector $\bar{\mathbf{t}}$. Herein, the *Neumann* boundary condition yields a horizontal (F_H) and vertical (F_V) force when integrated over the top-surface. For convenience, the traction vector is linearly increased over time until the resulting tip-loads of $F_H = 31.7\,\mathrm{N}$ and $F_V = 126.7\,\mathrm{N}$ are achieved at $t = 0.3\,\mathrm{s}$, respectively. Note that all free side surfaces are always drained ($\mathcal{P} = 0\,\mathrm{MPa}$) and the molar concentration of the surrounding fluid is held constant at $\bar{c}_m = 0.15\,\mathrm{mol/l}$. The computation is then carried out in parallel on the Beowulf Linux cluster of the Institute of Applied Mechanics (Chair of Continuum Mechanics) at the Universität Stuttgart using 84 CPU simultaneously, cf. footnote on page 124. During the simulation, a constant time increment of $\Delta t_n = 0.003\,\mathrm{s}$ is used for the backward *Euler* time integration. Taking into account three smaller time steps in the beginning of the simulation leads to a total of 102 time (*Euler*) steps.

The results of the simulation are displayed in Figure 6.22. Herein, the deformation behaviour is given at six different points in time, showing a total view of the deforming lumbar spine (vertebrae drawn in blue, IVD in red) as well as a perspective showing only the respective midsagittally cut discs. The colouring of the latter indicates the total pore pressure, where a blue colour corresponds to $p = -0.7\,\mathrm{MPa}$ and red indicates a pressure of $p = 1.6\,\mathrm{MPa}$. Like it is the case in the previous examples, the initial osmotic pressure $\Delta\pi_{0S}$ in Figure 6.22 (a) is fully compensated by the solid extra stress without an initial deformation of the solid skeleton. Moreover, note how the internal disc pressure increases gradually with the applied load over the first five deformation states (a) through (e), whereas it drastically rises between the last two steps (e) and (f). As expected, extreme values for total pore pressure are found in the lowest IVD of the L4-L5 motion segment, where the highest and lowest values for the pore pressure are observed in the ventral region and dorsal region, respectively.

The total computation time to achieve the maximum deformation for the intact lumbar spine is 8:44:49 [h:min:s] which can be split into the time needed for the assembly of the linearised system of equations, for ILU preconditioning, and for the solution of the linear systems using the GMRES method. In this context, the overall computation time partitions into 17:38 [min:s] for assembly, 51:17 [min:s] for preconditioning, and 7:30:30 [h:min:s] for solving. This corresponds to average computation times of six and 23 seconds which are needed for assembly and preconditioning per *Euler* step, respectively. The remaining time of 5:24 [min:s] is needed for data export of the solution files, each having a file size of about 16 MB. These numbers already indicate the efficiency of the parallel code, as most of the time is spent for solving the linearised system, while all other preliminary tasks need only a comparatively small amount of time. However, in order to obtain

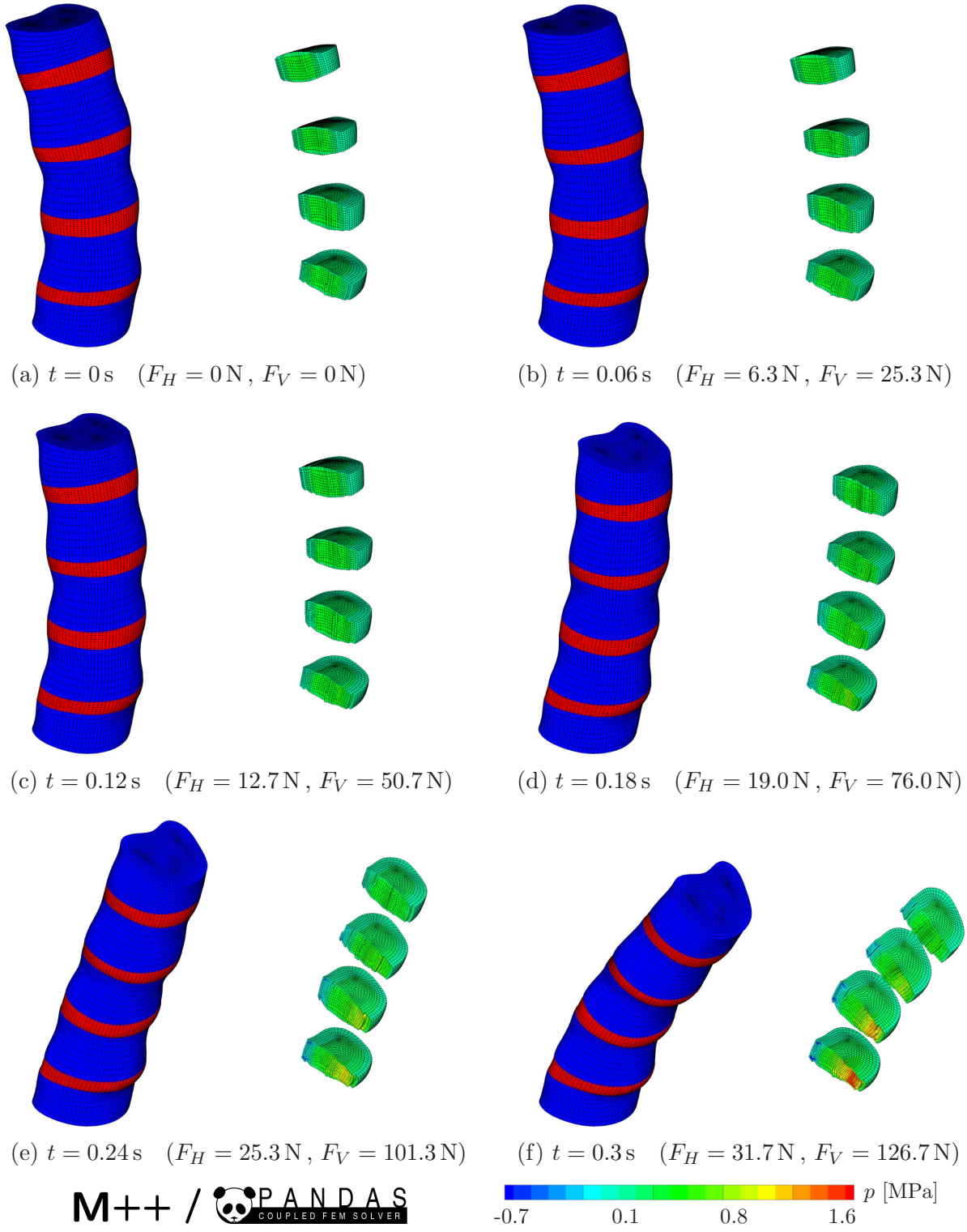

(a) $t = 0\,\mathrm{s}$ $(F_H = 0\,\mathrm{N}\,,\, F_V = 0\,\mathrm{N})$

(b) $t = 0.06\,\mathrm{s}$ $(F_H = 6.3\,\mathrm{N}\,,\, F_V = 25.3\,\mathrm{N})$

(c) $t = 0.12\,\mathrm{s}$ $(F_H = 12.7\,\mathrm{N}\,,\, F_V = 50.7\,\mathrm{N})$

(d) $t = 0.18\,\mathrm{s}$ $(F_H = 19.0\,\mathrm{N}\,,\, F_V = 76.0\,\mathrm{N})$

(e) $t = 0.24\,\mathrm{s}$ $(F_H = 25.3\,\mathrm{N}\,,\, F_V = 101.3\,\mathrm{N})$

(f) $t = 0.3\,\mathrm{s}$ $(F_H = 31.7\,\mathrm{N}\,,\, F_V = 126.7\,\mathrm{N})$

Figure 6.22: *Numerical results of the L1-L5 bending experiment showing the deformation behaviour at six points in time. The total view of the lumber spine has the vertebrae displayed in blue, while a red colour indicates an IVD. The pictures asides show only the midsagittally cut discs with the corresponding total pore pressure distribution according to the given scale.*

an impression on the convergence behaviour of the parallel solver M++, more detailed numbers need to be provided. In particular, within the 102 *Euler* (time) steps, a total of 164 linearised systems are assembled for the same number of *Newton* steps, which are iteratively solved with a total of 14 914 GMRES steps. More detailed information on this topic can be found in Table 6.7 including average as well as maximal and minimal values.

	computation time	*Newton* iterations	GMRES iterations	
average	5:09 [min:s]	1.6	146	per
maximum	15:19 [min:s]	2	355	*Euler*
minimum	0:23 [min:s]	1	40	step
average	3:10 [min:s]	—	91	per
maximum	8:38 [min:s]	—	270	*Newton*
minimum	1:35 [min:s]	—	40	step
average	2:45 [min:s]	—	—	of the
maximum	8:20 [min:s]	—	—	linear
minimum	1:11 [min:s]	—	—	solver

Table 6.7: *Important indicators needed to obtain an impression on the convergence behaviour of the parallel solver* M++ *during the solution of the nonlinear problem.*

Finally, note that the mesh used for this computation is already at level one, i. e., one regular refinement has been carried out with respect to the original mesh. Unfortunately, the computation using the next finer level was aborted due to singular element *Jacobi* matrices during the computation of the geometry transformation. To be more precise, this concerns the superio-ventral and inferio-ventral elements of the lowest IVD which are squeezed by the surrounding stiffer vertebrae, such that the corner angle of some elements reaches values past 180°. The same problem occurred for the presented computation on level one but due to the larger elements in the coarser mesh, the numerical difficulties started long after at $t = 0.3\,\mathrm{s}$, which corresponds to the presented maximum deformation state. However, a comparison of the results between level one and two showed a good agreement such that the solution obtained on the level-one grid is sufficiently converged.

6.5.2 Healthy versus Stiffened Motion Segment

In order to obtain information on the influence of a stiffened L4-L5 motion segment on the behaviour of the lumbar spine, the same BVP is computed again but now using the material parameters of the vertebrae for the lowest (stiffened) IVD. For a convenient comparison between the healthy and the stiffened state, both settings are loaded until a tip deflection of 54.3 mm is achieved. The corresponding tip-loads are $F_V = 84.9\,\mathrm{N}$, $F_H = 21.2\,\mathrm{N}$ and $F_V = 107.7\,\mathrm{N}$, $F_H = 26.9\,\mathrm{N}$ with loading times $t = 0.201\,\mathrm{s}$ and $t = 0.255\,\mathrm{s}$ for the healthy and the stiffened spine, respectively. The results of the 3-d simulations are depicted in Figure 6.23 showing the total pressure in the sagittal plane of the lumbar spine at the undeformed initial state and the final deformed states, respectively.

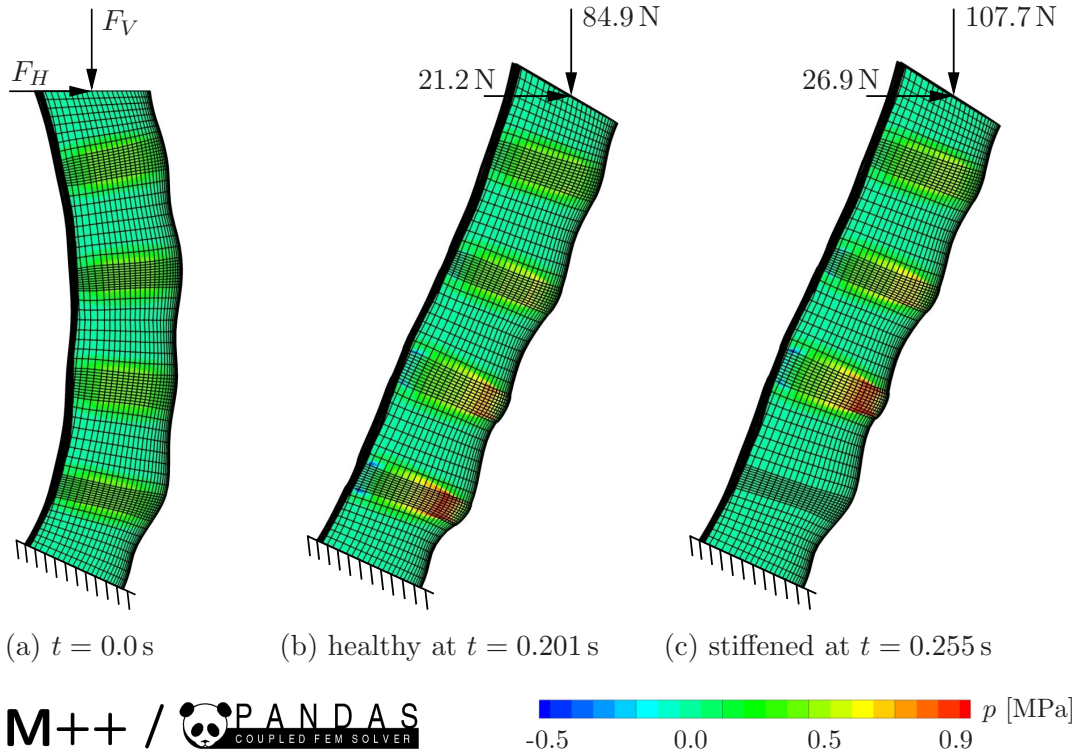

Figure 6.23: *Sagittal cut illustrating the load-deformation behaviour and the total pressure development inside the IVD. (a) Indicates the unloaded reference configuration, (b) the healthy lumbar spine and (c) the degenerated state having the L4-L5 motion segment stiffened.*

As expected, the force which is required to accomplish the same deformation with the stiffened lumbar spine is remarkably higher than the force needed for the healthy state of the lumbar spine. Moreover, the maximum total intradiscal pressure p in the L3-L4 disc is also raised from 0.7 MPa to 1.0 MPa comparing the healthy with the stiffened state. Note that this is even a higher value than the 0.95 MPa of total disc-pressure reached in the healthy L4-L5 disc. Hence, it is obvious that the stiffening of a motion segment causes a surplus load in the adjacent IVD, when deformations are kept constant. These studies are of particular interest, when a totally degenerated IVD has to be replaced. As flexible implants are still a challenging field for research, a simple cage implant is frequently used instead to fully demobilise the corresponding motion segment.

7 Summary and Outlook

7.1 Summary

The goal of this monograph was to present a model which is capable of describing the electro-chemically coupled deformation behaviour of saturated biological tissues in general and the intervertebral disc (IVD) in particular. In order to understand the necessary fundamentals from a biological point of view, a brief excursus into basic anatomy was presented firstly, thereby embracing the disc's structural and bio-chemical composition.

Moreover, a detailed continuum-mechanical modelling approach was followed which is based on the thermodynamically consistent Theory of Porous Media (TPM). Herein, the general idea of the TPM was presented starting from the general case of a saturated soft biological tissue, where its pore-fluid is actually a mixture of an incompressible liquid and dissolved ions. This general approach was conveniently reduced to the presented extended biphasic model using *Lanir*'s assumption, which is the simplest possibility to still include electro-chemical effects like osmosis driven swelling phenomena. The missing constitutive relations, needed to characterise the actual mechanical behaviour of the tissue, were then introduced in a modular manner. Herein, the focus was laid on the thermodynamical consistency of the proposed relations as well as on their admissibility in the finite deformation regime. In this regard, the isotropic part of the solid skeleton was modelled to behave viscoelastic using a generalised *Maxwell* model, where a very general *Ogden* law was used for the respective strain energies. In order to incorporate the purely elastic type-I collagen fibres, a polynomial strain energy was developed in accordance to the existing *Ogden* law, where it is possible to reproduce almost any nonlinear mechanical stress-strain behaviour. Moreover, the osmotic pressure contribution as well as the deformation-dependent *Darcy* filter law were included into the model such that they do not violate any thermodynamical restrictions.

As a next step, the obtained governing equations were rewritten in weak form which allowed for a convenient numerical treatment of the coupled system of partial differential equations using the Finite Element Method (FEM). In this regard, the spatial as well as the temporal discretisation was carried out using quadratic *Taylor-Hood* elements and the backward *Euler* time integration scheme, respectively. This finally led to a discrete system of coupled nonlinear partial differential equations. As the presented model also includes inelastic material behaviour of the isotropic solid skeleton, the global system of equations contains several local systems of evolution equations, which have to be solved before the global system can be solved. Following this, a multi-level *Newton* method was presented which allows for the efficient numerical treatment of both systems simultaneously. Finally, some concrete ideas were presented to couple the existing FE-code PANDAS to the parallel solver M++ or to any other commercial FE package.

The last part of the thesis is concerned with numerical examples which clearly embrace the capabilities of the presented time- and space-discrete set of governing equations. As a

prerequisite, the occurring problems during geometry acquisition in biomechanics as well as the associated mesh generation were discussed and a way of solving these problems was presented. Next, an algorithm was defined which is capable of computing the occurring inherent inhomogeneities with respect to fibre alignment and their corresponding location-dependent mechanical behaviour as well as the unequal distribution of the fixed negative charges. In a next step, the theoretically introduced material parameters were identified using experiments from the related literature. In this context, it was not always possible to directly determine all parameters using real-life experiments. Hence, a vast literature study was performed and the corresponding mean values for the respective parameters were presented.

Furthermore, in order to obtain an impression on the influence of the involved parameters on representative deformation modes of the spine, two parameter studies were performed on an L4-L5 motion segment in short-term bending and long-term compression. In this regard, it turned out that for short-term loading conditions, the IVD is mainly influenced by parameters characterising the solid skeleton, but especially the type-I collagen fibres were of prime importance. Hence, it can be summarised that special care should be taken regarding their inhomogeneous distribution as well as their location-specific mechanical behaviour, no matter if a single- or multiphasic model is used for simulation. A different result was obtained for the case of long-term loading conditions, where the permeability of the tissue plays also a key role.

Finally, a benchmark computation was presented addressing the deformation behaviour of the overall lumbar spine, thereby proving the efficiency of the underlying parallel solution strategy. Moreover, the same computation was performed on a degenerated lumbar spine having its L4-L5 motion segment stiffened. This led to a load increase in the neighbouring discs compared to the results of a similar deformation state of the healthy state.

7.2 Outlook

The present monograph successfully proved that the proposed extended biphasic model outlines a reasonable approach for the numerical simulation of the IVD. Following this, it is now possible to describe the healthy state of an IVD and the model can function as a numerical laboratory. This feature can significantly support research concerning the influence of the involved structural elements as well as the occurring inhomogeneities during other representative deformation modes, like pure torsion or torsional bending for instance. In this regard, it would be interesting to understand the reason for the inhomogeneously distributed constituents and what would happen, if the inhomogeneities were not included. Moreover, the influence of the loss of fixed negative charges with age on the fluid content of the IVD during long-term loading conditions can be studied straightforwardly. In this context, it is of general interest to extend the model towards degeneration effects resulting from regular ageing, mechanical damage or combinations of both. In order to do so, evolution equations need to be developed which describe the effects like the calcification process, the loss of fixed negative charges, etc. over time or during mechanical stimulus. However, the corresponding mechanisms, which are responsible for

ageing or degeneration, are still not fully investigated and understood, as they are often coupled to each other. Thus, a numerical model could substantially help to fully reveal these complicated processes.

Furthermore, the described model should be implemented into a commercial FE code, which is capable of capturing the contact forces in the facet joints of the articular processes. In this regard, the geometry model should be advanced to capture all attached processes as well as the surrounding ligaments. At the same time, material parameters, which could not be clearly determined in the present study, should be identified from additional experiments and most important, the found parameters need to be validated thereafter. For the passive state, i. e., having no active muscle contractions, this can be accomplished using *ex-vivo* experiments. This state will allow to completely simulate the healthy state of a spine segment, which may remarkably aid the design of new implants. However, the respective boundary conditions for the active case, i. e., where muscle contractions are also responsible for the applied loads, are not fully understood yet. In this regard it is suggested to firstly develop a coarser and numerically cheaper model, for instance, a model based on Multi Body Dynamics. Herein it is possible to conveniently describe the spine as a multi body system having active muscles as well as "dead loads" (resulting from the surrounding tissue) attached. With such a model it will be possible to obtain reasonable magnitudes of the loads during everyday activities or even during traumatic situations, which can be applied as boundary conditions for simulations using the presented more detailed model.

A Tensor Calculus

This part of the appendix provides a collection of rules which allow for a concise and convenient handling of the occurring tensor operations without going into the details of the sometimes lengthy formalisms of tensor calculus in basis notation. For more detailed information on the particulars, the interested reader is referred to the text of de Boer [23]. A compact summary of this text can also be found in the online lecture notes of the Institute of Applied Mechanics (Chair of Continuum Mechanics) at the Universität Stuttgart (Ehlers [50]), where much of the following content is taken from.

A.1 Tensor Algebra

For the following considerations let $\{\alpha, \beta\} \in R$ be arbitrary rational scalar quantities, $\{\mathbf{a}, \mathbf{b}, \mathbf{c}, \mathbf{d}\} \in \mathcal{V}^3$ be arbitrary vectors of the proper *Euklid*ian 3-d vector space $\mathcal{V}^3$, and $\{\mathbf{A}, \mathbf{B}, \mathbf{C}, \mathbf{D}\} \in \mathcal{V}^3 \otimes \mathcal{V}^3$ be arbitrary second-order tensors of the corresponding dyadic product space.

A.1.1 Collected Rules for Second-Order Tensors

Products of tensors with scalars or vectors:

$$\begin{aligned}
\alpha\,(\beta\,\mathbf{A}) &= (\alpha\,\beta)\,\mathbf{A} && \text{: associative law}\\
\mathbf{A}\,(\alpha\,\mathbf{a}) &= \alpha(\mathbf{A}\,\mathbf{a}) = (\alpha\,\mathbf{A})\,\mathbf{a} && \text{: associative law}\\
(\alpha+\beta)\,\mathbf{A} &= \alpha\,\mathbf{A} + \beta\,\mathbf{A} && \text{: distributive law}\\
\alpha\,(\mathbf{A}+\mathbf{B}) &= \alpha\,\mathbf{A} + \alpha\,\mathbf{B} && \text{: distributive law}\\
\mathbf{A}\,(\mathbf{a}+\mathbf{b}) &= \mathbf{A}\,\mathbf{a} + \mathbf{A}\,\mathbf{b} && \text{: distributive law}\\
(\mathbf{A}+\mathbf{B})\,\mathbf{a} &= \mathbf{A}\,\mathbf{a} + \mathbf{B}\,\mathbf{a} && \text{: distributive law}\\
\alpha\,\mathbf{A} &= \mathbf{A}\,\alpha && \text{: commutative law}\\
\mathbf{a} &= \mathbf{A}\,\mathbf{b} && \text{: linear mapping}\\
\mathbf{I}\,\mathbf{a} &= \mathbf{a} && \text{: } \mathbf{I} \text{ : identity element}\\
\mathbf{0}\,\mathbf{a} &= \mathbf{0} && \text{: } \mathbf{0} \text{ : zero element}
\end{aligned} \tag{A.1}$$

The scalar (inner) product of tensors:

$$\begin{aligned}
(\alpha\,\mathbf{A})\cdot\mathbf{B} &= \mathbf{A}\cdot(\alpha\,\mathbf{B}) = \alpha\,(\mathbf{A}\cdot\mathbf{B}) && \text{: associative law}\\
\mathbf{A}\cdot(\mathbf{B}+\mathbf{C}) &= \mathbf{A}\cdot\mathbf{B} + \mathbf{A}\cdot\mathbf{C} && \text{: distributive law}\\
\mathbf{A}\cdot\mathbf{B} &= \mathbf{B}\cdot\mathbf{A} && \text{: commutative law}\\
\mathbf{A}\cdot\mathbf{B} &= 0 \quad \forall\ \mathbf{A}\,, \text{ if } \mathbf{B} \equiv \mathbf{0}\\
\mathbf{A}\cdot\mathbf{A} &> 0 \quad \forall\ \mathbf{A} \neq \mathbf{0}\\
\mathbf{a}\cdot(\mathbf{a}\otimes\mathbf{b}) &= \mathbf{a}\cdot\mathbf{A}\,\mathbf{b}
\end{aligned} \tag{A.2}$$

The tensor product of tensors:

$$\begin{aligned}
\alpha\,(\mathbf{A}\,\mathbf{B}) &= (\alpha\,\mathbf{A})\,\mathbf{B} = \mathbf{A}\,(\alpha\,\mathbf{B}) && : \text{ associate law}\\
(\mathbf{A}\,\mathbf{B})\,\mathbf{a} &= \mathbf{A}\,(\mathbf{B}\,\mathbf{a}) && : \text{ associate law}\\
(\mathbf{A}\,\mathbf{B})\,\mathbf{C} &= \mathbf{A}\,(\mathbf{B}\,\mathbf{C}) && : \text{ associate law}\\
\mathbf{A}\,(\mathbf{B}+\mathbf{C}) &= \mathbf{A}\,\mathbf{B}+\mathbf{A}\,\mathbf{C} && : \text{ distributive law}\\
(\mathbf{A}+\mathbf{B})\,\mathbf{C} &= \mathbf{A}\,\mathbf{C}+\mathbf{B}\,\mathbf{C} && : \text{ distributive law}\\
\mathbf{A}\,\mathbf{B} &\neq \mathbf{B}\,\mathbf{A} && : \underline{\text{no}} \text{ commutative law}\\
\mathbf{I}\,\mathbf{A} &= \mathbf{A}\,\mathbf{I} = \mathbf{A} && : \mathbf{I} \text{ : identity element}\\
\mathbf{0}\,\mathbf{A} &= \mathbf{A}\,\mathbf{0} = \mathbf{0} && : \mathbf{0} \text{ : zero element}\\
(\mathbf{a}\otimes\mathbf{b})\,(\mathbf{c}\otimes\mathbf{d}) &= (\mathbf{b}\cdot\mathbf{c})\,\mathbf{a}\otimes\mathbf{d}
\end{aligned} \tag{A.3}$$

The transposed and inverse tensor:

$$\begin{aligned}
(\mathbf{a}\otimes\mathbf{b})^T &= (\mathbf{b}\otimes\mathbf{a}) & \mathbf{A}^{-1} &= (\det\mathbf{A})^{-1}\operatorname{adj}\mathbf{A}\\
(\alpha\,\mathbf{A})^T &= \alpha\,\mathbf{A}^T & \mathbf{A}^{-1} &= (\det\mathbf{A})^{-1}\operatorname{cof}\mathbf{A}^T\\
(\mathbf{A}\,\mathbf{B})^T &= \mathbf{B}^T\mathbf{A}^T & \longrightarrow\ \mathbf{A}^{-1} &\text{ exists if } \det\mathbf{A}\neq 0\\
\mathbf{a}\cdot(\mathbf{B}\,\mathbf{b}) &= (\mathbf{B}^T\mathbf{a})\cdot\mathbf{b} & \mathbf{A}\,\mathbf{A}^{-1} &= \mathbf{A}^{-1}\,\mathbf{A} = \mathbf{I}\\
\mathbf{A}\cdot(\mathbf{B}\,\mathbf{C}) &= (\mathbf{B}^T\mathbf{A})\cdot\mathbf{C} & (\mathbf{A}^{-1})^T &= (\mathbf{A}^T)^{-1} =: \mathbf{A}^{T-1}\\
(\mathbf{A}+\mathbf{B})^T &= \mathbf{A}^T+\mathbf{B}^T & (\mathbf{A}\,\mathbf{B})^{-1} &= \mathbf{B}^{-1}\mathbf{A}^{-1}
\end{aligned} \tag{A.4}$$

Herein, $\operatorname{adj}\mathbf{A}$ and $\operatorname{cof}\mathbf{A}^T$ denote the adjoint and the cofactor of $\mathbf{A}$, respectively. Moreover, the following rules can be given for these quantities as well as the related determinant and inverse of a tensor:

$$\begin{aligned}
\operatorname{adj}\mathbf{A} &= \operatorname{cof}\mathbf{A}^T\\
(\operatorname{cof}\mathbf{A})^T &= \operatorname{cof}\mathbf{A}^T\\
\operatorname{adj}(\mathbf{A}\,\mathbf{B}) &= \operatorname{adj}\mathbf{A}\operatorname{adj}\mathbf{B}\\
\det(\mathbf{A}\,\mathbf{B}) &= \det\mathbf{A}\det\mathbf{B}\\
\det(\alpha\,\mathbf{A}) &= \alpha^3\det\mathbf{A}\\
\det\mathbf{I} &= 1\\
\det\mathbf{A}^T &= \det\mathbf{A}\\
\det(\operatorname{adj}\mathbf{A}) &= \det(\operatorname{cof}\mathbf{A}) = (\det\mathbf{A})^2\\
\det\mathbf{A}^{-1} &= (\det\mathbf{A})^{-1}\\
\det(\mathbf{A}+\mathbf{B}) &= \det\mathbf{A}+\operatorname{cof}\mathbf{A}\cdot\mathbf{B}+\mathbf{A}\cdot\operatorname{cof}\mathbf{B}+\det\mathbf{B}
\end{aligned} \tag{A.5}$$

The trace operator:

$$\begin{aligned}
\operatorname{tr}\mathbf{A} &= \mathbf{A}\cdot\mathbf{I}\\
\operatorname{tr}(\alpha\,\mathbf{A}) &= \alpha\operatorname{tr}\mathbf{A}\\
\operatorname{tr}(\mathbf{a}\otimes\mathbf{b}) &= \mathbf{a}\cdot\mathbf{b}\\
\operatorname{tr}\mathbf{A}^T &= \operatorname{tr}\mathbf{A}\\
\operatorname{tr}(\mathbf{A}\,\mathbf{B}) &= \operatorname{tr}(\mathbf{B}\,\mathbf{A}) = \mathbf{A}\cdot\mathbf{B}^T = \mathbf{A}^T\cdot\mathbf{B}\\
\operatorname{tr}\mathbf{A}\,\mathbf{B}\,\mathbf{C} &= \operatorname{tr}\mathbf{B}\,\mathbf{C}\,\mathbf{A} = \operatorname{tr}\mathbf{C}\,\mathbf{A}\,\mathbf{B}
\end{aligned} \tag{A.6}$$

A.1.2 Collected Rules for Higher-Order Tensors

Third-order fundamental (*Ricci*) tensor and axial vector:

$$\begin{aligned}
\mathbf{a}\times\mathbf{b} &= \overset{3}{\mathbf{E}}(\mathbf{a}\otimes\mathbf{b}) && : \ \overset{3}{\mathbf{E}} \ : \ \textit{Ricci} \text{ permutation tensor} \\
\mathbf{a}\times\mathbf{B} &= [\overset{3}{\mathbf{E}}(\mathbf{a}\otimes\mathbf{B})]^{\underline{2}} && : \ (\bullet)^{\underline{2}} \ : \ \text{“incomplete” mapping} \\
\mathbf{A}\times\mathbf{B} &= \overset{3}{\mathbf{E}}(\mathbf{A}\,\mathbf{B}^T) && \\
\text{special case:} \quad \mathbf{I}\times\mathbf{B} &= \overset{3}{\mathbf{E}}\,\mathbf{B}^T = 2\,\overset{\mathrm{A}}{\mathbf{b}} && \text{with} \\
\overset{\mathrm{A}}{\mathbf{b}} &= \tfrac{1}{2}\overset{3}{\mathbf{E}}\,\mathbf{B}^T && : \ \overset{A}{\mathbf{b}} \ : \ \text{axial vector of } \mathbf{B}
\end{aligned} \tag{A.7}$$

For a better understanding of the properties of the *Ricci* permutation tensor, it is also given in basis notation:

$$\begin{aligned}
&\overset{3}{\mathbf{E}} = e_{ijk}\,(\mathbf{e}_i\otimes\mathbf{e}_j\otimes\mathbf{e}_k) \qquad \text{with the “permutation symbol” } e_{ijk} \\
&e_{ijk} = \begin{cases} 1 & : \text{even permutation} \\ -1 & : \text{odd permutation} \\ 0 & : \text{double indexing} \end{cases} \longrightarrow \begin{cases} e_{123} = e_{231} = e_{312} = 1 \\ e_{321} = e_{213} = e_{132} = -1 \\ \text{all remaining } e_{ijk} \text{ vanish} \end{cases}
\end{aligned} \tag{A.8}$$

Fourth-order fundamental tensors:

$$\begin{aligned}
\overset{4}{\mathbf{I}} := (\mathbf{I}\otimes\mathbf{I})^{\overset{23}{T}} \quad &\longrightarrow \quad (\mathbf{I}\otimes\mathbf{I})^{\overset{23}{T}}\mathbf{A} = \mathbf{A} && : \text{identical map} \\
(\mathbf{I}\otimes\mathbf{I})^{\overset{24}{T}} \quad &\longrightarrow \quad (\mathbf{I}\otimes\mathbf{I})^{\overset{24}{T}}\mathbf{A} = \mathbf{A}^T && : \text{transposing map} \\
\mathbf{I}\otimes\mathbf{I} \quad &\longrightarrow \quad (\mathbf{I}\otimes\mathbf{I})\,\mathbf{A} = (\mathbf{A}\cdot\mathbf{I})\,\mathbf{I} && : \text{tracing map}
\end{aligned} \tag{A.9}$$

Herein, the transpositions $(\bullet)^{\overset{ik}{T}}$ indicate an exchange of the i-th and k-th basis systems included into the tensor basis of higher order tensors. Note that further transpositions of $\mathbf{I}\otimes\mathbf{I}$ do not lead to further independent tensors. Moreover, the fundamental tensors from above exhibit the property:

$$\overset{4}{\mathbf{A}} = \overset{4}{\mathbf{A}}{}^T \qquad \text{with} \qquad \overset{4}{\mathbf{A}}{}^T = (\overset{4}{\mathbf{A}}{}^{\overset{13}{T}})^{\overset{24}{T}} \tag{A.10}$$

Properties of simple fourth-order tensors:

$$\begin{aligned}
\overset{4}{\mathbf{A}} &= (\mathbf{A}\otimes\mathbf{B})^{\overset{23}{T}} &&= (\mathbf{B}^T\otimes\mathbf{A}^T)^{\overset{14}{T}} \\
\overset{4}{\mathbf{A}}{}^T &= [(\mathbf{A}\otimes\mathbf{B})^{\overset{23}{T}}]^T &&= (\mathbf{A}^T\otimes\mathbf{B}^T)^{\overset{23}{T}} \\
\overset{4}{\mathbf{A}}{}^{-1} &= [(\mathbf{A}\otimes\mathbf{B})^{\overset{23}{T}}]^{-1} &&= (\mathbf{A}^{-1}\otimes\mathbf{B}^{-1})^{\overset{23}{T}} \\
\overset{4}{\mathbf{B}} &= (\mathbf{A}\otimes\mathbf{B})^{\overset{24}{T}} &&= [(\mathbf{A}\otimes\mathbf{B})^{\overset{13}{T}}]^T \\
\overset{4}{\mathbf{B}}{}^T &= [(\mathbf{A}\otimes\mathbf{B})^{\overset{24}{T}}]^T &&= (\mathbf{B}\otimes\mathbf{A})^{\overset{24}{T}} \\
\overset{4}{\mathbf{B}}{}^{-1} &= [(\mathbf{A}\otimes\mathbf{B})^{\overset{24}{T}}]^{-1} &&= (\mathbf{B}^{T-1}\otimes\mathbf{A}^{T-1})^{\overset{24}{T}}
\end{aligned} \tag{A.11}$$

A selection of related rules:

$$\begin{aligned}
(\mathbf{A}\otimes\mathbf{B})\overset{23}{}_T(\mathbf{C}\otimes\mathbf{D})\overset{23}{}_T &= (\mathbf{A}\,\mathbf{C}\otimes\mathbf{B}\,\mathbf{D})\overset{23}{}_T \\
(\mathbf{A}\otimes\mathbf{B})\overset{23}{}_T(\mathbf{C}\otimes\mathbf{D}) &= (\mathbf{A}\,\mathbf{C}\,\mathbf{B}^T\otimes\mathbf{D}) \\
(\mathbf{A}\otimes\mathbf{B})(\mathbf{C}\otimes\mathbf{D})\overset{23}{}_T &= (\mathbf{A}\otimes\mathbf{C}^T\mathbf{B}\,\mathbf{D}) \\
(\mathbf{A}\otimes\mathbf{B})\overset{23}{}_T\mathbf{C} &= \mathbf{A}\,\mathbf{C}\,\mathbf{B}^T \\
(\mathbf{A}\otimes\mathbf{B})\overset{23}{}_T\mathbf{a} &= [\mathbf{A}\otimes(\mathbf{B}\,\mathbf{a})]\overset{23}{}_T
\end{aligned} \tag{A.12}$$

$$\begin{aligned}
(\mathbf{A}\otimes\mathbf{B})\overset{24}{}_T(\mathbf{C}\otimes\mathbf{D})\overset{24}{}_T &= (\mathbf{A}\,\mathbf{D}^T\otimes\mathbf{B}^T\mathbf{C})\overset{23}{}_T \\
(\mathbf{A}\otimes\mathbf{B})\overset{23}{}_T(\mathbf{C}\otimes\mathbf{D})\overset{24}{}_T &= (\mathbf{A}\,\mathbf{C}\otimes\mathbf{D}\,\mathbf{B}^T)\overset{24}{}_T \\
(\mathbf{A}\otimes\mathbf{B})\overset{24}{}_T(\mathbf{C}\otimes\mathbf{D})\overset{23}{}_T &= (\mathbf{A}\,\mathbf{D}\otimes\mathbf{C}^T\mathbf{B})\overset{24}{}_T \\
(\mathbf{A}\otimes\mathbf{B})\overset{24}{}_T(\mathbf{C}\otimes\mathbf{D}) &= (\mathbf{A}\,\mathbf{C}^T\mathbf{B}\otimes\mathbf{D}) \\
(\mathbf{A}\otimes\mathbf{B})(\mathbf{C}\otimes\mathbf{D})\overset{24}{}_T &= (\mathbf{A}\otimes\mathbf{D}\,\mathbf{B}^T\mathbf{C}) \\
(\mathbf{A}\otimes\mathbf{B})\overset{24}{}_T\mathbf{C} &= \mathbf{A}\,\mathbf{C}^T\mathbf{B}
\end{aligned} \tag{A.13}$$

A.2 Tensor Analysis

Derivative of products of functions (product rule):

$$\begin{aligned}
(\mathbf{a}\otimes\mathbf{b})' &= \mathbf{a}'\otimes\mathbf{b}+\mathbf{a}\otimes\mathbf{b}' \\
(\mathbf{A}\,\mathbf{B})' &= \mathbf{A}'\,\mathbf{B}+\mathbf{A}\,\mathbf{B}' \\
(\mathbf{A}^{-1})' &= -\mathbf{A}^{-1}\,\mathbf{A}'\,\mathbf{A}^{-1}
\end{aligned} \tag{A.14}$$

A selection of useful derivatives:

$$\begin{aligned}
\frac{\partial\mathbf{A}}{\partial\mathbf{A}} &= (\mathbf{I}\otimes\mathbf{I})\overset{23}{}_T = \overset{4}{\mathbf{I}} \\
\frac{\partial\mathbf{A}^T}{\partial\mathbf{A}} &= (\mathbf{I}\otimes\mathbf{I})\overset{24}{}_T \\
\frac{\partial\mathbf{A}^{-1}}{\partial\mathbf{A}} &= -(\mathbf{A}^{-1}\otimes\mathbf{A}^{-1})\overset{23}{}_T \\
\frac{\partial\,\mathrm{tr}\,\mathbf{A}}{\partial\mathbf{A}} &= \mathbf{I} \\
\frac{\partial\,\mathrm{tr}\,(\mathrm{cof}\,\mathbf{A})}{\partial\mathbf{A}} &= (\mathbf{A}\cdot\mathbf{I})\,\mathbf{I}-\mathbf{A}^T \\
\frac{\partial\det\mathbf{A}}{\partial\mathbf{A}} &= \mathrm{cof}\,\mathbf{A} \\
\frac{\partial\,\mathrm{cof}\,\mathbf{A}}{\partial\mathbf{A}} &= \det\mathbf{A}\,[(\mathbf{A}^{T-1}\otimes\mathbf{A}^{T-1})-(\mathbf{A}^{T-1}\otimes\mathbf{A}^{T-1})\overset{24}{}_T]
\end{aligned} \tag{A.15}$$

$$
\begin{aligned}
\frac{\partial(\mathbf{A}\cdot\mathbf{I})\,\mathbf{I}}{\partial\mathbf{A}} &= (\mathbf{I}\otimes\mathbf{I}) \\
\frac{\partial(\mathbf{A}\,\mathbf{B})}{\partial\mathbf{B}} &= (\mathbf{A}\otimes\mathbf{I})^{\overset{23}{T}} \\
\frac{\partial(\mathbf{A}\,\mathbf{B})}{\partial\mathbf{A}} &= (\mathbf{I}\otimes\mathbf{B}^T)^{\overset{23}{T}} \\
\frac{\partial(\mathbf{A}\,\mathbf{A})}{\partial\mathbf{A}} &= (\mathbf{A}\otimes\mathbf{I})^{\overset{23}{T}} + (\mathbf{I}\otimes\mathbf{A}^T)^{\overset{23}{T}} \\
\frac{\partial(\mathbf{A}^T\mathbf{A})}{\partial\mathbf{A}} &= (\mathbf{A}^T\otimes\mathbf{I})^{\overset{23}{T}} + (\mathbf{I}\otimes\mathbf{A}^T)^{\overset{24}{T}} \\
\frac{\partial(\mathbf{A}\,\mathbf{A}^T)}{\partial\mathbf{A}} &= (\mathbf{A}\otimes\mathbf{I})^{\overset{24}{T}} + (\mathbf{I}\otimes\mathbf{A})^{\overset{23}{T}} \\
\frac{\partial(\mathbf{A}\,\mathbf{B}\,\mathbf{C})}{\partial\mathbf{B}} &= (\mathbf{A}\otimes\mathbf{C}^T)^{\overset{23}{T}}
\end{aligned}
\tag{A.16}
$$

Derivatives involving α, β, $\mathbf{a}$, $\mathbf{b}$, $\mathbf{A}$, and $\mathbf{B}$ as tensor functions of $\mathbf{C}$:

$$
\begin{aligned}
\frac{\partial(\alpha\,\beta)}{\partial\mathbf{C}} &= \alpha\,\frac{\partial\beta}{\partial\mathbf{C}} + \beta\,\frac{\partial\alpha}{\partial\mathbf{C}} \\
\frac{\partial(\alpha\,\mathbf{b})}{\partial\mathbf{C}} &= \mathbf{b}\otimes\frac{\partial\alpha}{\partial\mathbf{C}} + \alpha\,\frac{\partial\mathbf{b}}{\partial\mathbf{C}} \\
\frac{\partial(\alpha\,\mathbf{A})}{\partial\mathbf{C}} &= \mathbf{A}\otimes\frac{\partial\alpha}{\partial\mathbf{C}} + \alpha\,\frac{\partial\mathbf{A}}{\partial\mathbf{C}} \\
\frac{\partial(\mathbf{A}\,\mathbf{b})}{\partial\mathbf{C}} &= \left[\left(\frac{\partial\mathbf{A}}{\partial\mathbf{C}}\right)^{\overset{24}{T}}\right]^{\overset{23}{T}}\mathbf{b} + \left[\mathbf{A}\,\frac{\partial\mathbf{b}}{\partial\mathbf{C}}\right]^{\underline{3}} \\
\frac{\partial(\mathbf{a}\cdot\mathbf{b})}{\partial\mathbf{C}} &= \left[\left(\frac{\partial\mathbf{a}}{\partial\mathbf{C}}\right)^{\overset{13}{T}}\mathbf{b}\right]^T + \left[\left(\frac{\partial\mathbf{b}}{\partial\mathbf{C}}\right)^{\overset{13}{T}}\mathbf{a}\right]^T \\
\frac{\partial(\mathbf{A}\cdot\mathbf{B})}{\partial\mathbf{C}} &= \left(\frac{\partial\mathbf{A}}{\partial\mathbf{C}}\right)^T\mathbf{B} + \left(\frac{\partial\mathbf{B}}{\partial\mathbf{C}}\right)^T\mathbf{A} \\
\frac{\partial(\mathbf{A}\,\mathbf{B})}{\partial\mathbf{C}} &= \left(\left[\left(\frac{\partial\mathbf{A}}{\partial\mathbf{C}}\right)^{\overset{24}{T}}\mathbf{B}\right]^{\underline{4}}\right)^{\overset{24}{T}} + \left(\left[\left(\frac{\partial\mathbf{B}}{\partial\mathbf{C}}\right)^{\overset{14}{T}}\mathbf{A}^T\right]^{\underline{4}}\right)^{\overset{14}{T}}
\end{aligned}
\tag{A.17}
$$

Selected rules for the operators $\operatorname{grad}(\bullet)$ and $\operatorname{div}(\bullet)$:

$$\begin{aligned}
\operatorname{grad}(\phi\,\psi) &= \phi \operatorname{grad}\psi + \psi \operatorname{grad}\phi \\
\operatorname{grad}(\phi\,\mathbf{b}) &= \mathbf{b} \otimes \operatorname{grad}\phi + \phi \operatorname{grad}\mathbf{b} \\
\operatorname{grad}(\phi\,\mathbf{T}) &= \mathbf{T} \otimes \operatorname{grad}\phi + \phi \operatorname{grad}\mathbf{T} \\
\operatorname{div}(\mathbf{a} \otimes \mathbf{b}) &= \mathbf{a} \operatorname{div}\mathbf{b} + (\operatorname{grad}\mathbf{a})\,\mathbf{b} \\
\operatorname{div}(\phi\,\mathbf{b}) &= \mathbf{b} \cdot \operatorname{grad}\phi + \phi \operatorname{div}\mathbf{b} \\
\operatorname{div}(\phi\,\mathbf{T}) &= \mathbf{T} \operatorname{grad}\phi + \phi \operatorname{div}\mathbf{T} \\
\operatorname{div}(\mathbf{T}\,\mathbf{b}) &= (\operatorname{div}\mathbf{T}^T) \cdot \mathbf{b} + \mathbf{T}^T \cdot \operatorname{grad}\mathbf{b} \\
\operatorname{div}(\operatorname{grad}\mathbf{b})^T &= \operatorname{grad}\operatorname{div}\mathbf{b}
\end{aligned} \tag{A.18}$$

B Important Kinematical Relations

Transport behaviour of contravariant strain tensors

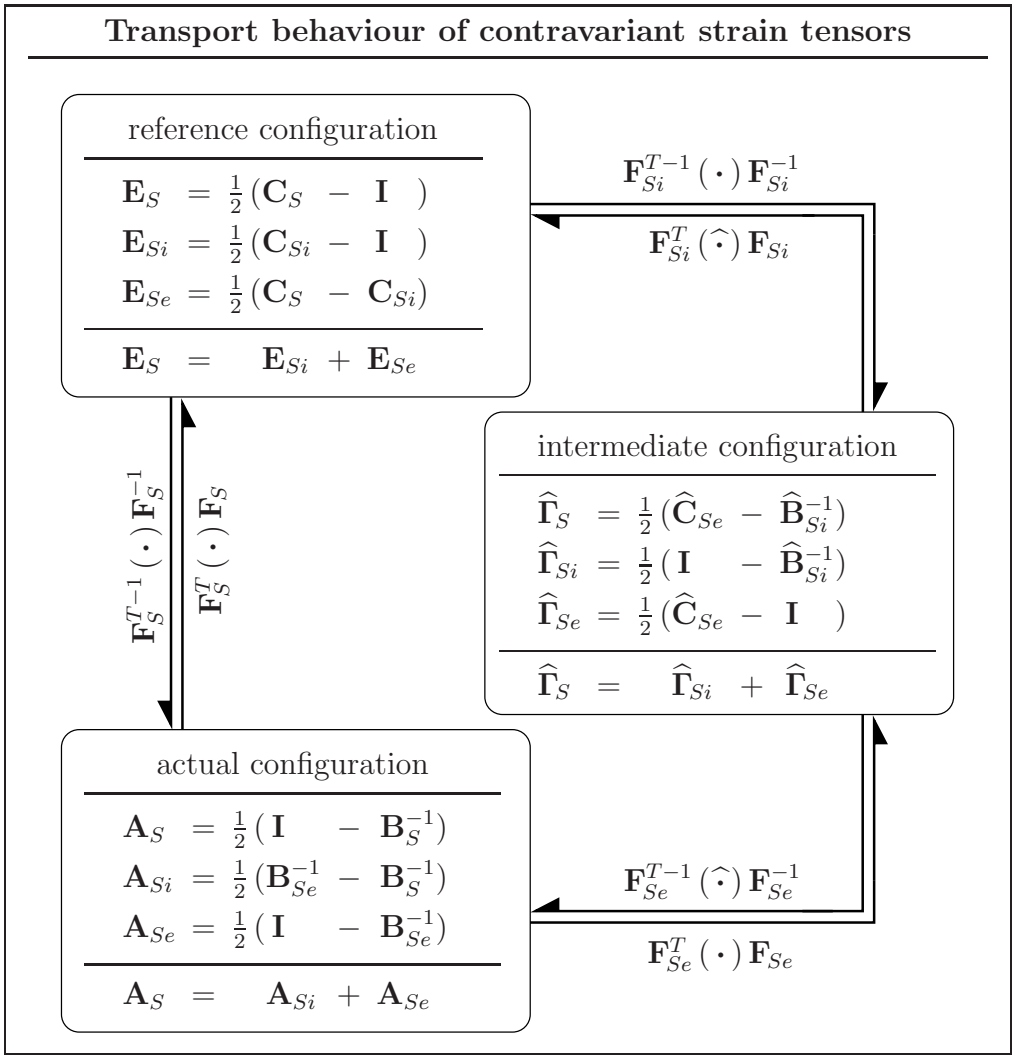

(B.1)

Transport behaviour of contravariant strain rate tensors

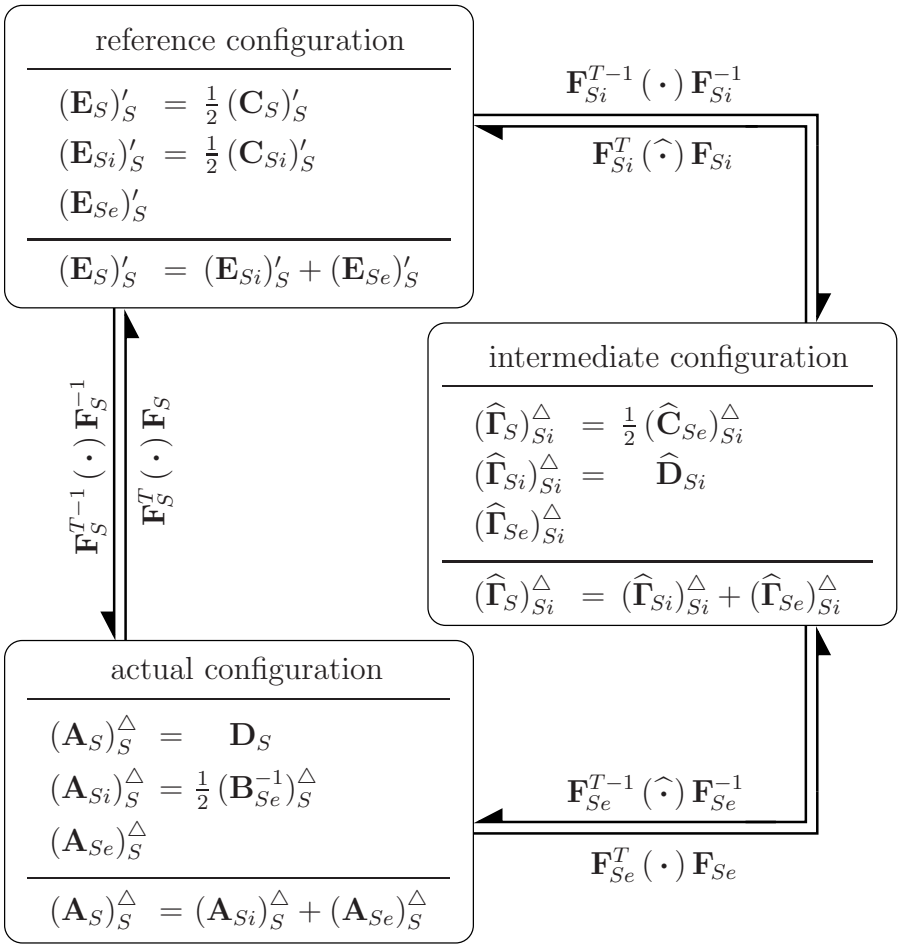

(B.2)

with the contravariant upper *Oldroyd* derivatives:

$$(\cdot)^{\triangle}_S = (\cdot)'_S + \mathbf{L}_S^T\,(\cdot) + (\cdot)\,\mathbf{L}_S\ ,$$

$$(\cdot)^{\triangle}_{Si} = (\cdot)'_S + \mathbf{L}_{Si}^T(\cdot) + (\cdot)\,\mathbf{L}_{Si}\,.$$

C Linearisation of the Balance Equations

For the linearisation of the balance equations it is convenient to proceed from a representation without the split of the solid extra stress $\mathbf{T}_E^S$ into mechanical and osmotic contributions. Following this, the directional *Gâteaux* derivatives $\mathcal{D}_{(\,.\,)}$ are taken from the weak forms of the standard biphasic model, i. e.,

$$\begin{aligned}
\mathcal{G}_{\mathbf{u}_S} &= \int_\Omega (\mathbf{T}_{\mathrm{E}}^S - \mathcal{P}\,\mathbf{I}) \cdot \operatorname{grad} \delta\mathbf{u}_S \,\mathrm{d}v - \int_\Omega (n^S \rho^{SR} + n^F \rho^{FR})\,\mathbf{g} \cdot \delta\mathbf{u}_S \,\mathrm{d}v - \int_{\Gamma_{\mathbf{t}}} \bar{\mathbf{t}} \cdot \delta\mathbf{u}_S \,\mathrm{d}a = 0 \\
\mathcal{G}_{\mathcal{P}} &= \int_\Omega \operatorname{div} (\mathbf{u}_S)'_S \,\delta\mathcal{P} \,\mathrm{d}v + \int_\Omega \Big[\, \frac{K^S}{\mu^{FR}} \,(\operatorname{grad} \mathcal{P} - \rho^{FR}\,\mathbf{g}) \,\Big] \cdot \operatorname{grad} \delta\mathcal{P} \,\mathrm{d}v + \int_{\Gamma_q} \bar{q}\,\delta\mathcal{P} \,\mathrm{d}a = 0\,.
\end{aligned} \tag{C.1}$$

The linearisation of the functional $\boldsymbol{\mathcal{G}}(\boldsymbol{u}, \boldsymbol{u}', \delta\boldsymbol{u}) = [\boldsymbol{\mathcal{G}}_{\mathbf{u}_S}\,,\, \boldsymbol{\mathcal{G}}_{\mathcal{P}}]^T$ around the expansion point $\widetilde{\boldsymbol{u}} = [\widetilde{\mathbf{u}}_S, \widetilde{\mathcal{P}}]$ can be given by the first-order *Taylor*[1] series expansion

$$\boldsymbol{\mathcal{G}}_{\mathrm{lin}}(\delta\boldsymbol{u}, \boldsymbol{u}, \boldsymbol{u}') = \widetilde{\boldsymbol{\mathcal{G}}} + \mathcal{D}_{\Delta\boldsymbol{u}}\,\widetilde{\boldsymbol{\mathcal{G}}} + \mathcal{D}_{\Delta\boldsymbol{u}'}\,\widetilde{\boldsymbol{\mathcal{G}}} \qquad \text{with} \qquad \widetilde{\boldsymbol{\mathcal{G}}} = \boldsymbol{\mathcal{G}}(\widetilde{\boldsymbol{u}}, \widetilde{\boldsymbol{u}}', \delta\boldsymbol{u})\,. \tag{C.2}$$

Herein, the *Gâteaux* differentials $\mathcal{D}_{\Delta\boldsymbol{u}}$ and $\mathcal{D}_{\Delta\boldsymbol{u}'}$ can be expressed in matrix form

$$\mathcal{D}_{\Delta\boldsymbol{u}}\,\widetilde{\boldsymbol{\mathcal{G}}} = \left[\begin{array}{c:c} \mathcal{D}_{\Delta\mathbf{u}_S}\,\mathcal{G}_{\mathbf{u}_S} & \mathcal{D}_{\Delta\mathcal{P}}\,\mathcal{G}_{\mathbf{u}_S} \\ \hdashline \mathcal{D}_{\Delta\mathbf{u}_S}\,\mathcal{G}_{\mathcal{P}} & \mathcal{D}_{\Delta\mathcal{P}}\,\mathcal{G}_{\mathcal{P}} \end{array}\right], \quad \mathcal{D}_{\Delta\boldsymbol{u}'}\,\widetilde{\boldsymbol{\mathcal{G}}} = \left[\begin{array}{c:c} \mathcal{D}_{\Delta(\mathbf{u}_S)'_S}\,\mathcal{G}_{\mathbf{u}_S} & \mathcal{D}_{\Delta(\mathcal{P})'_S}\,\mathcal{G}_{\mathbf{u}_S} \\ \hdashline \mathcal{D}_{\Delta(\mathbf{u}_S)'_S}\,\mathcal{G}_{\mathcal{P}} & \mathcal{D}_{\Delta(\mathcal{P})'_S}\,\mathcal{G}_{\mathcal{P}} \end{array}\right], \tag{C.3}$$

thereby representing all possible partial derivatives of (C.1) with respect to all unknowns in $\boldsymbol{u}$. The detailed derivation of the corresponding linearisations can be found in Eipper [67], Mahnkopf [129] or Markert [131]. Herein, the surface integrals (*Neumann* boundaries) were assumed to be independent of the deformation and thus, do not contribute to the linearisation. In particular, the individual terms in $(\mathrm{C.3})_1$ can be given as follows:

$$\begin{aligned}
\mathcal{D}_{\Delta\mathbf{u}_S}\,\mathcal{G}_{\mathbf{u}_S} \;=\; & \int_\Omega \Big[\, \tfrac{1}{2}\, J_S^{-1}\, \overset{4}{\boldsymbol{\mathcal{C}}}{}^S \,(\operatorname{grad} \Delta\mathbf{u}_S + \operatorname{grad}^T \Delta\mathbf{u}_S) + (\operatorname{grad} \Delta\mathbf{u}_S)\,\mathbf{T}_E^S \,\Big] \cdot \operatorname{grad} \delta\mathbf{u}_S \,\mathrm{d}v \;+ \\
& + \int_\Omega \mathcal{P}\,\Big[\, \operatorname{grad}^T \Delta\mathbf{u}_S - (\operatorname{div} \Delta\mathbf{u}_S)\,\mathbf{I} \,\Big] \cdot \operatorname{grad} \delta\mathbf{u}_S \,\mathrm{d}v \;+ \\
& + \int_\Omega \rho^{FR}\,(\operatorname{div} \Delta\mathbf{u}_S)\,\mathbf{g} \cdot \delta\mathbf{u}_S \,\mathrm{d}v\,, \\
\mathcal{D}_{\Delta\mathcal{P}}\,\mathcal{G}_{\mathbf{u}_S} \;=\; & -\int_\Omega \Delta\mathcal{P}\,\mathbf{I} \cdot \operatorname{grad} \delta\mathbf{u}_S \,\mathrm{d}v\,,
\end{aligned} \tag{C.4}$$

[1] *Brook Taylor* (1685–1731): English mathematician who published his most important work *Methodus Incrementorum Directa et Inversa* in 1715, thereby adding a new branch to higher mathematics. According to *Lagrange*, *Taylor*'s theorem is the main foundation of differential calculus.

$$
\begin{aligned}
\mathcal{D}_{\Delta \mathbf{u}_S} \mathcal{G}_{\mathcal{P}} \;=\; & \int_{\Omega} \left(\operatorname{div} (\mathbf{u}_S)'_S \operatorname{div} \Delta \mathbf{u}_S - \operatorname{grad} (\mathbf{u}_S)'_S \cdot \operatorname{grad}^T \Delta \mathbf{u}_S \right) \delta \mathcal{P} \, \mathrm{d}v \; + \\
& + \int_{\Omega} \Big[\Big(\frac{K^S}{\mu^{FR}} + \frac{1}{\mu^{FR}} \frac{\partial K^S}{\partial J_S} \Big) \operatorname{grad} \mathcal{P} \operatorname{div} \Delta \mathbf{u}_S \; - \\
& \qquad - \frac{K^S}{\mu^{FR}} \operatorname{grad} \mathcal{P} \left(\operatorname{grad} \Delta \mathbf{u}_S + \operatorname{grad}^T \Delta \mathbf{u}_S \right) \Big] \cdot \operatorname{grad} \delta \mathcal{P} \, \mathrm{d}v \,, \\
\mathcal{D}_{\Delta \mathcal{P}} \mathcal{G}_{\mathcal{P}} \;=\; & \int_{\Omega} \frac{K^S}{\mu^{FR}} \operatorname{grad} \Delta \mathcal{P} \cdot \operatorname{grad} \delta \mathcal{P} \, \mathrm{d}v \,,
\end{aligned}
\tag{C.5}
$$

whereas all terms in $(\mathrm{C}.3)_2$ vanish except for

$$
\mathcal{D}_{\Delta (\mathbf{u}_S)'_S} \mathcal{G}_{\mathcal{P}} \;=\; \int_{\Omega} \operatorname{div} \Delta (\mathbf{u}_S)'_S \, \delta \mathcal{P} \, \mathrm{d}v \,. \tag{C.6}
$$

The missing derivative of the deformation-dependent intrinsic permeability (4.127) in $(\mathrm{C}.5)_1$ can be given as:

$$
\frac{\partial K^S}{\partial J_S} = \frac{\kappa \, K^S_{0S}}{1 - n^S_{0S}} \Big(\frac{J_S - n^S_{0S}}{1 - n^S_{0S}} \Big)^{\kappa - 1} . \tag{C.7}
$$

Moreover, $\overset{4}{\boldsymbol{\mathcal{C}}}{}^S$ denotes the consistent material tangent, whereas the osmotic contribution in the previously presented form (5.22) needs to be modified in order to meet the requirements of the chosen initial conditions, which are discussed in Subsection 5.3.3. In particular, the osmotic part needs to be substituted with the following term:

$$
\overset{4}{\boldsymbol{\mathcal{C}}}{}^{\mathrm{S}}_{\mathrm{OSM}} \;=\; \left[\frac{J_S^2 \, R \, \Theta \, (c^{fc}_m)^2}{\sqrt{4 \, \bar{c}^{\,2}_m + (c^{fc}_m)^2} \, (J_S - n^S_{0S})} - J_S \, \Delta^*_{\pi} \right] \mathbf{I} \otimes \mathbf{I} + \; 2 \, J_S \, \Delta^*_{\pi} \, (\mathbf{I} \otimes \mathbf{I})^{\overset{23}{T}} , \tag{C.8}
$$

where the initial osmotic pressure (5.26) is always subtracted from the actual osmotic pressure (4.97), i. e., $\Delta^*_{\pi} = \Delta \pi - \Delta \pi_{0S}$.

Bibliography

[1] Acartürk, A.: *Simulation of Charged Hydrated Porous Media*. Dissertation, Bericht Nr. II-18 aus dem Institut für Mechanik (Bauwesen), Universität Stuttgart 2009.

[2] Adam, G.; Läuger, P. & Stark, G.: *Physikalische Chemie und Biophysik*. Springer-Verlag, Berlin 1995.

[3] Agur, A. M. R. & Dalley, A. F. (eds.): *Grant's Atlas of Anatomy*. Lippincott Williams & Wilkins 2004.

[4] Ammann, M.: *Parallel finite element simulations of localization phenomena in porous media*. Dissertation, Bericht Nr. II-11 aus dem Institut für Mechanik (Bauwesen), Universität Stuttgart 2005.

[5] Antoniou, J.; Steffen, T.; Nelson, F.; Winterbottom, N.; Hollander, A. P.; Poole, R. A. & Aebi, M.: The human lumbar intervertebral disc: Evidence for changes in the biosynthesis and denaturation of the extracellular matrix with growth. *Journal of Clinical Investigation* **98** (1996), 996–1003.

[6] Apel, N.: *Approaches to the description of anisotropic material behaviour at finite elastic and plastic deformations – Theory and numerics*. Dissertation, Bericht Nr. I-12 aus dem Institut für Mechanik (Bauwesen), Universität Stuttgart 2004.

[7] Argoubi, M. & Shirazi-Adl, A.: Poroelastic creep response analysis of a lumbar motion segment in compression. *Journal of Biomechanics* **29** (1996), 1331–1339.

[8] Arnold, D. N.; Brezzi, F. & Fortin, M.: A stable finite element for the stokes equations. *Calcolo* **21** (1984), 337–344.

[9] Ashton-Miller, J. A. & Schultz, A. B.: Biomechanics of the human spine. In Mow, V. C. & Hayes, W. C. (eds.): *Basic Orthopaedic Biomechanics*. Lippincott-Raven, New York 1997, pp. 353–393.

[10] Ayad, S. & Weiss, J. B.: Biochemistry of the intervertebral disc. In Jayson, M. I. V. (ed.): *The Lumbar Spine and Back Pain.* Churchill Livingstone, New York 1987, 3rd edn., pp. 100–137.

[11] Ayotte, D. C.; Ito, K.; Perren, S. M. & Tepic, S.: Direction-dependent constriction flow in a poroelastic solid: The intervertebral disc valve. *ASME Journal of Biomechanical Engineering* **122** (2000), 587–593.

[12] Bachrach, N. M.; Mow, V. C. & Guilak, F.: Incompressibility of the solid matrix of articular cartilage under high hydrostatic pressures. *Journal of Biomechanics* **31** (1998), 445–451.

[13] Ball, J. M.: Convexity conditions and existence theorems in nonlinear elasticity. *Archive for Rational Mechanics and Analysis* **63** (1977), 337–403.

[14] Balzani, D.: *Polyconvex anisotropic energies and modeling of damage applied to arterial walls*. Dissertation Bericht Nr. 2, Fachbereich Bauwissenschaften, Institut für Mechanik, Universität Duisburg-Essen 2006.

[15] Balzani, D.; Neff, P.; Schröder, J. & Holzapfel, G.: A polyconvex framework for soft biological tissues. Adjustment to experimental data. *International Journal of Solids and Structures* **43** (2006), 6052–6070.

[16] Bathe, K. J.: *Finite-Elemente-Methoden*. Springer-Verlag, Berlin 1990.

[17] Benzi, M.; Golub, G. H. & Liesen, J.: Numerical solution of saddle point problems. *Acta Numerica* **14** (2005), 1–137.

[18] Biot, M. A.: General theory of three dimensional consolidation. *Journal of Applied Physics* **12** (1941), 155–164.

[19] Bishop, A. W.: The effective stress principle. *Teknisk Ukeblad* **39** (1959), 859–863.

[20] Boehler, J. P.: On irreducible representations for isotropic scalar functions. *Zeitschrift für angewandte Mathematik und Mechanik* **57** (1977), 323–327.

[21] Boehler, J. P.: A simple derivation of representations for non-polynominal constitutive equations in some case of anisotropy. *Zeitschrift für angewandte Mathematik und Mechanik* **59** (1979), 157–167.

[22] Boehler, J. P.: Introduction of the invariant formulation of anisotropic constitutive equations. In Boehler, J. P. (ed.): *Applications of Tensor Functions in Solid Mechanics*. Springer-Verlag, Wien 1987, CISM Courses and Lectures No. 292, pp. 13–30.

[23] de Boer, R.: *Vektor und Tensorrechnung für Ingenieure*. Springer-Verlag, Berlin 1982.

[24] de Boer, R.: *Theory of Porous Media.* Springer-Verlag, Berlin 2000.

[25] de Boer, R. & Ehlers, W.: *Theorie der Mehrkomponentenkontinua mit Anwendung auf bodenmechanische Probleme*. Forschungsberichte aus dem Fachbereich Bauwesen, Heft 40, Universität-GH-Essen 1986.

[26] Bowen, R. M.: Theory of mixtures. In Eringen, A. C. (ed.): *Continuum Physics*. Academic Press, New York 1976, vol. III, pp. 1–127.

[27] Bowen, R. M.: Incompressible porous media models by use of the theory of mixtures. *International Journal of Engineering Science* **18** (1980), 1129–1148.

[28] Bowen, R. M.: Compressible porous media models by use of the theory of mixtures. *International Journal of Engineering Science* **20** (1982), 697–735.

[29] Braess, D.: *Finite Elements: Theory, Fast Solvers, and Applications in Solid Mechanics*. Cambridge University Press, Cambridge 2007, 3. edn.

[30] Brenan, K. E.; Campbell, S. L. & Petzold, L. R.: *Numerical Solution of Initial-Value Problems in Differential-Algebraic Equations*. Elsevier, New York 1989.

[31] Brezzi, F. & Fortin, M.: *Mixed and Hybrid Finite Element Methods*. Springer-Verlag, New York 1991.

[32] Broberg, K. B.: Slow deformation of intervertebral discs. *Journal of Biomechanics* **26** (1993), 501–512.

[33] Chen, Y.; Chen, X. & Hisada, T.: Non-linear finite element analysis of mechanical electrochemical phenomena in hydrated soft tissues based on triphasic theory. *International Journal for Numerical Methods in Engineering* **65** (2006), 147–173.

[34] Ciarlet, P. G.: *Mathematical Elasticity, Vol. 1: Three Dimensional Elasticity*. North-Holland, Amsterdam 1988.

[35] Coleman, B. D. & Noll, W.: The thermodynamics of elastic materials with heat conduction and viscosity. *Archive for Rational Mechanics and Analysis* **13** (1963), 167–178.

[36] Dacorogna, B.: *Direct Methods in the Calculus of Variations*. Springer-Verlag, Berlin 1989.

[37] Darcy, H.: *Les Fontaines Publiques de la Ville de Dijon*. Dalmont, Paris 1856.

[38] Diebels, S.: *Mikropolare Zweiphasenmodelle: Formulierung auf Basis der Theorie Poröser Medien*. Habilitation, Bericht Nr. II-4 aus dem Institut für Mechanik (Bauwesen), Universität Stuttgart 2000.

[39] Diebels, S. & Ehlers, W.: On the fundamental concepts of multiphase micropolar materials. *Technische Mechanik* **16** (1996), 77–88.

[40] Diebels, S.; Ellsiepen, P. & Ehlers, W.: Error-controlled Runge-Kutta time integration of a viscoplastic hybrid two-phase model. *Technische Mechanik* **19** (1999), 19–27.

[41] Donnan, F. G.: Theorie der Membrangleichgewichte und Membranpotentiale bei Vorhandensein von nicht dialysierenden Elektrolyten. Ein Beitrag zur physikalisch-chemischen Physiologie. *Zeitschrift für Elektrochemie und angewandte physikalische Chemie* **17** (1911), 572–581.

[42] Dowell, E. H. & Hall, K. C.: Modeling of fluid-structure interaction. *Annual Reviews of Fluid Mechanics* **33** (2001), 445–490.

[43] Ebara, S.; Iatridis, J. C.; Setton, L. A.; Foster, R. J.; Mow, V. C. & Weidenbaum, M.: Tensile properties of nondegenerate human lumbar anulus fibrosus. *Spine* **21** (1996), 452–461.

[44] Eberlein, R.; Holzapfel, G. A. & Fröhlich, M.: Multi-segment FEA of the human lumbar spine including the heterogeneity of the anulus fibrosus. *Computational Mechanics* **34** (2004), 147–165.

[45] Eberlein, R.; Holzapfel, G. A. & Schulze-Bauer, C. A. J.: An anisotropic model for annulus tissue and enhanced finite element analysis of intact lumbar disc bodies. *Computer Methods in Biomechanical and Biomedical Engineering* **4** (2001), 209–229.

[46] Effelsberg, J.: *Untersuchung der Diffusions- und Strömungsprozesse in der menschlichen Bandscheibe mittels Magnetresonanztomographie*. Diploma Thesis, Bericht Nr. 07-II-2 aus dem Institut für Mechanik (Bauwesen), Universität Stuttgart 2007.

[47] Ehlers, W.: *Poröse Medien – ein kontinuumsmechanisches Modell auf der Basis der Mischungstheorie*. Habilitation, Forschungsberichte aus dem Fachbereich Bauwesen, Heft 47, Universität-GH-Essen 1989.

[48] Ehlers, W.: Toward finite theories of liquid-saturated elasto-plastic Porous Media. *International Journal of Plasticity* **7** (1991), 433–475.

[49] Ehlers, W.: Constitutive equations for granular materials in geomechanical context. In Hutter, K. (ed.): *Continuum Mechanics in Environmental Sciences and Geophysics*. Springer-Verlag, Wien 1993, CISM Courses and Lectures No. 337, pp. 313–402.

[50] Ehlers, W.: *Vector and Tensor Calculus: An Introduction*. Lecture notes, Institute of Applied Mechanics (Chair of Continuum Mechanics), Universität Stuttgart 1995–2009, URL `http://www.mechbau.uni-stuttgart.de/ls2`.

[51] Ehlers, W.: Grundlegende Konzepte in der Theorie Poröser Medien. *Technische Mechanik* **16** (1996), 63–76.

[52] Ehlers, W.: Foundations of multiphasic and porous materials. In Ehlers, W. & Bluhm, J. (eds.): *Porous Media: Theory, Experiments and Numerical Applications*. Springer-Verlag, Berlin 2002, pp. 3–86.

[53] Ehlers, W. & Acartürk, A.: The role of weakly imposed Dirichlet boundary conditions for numerically stable computations of swelling phenomena. *Computational Mechanics* **43** (2009), 545–557.

[54] Ehlers, W. & Ellsiepen, P.: PANDAS: Ein FE-System zur Simulation von Sonderproblemen der Bodenmechanik. In Wriggers, P.; Meiner, U.; Stein, E. & Wunderlich, W. (eds.): *Finite Elemente in der Baupraxis - FEM '98*. Ernst & Sohn 1998, pp. 391–400.

[55] Ehlers, W. & Ellsiepen, P.: Theoretical and numerical methods in environmental continuum mechanics based on the Theory of Porous Media. In Schrefler, B. A. (ed.): *Environmental Geomechanics*. Springer-Verlag, Wien 2001, CISM Courses and Lectures No. 417, pp. 1–81.

[56] Ehlers, W.; Ellsiepen, P.; Blome, P.; Mahnkopf, D. & Markert, B.: *Theoretische und numerische Studien zur Lösung von Rand- und Anfangswertproblemen in der Theorie Poröser Medien, Abschlußbericht zum DFG-Forschungsvorhaben Eh 107/6-2*. Bericht Nr. 99-II-1 aus dem Institut für Mechanik (Bauwesen), Universität Stuttgart 1999.

[57] Ehlers, W.; Graf, T. & Ammann, M.: Deformation and localization analysis of partially saturated soil. *Computer Methods in Applied Mechanics and Engineering* **193** (2004), 2885–2910.

[58] Ehlers, W.; Karajan, N. & Markert, B.: A porous media model describing the inhomogeneous behaviour of the human intervertebral disc. *Materials Science and Engineering Technology* **37** (2006), 546–551.

[59] Ehlers, W.; Karajan, N. & Markert, B.: An extended biphasic model for charged hydrated tissues with application to the intervertebral disc. *Biomechanics and Modeling in Mechanobiology* **8** (2009), 233–251.

[60] Ehlers, W.; Karajan, N. & Wieners, C.: Parallel 3-d simulation of a biphasic porous media model in spine mechanics. In Ehlers, W. & Karajan, N. (eds.): *Proceedings of the 2nd GAMM Seminar on Continuum Biomechanics*. Bericht Nr. II-16 aus dem Institut für Mechanik (Bauwesen), Universität Stuttgart 2007, pp. 11–20.

[61] Ehlers, W. & Markert, B.: Intrinsic viscoelasticity of porous materials. In Sändig, A. M.; Schiehlen, W. & Wendland, W. L. (eds.): *Multifield Problems – State of the Art*. Springer-Verlag, Berlin 2000, pp. 143–150.

[62] Ehlers, W. & Markert, B.: On the viscoelastic behaviour of fluid-saturated porous materials. *Granular Matter* **2** (2000), 153–161.

[63] Ehlers, W. & Markert, B.: A linear viscoelastic biphasic model for soft tissues based on the Theory of Porous Media. *ASME Journal of Biomechanical Engineering* **123** (2001), 418–424.

[64] Ehlers, W.; Markert, B. & Acartürk, A.: Large strain viscoelastic swelling of charged hydrated porous media. In Auriault, J.-L.; Geindreau, C.; Royer, P.; Bloch, J. F.; Boutin, C. & Lewandowska, J. (eds.): *Poromechanics II, Proceedings of the 2nd Biot Conference on Poromechanics*. Swets & Zeitlinger, Lisse 2002, pp. 185–191.

[65] Ehlers, W.; Markert, B. & Acartürk, A.: Swelling phenomena of hydrated porous materials. In Abousleiman, Y. N.; Cheng, A. H.-D. & Ulm, F.-J. (eds.): *Poromechanics III, Proceedings of the 3rd Biot Conference on Poromechanics*. Balkema at Taylor & Francis, Leiden 2005, pp. 781–786.

[66] Ehlers, W.; Markert, B. & Karajan, N.: A coupled FE analysis of the intervertebral disc based on a multiphasic TPM formulation. In Holzapfel, G. A. & Ogden, R. W. (eds.): *Mechanics of Biological Tissue*. Springer-Verlag, Berlin 2006, pp. 373–386.

[67] Eipper, G.: *Theorie und Numerik finiter elastischer Deformationen in fluidgesättigten Porösen Medien*. Dissertation, Bericht Nr. II-1 aus dem Institut für Mechanik (Bauwesen), Universität Stuttgart 1998.

[68] El-Bohy, A. A.; Yang, K.-H. & King, A. I.: Experimental verification of facet load transmission by direct measurement of facet lamina contact pressure. *Journal of Biomechanics* **22** (1989), 931–941.

[69] Elliott, D. A. & Setton, L. A.: A linear material model for fiber-induced anisotropy of the anulus fibrosus. *ASME Journal of Biomechanical Engineering* **122** (2000), 173–179.

[70] Ellsiepen, P.: *Zeit- und ortsadaptive Verfahren angewandt auf Mehrphasenprobleme pröser Medien*. Dissertation Bericht Nr. II-3 aus dem Institut für Mechanik (Bauwesen), Universität Stuttgart 1999.

[71] Ellsiepen, P. & Hartmann, S.: Remarks on the interpretation of current non-linear finite element analyses as differential-algebraic equations. *International Journal for Numerical Methods in Engineering* **51** (2001), 679–707.

[72] European Foundation for the Improvement of Living and Working Conditions: Managing musculoskeletal disorders. Dublin (2007), URL `http://www.eurofound.europa.eu/ewco/studies/tn0611018s`.

[73] Eyre, D. R.: Biochemistry of the intervertebral disc. *Connective Tissue Research* **8** (1979), 227–291.

[74] Eyre, D. R. & Muir, H.: Types I and II collagens in intervertebral discs: Interchanging radial distribution in annulus fibrosus. *Biochemical Journal* **157** (1976), 267–270.

[75] Eyre, D. R. & Muir, H.: Quantitative analysis of types I and II collagens in human intervertebral discs at various ages. *Biochimica et Biophysica Acta* **492** (1977), 29–42.

[76] Frijns, A. J. H.; Huyghe, J. M. & Janssen, J. D.: A validation of the quadriphasic mixture theory for intervertebral disc tissue. *International Journal of Engineering Science* **35** (1997), 1419–1429.

[77] Frijns, A. J. H.; Huyghe, J. M.; Kaasschieter, E. F. & Wijlaars, M. W.: Numerical simulation of deformations and electrical potentials in a cartilage substitute. *Biorheology* **40** (2003), 123–131.

[78] Frymoyer, J. W. & Cats-Baril, W. L.: An overview of the incidences and costs of low back pain. *Orthopedic Clinics of North America* **22** (1991), 263–271.

[79] Fung, Y. C.: *Biomechanics: Mechanical Properties of Living Tissues*. Springer-Verlag, New-York 1981.

[80] Godfrey, M. D. & Hendry, D. F.: The computer as von Neumann planned it. *IEEE Annals of the History of Computing* **15** (1993), 11–21.

[81] Grace, J. H. & Young, A.: *The Algebra of Invariants*. Cambridge University Press, Cambridge 1903.

[82] Gray, H.: *Anatomy of the Human Body*. Lea & Febiger, Philadelphia 1918.

[83] Gu, W. Y.; Mao, X. G.; Foster, R. J.; Weidenbaum, M.; Mow, V. C. & Rawlins, B.: The anisotropic hydraulic permeability of human lumbar anulus fibrosus. *Spine* **24** (1999), 2449–2455.

[84] Gurevich, G. B.: *Foundations of the Theory of Algebraic Invariants*. P. Noordhoff, Groningen 1964.

[85] Gurtin, M. E. & Williams, W. O.: On the inclusion of the complete symmetry group in the unimodular group. *Archive for Rational Mechanics and Analysis* **23** (1966), 163–172.

[86] Hairer, E.; Nørsett, S. P. & Wanner, G.: *Solving Ordinary Differential Equations I – Nonstiff Problems*. Springer-Verlag, Berlin 1993, 2 edn.

[87] Hairer, E. & Wanner, G.: *Solving Ordinary Differential Equations II – Stiff and Differential-Algebraic Problems*. Springer-Verlag, Berlin 1991.

[88] Hansbo, P. & Hermansson, J.: Nitsche's method for coupling non-matching meshes in fluid-structure vibration problems. *Computational Mechanics* **32** (2003), 134–139.

[89] Hassanizadeh, S. M. & Gray, W. G.: General conservation equations for multi-phase systems: 1. averaging procedure. *Advances in Water Resources* **2** (1979), 131–144.

[90] Hassanizadeh, S. M. & Gray, W. G.: High velocity flow in porous media. *Transport in Porous Media* **2** (1987), 521–531.

[91] Haupt, P.: Foundations of continuum mechanics. In Hutter, K. (ed.): *Continuum Mechanics in Environmental Sciences and Geophysics*. Springer-Verlag, Wien 1993, CISM Courses and Lectures No. 337, pp. 1–77.

[92] Hayes, W. C. & Bodine, A. J.: Flow-independent viscoelastic properties of articular cartilage matrix. *Journal of Biomechanics* **11** (1978), 407–419.

[93] Holm, S. & Nachemson, A.: Variations in the nutrition of the canine intervertebral disc induced by motion. *Spine* **8** (1983), 866–974.

[94] Holzapfel, G.; Gasser, T. C. & Ogden, R. W.: A new constitutive framework for arterial wall mechanics and a comparative study of material models. *Journal of Elasticity* **61** (2000), 1–48.

[95] Holzapfel, G. A. & Gasser, T. C.: A viscoelastic model for fiber-reinforced composites at finite strains: Continuum basis, computational aspects and applications. *Computer Methods in Applied Mechanics and Engineering* **190** (2001), 4379–4403.

[96] Holzapfel, G. A.; Schulze-Bauer, C. A. J.; Feigl, G. & Regitnig, P.: Mono-lamellar mechanics of the human lumbar anulus fibrosus. *Biomechanics and Modeling in Mechanobiology* **3** (2005), 125–140.

[97] Hsieh, A. H.; Wagner, D. R.; Cheng, L. Y. & Lotz, J. C.: Dependence of mechanical behavior of the murine tail disc on regional material properties: A parametric finite element study. *Journal of Biomechanical Engineering* **127** (2005), 1158–1167.

[98] Hukins, D. W. L.: Properties of spinal materials. In Jayson, M. I. V. (ed.): *The Lumbar Spine and Back Pain.* Churchill Livingstone, New York 1987, 3rd edn., pp. 138–160.

[99] Huyghe, J. M.; Houben, G. B. & Drost, M. R.: An ionised/non-ionised dual porosity model of intervertebral disc tissue. *Biomechanics and Modeling in Mechanobiology* **2** (2003), 3–19.

[100] Iatridis, J. C.; Laible, J. P. & Krag, M. H.: Influence of fixed charge density magnitude and distribution on the intervertebral disc: Applications of a Poroelastic and Chemical Electric (PEACE) model. *Journal of Biomechanical Engineering* **125** (2003), 12–24.

[101] Iatridis, J. C.; a. Setton, L.; Weidenbaum, M. & Mow, V. C.: The viscoelastic behavior of the non-degenerate human lumbar nucleus pulposus in shear. *Journal of Biomechanics* **30** (1997), 1005–1013.

[102] Iatridis, J. C.; Setton, L. A.; Foster, R. J.; Rawlins, B. A.; Weidenbaum, M. & Mow, V. C.: Degeneration affects the anisotropic and nonlinear behaviors of human anulus fibrosus in compression. *Journal of Biomechanics* **31** (1998), 535–544.

[103] Iatridis, J. C.; Weidenbaum, M.; Setton, L. A. & Mow, V. C.: Is the nucleus pulposus a solid or a fluid? Mechanical behaviors of the human intervertebral disc. *Spine* **21** (1996), 1174–1184.

[104] Itskov, M. & Aksel, N.: A class of orthotropic and transversely isotropic hyperelastic constitutive models based on a polyconvex strain energy function. *International Journal of Solids and Structures* **41** (2004), 3833–3848.

[105] Jayson, M. I. V. (ed.): *The Lumbar Spine and Back Pain.* Churchill Livingstone, New York 1987, 3rd edn.

[106] Kaasschieter, E. F.; Frijns, A. J. H. & Huyghe, J. M.: Mixed finite element modelling of cartilaginous tissues. *Mathematics and Computers in Simulation* **61** (2003), 549–560.

[107] Karajan, N. & Ehlers, W.: Discussion on Appropriate Material Parameters for the IVD. *Proceedings in Applied Mathematics and Mechanics* **7** (2007), 4020003–4020004.

[108] Klawonn, A. & Pavarino, L. F.: Overlapping Schwarz methods for mixed linear elasticity and Stokes problems. *Computer Methods in Applied Mechanics and Engineering* **165** (1998), 233–245.

[109] Klawonn, A. & Pavarino, L. F.: A comparison of overlapping Schwarz methods and block preconditioners for saddle point problems. *Numerical Linear Algebra with Applications* **7** (2000), 1–25.

[110] Kleiber, M.: Kinematics of deformation processes in materials subjected to finite elastic-plastic strains. *International Journal of Engineering Science* **13** (1975), 513–525.

[111] Klisch, S. M. & Lotz, J. C.: Application of a fiber-reinforced continuum theory to multiple deformations of the annulus fibrosus. *Journal of Biomechanics* **32** (1999), 1027–1036.

[112] Klisch, S. M. & Lotz, J. C.: A special theory of biphasic mixtures and experimental results for human annulus fibrosus tested in confined compression. *ASME Journal of Biomechanical Engineering* **122** (2000), 180–188.

[113] Lai, W. M.; Hou, J. S. & Mow, V. C.: A triphasic theory for the swelling and deformation behaviours of articular cartilage. *ASME Journal of Biomechanical Engineering* **113** (1991), 245–258.

[114] Laible, J. P.; Pflaster, D. S.; Krag, M. H.; Simon, B. R. & Haugh, L. D.: A poroelastic-swelling finite element model with application to the intervertebral disc. *Spine* **18** (1993), 659–670.

[115] Lambrecht, M.: *Theorie und Numerik von Materialinstabilitäten elastoplastischer Festkörper auf der Grundlage inkrementeller Variationsformulierungen*. Dissertation, Bericht Nr. I-8 aus dem Institut für Mechanik (Bauwesen), Universität Stuttgart 2002.

[116] Lanir, Y.: Biorheology and fluid flux in swelling tissues I. Bicomponent theory for small deformations, including concentration effects. *Biorheology* **24** (1987), 173–187.

[117] Latza, U.; Kohlmann, T.; Deck, R. & Raspe, H.: Influence of occupational factors on the relation between socioeconomic status and self-reported back pain in a population-based sample of German adults with back pain. *Spine* **25** (2000), 1390–1397.

[118] Lee, C.-K.; Kim, Y. E.; Lee, C.-S.; Hong, Y.-M.; Jung, J.-M. & Goel, V. K.: Impact response of the intervertebral disc in a finite-element model. *Spine* **25** (2000), 2431–2439.

[119] Lee, E. H.: Elastic-plastic deformation at finite strains. *Journal of Applied Mechanics* **36** (1969), 1–6.

[120] Li, L. P.; Shirazi-Adl, A. & Buschmann, M. D.: Investigation of mechanical behavior of articular cartilage by fibril reinforced poroelastic models. *Biorheology* **40** (2003), 227–233.

[121] Li, L. P.; Soulhat, J.; Buschmann, M. D. & Shirazi-Adl, A.: Nonlinear analysis of cartilage in unconfined ramp compression using a fibril reinforced poroelastic model. *Clinical Biomechanics* **14** (1999), 673–682.

[122] Lide, D. R.: *CRC Handbook of Chemistry and Physics*. CRC Press, Boca Raton 2003.

[123] Lim, T.-H. & Hong, J. H.: Poroelastic properties of bovine vertebral trabecular bone. *Journal of Orthopaedic Research* **18** (2000), 671–677.

[124] Lis, A. M.; Black, K. M.; Korn, H. & Nordin, M.: Association between sitting and occupational LBP. *European Spine Journal* **16** (2007), 283–298.

[125] Liu, I.-S.: Method of Lagrange multipliers for exploitation of the entropy principle. *Archive for Rational Mechanics and Analysis* **46** (1972), 131–148.

[126] Liu, I.-S. & Müller, I.: Thermodynamics of mixtures of fluids. In Truesdell, C. (ed.): *Rational Thermodynamics*. Springer-Verlag, New York 1984, 2nd edn., pp. 264–285.

[127] van Loon, R.; Huyghe, F. M.; Wijlaars, M. W. & Baaijens, F. P. T.: 3D FE implementation of an incompressible quadriphasic mixture model. *International Journal for Numerical Methods in Engineering* **57** (2003), 1243–1258.

[128] Ludescher, B.; Effelsberger, J.; Martirosian, P.; Steidle, G.; Markert, B.; Claussen, C. & Schick, F.: T2- and diffusion-maps reveal diurnal changes of intervertebral disc composition: An in vivo MRI study at 1.5 Tesla. *Journal of Magnetic Resonance Imaging* **28** (2008), 252–257.

[129] Mahnkopf, D.: *Lokalisierung fluidgesättigter poröser Festkörper bei finiten elastoplastischen Deformationen*. Dissertation, Bericht Nr. II-5 aus dem Institut für Mechanik (Bauwesen), Universität Stuttgart 2000.

[130] Marchand, F. & Ahmed, A. M.: Investigation of the laminate structure of the lumbar disc anulus. *Spine* **15** (1990), 402–410.

[131] Markert, B.: *Porous media viscoelasticity with application to polymeric foams*. Dissertation, Bericht Nr. II-12 aus dem Institut für Mechanik (Bauwesen), Universität Stuttgart 2005.

[132] Markert, B.: A constitutive approach to 3-d nonlinear fluid flow through finite deformable porous continua with application to a high-porosity polyurethane foam. *Transport in Porous Media* **70** (2007), 427–450.

[133] Markert, B.: A biphasic continuum approach for viscoelastic high-porosity foams: Comprehensive theory, numerics, and application. *Archives of Computational Methods in Engineering* **15** (2008), 371–446.

[134] Markert, B.; Ehlers, W. & Karajan, N.: A general polyconvex strain-energy function for fiber-reinforced materials. *Proceedings in Applied Mathematics and Mechanics* **5** (2005), 245–246.

[135] Marsden, J. E. & Hughes, T. J. R.: *Mathematical Foundations of Elasticity*. Dover Publications 1994, reprint of Prentice-Hall 1983.

[136] Mayer, J.: A multilevel crout ILU preconditioner with pivoting and row permutation. *Numerical Linear Algebra with Applications* **14** (2007), 771–789.

[137] Mayer, J.: Symmetric permutations for I-matrices to delay and avoid small pivots during factorization. *SIAM Journal on Scientific Computing* **30** (2008), 982–996.

[138] Miller, J. A. A.; Haderspeck, K. A. & Schultz, A. B.: Posterior element loads in lumbar motion segments. *Spine* **8** (1983), 331–337.

[139] Mills, N.: Incompressible mixture of Newtonian fluids. *International Journal of Engineering Science* **4** (1966), 97–112.

[140] Mohr, P. J.; Taylor, B. N. & Newell, D. B. (eds.): *CODATA Recommended Values of the Fundamental Physical Constants: 2006*. National Institute of Standards and Technology, Gaithersburg 2007.

[141] Mooney, M.: A theory of large elastic deformation. *Journal of Applied Physics* **11** (1940), 582–592.

[142] Morrey, C. B.: Quasi-convexity and the lower semicontinuity of multiple integrals. *Pacific Journal of Mathematics* **2** (1952), 25–53.

[143] Mow, V. C.; Ateshian, G. A.; Lai, W. M. & Gu, W. Y.: Effects of fixed charges on the stress-relaxation behavior of hydrated soft tissues in a confined compression problem. *International Journal of Solids and Structures* **35** (1998), 4945–4962.

[144] Mow, V. C.; Gibbs, M. C.; Lai, W. M.; Zhu, W. B. & Athanasiou, K. A.: Biphasic indentation of articular cartilage - II. A numerical algorithm and an experimental study. *Journal of Biomechanics* **22** (1989), 853–861.

[145] Mow, V. C. & Hayes, W. C.: *Basic Orthopaedic Biomechanics*. Lippincott-Raven, New York 1997.

[146] Mow, V. C.; Kuei, S. C.; Lai, W. M. & Armstrong, C. G.: Biphasic creep and stress relaxation of articular cartilage in compression: Theory and experiments. *ASME Journal of Biomechanical Engineering* **102** (1980), 73–84.

[147] Mow, V. C. & Ratcliffe, A.: Structure and function of articular cartilage and meniscus. In Mow, V. C. & Hayes, W. C. (eds.): *Basic Orthopaedic Biomechanics*. Lippincott-Raven, New York 1997, pp. 113–177.

[148] Nachemson, A. L.: Disc pressure measurements. *Spine* **8** (1981), 93–97.

[149] Nachemson, A. L.: Lumbar intradiscal pressure. In Jayson, M. I. V. (ed.): *The Lumbar Spine and Back Pain*. Churchill Livingstone, New York 1987, 3rd edn., pp. 191–203.

[150] Naylor, A.: The biophysical and biochemical aspects of intervertebral disc herniation and degeneration. *Annals of the Royal College of Surgeons of England* **31** (1962), 91–114.

[151] Netter, F. H.: *Atlas of Human Anatomy*. Saunders–Elsevier, Amsterdam 2006.

[152] Noll, W.: On the continuity of the fluid and solid states. *Journal of Rational Mechanics and Analysis* **4** (1955), 3–81.

[153] Noll, W.: A mathematical theory of the mechanical behavior of continous media. *Archive for Rational Mechanics and Analysis* **2** (1958), 197–226.

[154] Ochia, R. S. & Ching, R. P.: Hydraulic resistance and permeability in human lumbar vertebral bodies. *Journal of Biomechanical Engineering* **124** (2002), 533–537.

[155] Ogden, R. W.: Large deformation isotropic elasticity – On the correlation of theory and experiment for compressible rubberlike solids. In *Proceedings of the Royal Society of London, Series A*. 1972, vol. 328, pp. 323–338.

[156] Ogden, R. W.: Large deformation isotropic elasticity – On the correlation of theory and experiment for incompressible rubberlike solids. In *Proceedings of the Royal Society of London, Series A*. 1972, vol. 326, pp. 565–584.

[157] Ogden, R. W.: *Nonlinear Elastic Deformations*. Ellis Harwood, Chichester 1984.

[158] PANDAS: A coupled FEM solver. URL `http://www.get-pandas.com`.

[159] Paoli, P.: *Second European survey on working conditions*. Report of the European Foundation for the Improvement of Living and Working Conditions, Dublin 1997, URL `http://www.eurofound.europa.eu/publications/-htmlfiles/ef9726.htm`.

[160] Papastavridis, J. G.: *Tensor Calculus and Analytical Dynamics*. CRC Press LLC 1999.

[161] Parent-Thirion, A.; Macías, E. F.; Hurley, J. & Vermeylen, G.: *Fourth European Working Conditions Survey*. Report of the European Foundation for the Improvement of Living and Working Conditions, Dublin 2007, URL `http://www.eurofound.europa.eu/publications/htmlfiles/ef0698.htm`.

[162] Pearcy, M.; Portek, I. F. & Shepherd, J.: Three-dimensional X-ray analysis of normal movement in the lumbar spine. *Spine* **9** (1984), 294–297.

[163] Pearcy, M. & Tibrewal, S. B.: Axial rotation and lateral bending in the normal lumbar spine measured by three-dimensional radiography. *Spine* **9** (1984), 582–587.

[164] Powell, M. J. D.: A direct search optimization method that models the objective and constraint functions by linear interpolation. In Gomez, S. & Hennart, J. P. (eds.): *Advances in Optimization and Numerical Analysis*. Kluwer Academic Publishers 1994, pp. 51–67.

[165] Press, W. H.; Teukolsky, S. A.; Vetterling, W. T. & Flannery, B. P.: *Numerical Recipes: The Art of Scientific Computing*. Cambridge University Press, Cambridge 2007, 3rd edn.

[166] Raspe, H.; Hueppe, A. & Neuhauser, H.: Back pain, a communicable disease? *International Journal of Epidemiology* **37** (2008), 69–74.

[167] Reese, S. & Govindjee, S.: A theory of finite viscoelasticity and numerical aspects. *International Journal of Solids and Structures* **35** (1998), 3455–3482.

[168] Riches, P. E.; Dhillon, N.; Lotz, J.; Woods, A. W. & McNally, D. S.: The internal mechanics of the intervertebral disc under cyclic loading. *Journal of Biomechanics* **35** (2002), 1263–1271.

[169] Rivlin, R. S.: Large elastic deformations of isotropic materials. *Proceedings of the Royal Society of London Series A* **241** (1948), 379–397.

[170] Rivlin, R. S. & Ericksen, J. L.: Stress-deformation relations for isotropic materials. *Journal of Rational Mechanics and Analysis* **4** (1955), 323–425.

[171] Saad, Y. & Schultz, M. H.: GMRES: A generalized minimal residual algorithm for solving nonsymmetric linear systems. *SIAM Journal on Scientific and Statistical Computing* **7** (1986), 856–869.

[172] Sandhu, R. S. & Wilson, E. L.: Finite-element analysis of seepage in elastic media. *ASCE Journal of the Engineering Mechanics Division* **95** (1969), 641–652.

[173] Schenke, M.: *Development of an interface between ABAQUS and PANDAS*. Master Thesis, Bericht Nr. 08-II-12 aus dem Institut für Mechanik (Bauwesen), Universität Stuttgart 2008.

[174] Schmidt, C. O.; Raspe, H.; Pfingsten, M.; Hasenbring, M.; Basler, H. D.; Eich, W. & Kohlmann, T.: Back pain in the german adult population. Prevalence, severity, and sociodemographic correlations in a multiregional survey. *Spine* **32** (2007), 2005–2011.

[175] Schmidt, H.; Heuer, F.; Drumm, J.; Klezl, Z.; Claes, L. & Wilke, H.-J.: Application of a calibration method provides more realistic results for a finite element model of a lumbar spinal segment. *Clinical Biomechanics* **22** (2007), 377–384.

[176] Schmidt, H.; Heuer, F.; Simon, U.; Kettler, A.; Rohlmann, A.; Claes, L. & Wilke, H.-J.: Application of a new calibration method for a three-dimensional finite element model of a human lumbar annulus fibrosus. *Clinical Biomechanics* **21** (2006), 337–344.

[177] Schröder, J.: *Theoretische und algorithmische Konzepte zur phänomenologischen Beschreibung anisotropen Materialverhaltens*. Dissertation, Bericht Nr. I-1 aus dem Institut für Mechanik (Bauwesen), Universität Stuttgart 1996.

[178] Schröder, J.: *Homogenisierungsmethoden der nichtlinearen Kontinuumsmechanik unter Beachtung von Stabilitätsproblemen*. Habilitation, Bericht Nr. I-7 aus dem Institut für Mechanik (Bauwesen), Universität Stuttgart 2000.

[179] Schröder, J. & Neff, P.: Invariant formulation of hyperelastic transverse isotropy based on polyconvex free energy functions. *International Journal of Solids and Structures* **40** (2003), 401–445.

[180] Schröder, Y.; Sivan, S.; Wilson, W.; Merkher, Y.; Huyghe, J. M.; Maroudas, A. & Baaijens, F. P. T.: Are disc pressure, stress and osmolarity affected by intra- and extrafibrillar fluid exchange? *Journal of Orthopaedic Research* **25** (2007), 1317–1324.

[181] Schwarz, H. R.: *Methode der finiten Elemente*. Teubner, Stuttgart 1991.

[182] Shirazi-Adl, A.: Nonlinear stress analysis of the whole lumbar spine in torsion-mechanics of facet articulation. *Journal of Biomechanics* **27** (1994), 289–299.

[183] Shirazi-Adl, A.: Analysis of large compression loads on lumbar spine in felxion and torsion using a novel wrapping element. *Journal of Biomechanics* **39** (2006), 267–275.

[184] Shirazi-Adl, A.; Ahmed, A. M. & Shrivastava, S. C.: A finite element study of a lumbar motion segment subjected to pure sagittal plane moments. *Journal of Biomechanics* **19** (1986), 331–350.

[185] Shirazi-Adl, A.; Ahmed, A. M. & Shrivastava, S. C.: Mechanical response of a lumbar motion segment in axial torque alone and combined with compression. *Spine* **11** (1986), 914–927.

[186] Šilhavý, M.: *The Mechanics and Thermodynamics of Continuous Media*. Springer-Verlag, Berlin 1997.

[187] Simo, J. C. & Taylor, R. L.: Consistent tangent operators for rate-independent elastoplasticity. *Computer Methods in Applied Mechanics and Engineering* **48** (1985), 101–118.

[188] Skaggs, D. L.; Weidenbaum, M.; Iatridis, J. C.; Ratcliffe, A. & Mow, V. C.: Regional variation in tensile properties and biochemical composition of the human lumbar anulus fibrosus. *Spine* **19** (1994), 1310–1319.

[189] Skempton, A. W.: Significance of Terzaghi's concept of effective stress (Terzaghi's discovery of effective stress). In Bjerrum, L.; Casagrande, A.; Peck, R. B. & Skempton, A. W. (eds.): *From Theory to Practice in Soil Mechanics*. Wiley, New York 1960, pp. 42–53.

[190] Smith, G. F.: On isotropic functions of symmetric tensors, skew-symmetric tensors and vectors. *International Journal of Engineering Science* **9** (1971), 899–916.

[191] Snijders, H.; Huyghe, J. M. & Janssen, J. D.: Triphasic finite element model for swelling porous media. *International Journal for Numerical Methods in Fluids* **20** (1995), 1039–1046.

[192] Spencer, A. J. M.: Theory of Invariants. In Eringen, A. C. (ed.): *Continuum Physics, Vol. 1*. Academic Press, New York 1971, pp. 239–353.

[193] Spencer, A. J. M.: *Deformations of Fiber-Reinforced Materials*. Oxford University Press 1972.

[194] Spencer, A. J. M.: The formulation of constitutive equations for anisotropic solids. In Boehler, J. P. (ed.): *Mechanical Behavior of Anisotropic Solids*. Martinus Nijhoff Publishers, The Haque 1982, Proceedings of the Euromech Colloquium 115, pp. 2–26.

[195] Spencer, A. J. M.: Constitutive theory for strongly anisotropic solids. In Spencer, A. J. M. (ed.): *Continuum Theory of the Mechanics of Fibre Reinforced Composites*. Springer-Verlag, Wien 1984, CISM Courses and Lectures No. 282, pp. 1–32.

[196] Spencer, A. J. M.: Isotropic polynominal invariants and tensor functions. In Boehler, J. P. (ed.): *Applications of Tensor Functions in Solid Mechanics*. Springer-Verlag, Wien 1987, CISM Courses and Lectures No. 292, pp. 141–169.

[197] Spencer, A. J. M. & Rivlin, R. S.: Isotropic integrity bases for vectors and second-order tensors. *Archive for Rational Mechanics and Analysis* **9** (1962), 45–63.

[198] Spitzer, V.; Ackerman, M. J.; Scherzinger, A. L. & Whitlock, D.: The visible human male: A technical report. *Journal of the American Medical Informatics Association* **3** (1996), 118–130.

[199] Sten-Knudsen, O.: *Biological Membranes: Theory of Transport, Potentials and Electric Impulses*. Cambridge University Press, Cambridge 2002.

[200] Svendson, B. & Hutter, K.: On the thermodynamics of a mixture of isotropic materials with constraints. *International Journal of Engineering Science* **33** (1995), 2021–2054.

[201] Szirmai, J. A.: Structure of the intervertebral disc. In Balazs, E. A. (ed.): *Chemistry and Molecular Biology of the Intercellular Matrix*. Academic Press, London 1970, vol. 3, pp. 1279–1308.

[202] Taylor, C. & Hood, P.: A numerical solution of the Navier-Stokes equations using the finite element technique. *Computers and Fluids* **1** (1973), 73–100.

[203] Tezduyar, T. E.: Finite element methods for flow problems with moving boundaries and interfaces. *Archives of Computational Methods in Engineering* **8** (2001), 83–130.

[204] Treloar, L. R. G.: *The Physics of Rubber Elasticity*. Clarendon Press, Oxford 1975, 3rd edn.

[205] Truesdell, C.: *A new Definition of a Fluid, II. The Maxwellian fluid*. Tech. Rep. P-3553, § 19, US Naval Research Laboratory 1949.

[206] Truesdell, C.: Thermodynamics of diffusion. In Truesdell, C. (ed.): *Rational Thermodynamics*. Springer-Verlag, New-York 1984, 2nd edn., pp. 219–236.

[207] Truesdell, C. & Noll, W.: *The Nonlinear Field Theories of Mechanics*. Band III/3., Springer-Verlag, Berlin 1965.

[208] Truesdell, C. & Toupin, R. A.: The classical field theories. In Flügge, S. (ed.): *Handbuch der Physik*. Springer-Verlag, Berlin 1960, Band III/1.

[209] Tsuji, H.; Hirano, N.; Ohshima, H.; Ishihara, H.; Terahata, N. & Motoe, T.: Structural variation of the anterior and posterior anulus fibrosus in the development of human lumbar intervertebral disc. A risk factor for intervertebral disc rupture. *Spine* **18** (1993), 204–210.

[210] Tyrrell, A. R.; Reilly, T. & Troup, J. D. G.: Circadian variation in stature and the effects of spinal loading. *Spine* **10** (1985), 161–164.

[211] Urban, J. P. G. & Holm, S.: Intervertebral disc nutrition as related to spinal movements and fusion. In Hargens, A. R. (ed.): *Tissue Nutrition and Viability*. Springer-Verlag, Berlin 1986, pp. 101–119.

[212] Urban, J. P. G.; Holm, S.; Maroudas, A. & Nachemson, A.: Nutrition of the intervertebral disc: Effect of fluid flow on solute transport. *Clinical Orthopaedics* **170** (1982), 296–302.

[213] Urban, J. P. G. & Maroudas, A.: The measurement of fixed charged density in the intervertebral disc. *Biochimica et Biophysica Acta* **586** (1979), 166–178.

[214] Urban, J. P. G. & Roberts, S.: Intervertebral disc. In Comper, W. D. (ed.): *Extracellular Matrix, Volume 1: Tissue Function*. Harwood Academic Publishers, Amsterdam 1996, pp. 203–233.

[215] Vanharanta, H.; Guyer, R. D.; Ohnmeiss, D. D.; Stith, W. J.; Sachs, B. L.; Aprill, C.; Spivey, M.; Rashbaum, R. F.; Hochschuler, S. H.; Videman, T.; Selby, D. K.; Terry, A. & Mooney, V.: Disc deterioration in low-back syndromes. A prospective, multi-center CT/discography study. *Spine* **13** (1988), 1349–1351.

[216] Varga, O. H.: *Stress-Strain Behavior of Elastic Materials*. Interscience, New York 1966.

[217] Visible Human Server: Computer Science Department, *École Polytechnique Fédérale de Lausanne*. URL `http://visiblehuman.epfl.ch/`.

[218] von Neuman, J.: *First Draft of a Report on the EDVAC*. Moore School of Electrical Engineering, University of Pennsylvania 1945.

[219] Walker, D. W. & Dongarra, J. J.: MPI: A standard message passing interface. *Super Computer* **12** (1996), 56–68.

[220] Wall, W. A.: *Fluid-Struktur-Interaktion mit stabilisierten Finiten Elementen*. Dissertation, Bericht Nr. 31 aus dem Institut für Baustatik, Universität Stuttgart 1999.

[221] Wang, C. C.: On representations for isotropic functions, part I and II. *Archive for Rational Mechanics and Analysis* **33** (1969), 249–287.

[222] Wang, C. C.: A new representation theorem for isotropic functions: An answer to Professor G. F. Smith's criticism of my papers on representations for isotropic functions, part I and II. *Archive for Rational Mechanics and Analysis* **36** (1970), 166–223.

[223] Wang, C.-C. & Truesdell, C.: *Introduction to Rational Elasticity*. Noordhoff International Publishing, Leyden 1973.

[224] Weyl, H.: *The Classical Groups, Their Invariants and Representation*. Princeton University Press, Princeton, New Jersey 1946.

[225] White, A. A. & Panjabi, M. M.: *Clinical Biomechanics of the Spine*. Lippincott Williams, Philadelphia 1990, 2nd edn.

[226] Wieners, C.: M++. URL `http://www.mathematik.uni-karlsruhe.de/~wieners`.

[227] Wieners, C.: Taylor-Hood elements in 3D. In Wendland, W. L. & Efendiev, M. (eds.): *Analysis and Simulation of Multifield Problems*. Springer-Verlag, Berlin 2003, pp. 189–196.

[228] Wieners, C.: Distributed Point Objects. A new concept for parallel finite elements. In Kornhuber, R.; Hoppe, R.; Périaux, J.; Pironneau, O.; Widlund, O. & Xu, J. (eds.): *Domain Decomposition Methods in Science and Engineering*. Springer-Verlag 2004, Lecture Notes in Computational Science and Engineering 40, pp. 175–183.

[229] Wieners, C.; Ammann, M. & Ehlers, W.: Distributed Point Objects: A new concept for parallel finite elements applied to a geomechanical problem. *Future Generation Computer Systems* **22** (2006), 532–545.

[230] Wieners, C.; Ammann, M.; Ehlers, W. & Graf, T.: Parallel Krylov methods and the application to 3-d simulations of a tri-phasic porous media model in soil mechanics. *Computational Mechanics* **36** (2005), 409–420.

[231] Wieners, C.; Ehlers, W.; Ammann, M.; Karajan, N. & Markert, B.: Parallel solution methods for porous media models in biomechanics. *Proceedings in Applied Mathematics and Mechanics* **5** (2005), 35–38.

[232] Wilke, H.-J. & Claes, L. E. (eds.): *Die traumatische und degenerative Bandscheibe.* Hefte zur Zeitschirft „Der Unfallchirurg“ 271, Springer-Verlag, Berlin 1999.

[233] Wilke, H.-J.; Neef, P.; Caimi, M.; Hoogland, T. & Claes, L. E.: New in vivo measurements of pressures in the intervertebral disc in daily life. *Spine* **24** (1999), 755–762.

[234] Wilson, W.; van Donkelar, C. C. & Huyghe, J. M.: A comparison between mechano-electrochemical and biphasic swelling theories for soft hydrated tissues. *ASME Journal of Biomechanical Engineering* **127** (2005), 158–165.

[235] Wriggers, P.: *Konsistente Linearisierung in der Kontinuumsmechanik und ihre Anwendung auf die Finite-Elemente-Methode.* Habilitation, Technischer Bericht F 88/4, Forschungs und Seminarberichte aus dem Bereich der Mechanik der Universität Hannover 1988.

[236] Wu, J. S. S. & Chen, J. H.: Clarification of the mechanical behavior of spinal motion segments through a three-dimensional poroelastic mixed finite element model. *Medical Engineering and Physics* **18** (1996), 215–224.

[237] Zheng, Q.-S.: Theory of representations for tensor functions – A unified invariant approach to constitutive equations. *Applied Mechanics Reviews* **47** (1994), 545–587.

[238] Zheng, Q.-S. & Boehler, J. P.: The description, classification, and reality of material and physical symmetries. *Acta Mechanica* **102** (1994), 73–89.

[239] Zheng, Q.-S. & Spencer, A. J. M.: Tensors which characterize anisotropies. *International Journal of Engineering Science* **31** (1993), 679–693.

[240] Zienkiewicz, O. C. & Taylor, R. L.: *The Finite Element Method for Solid and Structural Mechanics, Vol. 2.* Butterworth-Heinemann, Oxford 2005, 6th edn.

[241] Zienkiewicz, O. C. & Taylor, R. L.: *The Finite Element Method. The Basis, Vol. 1.* Butterworth-Heinemann, Oxford 2005, 6th edn.

[242] Zienkiewicz, O. C.; Taylor, R. L.; Sherwin, S. J. & Peiró, J.: On discontinuous Galerkin methods. *International Journal for Numerical Methods in Engineering* **58** (2003), 1119–1148.

Curriculum Vitae

Personal Data:

Name:	Nils Karajan
Parents:	Prof. Dr.-Ing. Rolf Heinz Karajan and Sieglinde Karajan
Siblings:	Dipl.-Ing. (FH) Katrin Karajan, Dr. techn. Jürgen Karajan, Dipl.-Ing. Axel Karajan
Date of birth:	March 13, 1977
Place of birth:	Waiblingen, Germany
Nationality:	German
Marital status:	unmarried

Education:

09/1983 – 07/1987	elementary school "Grundschule im Schelmenholz"
09/1987 – 06/1997	secondary/high school "Lessing Gymnasium Winnenden"
06/1997	degree: "Allgemeine Hochschulreife" (high school diploma)
09/1997 – 12/2002	studies in civil engineering at the "Universität Stuttgart" major subject: "Allgemeines Bauingenieurwesen"
12/2002	degree: "Diplom-Ingenieur (Dipl.-Ing.) Bauingenieurwesen"

Education in Foreign Countries:

09/1993 – 12/1993	Water Valley High School, Mississippi, USA
12/1993 – 07/1994	Biloxi High School, Mississippi, USA
09/2000 – 06/2001	University of Calgary, Canada

Internships:

08/1994 – 08/1996	Eimer HighCast GmbH, Korb, Germany
06/1997 – 07/1997	Rolf & Paul Käfer GmbH, Winnenden, Germany
08/1997 – 10/1997	Rolf Bauder GmbH, Winnenden, Germany
02/1996 – 09/1998	Karajan Ingenieure GmbH, Stuttgart, Germany
10/1998 – 12/2002	student teaching assistant at several institutes of the Faculty of Civil Engineering and Surveying

Professional Occupation:

01/2003 – 03/2009	assistant lecturer at the Institute of applied Mechanics (Civil Engineering) at the Universität Stuttgart, Germany

Released Report Series

II-1 Gernot Eipper: *Theorie und Numerik finiter elastischer Deformationen in fluidgesättigten porösen Festkörpern*, June 1998.

II-2 Wolfram Volk: *Untersuchung des Lokalisierungsverhaltens mikropolarer poröser Medien mit Hilfe der Cosserat-Theorie*, May 1999.

II-3 Peter Ellsiepen: *Zeit- und ortsadaptive Verfahren angewandt auf Mehrphasenprobleme poröser Medien*, July 1999.

II-4 Stefan Diebels: *Mikropolare Zweiphasenmodelle: Formulierung auf der Basis der Theorie Poröser Medien*, March 2000.

II-5 Dirk Mahnkopf: *Lokalisierung fluidgesättigter poröser Festkörper bei finiten elastoplastischen Deformationen*, March 2000.

II-6 Heiner Müllerschön: *Spannungs-Verformungsverhalten granularer Materialien am Beispiel von Berliner Sand*, August 2000.

II-7 Stefan Diebels (Ed.): *Zur Beschreibung komplexen Materialverhaltens: Beiträge anläßlich des 50. Geburtstages von Herrn Prof. Dr.-Ing. Wolfgang Ehlers*, August 2001.

II-8 Jack Widjajakusuma: *Quantitative Prediction of Effective Material Parameters of Heterogeneous Materials*, June 2002.

II-9 Alexander Droste: *Beschreibung und Anwendung eines elastisch-plastischen Materialmodells mit Schädigung für hochporöse Metallschäume*, October 2002.

II-10 Peter Blome: *Ein Mehrphasen-Stoffmodell für Böden mit Übergang auf Interface-Gesetze*, October 2003.

II-11 Martin Ammann: *Parallel Finite Element Simulations of Localization Phenomena in Porous Media*, April 2005.

II-12 Bernd Markert: *Porous Media Viscoelasticity with Application to Polymeric Foams*, July 2005.

II-13 Saeed Reza Ghadiani: *A Multiphasic Continuum Mechanical Model for Design Investigations of an Effusion-Cooled Rocket Thrust Chamber*, September 2005.

II-14 Wolfgang Ehlers & Bernd Markert (Eds.): *Proceedings of the 1st GAMM Seminar on Continuum Biomechanics*, September 2005.

II-15 Bernd Scholz: *Application of a Micropolar Model to the Localization Phenomena in Granular Materials: General Model, Sensitivity Analysis and Parameter Optimization*, November 2007.

II-16 Wolfgang Ehlers & Nils Karajan (Eds.): *Proceedings of the 2nd GAMM Seminar on Continuum Biomechanics*, December 2007.

II-17 Tobias Graf: *Multiphasic Flow Processes in Deformable Porous Media under Consideration of Fluid Phase Transitions*, June 2008.

II-18 Ayhan Acartürk: *Simulation of Charged Hydrated Porous Materials*, March 2009.

II-19 Nils Karajan: *An Extended Biphasic Description of the Inhomogeneous and Anisotropic Intervertebral Disc*, March 2009.